SANDIA REPORT

SAND87—0912 • UC—700
Unlimited Release
Printed June 1989

Evaluation of Systems and Components for Hybrid Optical Firing Sets

Murphy J. Landry, Jeffrey W. Rupert, Anthony Mittas

Prepared by
Sandia National Laboratories
Albuquerque, New Mexico 87185 and Livermore, California 94550
for the United States Department of Energy
under Contract DE-AC04-76DP00789

When printing a copy of any digitized SAND Report, you are required to update the markings to current standards.

Issued by Sandia National Laboratories, operated for the United States Department of Energy by Sandia Corporation.

NOTICE: This report was prepared as an account of work sponsored by an agency of the United States Government. Neither the United States Government nor any agency thereof, nor any of their employees, nor any of their contractors, subcontractors, or their employees, makes any warranty, express or implied, or assumes any legal liability or responsibility for the accuracy, completeness, or usefulness of any information, apparatus, product, or process disclosed, or represents that its use would not infringe privately owned rights. Reference herein to any specific commercial product, process, or service by trade name, trademark, manufacturer, or otherwise, does not necessarily constitute or imply its endorsement, recommendation, or favoring by the United States Government, any agency thereof or any of their contractors or subcontractors. The views and opinions expressed herein do not necessarily state or reflect those of the United States Government, any agency thereof or any of their contractors or subcontractors.

Printed in the United States of America. This report has been reproduced directly from the best available copy.

Available to DOE and DOE contractors from
Office of Scientific and Technical Information
PO Box 62
Oak Ridge, TN 37831

Prices available from (615) 576-8401, FTS 626-8401

Available to the public from
National Technical Information Service
US Department of Commerce
5285 Port Royal Rd
Springfield, VA 22161

NTIS price codes
Printed copy: A07
Microfiche copy: A01

SAND87–0912
Unlimited Release
Printed June 1989

Distribution
Category UC–700

Evaluation of Systems and Components for Hybrid Optical Firing Sets

Murphy J. Landry, Jeffrey W. Rupert, Anthony Mittas
Advanced Firing Set Division
Sandia National Laboratories
Albuquerque, NM 87185

Abstract

High-energy density light appears to be a unique energy form that may be used to enhance the nuclear safety of weapon systems. Hybrid optical firing sets (HOFS) utilize the weak-link/strong-link exclusion region concept for nuclear safety; this method is similar to present systems, but uses light to transmit power across the exclusion region barrier. This report describes the assembling, operating, and testing of fourteen HOFS. These firing sets were required to charge a capacitor-discharge unit to 2.0 and 2.5 kV (100 mJ) in less than 1 s. First, we describe the components, the measurement techniques used to evaluate the components, and the different characteristics of the measured components. Second, we describe the HOFS studied, the setups used for evaluating them, and the resulting characteristics. Third, we make recommendations for improving the overall performance and suggest the best HOFS for packaging.

Acknowledgments

The authors express their appreciation to the following personnel:

T. D. Donham (2364) for his support and encouragement during the entire project.

J. Castaneda (1128) for technical support and assistance.

J. K. Rice (1270) for the use of his laboratory space to perform our measurements.

The staff at SDL, Inc., especially D. R. Scifres, P. Cross, and D. Evans, for technical discussions and for making available advanced prototype laser diodes for test and evaluation. Also appreciated were the technical discussions with D. Welsh and the helpful efforts of J. R. Klein for getting laser diodes back and forth to us, and for their participation in our lengthy discussions.

The staff at MDAC/OEC, especially B. A. Soltz, for believing that they could produce broad-striped, high-powered laser diodes and then furnishing us with the diodes for test and evaluation. The help of H. J. Vollmer in getting laser diodes to us over several months and loaning us one of his test jigs to facilitate testing the diodes is greatly appreciated.

L. A. Godfrey of Applied Solar Energy Corporation for his perseverance in developing the hybrid 2-, 10-, and 16-V GaAs cells.

J. M. Gee (6224) for his helpful participation in our technical discussions. We are also grateful to Gee and to B. R. Hansen (6224) for the optical measurements they performed on the PVA GaAs cells.

D. Galluzzo of Gamma High Voltage Research, Inc., for providing a modified dc-dc voltage converter that worked with four types of GaAs cells.

Contents

Acronyms and Abbreviations 13

1. Introduction 15
   1.1 Enhanced Nuclear Safety in Abnormal Environments 15
   1.2 Optical Isolation and Coupling 15
   1.3 The Optical Firing Set 15
   1.4 The Hybrid Optical Firing Set 15
   1.5 Optical Energy Transfer 16
   1.6 The Xenon Arc 16
   1.7 Roberts Demonstration Circuit 16
   1.8 Transfer of Modulated Optical Energy 16
   1.9 Sandia Goals 17
   1.10 Organization of the Report 17

2. Description of the Components 18
   2.1 Laser Diode Driver 18
   2.2 Laser Diodes 18
      2.2.1 Specifications for SDL LDs 19
      2.2.2 Specifications for MDAC/OEC LDs 21
   2.3 Optical Couplers 23
      2.3.1 Fiber Optics 24
      2.3.2 GRIN Lenses 24
      2.3.3 FO and Lens Collimators 25
   2.4 Beam Interrupter-Coupler 26
   2.5 PVA GaAs Cells 27
   2.6 Dc-to-Dc Converters 28

3. Techniques Used to Measure Component Characteristics 29

4. Component Characteristics 36
   4.1 Laser Diodes 36
      4.1.1 Optical Power 36
      4.1.2 Efficiencies 42
      4.1.3 Degradation 45
      4.1.4 Beam Intensity Distribution 49
      4.1.5 Summary 62
   4.2 Couplers 63
      4.2.1 GRIN Lenses 64
      4.2.2 Fiber Optics 65
      4.2.3 Beam Intensity Distribution 75
      4.2.4 Summary 92
   4.3 Beam Interrupter-Coupler 96
      4.3.1 P-C Lens Collimation for Different FOs as Input 96
      4.3.2 Transmission Through Aperture as Prism Rotates 98

Contents (continued)

4.4 PVA GaAs Cells 99
4.4.1 Electrical Power 99
4.4.2 Optimum R_p 101
4.4.3 Efficiency 103
4.4.4 I vs. V Curves 104
4.4.5 Fill Factor 106
4.4.6 Summary 106

5. HOFS Systems Configurations 108
5.1 HOFS Systems Configuration Summarized 108
5.2 First-Generation HOFS 1′ and 1-8 110
5.3 Second-Generation HOFS, 9-14 and 14′ 112

6. Characteristics of the HOFS Systems Measured 114
6.1 Cell and Converter Efficiencies 115
6.1.1 First-Generation HOFS, 1-8 115
6.1.2 Second-Generation HOFS, 9-14 116
6.2 HOFS System Efficiencies 117
6.2.1 First-Generation HOFS, 1-8 118
6.2.2 Second-Generation HOFS, 9-14 and 14′ 119
6.3 HOFS System Charge Times 121
6.3.1 First-Generation HOFS, 1-8 121
6.3.2 Second-Generation HOFS, 9-14 and 14′ 122
6.4 Summary of HOFS 1′, 1-14, and 14′ 124
6.4.1 First-Generation HOFS 1′, 1-8 124
6.4.2 Second-Generation HOFS 9-14 and 14′ 124
6.4.3 Best HOFS System Efficiency 124

7. Conclusions 126
7.1 Efficiencies of Dc-Dc Converters and GaAs Cell Combination 126
7.2 HOFS System Charge Time 126

References 128

Figures

1 Simplified Block Diagram of the Hybrid Optical Firing Set System 15
2 Detailed Block Diagram of the Hybrid Optical Firing Set System 16
3 Block Diagram of LD Current Driver Built at SNLA 18
4 Configuration of SDL Multi-Striped 100-mW, 500-mW, 1-W, 4-W, and 8-W LDs 21
5 Configuration of MDAC/OEC Developmental Single-Striped LDs 23
6 Four Types of Optical Coupling Schemes 23
7 In-Line Beam Interrupter-Coupler Configuration 26
8 Out-of-Line Beam Interrupter-Coupler Configuration 26
9 Configuration of PVA GaAs Concentrator Cells Fabricated by ASEC 27
10 Circuit Used in Gamma Dc-to-Dc Converters, Which Use a Jensen Oscillator 28
11 Photograph of Energy Meter in Front of SDL 100-mW LD 30
12 Photograph of Energy Meter in Front of 600-μm FO 31
13 Photograph of FO Butt-Coupled to SDL 100-mW LD 32
14 Setup Used to Measure Transmission of GRIN Lenses, GRIN Lenses and FO Combination, and FO 33

Figures (continued)

15 Setup Used to Measure the LD Beam Dimension Out of P-C Lens Coupled to a FO 33
16 Setup Used to Measure the Transmission Through a 3.8-mm Aperture Located Different Distances From Prism as It Is Rotated 34
17 Photograph of Safety Box With High-Voltage Components 35
18 Optical Power vs. Current for Six SDL 100-mW LDs Operating up to 100 mW 36
19 Optical Power vs. Current for Two SDL 100-mW LDs Operating up to 400 mW, Four Times Their Rated Power Levels 37
20 Erratic Behavior of SDL 100-mW LD A195 Undergoing Degradation 37
21 Optical Power vs. Current for Two SDL 500-mW LDs Operating up to 500 mW, at 1-min Intervals 38
22 Optical Power vs. Current for Two SDL 500-mW LDs Operating up to 2 W, Four Times Their Rated Power Levels, at 3- and 10-min Intervals 38
23 Optical Power vs. Current for Special SDL 500-mW LD C347 Operating up to 500 mW, TE-Cooled at 1-min Intervals 38
24 Optical Power vs. Current for SDL 1-W LD C338 Operating up to 1 W, TE- and Fin-Cooled at 2-min Intervals 39
25 Optical Power vs. Current for Three 4-W and One 8-W Prototype SDL LDs 39
26 Optical Power vs. Current for Four Coated-Cavity-Mirror MDAC/OEC Developmental 1-W LDs Operating up to Their Catastrophic Levels 40
27 Optical Power vs. Current for Seven Uncoated-Cavity-Mirror MDAC/OEC Developmental 2-W LDs Operating up to Their Catastrophic Levels 41
28 Optical Power vs. Current for Two Extra-Long Coated-Cavity-Mirror MDAC/OEC Developmental 5-W LDs Operating up to Their Catastrophic Levels 41
29 Efficiency vs. Optical Power for Six SDL 100-mW LDs Operating up to 100 mW 42
30 Efficiency vs. Optical Power for Three SDL 100-mW LDs Operating up to 400 mW, Four Times Their Rated Power Levels 42
31 Efficiency vs. Optical Power for Two SDL 500-mW LDs Operating up to 500 mW 43
32 Efficiency vs. Optical Power for Two SDL 500-mW LDs Operating up to 2 W, Four Times Their Rated Power Levels 43
33 Efficiency vs. Optical Power Using SDL 500-mW LD C347 Operating up to 500 mW, TE-Cooled at 2-min Intervals 43
34 Efficiency vs. Optical Power Using SDL 1-W LD C338 Operating up to 1 W, TE-Cooled at 2-min Intervals 43
35 Efficiency vs. Optical Power for Three 4-W and One 8-W Prototype SDL LDs 44
36 Efficiency vs. Optical Power for Seven Uncoated-Cavity-Mirror MDAC/OEC Developmental 2-W LDs Operating up to Their Catastrophic Levels 44
37 Efficiency vs. Optical Power for Four Coated-Cavity-Mirror MDAC/OEC Developmental 1-W LDs Operating up to Their Catastrophic Levels 45
38 Efficiency vs. Optical Power for Two Extra-Long Coated-Cavity-Mirror MDAC/OEC Developmental 5-W LDs Operating up to Their Catastrophic Levels 45
39 Degradation Due to Heating Illustrated by Optical Power vs. Current of SDL 100-mW LD B126 Operating up to 400 mW, Four Times Its Rated Power Level, at 10-min and 30-s Time Intervals 45
40 Degradation Due to Heating Illustrated by Optical Power vs. Current of SDL 500-mW LD A841 Operating up to 2 W, Four Times Its Rated Power Level, at 10-min, 2-min, and 30-s Time Intervals 46

Figures (continued)

41 Degradation Due to Heating Illustrated by Optical Power vs. Current of SDL 500-mW LD A840 Operating up to 500 mW, Its Rated Power Level, at 1- and 5-min Time Intervals 46
42 Degradation Due to Heating Illustrated by Optical Power vs. Current of SDL 500-mW LD A840, TE-Cooled, Operating up to 2 W, Four Times Its Rated Power Level, at 5-, 3- and 1-min Intervals 47
43 Degradation Due to Heating Illustrated by Optical Power vs. Current of SDL 500-mW LD A840, TE- and Fin-Cooled, Operating up to 2 W, Four Times Its Rated Power Level, at 3-min Intervals 47
44 Degradation Due to Heating Illustrated by Efficiency vs. LD Optical Power of SDL 500-mW LD A840, TE- and Fin-Cooled, Operating up to 2 W, Four Times Its Rated Power Level, at 3-min Intervals 47
45 Aging Illustrated by Optical Power vs. Current of SDL 500-mW LD A841 Operating up to 2 W, Four Times Its Rated Power Level, at Different Times During Its Life 48
46 Aging Illustrated by Efficiency vs. Optical Power of SDL 500-mW LD A841 Operating up to 2 W, Four Times Its Rated Power Level, at Different Times During Its Life 48
47 Aging Illustrated by Optical Power vs. Current of Four Prototype SDL LDs: Two 4-W LDs and an 8-W LD Operating up to 2 and 2.8 W at Different Times During Their Lives 48
48 Aging Illustrated by Efficiency vs. Optical Power of Four Prototypes SDL LDs: Two 4-W LDs and an 8-W LD Operating up to 2 and 2.8 W at Different Times During Their Lives 48
49 Contours and Profiles of Intensity Distribution of the Output Beam of SDL 100-mW LD A322 Operating at 99.8 mW (I) and 395 mW (II), Recorded 9.6 mm From the LD Mirror 49
50 Contours and Profiles of Intensity Distribution of the Output Beam of SDL 500-mW LD A840 Operating at 522 mW (I) and 1952 mW (II), Recorded 9.6 mm From the LD Mirror 50
51 Contours and Profiles of Intensity Distribution of the Output Beam Early in the Life of SDL 8-W LD BN968 51
52 Contours and Profiles of Intensity Distribution of the Output Beam Later in the Life of SDL 8-W LD BN968 52
53 Contours and Profiles of Intensity Distribution of the Output Beam of SDL 8-W LD BN968 Operating at 1 W as Shots Accumulate 54
54 Contours and Profiles of Intensity Distribution of the Output Beam of SDL 8-W LD BN968 Operating at 2 W as Shots Accumulate 55
55 Contours and Profiles of Intensity Distribution of the Output Beam of SDL 8-W LD BN968 Taken at Different Times After LD Turn-On 56
56 Contours and Profiles of Intensity Distribution of the Output Beam Early in the Life of SDL 4-W LD RP542 59
57 Contours and Profiles of Intensity Distribution of the Output Beam Later in the Life of SDL 4-W LD RP542 60
58 Contours and Profiles of Intensity Distribution of the Output Beam of SDL 4-W LD RP542 Taken at Different Times After LD Turn-On 62
59 Transmission of Five GRIN Lenses With 0.23-, 0.25-, 0.29-, 0.5A-, and 0.5B-Pitch Using SDL 100-mW LD A322 as Source, Operating at 17-, 100-, and 400-mW Power Levels 64
60 Transmission of Five GRIN Lenses With 0.23-, 0.25-, 0.29-, 0.5A-, and 0.5B-Pitch Using SDL 500-mW LD A841 as Source, Operating at 60-, 500-, and 2000-mW Power Levels 65
61 Optical Power Detected vs. Distance From Source Using SDL 100-mW LD B126 and 0.23-Pitch GRIN Lens as Source With 0.368-dia Apertured Energy Meter 65
62 Transmission of 1000-μm FO_4 #1 vs. Optical Power Using SDL 100-mW LD A322, LD A322 and 0.5A-Pitch GRIN Lens, and LD A322 and 0.5B-Pitch GRIN Lens as Sources 66
63 Transmission of 600-μm FO_3 #1 vs. Optical Power Using SDL 100-mW LD A322, LD A322 and 0.5A-Pitch GRIN Lens, and LD A322 and 0.5B-Pitch GRIN Lens as Sources 66
64 Transmission of 1000-μm FO_4 #1 vs. Optical Power Using SDL 500-mW LD A841, LD A841 and 0.5A-Pitch GRIN Lens, and LD A841 and 0.5B-Pitch GRIN Lens as Sources 67
65 Transmission of 600-μm FO_3 #1 vs. Optical Power Using SDL 500-mW LD A841, LD A841 and 0.5A-Pitch GRIN Lens, and LD A841 and 0.5B-Pitch GRIN Lens as Sources 67

Figures (continued)

66 Transmission of 600-μm FO_3 #1 vs. Optical Power Using Two SDL 100-mW LDs as Sources 68
67 Transmission of 600-μm FO_3 #1 vs. Optical Power Using Two SDL 500-mW LDs as Sources, With FO Ends Repolished Twice 68
68 Transmission of 600-μm FO_3 #1 and 1000-μm FO_4 #1 vs. Optical Power Using SDL 100-mW LD A322 as Source 68
69 Transmission of 600-μm FO_3 #1 and 1000-μm FO_4 #1 vs. Optical Power Using SDL 500-mW LD A841 as Source 69
70 Transmission of 200-μm FO_2 #1 vs. Optical Power Using Two Prototype SDL 4-W LDs as Sources 69
71 Transmission of 200-μm FO_2 #1 vs. Optical Power Using a Prototype SDL 8-W LD as Source, FO Is Aligned When LD Is Emitting 2 W 71
72 Transmission of 200-μm FO_2 #1 vs. Optical Power Using a Prototype SDL 8-W LD as Source, FO Is Aligned at Each LD Optical Power Level 71
73 Transmission of 200-μm FO_2 #1 vs. X Position Using a Prototype SDL 8-W LD as Source for Four Incident LD Optical Power Levels 72
74 Transmission of 200-μm FO_2 #1 vs. Y Position Using a Prototype SDL 8-W LD as Source for Four Incident LD Optical Power Levels 72
75 Transmission of 200-μm FO_2 #1 vs. X Position Using a Prototype SDL 8-W LD as Source for Three Incident LD Optical Power Levels 73
76 Transmission of 200-μm FO_2 #1 vs. Y Position Using a Prototype SDL 8-W LD as Source for Three Incident LD Optical Power Levels 73
77 Transmission of 600-, 400-, 200-, and 100-μm FOs vs. Optical Power Using SDL 4-W LD Operating at 0.5, 1, and 1.8 W of Output Optical Power 74
78 Transmission of P-C Lens vs. Optical Power Level Using Four FOs Coupled to SDL 4-W LD RP542 as Sources, With the LD Operating at 0.5, 1, and 1.8 W of Output Optical Power 75
79 Transmission of 100-μm FO_1 #1 vs. Optical Power Using Four MDAC/OEC 1-W LDs as Sources, Operating With 0.5 W, up to 1.5 W, 0.9 W, and up to 0.6 W of Output Optical Power 75
80 Contours and Profiles of Intensity Distribution of the Output of 0.23-Pitch GRIN Lens Butt-Coupled to SDL 100-mW LD Operating at 400 mW 76
81 Contours and Profiles of Intensity Distribution of the Output of 600-μm FO_3 #1 Butt-Coupled to SDL 100-mW LD Operating at 99.5 mW (I) and 395 mW (II) 77
82 Contours and Profiles of Intensity Distribution of Output of 600-μm FO_3 #1 Butt-Coupled to SDL 500-mW LD Operating at 515 mW (I) and 1911 mW (II) 77
83 Contours and Profiles of Intensity Distribution of the Output of Two 104.3-cm-long 600-μm FO_3 #1 and FO_3 #4 Looped and Straight, Recorded Close (5.13 mm) and Far (7.13 mm) From FO Output End and 9.08 mm and 11.08 mm 78
84 Contours and Profiles of Intensity Distribution of the Output of Two 49.4-cm-long 600-μm FO_3 #1 and FO_3 #7 Straight, Recorded Close (5.13 mm) and Far (7.13 mm) From FO Output End 79
85 Contours and Profiles of Intensity Distribution of the Output of 600-μm FO_3 #7 Recorded 5.13 mm From FO Output End After Successively Cutting in Half Four Times 80
86 Contours and Profiles of Intensity Distribution of the Output of 600-μm FO_3 #7 Recorded 7.13 mm From FO Output End After Successively Cutting in Half Four Times 81
87 Contours and Profiles of Intensity Distribution of the Output of 49.4-cm-long 600-μm FO_3 #1 Recorded at Varying Distances From FO Output End 83
88 Contours and Profiles of Intensity Distribution of the Output of 97.3-cm-long 200-μm FO_2 #1 Recorded at Varying Distances From FO Output End 84
89 Contours and Profiles of Intensity Distribution of the Output of 101.2-cm-long 200-μm FO_2 #2 Recorded 7.13 mm From FO Output End After Successively Cutting in Half Five Times 86
90 Contours and Profiles of Intensity Distribution of the Output of 101.2-cm-long 200-μm FO_2 #2 Recorded 9.13 mm From FO Output End After Successively Cutting in Half Five Times 87

Figures (continued)

91 Contours and Profiles of Intensity Distribution of the Output of 101.2-cm-long 200-μm FO_2 #2 Recorded at Varying Distances From FO Output End 88

92 Contours and Profiles of Intensity Distribution of the Output of 49.4-cm-long 200-μm FO_2 #2 Recorded at Varying Distances From FO Output End 88

93 Contours and Profiles of Intensity Distribution of the Output of 24.8-cm-long 200-μm FO_2 #2 Recorded at Varying Distances From FO Output End 89

94 Contours and Profiles of Intensity Distribution of the Output of 101.2-cm-long 200-μm FO_2 #2 Looped and Straight and 4.2-cm-long Straight Recorded Close (7.13 mm) and Far (9.13 mm) From FO Output End 90

95 Contours and Profiles of Intensity Distribution of the Output of 12.2-cm-long 200-μm FO_2 #2 Aligned to SDL RP542 and Then Misaligned in Both X and Y Axes 91

96 Contours and Profiles of Intensity Distribution of the Output of 9.04-mm-long SDL 100-μm FO Stub Recorded at Varying Distances From FO Output End 94

97 X Dimension of LD Beam Emitting 0.5 W Transmitted Through 600-, 400-, 200-, and 100-μm FOs vs. Distance From the P-C Lens 96

98 Y Dimension of LD Beam Emitting 0.5 W Transmitted Through 600-, 400-, 200-, and 100-μm FOs vs. Distance From the P-C Lens 96

99 X Dimension of LD Beam Emitting 1 W Transmitted Through 600-, 400-, 200-, and 100-μm FOs vs. Distance From the P-C Lens 97

100 Y Dimension of LD Beam Emitting 1 W Transmitted Through 600-, 400-, 200-, and 100-μm FOs vs. Distance From the P-C Lens 97

101 X Dimension of LD Beam Emitting 1.8 W Transmitted Through 600-, 400-, 200-, and 100-μm FOs vs. Distance From the P-C Lens 97

102 Y Dimension of LD Beam Emitting 1.8 W Transmitted Through 600-, 400-, 200-, and 100-μm FOs vs. Distance From the P-C Lens 97

103 Transmitted LD Output Optical Power Through 3.8-mm Aperture vs. Prism Angular Displacement for LD Beam Collimated by 94.5-cm-long, 200-μm-dia FO_2 #1 and P-C Lens Combination With Aperture at 52.0-, 67.8-, and 97.2-mm Distance From the P-C Lens 98

104 Electrical Power Generated by 1-V PVA GaAs Cell #10 vs. Load Resistance for 300, 400, 500, 600, 800, 1000, 1250, and 1500 mW of Optical Power Incident on the Cell Using SDL 500-mW LD Coupled to 600-μm FO_3 #1 as Source 99

105 Electrical Power Generated by 2-V PVA GaAs Cell #12 vs. Load Resistance for 300, 500, 600, 800, 1000, 1250, and 1500 mW of Optical Power Incident on the Cell Using SDL 500-mW LD Coupled to 600-μm FO_3 #1 as Source 100

106 Electrical Power Generated by 10-V PVA GaAs Cell #3 vs. Load Resistance for 300, 400, 500, 600, 800, 1000, 1250, and 1500 mW of Optical Power Incident on the Cell Using SDL 500-mW LD Coupled to 600-μm FO_3 #1 as Source 100

107 Electrical Power Generated by 16-V PVA GaAs Cell #39 vs. Load Resitance for 100, 850, and 1500 mW of Optical Power Incident on the Cell Using SDL 500-mW LD Coupled to 600-μm FO_3 #1 as Source 101

108 Electrical Power Generated by 10-V PVA GaAs Cell #5 vs. Load Resistance for 800, 1000, 1250, and 1650 mW of Optical Power Incident on the Cell Using SDL 500-mW LD Coupled to 600-μm FO_3 #1 as Source 101

109 Optimum Load Resistance for 1-, 2-, 10-, and 16-V PVA GaAs Cells vs. Incident LD Optical Power Using SDL 500-mW LD Coupled to 600-μm FO_3 #1 as Source 102

110 Maximum Efficiency for 1-, 2-, 10-, and 16-V PVA GaAs Cells vs. Incident LD Optical Power Using SDL 500-mW LD Coupled to 600-μm FO_3 #1 as Source 103

111 Current for 1-V PVA GaAs Cell #10 vs. Voltage for 100, 200, 400, 600, 800, 1000, 1250, and 1500 mW of Optical Power Incident on the Cell Using SDL 500-mW LD Coupled to 600-μm FO_3 #1 as Source 104

Figures (continued)

112 Current for 2-V PVA GaAs Cell #12 vs. Voltage for 100, 300, 500, 600, 800, 1000, 1250, and 1500 mW of Optical Power Incident on the Cell Using SDL 500-mW LD Coupled to 600-μm FO_2 #1 as Source 104

113 Current for 10-V PVA GaAs Cell #3 vs. Voltage for 100, 300, 500, 600, 800, 1000, 1250, and 1500 mW of Optical Power Incident on the Cell Using SDL 500-mW LD Coupled to 600-μm FO_2 #1 as Source 105

114 Current for 16-V PVA GaAs Cell #39 vs. Voltage for 100, 800, and 1500 mW of Optical Power Incident on the Cell Using SDL 500-mW LD Coupled to 600-μm FO_2 #1 as Source 105

115 Short-Circuit Current for 2-V Cell #12 vs. Incident Optical Power Density and Distance Between 200-μm FO_2 #1 and Cell, With LD Emitting 1 W Into the FO and FO Transmitting 0.83 W Onto the Cell 106

116 Fill Factor for 1-, 2-, 10-, and 16-V GaAs Cells vs. Incident Optical Power Using SDL 500-mW LD Coupled to 600-μm FO_2 #1 as Source 106

117 Basic Block Diagram of Setup Used to Test HOFS Systems 1 Through 14 and 14′ 110

118 Block Diagram of Setup Used to Test HOFS System 1′ Using Breadboard LD Driver 110

119 Block Diagram of Setup Used to Test HOFS System 1 110

120 Photograph of HOFS 2 Showing Components Mounted Onto Kinematic Mounts, Allowing for X, Y, and Z Motions 111

121 Block Diagram of Setup Used to Test HOFS System 4 112

122 Photograph of HOFS System 4 Showing Components Mounted Onto Kinematic Mounts, Allowing for X, Y, and Z Motions 113

123 Voltage Trace Recorded by OSC #2 of the Voltage Across R_3 of the Resistor Network Across the HV Capacitor of HOFS System 1 114

124 Voltage Trace Recorded by OSC #2 of Voltage Across R_3 of the Resistor Network Across the HV Capacitor of HOFS System 1 Kept Constant After 5 s of Charge 114

125 Efficiency of the Combination PVA GaAs Cell and dc-to-dc Converter vs. LD Output Optical Power for 1/e of V_m for Eight HOFS Systems Described in Table 13 115

126 Efficiency of the Combination PVA GaAs Cell and dc-to-dc Converter vs. LD Output Optical Power for 100 and 220 mJ of Energy Charge for Eight HOFS Systems Described in Table 13 115

127 Efficiency of the Combination PVA GaAs Cell and dc-to-dc Converter vs. LD Output Optical Power for 90% of V_m for Eight HOFS Systems Described in Table 13 116

128 Efficiency of the Combination PVA GaAs Cell and dc-to-dc Converter vs. LD Output Optical Power for 1/e of V_m for Six HOFS Systems Described in Table 13 117

129 Efficiency of the Combination PVA GaAs Cell and dc-to-dc Converter vs. LD Output Optical Power for 100 and 220 mJ of Energy Charge for Six HOFS Systems Described in Table 13 117

130 Efficiency of the Combination PVA GaAs Cell and dc-to-dc Converter vs. LD Output Optical Power for 90% of V_m for Six HOFS Systems Described in Table 13 117

131 Total System Efficiency vs. LD Output Optical Power for 1/e of V_m for Eight HOFS Systems Described in Table 13 118

132 Total System Efficiency vs. LD Output Optical Power for 100 and 220 mJ of Charge for Eight HOFS Systems Described in Table 13 118

133 Total System Efficiency vs. LD Output Optical Power for 90% of V_m for Eight HOFS Systems Described in Table 13 118

134 Total System Efficiency vs. LD Output Optical Power for 1/e of V_m for Six HOFS Systems Described in Table 13 119

135 Total System Efficiency vs. LD Output Optical Power for 100 and 220 mJ of Charge on Six HOFS Systems Described in Table 13 119

136 Total System Efficiency vs. LD Output Optical Power for 90% of V_m for Six HOFS Systems Described in Table 13 120

Figures (continued)

137 Total System Efficiency vs. FO to Cell Distance From 0.19 in. (4.78 mm) to 0.48 in. (12.14 mm) for 100 mJ of Charge for HOFS 14′ Described in Table 13 120
138 Charge Time of HOFS Capacitor vs. LD Output Optical Power for 1/e of V_m for Eight HOFS Systems Described in Table 13 121
139 Charge Time of HOFS Capacitor vs. LD Output Optical Power for 100 and 220 mJ of Charge for Eight HOFS Systems Described in Table 13 121
140 Charge Time of HOFS Capacitor vs. LD Output Optical Power for 90% of V_m for Eight HOFS Systems Described in Table 13 121
141 Charge Time of HOFS Capacitor vs. LD Output Optical Power for 1/e of V_m for Six HOFS Systems Described in Table 13 122
142 Charge Time of HOFS Capacitor vs. LD Output Optical Power for 100 and 220 mJ of Charge for Six HOFS Systems Described in Table 13 122
143 Charge Time of HOFS Capacitor vs. LD Output Optical Power for 90% of V_m for Six HOFS Systems Described in Table 13 123
144 Charge Time of HOFS Capacitor vs. FO to Cell Distance From 0.188 in. (4.78 mm) to 0.478 in. (12.14 mm) for 100 mJ of Charge on HOFS System 14′ Described in Table 13. 124
145 Block Diagram Summarizing HOFS System and Component Efficiencies for the Best HOFS System (14), Measured and Predicted HOFS System, and Component Efficiencies Achievable in the Near Future 127

Tables

1 SDL Laser Specifications 20
2 MDAC/OEC Laser Specifications 22
3 Characteristics of GaAs Cells Measured by ASEC or SNLA With White Light 28
4 Beam Specifications for SDL 8-W LD BN968 Data 57
5 Beam Specifications for SDL 4-W LD RP542 Data 61
6 Beam Specifications for Different 600-μm FOs and FO Lengths 82
7 Beam Specifications for Two FOs at Different Positions From the End of Two FOs 85
8 Beam Specifications for 200-μm FO_2 #2 of Different Lengths 93
9 Beam Specifications for 9.0-mm-long, 100-μm FO Stub at Different Distances From Its Output End 95
10 a and b Coefficients for Equation 34 102
11 Predicted R_p Values of Four GaAs Cells for Different Optical Powers 103
12 Characteristics of PVA GaAs Cells Measured With 1.5 W of Incident LD Optical Power 107
13 Components of the Hybrid Optical Firing Set Systems 109
14 Performance Characteristics of the Hybrid Optical Firing Set Systems 125

Acronyms and Abbreviations

ASEC	Applied Solar Energy Corporation
AST	Asterisks
BIC	Beam interrupter-coupler
CC	Correlation coefficient
CDU	Capacitor discharge unit
CFS	Conventional firing set
CID	Charge injection device
CIR	Circles
CW	Continuous wave
DH	Double heterostructure
EM	Energy/power meter
EMR	Electromagnetic radiation
FF	Fill factor
FO	Fiber optics
FWHM	Full-width half-maximum
GRIN	Graded index
H	Horizontal
HE	High explosives
HE-NE	Helium-Neon
H/L	High/low
HOFS	Hybrid optical firing set
HP	Hewlett Packard
HR/AR	High-reflective/anti-reflective
HV	High voltage
IR	Infrared
L	Loop
LANL	Los Alamos National Laboratory
LCB	Large copper block
LD	Laser diode
LED	Light-emitting diode
MDAC/OEC	McDonnell Douglas Astronautics Company/Optoelectronics Center
MOCVD	Metal-Organic Chemical Vapor Deposition
MQW	Multiple-quantum well
NA	Numerical aperture
nf	No fit
NGOL	Nd^{3+} glass oscillator laser
OFS	Optical firing set
OSC	Oscilloscope
P-C	Plano-convex
PETN	Pentaerythritol tetranitrate
PVA	Photovoltaic array
RC	Resistor capacitor

S	Straight
SDL	Spectra Diode Laboratory
SL	Strong link
SNLA	Sandia National Laboratories, Albuquerque
SNLL	Sandia National Laboratories, Livermore
SQS	Squares
SQW	Single-quantum well
TE	Thermoelectric
TRI	Triangles
TTL	Transistor-transistor logic
V	Vertical

Evaluation of Systems and Components for Hybrid Optical Firing Sets

1. Introduction

1.1 Enhanced Nuclear Safety in Abnormal Environments

During the 1970s, Sandia National Laboratories (SNL) introduced the weak-link/strong-link, exclusion region concept into the design of nuclear weapons to provide enhanced nuclear safety in abnormal environments. Isolation of the exclusion region was controlled by a unique signal (electro-mechanical strong links) that operated electrical switch contacts.

In the 1980s, the wireless firing set was developed and put into production in the W88 warhead. The wireless concept uses magnetic coupling across the exclusion-region barrier to replace the electrical switch contacts. As a further improvement, optical technologies are being considered for firing set designs for the 1990s.

1.2 Optical Isolation and Coupling

Optical coupling into the exclusion region may be used with two general concepts: (1) Optical pulses generated outside the exclusion region are transmitted by fiber optics to directly and promptly initiate the detonator/high explosives. (2) Optical energy is transmitted across the exclusion region barrier to charge a capacitor discharge unit (CDU) that initiates the detonators. In either concept, safety is enhanced by the unique energy form of high-energy density light. Inadvertent coupling of significant undesired energy such as lightning, EMR, and high-voltage electrical power to the light paths appears to be very unlikely.

1.3 The Optical Firing Set

One of our main interests is in the prompt initiation of high explosives (HE) using an optical pulse. In this concept, the HE in the weapon is initiated by the optical pulse directly, which is generated outside the exclusion region and coupled inside by a dielectric coupler. Previous efforts[1-6] indicate that optical initiation of secondary HE, e.g., PETN, HNX, etc., is possible. However, the present stage of development of the source (solid-state laser) toward the environmental weapon requirements requires us to consider an alternative method, a Hybrid Optical Firing Set (HOFS).

1.4 The Hybrid Optical Firing Set

Figure 1 shows the hybrid optical firing set (HOFS) as an intermediate alternative to the complete optical firing set (OFS). In this concept, the main objective is to use optical energy across the exclusion region barrier. In the HOFS, a CDU is used to initiate the explosives.

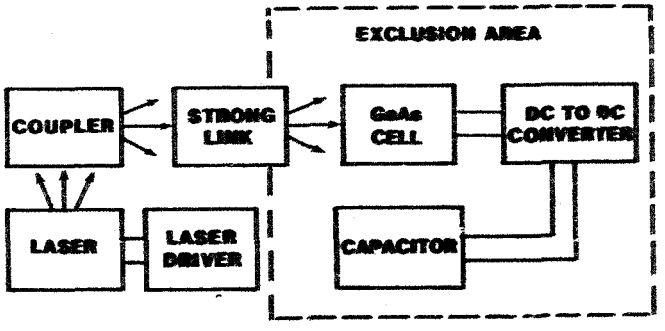

Figure 1. Simplified Block Diagram of the Hybrid Optical Firing Set System

In this concept, the electrical energy is converted into optical energy via a high-power laser diode (LD) external to the exclusion region. The optical energy is coupled into the exclusion region through an optical coupler. Once the optical energy is inside the exclusion region, it is converted back into electrical energy by an optical detector cell. The voltage is stepped up by a dc-dc converter, and stored in a capacitor. The intended functions can then be performed as usual (Figure 2). The transfer of small amounts of optical energy for the dc-dc trigger and the low-voltage converter is readily available. Previous to this study the transfer of large amounts of optical energy for the dc-dc converter high voltage (HV) was not available. This report documents our investigation of large amounts of energy transfers across boundaries.

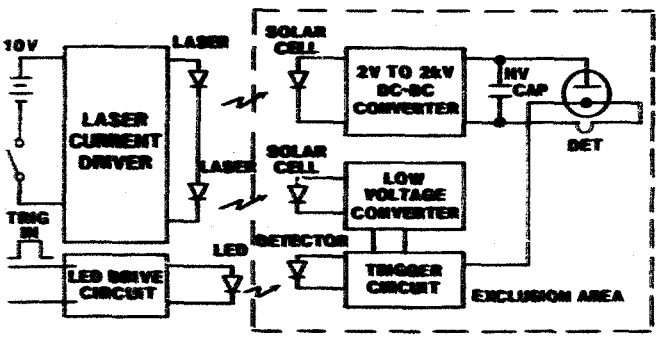

Figure 2. Detailed Block Diagram of the Hybrid Optical Firing Set System

1.5 Optical Energy Transfer

In 1980, M. M. Robertson[7,8] investigated several techniques for optical energy transfer. The state-of-the-art 10-mW semiconductor LDs and GaAs/Si cells limited the rate of energy transfer. One of the techniques consisted of a LD and fiber optics (FO) that coupled 6.9 mW of optical energy onto the surface of an SNLA single-junction back-surface Si solar cell. The efficiency of the cell was 7% when loaded by a special low-voltage dc-dc voltage converter.[9] The 0.25 V from the cell was increased and regulated to 2.89 V, for a conversion efficiency of 54%. The converter was used to drive a quartz oscillator, which consumed 0.29 mW. The cell and dc-dc converter efficiencies were 3.8%. Unfortunately, no attempts were made to charge a high-voltage capacitor.

1.6 The Xenon Arc

In a follow-on experiment, Robertson used a xenon arc focused into a FO bundle (which was optically coupled to a Si photovoltaic "Quad" cell) to charge the capacitor in an MC2901 weapon component. The 290 mW of optical power incident onto the cell allowed the dc-dc converter to charge the capacitor to 380 V in 18.5 s, whereas the conventional power source required 6 to 8 s.

1.7 Roberts Demonstration Circuit

In 1985, R. P. Roberts[10] configured and constructed a demonstration circuit in which a 0.05-μF capacitor was charged to 2 kV, using two Spectra Diode Laboratory (SDL) 100-mW high-powered phase-locked[11-13] (GaAl)As LDs and two 1-V photovoltaic array (PVA) GaAs cells. Since the LDs were overdriven, the HOFS system could charge the capacitor to about 70 mJ in ~5 s. Two other signals were generated:

- Low-voltage signals under 100 V developed from another LD/cell combination
- A high-voltage trigger signal developed from a light-emitting diode (LED)/cell combination.

1.8 Transfer of Modulated Optical Energy

In April 1987, B. A. Tuttle *et al.*[14] demonstrated and reported the transfer of modulated optical energy (which is generated in a LD) through a 9.5-mm-long FO charging a 30-μF capacitor to the low voltage of 27 V dc in 3 s. The SDL-2422 200-mW LD is operated at a pulse rate of 100 kHz (5-μs pulse duration) for a 50% duty cycle. The 100 mW of peak optical power out of the FO is equal to 8% of electrical power into the LD. The 30% efficiency of the 0.13-cm^2 GaAs cell and the 58% efficiency of the transformer result in a total system efficiency of $0.08 \times 0.30 \times 0.58 = 1.3\%$.

1.9 Sandia Goals

In April 1986, Organization 2364 took as requirements of HOFS systems the storing of at least 100 mJ of energy in a capacitor at a voltage between 2 and 2.5 kV in less than 1 s. This report describes the assembling, operation, and testing of fourteen HOFS systems with the goal of satisfying this requirement. We attempted to use components in the HOFS systems that were off-the-shelf items, available in large quantities, and could be made insensitive to radiation environments.

1.10 Organization of the Report

In this report, we first describe the components used in the HOFS systems, the measurement techniques used to evaluate these components, and the different characteristics of these components measured. Next, we describe the HOFS systems studied, the different setups used to evaluate three systems, and the different characteristics of the systems measured. Finally, we give our recommendations for improving the overall performance of the HOFS systems.

2. Description of the Components

The components of the HCFS systems include a LD current driver, LDs, optical couplers, strong links, photovoltaic cells, dc-dc voltage converters, capacitors, and test equipment. All but the last two components are described in this section.

After we began this project, improved components—in particular, new LDs—became available. These new LDs prompted us to test different FO couplers, photovoltaic cells, and dc-dc converters. This accounts for:

- The varying output optical power data on the different LDs
- The FO with different diameters
- The dc-dc converter with different input voltage

The data are presented in chronological order.

2.1 Laser Diode Driver

Figure 3 is a block diagram of the special LD current driver system built at SNLA. The driver system is able to drive two LDs independently. System control is a 4-pole double-throw switch that supplies power to the LDs, triggers the three counters and the timer, and starts the clock. Direct-Current Power Supply 1 and 2 (Hewlett-Packard Model 6257B) delivers the current to the LDs via the high/low (H/L) current drivers.

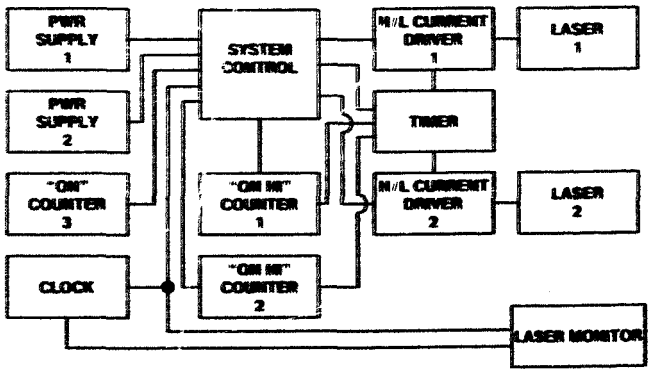

Figure 3. Block Diagram of LD Current Driver Built at SNLA

The timer provides a pulse to the H/L current drivers when the system is turned on; the pulse is TTL low for 5 s, then remains high until the system is turned off. While the pulse is low, the H/L current driver supplies a high current to the LDs as controlled by the dc power supply. When the pulse is high, a lower current is supplied; this current is controlled by a variable resistor. The H/L current drivers can also be bypassed; in this case, the LDs can be driven at high current only. The three counters were designed and built at SNLA and use TTL logic:

- The "ON HIGH" Counters 1 and 2 count the number of times the LDs are driven at high current. The counters are triggered by System Control if the H/L current drivers have not been bypassed. The count registered is multiplied by the timer pulse duration and determines how long the LDs were driven by the high current.
- The "ON" Counter 3 counts the number of times the system was turned on, and is not dependent on whether or not the H/L current drivers have been bypassed.

The clock, designed and built at SNLA, is turned on by System Control and provides a 1-Hz pulse. Together with a Hewlett-Packard (HP) Universal Counter, Model 5335A, it counts in seconds the length of time the LD has been on. The HP counter was used because it can register a very long count, and this is important in longevity testing.

The laser monitor, in conjunction with the clock, is a circuit that allows a longevity test to be run on the LDs. The clock is automatically shut off by a photovoltaic cell monitor circuit when the LD optical power falls below a predetermined level. This circuit can also be bypassed for normal operation.

2.2 Laser Diodes

Two types of semiconductor LDs were tested:

- The narrow, multistriped[15] double-heterostructure (DH) LDs constructed by SDL
- The broad, single-striped LDs constructed by McDonnell Douglas Astronautics Company/Optoelectronics Center (MDAC/OEC).

We tested fourteen SDL commercial LDs:

- Ten SDL-2410-H1 Type 100-mW LDs
- Two SDL-2450-H1 Type 500-mW LDs
- One SDL-2430-H1 Type 500-mW LD
- One SDL-2460-H1 Type 1-W LD.

We tested four SDL engineering prototypes:

- One S-7074/7081 S/N BM498 Type 4-W LD
- One S-7081 S/N RB883 Type 4-W LD
- One S-7081 S/N RP542 Type 4-W LD
- One S-7086 S/N BN968 Type 8-W LD.

We tested fourteen MDAC/OEC experimental LDs:

- Two E204A Type 1-W LDs
- Two E220A Type 1-W LDs
- Two E204Q Type 2-W LDs
- Two E170R Type 2-W LDs
- Four E170T Type 2-W LDs
- Two E170T Type 5-W LDs.

2.2.1 Specifications for SDL LDs

Table 1 lists the specifications of the different SDL LDs, all of which (except for the engineering prototypes) are rated for >10,000 h of continuous operation at 25°C when operated at or below rated power. Except for the engineering prototype, all SDL LDs tested were mounted in a standard TO-3 can. The can configuration is quite large.

Like the engineering prototype, the SDL commercial LDs are available mounted on a small C-package heatsink with dimensions of 6.35 mm × 3.25 mm × 1.27 mm. The SDL-2410-H1 is also available with its heatsink mounted on a thermoelectric (TE) cooler, which keeps the heatsink (and thus the LD) at a constant temperature during operation. A light detector internal to the TO-3 monitors the operational status of the LD. For this study, all the LDs were operated while secured to a fin heatsink or to a TE cooler external to the TO-3 can or the C-package.

Figure 4 shows the multi-heterojunction configuration of SDL LDs higher-powered phase array.[16,17] These LDs were fabricated by the Metal-Organic Chemical Vapor Deposition (MOCVD) technique.[18] The active regions of the SDL-2410-H1 and the SDL-2450-H1 LDs consist of multiple-quantum-well (MQW) layers for all the LDs with the GaAlAs concentration in alternate layers of $Ga_{0.94}Al_{0.06}As$ and $Ga_{0.8}Al_{0.2}As$.

The active regions of the SDL-2430-H1, SDL-2460-H1, and S-7074/7081 and S-7081 engineering prototypes[19-21] are single-quantum wells (SQW) of unknown characteristics. The active regions of both types of quantum wells are between p and n type layers of $Ga_{0.6}Al_{0.4}As$ and GaAs. The p GaAs layer is proton-implanted so as to create the optical channels in the active layers. The 10-μm-wide implants are spaced 3.5 μm apart. The $Ga_{0.6}Al_{0.4}As$ layers immediately next to the active layer

- Continue electric carriers due to difference in bandgap energy and thus enhance the optical gain in the active region
- Confine the intercavity laser light to the active region due to the difference in the refractive index between the layers.

The emitting area of each stripe is ~1×5 μm.

The SDL-2410-H1 and SDL-2430-H1 contain 10 closely coupled, gain-guided, active striped lasers. The SDL-2450-H1 and SDL-2460-H1 contain 40 stripes, which create an effective 1×100-μm emitting area and a 1×400-μm emitting area, respectively.

The cavity lengths for the SDL-2410-H1 and SDL-2450-H1 are about 250 μm; the cavity lengths of the SDL-2430-H1, SDL-2460-H1, and the engineering prototypes are longer.

All the LDs have a 95% R mirror on the back facet and an alumina (Al 203) 30% R mirror on the output facet. (The engineering prototypes have a 5% R mirror on the output facet.)

The radiation intensity pattern in phase-array LDs is given by

$$I(\theta) \propto \cos^2\theta \, E(\theta)^2 \, G(\theta) \tag{1}$$

where $\cos^2\theta$ is an inclination, $E(\theta)$ is the Fourier transform of the single emitter near field, i.e., the far field of one emitter in the array.

$G(\theta)$ is the sampling function:

$$G(\theta) = \frac{1 - \cos\left[N(k_o D \tan\theta + \phi)\right]}{1 - \cos\left(k_o D \tan\theta + \phi\right)} . \tag{2}$$

Table 1. SDL Laser Specifications

LASER DIODE (#)	THRES-HOLD CURRENT (mA)	DIFF Q.E. (%)	SLOPE EFF (W/A)	ELECT-ICAL EFF (%)	DIVER-GENCE (degs)	CURRENT RATED POWER (mA)	CURRENT MAX@ POWER (mA)	WAVE-LENGTH (nm)	APER-TURE (um)
COMMERCIAL									
SDL-2410-H1 100 mW									
A194	241	57	0.87	12.1′	10 x 35	357	736+	807	100
A195	245	54	0.82	11.9′	10 x 35	367	750*	807	100
A196	239	55	0.84	12.8′	10 x 35	357	–	807	100
A198	242	55	0.84	13.0′	10 x 35	361	734$	805	100
A200	243	51	0.79	13.5′	10 x 35	370	734++	807	100
A321	253	51	0.79	20.7	10 x 35	376	615**	806	100
A322	250	56	0.85	23.6	10 x 35	367	725	806	100
B123	237	60	0.91	17.2′	10 x 35	348	–	813	100
B124	220	51	0.78	17.8′	10 x 35	349	–	816	100
B126	205	54	0.83	33.2	10 x 35	325	657	806	100
SDL-2450-H1 500 mW									
A840	816	57	0.86	26.2	10 x 35	1399	3386	817	400
A841	826	54	0.82	25.8	10 x 35	1438	3380	816	400
SDL-2430-H1 500 mW									
C347	203	55	1.13	39.7	10 x 40	800	660	808	100
SDL-2460-H1 1 W									
C338	428	51	0.99	38.0	10 x 40	1741	1417	816	200
ENGINEERING PROTOTYPES									
S-7074/7081 4 W									
BM498	600	58	0.82	37.4	10 x 17	5200	5005	814	100
RB883	600	69	0.87	39.4	10 x 17	4400		798	100
RP542	600	68	1.15	37.9	10 x 17	4400	2600	798	100
S-7086 8 W									
BN968	1320	–	1.14	33.6	10 x 15	5000	4400	798	200

@ measured at SNLA + output 168 mW with GRIN * output 110 mW no GRIN

$ output 172 mW no GRIN ++ output 200 mW with GRIN ** output 300 mW no GRIN

′ measured at rated power

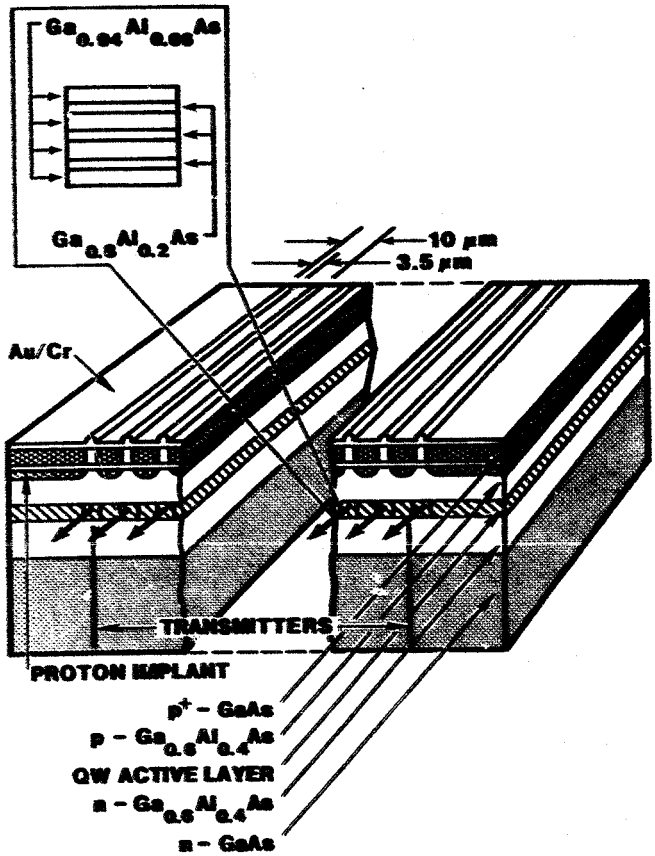

Figure 4. Configuration of SDL Multi-Striped 100-mW, 500-mW, 1-W, 4-W, and 8-W LDs

In Eq. (2), $k_o = 2\pi/\lambda$, N is equal to the number of stripes, D is the stripe periodicity, and ϕ is the phase shift between adjacent stripes. Zero-phase shift yields a symmetric pattern about $\theta = 0$ with a central maximum of $G(0°) = N^2$. The full-width half-maximum (FWHM) of the central lobe is ~0.46° for $\lambda = 0.816$ μm, N = 10, and D = 10 μm.

For other values of ϕ, the principal lobe radiates at

$$\theta = \tan^{-1}(-\phi/k_o D) \quad (3)$$

and for $\phi = \pi$, the pattern is symmetric again.

The sampling function is small at $\theta = 0°$, and is a maximum at

$$\theta_{max} = \pm\tan^{-1}(\lambda/2D) \quad (4)$$

which is approximately 2.3° for $\lambda = 0.816$ μm and D = 10 μm, or a separation between lobes of 4.7°.

2.2.2 Specifications for MDAC/OEC LDs

Table 2 lists the specifications of the different MDAC/OEC LDs tested. These LDs were tested during the initial stage of developing a 5-W continuous-operation LD, which has a nominal 1×250-μm aperture. All LDs tested, except two, were mounted on MDAC/OEC's standard large copper block (LCB) heatsink. The dimension of the heatsink is 1.5×3.7×4.7 mm. The remaining two LDs were mounted on a Type 2A heatsink inside a TO-18 can.

In our test, the temperature of the LCB or the TO-18 is controlled to 19.9°C by a TE cooler. In their intended operation configuration, the LDs would be cooled only by radiating heat fins or by internal TE coolers. Eventually, these LDs will be available only in a TO-3 can or on a LCB.

Figure 5 shows the configuration of the MDAC/OEC LDs. Like the SDL LDs, the MDAC/OEC LDs are fabricated by the MOCVD technique. The following layers are grown on a 2° off [100], Si-doped, horizontal Bridgman substrate:

- 0.5 μm GaAs:Se(10^{18} cm^{-3}) n buffer
- 1.0 μm $Al_{0.15}Ga_{0.85}As$:Se(10^{17} cm^{-3}) n buffer
- 1.5 μm $Al_{0.60}Ga_{0.40}As$:Se(10^{17} cm^{-3}) n optical confinement layer
- 0.2 μm $Al_xGa_{1-x}As$ undoped linearly graded (x = 0.6 to 0.3) layer
- 5 nm GaAs undoped SQW
- 0.2 μm $Al_xGa_{1-x}As$ undoped linearly graded (x = 0.3 to 0.6) layer
- 1.5 μm $Al_{0.60}Ga_{0.40}As$:Zn (10_{18} cm^{-3}) p optical confinement layer
- 0.2 μm GaAs:Se (10^{17} cm^{-3}) blocking cap.

The SQW active area has no Al; therefore, the emitting wavelengths of the MDAC/OEC LDs are longer than those of the SDL LDs. The MDAC/OEC LDs emit at ~880 nm, whereas the SDL LDs emit at ~820 nm.

The adjacent n buffer layers have 0% and 15% Al concentration. The two n and p confining layers on either side of the quantum well are rich in Al with 60% concentration. All layers are grown at 750°C at a V–III ratio of 30. The graded layers and quantum well are grown at a rate of 100 nm/min, whereas all the others are grown at twice that rate.[22] The width of the broad-striped LD is 60 μm or 150 μm; its length varies from nominally 400 μm to >1000 μm. The exact length is proprietary to MDAC/OEC.

Table 2. MDAC/OEC Laser Specifications

LASER DIODE (#)	CAVITY WXL (um)	START V_D (V)	START I_D (mA)	START P_O (mW)	DAMAGED V_D (V)	DAMAGED I_D (A)	DAMAGED P_O (W)	THRESH-HOLD (mA)	EFF (%)
2-W LDs COATED									
E204A-6	60X450	1.654	58	1.4	2.287	1.626	1.674	40	48.5
E204A-3	60X450	1.658	63	1.5	1.968	0.752	0.708	80	48.0
E220A-2	60X450	1.637	79	1.9	1.969	0.895	0.599	80	48.0
E220A-1	60X450	1.607	49	1.3	2.011	1.029	1.044	80	50.0
2-W LDs UNCOATED									
E204Q-1	150X900	1.661	200	3.8	2.440	3.216	1.748	80	26.0
E204Q-9	150X900	-	-	-	-	-	-	-	-
E170T-4	150X450	1.497	137	3.4	2.126	2.843	1.694	80	30.0
E170T-5	150X450	1.452	70	1.1	1.990	2.741	1.590	80	31.5
E170R-4	150X700	1.577	394	72.0	2.102	3.402	2.040	80	30.0
E170R-1	150X700	1.536	351	85.0	1.971	3.230	2.100	70	38.0
E170T-1+	150X700	1.517	374	67.0	1.697	2.119	1.065	80	30.0
E170T-3+	150X700	1.516	372	65.0	1.784	2.770	1.218	140	30.0
5-W LDs COATED									
E170T-2-10	150X1200	1.534	443	105.0	1.801*	2.318	2.050	240	49.0
E170T-2-9	150X1200	1.526	449	108.0	2.137	5.552	5.030	240	50.0

+ TO-18 CAN * SEVEN LD SHOTS AT THIS LEVEL

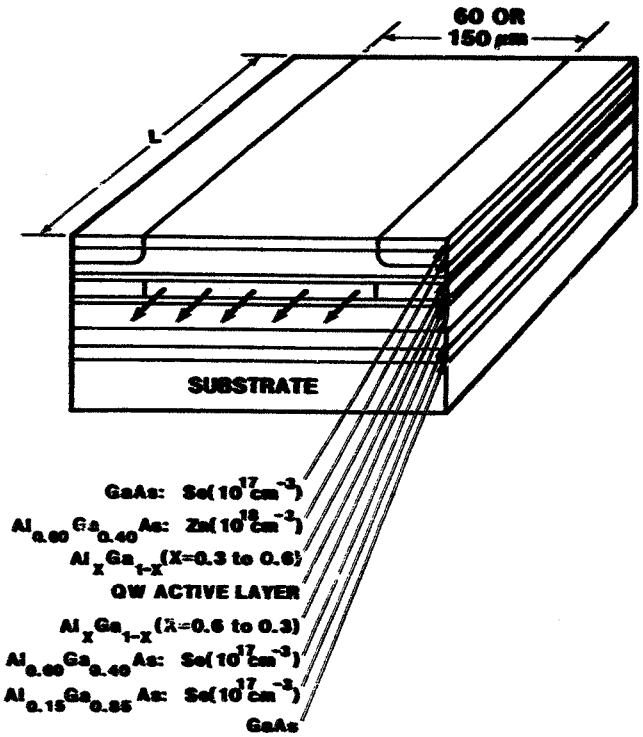

Figure 5. Configuration of MDAC/OEC Developmental Single-Striped LDs

The area of the emitting stripe of each MDAC/OEC LD varies as specified in Table 2. In general, the emitting volumes of the MDAC/OEC individual LDs were larger than those of the SDL LDs (with the possible exception of the SDL engineering prototype LDs). Many of the MDAC/OEC LDs tested had no coatings on the LD cavity mirrors.

The catastrophic damage level listed in Table 2 should be about two times larger when high-reflective/anti-reflective (HR/AR) coatings are deposited on the back and front facets, respectively.

2.3 Optical Couplers

The optical coupler, which transmits optical energy from the LD to the cell through the strong link, must have certain unique characteristics:

1. It must have a high-acceptance angle or numerical aperture (NA). (The angle or aperture is necessary to accept the large divergent LD beam of ~40°.)
2. It must be able to transmit multimode laser light energy.
3. It must be able to transmit large optical power.
4. It must be able to collimate the output of the LD sufficiently so as to allow the light to propagate through a 4-mm aperture located 5 to 10 cm from the LD.
5. It must be capable of forming high hermetic seals.
6. It must be capable of surviving shock and vibration environments.
7. It must be insensitive to high-radiation environments.

Some possible coupling schemes are shown in Figure 6. The optical coupler can be

- a direct scheme
- a lens
- a fiber optic
- a fiber optic and lens combination.

We considered

- a graded index (GRIN) lens
- fiber optics
- a fiber optic and GRIN lens combination
- a fiber optic and spherical lens combination.

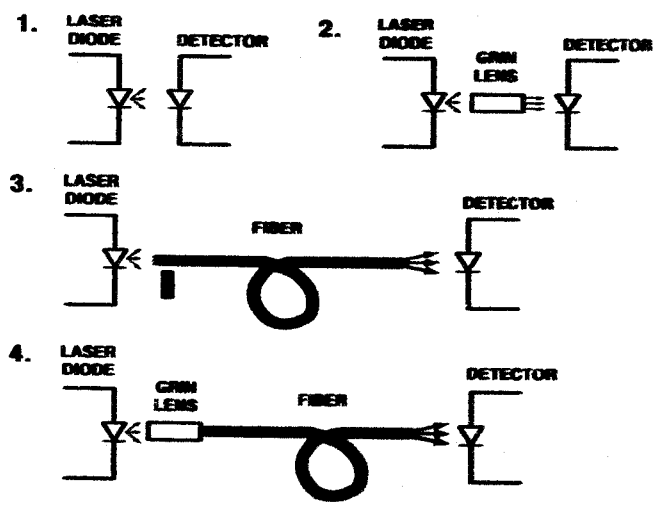

Figure 6. Four Types of Optical Coupling Schemes: (1) Direct, (2) GRIN or conventional lenses, (3) FO, and (4) GRIN or conventional lenses and FO

Satisfying Characteristics 1–7

- The direct option satisfies characteristics 1–3, 6, and 7.
- The FO option satisfies characteristics 1–3, 6, and 7.
- The GRIN lens, FO and GRIN lens combination satisfies characteristics 1–6, but does not satisfy 7 as well as the FO.
- The FO and spherical lens combination satisfies 1–7.

2.3.1 Fiber Optics

The FOs used in the coupler are made by Ensign-Bickford and have cores that are

- 100 μm in diameter (FO_1 Model #HCS-112T)
- 200 μm in diameter (FO_2 Model #HCR-MO202T-12)
- 400 μm in diameter (FO_5 Model #HCR-412T)
- 600 μm in diameter (FO_3 Model #HCR-612T)
- 1000 μm in diameter (FO_4 Model #HCR-1012T).

The FOs, which have a step index and a large NA (NA=0.37), are 1 m long. They are made of a fused quartz core and hard plastic cladding. The combination of plastic on fuzed quartz core material is less sensitive to radiation environment[23] and has a larger NA (NA=0.37) than the glass-on-glass type FO such as:

- Fused quartz cores and boron-doped fused quartz cladding (NA=0.16)
- Fused quartz and fluorine-doped[24] (NA=0.24) fused quartz cladding.

The NA of a fiber optic is given by

$$NA = N_a \sin\theta_a = N_c \sin(90 - \theta_c) = N_c^2 - N_{cl}^2, \quad (5)$$

where

N_a = the refractive index outside the FO
N_c = the refractive index of the core
N_{cl} = the refractive index of the cladding
θ_a = half the acceptance angle or is the incident angle
θ_c = the critical angle of reflection at the core and cladding interface.

A large fiber optic NA is required if the FO is butt-coupled to the LD as is done for this study. If boron- or fluorine-doped FOs are used as a coupler, a lens is required between the LD and the FO in order to reduce the NA of the LD light. The emitting aperture d_1 by t_1 of the LD with $d_1 \gg t_1$ would be coupled into the FO of diameter d_2 by a lens of focal length F. The coupling parameters are determined using the lens formula and magnification. The lens formula is given by

$$\frac{1}{S_1} + \frac{1}{S_2} = \frac{1}{F}, \quad (6)$$

where S_1 is the LD-to-lens distance and S_2 is the FO-to-lens distance.

The magnification, M, is given by

$$M = \frac{S_2}{S_1} = \frac{d_2}{d_1} = \tan\frac{(\sin^{-1} NA_{LD})}{\tan(\sin^{-1} NA_{FO})}, \quad (7)$$

where NA_{LD} is the NA of the LD and NA_{FO} is the NA of the FO.

The magnification is restricted by the diameter, d_2 of the FO so that the aperture of the FO is not overfilled. The LD-to-lens distance, S_1 is given by

$$S_1 = F\left[1 + \left(\frac{d_1}{d_2}\right)\right] \quad (8)$$

and the FO-to-lens distance, S_2, is given by

$$S_2 = F\left[1 + \left(\frac{d_2}{d_1}\right)\right]. \quad (9)$$

The LD-to-lens and lens-to-FO distances are dependent on the NAs of both the LD and FO through the d_2/d_1 ratio or its reciprocal. In the limit with $d_1 = d_2$ then

$$S_1 = S_2 = 2F, \quad (10)$$

so at these LD-to-lens and lens-to-FO distances the lens is not affecting the NAs. We have considered and modeled this lens option coupling scheme as an alternative to butt coupling, but we have not instrumented it into the HOFS systems.

2.3.2 GRIN Lenses

The GRIN lenses used as optical couplers are made from SELFOC (trademark of Nippon Sheet Glass Co., Ltd.) material. The refractive index[25] at a distance r from the optical axis is given by:

$$N(r) = N_a\left(\frac{1 - r^2 A}{2}\right), \quad (11)$$

where

$N(r)$ = the refractive index at any point r,
N_o = the refractive index on the optical axis
A = the refractive index gradient constant
r = the radial distance from the optical axis.

The maximum acceptance angle is

$$2\theta_a = 2\sin^{-1}\left(\frac{N_o r_o A^{1/2}}{N_a}\right), \quad (12)$$

where

r_o = the radius of the GRIN lens, which is 0.9 mm for all GRIN lenses tested
$A^{1/2}$ = 0.332 for the 0.23-, 0.29- and 0.5A-pitch GRIN lenses and 0.432 for the 0.25- and 0.5B-pitch GRIN lenses.

The NA of the GRIN lenses for axial rays is given by

$$NA_{ax} = N_a \sin\theta_a = (N_o r_o A^{1/2}). \quad (13)$$

The GRIN lenses tested had different NAs:

- The 0.23-, 0.29-, and 0.5A-pitch had an NA of 0.46
- The 0.25- and 0.5B-pitch had an NA of 0.6.

These NAs are sufficiently large to transmit the entire large diverging LD beam. The GRIN lenses are not as insensitive to radiation environment as the FO, but they can form a higher hermetic seal than the Ensign-Beckford FO.

2.3.3 FO and Lens Collimators

The FO and GRIN lens or FO and spherical lens collimators consist of an FO and SELFOC GRIN or an FO and a conventional plano-convex (P-C) quartz lens. For the FO and GRIN lens combination, the output half-angle divergence is given by

$$\Delta\theta_G = \frac{N_o A^{1/2} d_f}{2} \quad (14)$$

where d_f is the diameter of the FO. In order to minimize $\Delta\theta_G$, either N_o, $A^{1/2}$, or d_f of the FO must be made small. For efficient coupling, $NA_G > NA_{FO}$, which limits both N_o and $A^{1/2}$ and where NA_G is given by

$$NA_G = N_o A^{1/2} r_o\left[1 - \left(\frac{r_f}{r_o}\right)^2\right]. \quad (15)$$

This leaves the diameter of the FO as a variable; however, that too is limited. In this case, it is limited to the size of the LD aperture, which varies from 100 to 400 μm.

At the onset of this project, the 100-mW LDs had 100-μm apertures and the 500-mW LDs had 400-μm apertures. Since it appeared then that the 500-mW 400-μm LD would be chosen for the source, only 600-μm FOs were considered as FO couplers. Toward the end of the project, a 500-mW and several 4-W LDs having 100-μm apertures became available. This prompted us to consider 200- and 100-μm-dia FOs as FO couplers.

The $\Delta\theta_G$ for 100-, 200-, and 600-μm-dia FOs coupled into a 0.25-pitch GRIN lens is 1.52°, 3.04°, and 9.11°, which is a cone with a diameter of 3.6, 9.0, and 30.6 mm, respectively, at a 102-mm distance, and 1.5, 3.6, and 14.5 mm, respectively, at a 51-mm distance from the GRIN lens output surface. In the limit, the axial ray produces a minimum diameter of 1.5 mm at any distance.

For the FO and spherical lens combination, the half-angle divergence, $\Delta\theta_s$, is given by

$$\Delta\theta_s = \tan^{-1}\left(\frac{d_f}{2F_s}\right), \quad (16)$$

where F_s is the focal length of the lens. The thin lens paraxial approximation is used. The diameter d_c of the light cone leaving the lens at the distance d_{LC} from the lens is given by

$$d_c = d_f\left[\left(\frac{2F_s}{d_f}\right)\tan(\sin^{-1} NA_{FO}) + \left(\frac{d_{LC}}{F_s} - 1\right)\right]. \quad (17)$$

The $\Delta\theta_s$ for 100-, 200-, 400-, and 600-μm FOs coupled into a 3.6-mm-dia, 3.5-mm focal length P-C quartz lens is 0.82°, 1.6°, 3.3°, and 4.91°, respectively, which is a cone with a diameter of 4.1, 5.5, 8.1, and 10.8 mm, respectively, at a distance of 50 mm from the surface of the spherical lens. The diameter of the lens must be ≥3.38 mm for the four FOs considered.

The focal length of a GRIN lens is given by

$$F_G = [N_o A^{1/2} \sin(A^{1/2} z)]^{-1}, \quad (18)$$

where Z is the length of the GRIN lens and $A^{1/2} Z$ = pitch = π/2 for the 0.25 pitch lens. Eq. (18) reduces to

$$F_G\ (0.25\ \text{pitch}) = (N_o A^{1/2})^{-1}. \quad (19)$$

For $N_o = 1.6$ and $A^{1/2} = 0.332\ mm^{-1}$, $F_G = 1.88$ mm. The 0.25-pitch GRIN lens does not produce as small a

cone diameter at 102 and 51 mm from its output surface as the spherical lens because F_G is much smaller than the 3.5-mm focal length, F_s.

In trying to determine the pitch of a GRIN lens so that its focal length is equal to that of the spherical lens, we considered the Ray Trace Matrix for GRIN lenses.[26] These equations result in at least two solutions:

- One solution is for incident-converging rays. This requires that the image or object be inside the GRIN. Since this would require another lens in the optical train, this solution offers no particular advantage to us at present.
- A second solution is for incident-diverging rays. This results in a Z=1.71 mm and a pitch of 0.09 for F_G=3.5 mm. Since this is about the physical size of the spherical lens, it offers no obvious advantages.

For 100-, 200-, and 600-μm-dia FOs, the diameter of the GRIN lens must be at least 2.86, 2.96, and 3.30 mm, respectively, in order to produce the same cone diameters as the spherical lens. These diameters are on the limits[27] of practical sizes for the GRIN lenses currently produced.

2.4 Beam Interrupter-Coupler

The beam interrupter-coupler (BIC) is used in a strong link (SL); the SL is a beam shutter combined with a beam deflector. The BIC ensures blocking of the optical energy from the exclusion area. The controls of the elements of the SL require a unique signal in order to rotate the deflecting surfaces from the blocked to the unblocked position. For nuclear applications, except under authorized conditions, denial to the exclusion area must be ensured to 1 part in 10^6. Organization 2543 has the responsibility for SL development; however, since the SL is part of the HOFS system, the elements used in the SL must conform to the specifications of the firing set.

Some possible BIC schemes are shown in Figure 7 and in parts a and b of Figure 8. The scheme for the out-of-line components in parts a and b is preferred over the scheme for the in-line components in Figure 7. In case of an accident to the weapon, the probability of the LD source being able to deliver energy to the cell is greatly reduced for the out-of-line scheme compared to the in-line scheme.

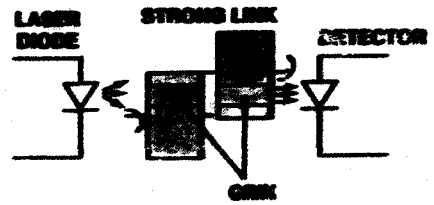

Figure 7. In-Line Beam Interrupter-Coupler Configuration

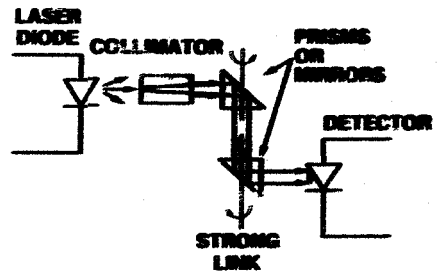

(a)

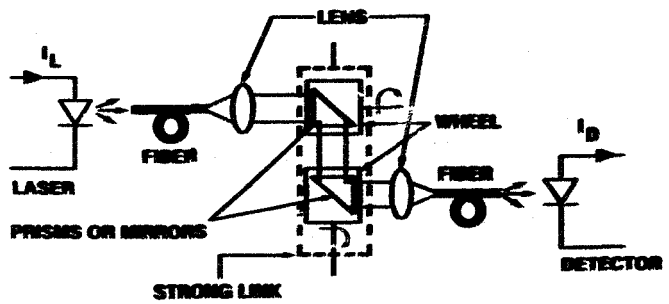

(b)

Figure 8. Out-of-Line Beam Interrupter-Coupler Configuration. (a) GRIN or conventional lens collimator combined with prism or mirrors in wheels, or (b) FO and GRIN or conventional lens collimator combined with prisms or mirrors in wheels.

The divergence of the LD beam out of the P-C lens is given by

$$\Delta\theta_s = \tan^{-1}\left(\frac{d_f}{2F_{s'}}\right), \tag{20}$$

where d_f is the diameter of the FO and $F_{s'}$ is the focal length of lens P-C.

2.5 PVA GaAs Cells

Figure 9 shows a schematic of the configuration of the GaAs PVA cells. These cells, made by Applied Solar Energy Corporation (ASEC), are tested and used in the HOFS systems. The active layers are grown on a thick, 350-μm GaAs substrate doped to about 10^{18} cm^{-3} of Se, using the MOCVD technique. These layers include the following characteristics:

- A metal-conducting layer is deposited onto the backside of the GaAs substrate.
- The first layer, the n-base, is grown until it is ~10 μm thick. It is then doped with ~10^{17} cm^{-3} of Se.
- The p-emitter layer is grown until it is ~0.6 μm thick. It is then doped with ~10^{18} cm^{-3} of Zn.
- The final top layer is a thin, transparent, GaAlAs layer and is grown until it is ~0.1 μm thick. It is then doped with about 10^{17} to 10^{18} cm^{-3} of Zn. This layer passivates the optical input surface of the cell. A final anti-reflective coating is placed over this layer after the bonding contacts are deposited.

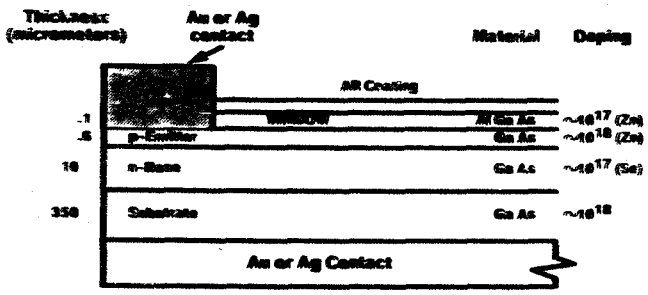

Figure 9. Configuration of PVA GaAs Concentrator Cells Fabricated by ASEC

The 1-V PVA cell is a monolithic structure; the 2-, 10-, and 16-V cells are hybrid structures. The 1-V cell is designed to operate at a concentration of about 100 suns, where one sun is 137.1 mW/cm^2 for space applications and 100 mW/cm^2 for terrestrial applications.

The hybrid cells are fabricated by cutting cells into segments and then connecting the segments in electrical series. Each segment produces about 1 V. The 2-V cell is made by dividing a 1-V cell in half, then refitting and connecting the two pieces in electrical series. The 10- and 16-V cells are made by cutting cells in pie segments, then refitting them to approximate a circle and connecting the segments in electrical series.

Specifications for PVA GaAs Cells

The characteristics of the GaAs cells tested by ASEC or SNLA are given in Table 3. PVA Cells 10 and 3 were tested by SNLA. The data listed for these cells are for maximum efficiency measured for solar illumination, n_s. The predicted efficiency for monochromatic illumination (n_λ) of 820 nm is given by

$$n_\lambda = n_s \times S(\lambda) \times \frac{P_s}{I_{sco}}, \tag{21}$$

where

$S(\lambda)$ = the spectral response (mA/mW) at a specific wavelength
P_s = the solar intensity at one sun (100 mW/cm^2)
I_{sco} = the short-circuit current density at one sun (mA/cm^2).

The estimated P_λ, which is the optical power required at a specific wavelength to get the concentration solar short-circuit current, I_{sc}, out of the cell, is given by

$$P_\lambda = \frac{I_{sc}}{S(\lambda)}. \tag{22}$$

The efficiency for solar illumination, n_s, is given by

$$n_s = \frac{P_e}{P_{s'}}, \tag{23}$$

where P_e is the voltage, V_{max} across the optimum load resistor times the current, I_{max}, through the optimum load resistor for the cell with solar illumination under a concentration factor of F_s suns.

$P_{s'}$, the solar power at F_s suns, is given by

$$P_{s'} = P_s \times F_s \times A_c, \tag{24}$$

where A_c is the area of the cell.

The fill factor (FF), a measure of the squareness of the I–V curves of the cell, is given by

$$FF = \frac{(I_{max} \times V_{max})}{(I_{sc} \times V_{oc})}, \tag{25}$$

where I_{sc} is the short-circuit current through the cell and V_{oc} is the open-circuit voltage across the cell.

Table 3. Characteristics of GaAs Cells Measured by ASEC or SNLA With White Light

PVA SER #	PVA SEG #	FACTOR F_S	CONCENTRATION V_{OC} V	V_{max} V	I_{SC} mA	I_{max} mA	P_λ mW	FF SOLAR	S_λ A/W	I_{SCO} mA/CM^2	n n_S %	n_λ %	CELL AREA CM^2
10+	1	103	1.08	.95	330.0	312.0	632	.830	.520	25.4	22.8	46.6*	.126
12	2	19.6	2.00	1.55	36.6	36.6	167	.695	.245	17.8	18.2	34.1	.117
3+	10	8.1	9.24	6.08	10.0	9.0	46	.502	.030	2.6	7.2	14.8*	.785
39	16	16.7	16.00	11.20	16.4	13.9	590	.593	.028	1.7	12.2	26.4	.565

+ MEASURED AT SNLA * MAX VALUE

2.6 Dc-Dc Converters

The two types of dc-dc converters used and tested in the HOFS systems are made by Venus Scientific Corp. and Gamma High Voltage Research, Inc. Both types of converters use oscillators to chop the dc input voltage in order for it to be up-converted.

Figure 10 shows the diagram of the Jensen oscillator circuit used by Gamma in its converters.

- Input is resistor-capacitor (RC) coupled by R_1 and C_6 whose values are 50 Ω and 0.47 μF, respectively.
- Transistors Q_1 and Q_2 are 2N4923.
- Capacitor C_5 is 0.1 μF.
- Diodes D_5 and D_6 are 1N4936.
- Capacitors C_1 through C_8 are 500 pF.
- Diodes D_1 through D_8 are high-voltage diodes.
- Resistors R_1, R_2, and R_3 are nominally 50, 1.5, and 1.5 Ω, respectively.
- Transformer T_1, which has a Ferroxcube Type 3C82218 Ferrite core, has primary, secondary, and feedback windings.
- The feedback winding, located in the base circuit of the transistors along with the stray capacitances and Capacitor C_5, determines the frequency of oscillation (~30 kHz).
- The turns ratio of T_1 is different for the 1-, 2-, 10-, and 16-V converters.
- The input dc voltage is up-converted by the multiplication factor, M_V, of the converter, which is given by

$$M_V = \frac{Q(N_s)}{\frac{N_p}{2}}, \qquad (26)$$

where

N_s = the number of turns in the secondary
N_p = the number of turns in the primary
Q = the multiplier in the secondary circuit of T_1.

The Q value is 8 for the 1- and 2-V converters and 4 for the 10- and 16-V converters.

For the 1- and 2-V converters, the primary of T_1 has 6 turns center-tapped, whereas the secondary has 850 and 450 turns, respectively. For the 10- and 16-V converters the primary of T_1 has 18 turns center-tapped, whereas the secondary has 800 and 400 turns, respectively.

The converter M_V is about 2267, 1200, 355, and 177 for the 1-, 2-, 10-, and 16-V converters, respectively.

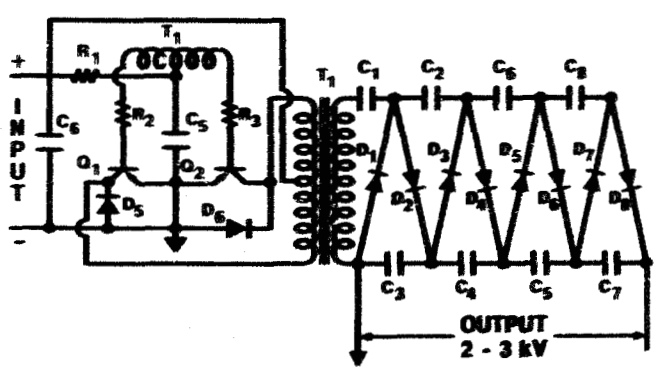

Figure 10. Circuit Used in Gamma Dc-to-Dc Converters, Which Use a Jensen Oscillator

3. Techniques Used to Measure Component Characteristics

The techniques used to measure the characteristics of the different components are also used to test the HOFS systems. A Scientech energy/power meter (EM) is used for all the power measurements. Figures 11 and 12 are photographs of the EM in front of the LD and FO, respectively.

- The EM is placed in front of FOs, SDL LDs in TO-3 cans, SDL LD_2 in C-packages, MDAC/OEC LDs in TO-18 cans, and MDAC/OEC LDs on LCBs.
- The EM is placed a distance of 2.54, 4.3, 1.0, 4.3, and 5.3 mm, respectively.
- The distances create subtended collecting angles for the 25.4-mm-dia EM surface of 157°, 143°, 171°, 143°, and 135°, respectively.
- The angles are 3.7 times larger than the 43° total divergence of the FOs; 3.6 times larger than the 40° total divergence of SDL LDs in TO-3 cans; 10 times larger than the 17° total divergence of engineering prototype SDL LDs; 3 times larger than the 45° total divergence of the MDAC/OEC LDs in TO-18 cans; and 3 times larger than the 45° total divergence of the MDAC/OEC LDs on LCBs.

The FO cables are placed butt-on-end against the GRIN lens, the window of the SDL and MDAC/OEC LDs, SDL LDs in C-packages, and the MDAC/OEC LDs on LCBs. This corresponds to about 0.1, 0.3, 0.025, and 0.03 mm from the GRIN lens or laser-cavity mirror, respectively.

Figure 13 is a photograph of the FO butt-coupled to the window of an SDL LD. The 1-m-long FO is looped in a 16.5-cm-wide × 21.5-cm-high loop to simulate the bending that the FO would make when placed among other components in a HOFS system.

Figure 14 shows the setup used to measure the transmission of the GRIN, GRIN and FO combination, and FO

- The X, Y, and Z axes are horizontal, vertical, and along the optical for all the mounts except for the camera. For the camera, Y axis is horizontal and the X axis is vertical, whereas Z is still the optical axis.
- The LD is secured to an optical table and can be rotated relative to the horizontal (H) and vertical (V) axes.
- The GRIN is mounted on a V-notched block that can be translated in X, Y, and Z and rotated about the H and V axes.
- The FO is secured in a similar manner at its input end. At its output, it is stationery except for the rotation and height adjustment available from the pole holding the V-notched block into which the FO is mounted.
- The EM and PVA cells are secured on a pole mounted on an X, Y, and Z translator. This allows for rotation about H for the EM and about V for the cells.
- The GRIN, FO (input), EM, and cell are each mounted on kinematic mounts that allow the fast removing and precise repositioning of components in minimum time.
- A telescope is positioned on the table to facilitate alignment of the LDs, GRIN lenses, and P-C lens.
- The FO or GRIN lens is aligned to the LDs by scanning the input end of either the FO or GRIN in the X and Y directions for the maximum power out of the opposite end and then reducing the distance (in the Z direction) until the distance between the FO or GRIN and the LD window or the GRIN and the FO approaches zero. This is facilitated by observing the disappearance of the reflection between the specific components as the separation distance decreases to zero.

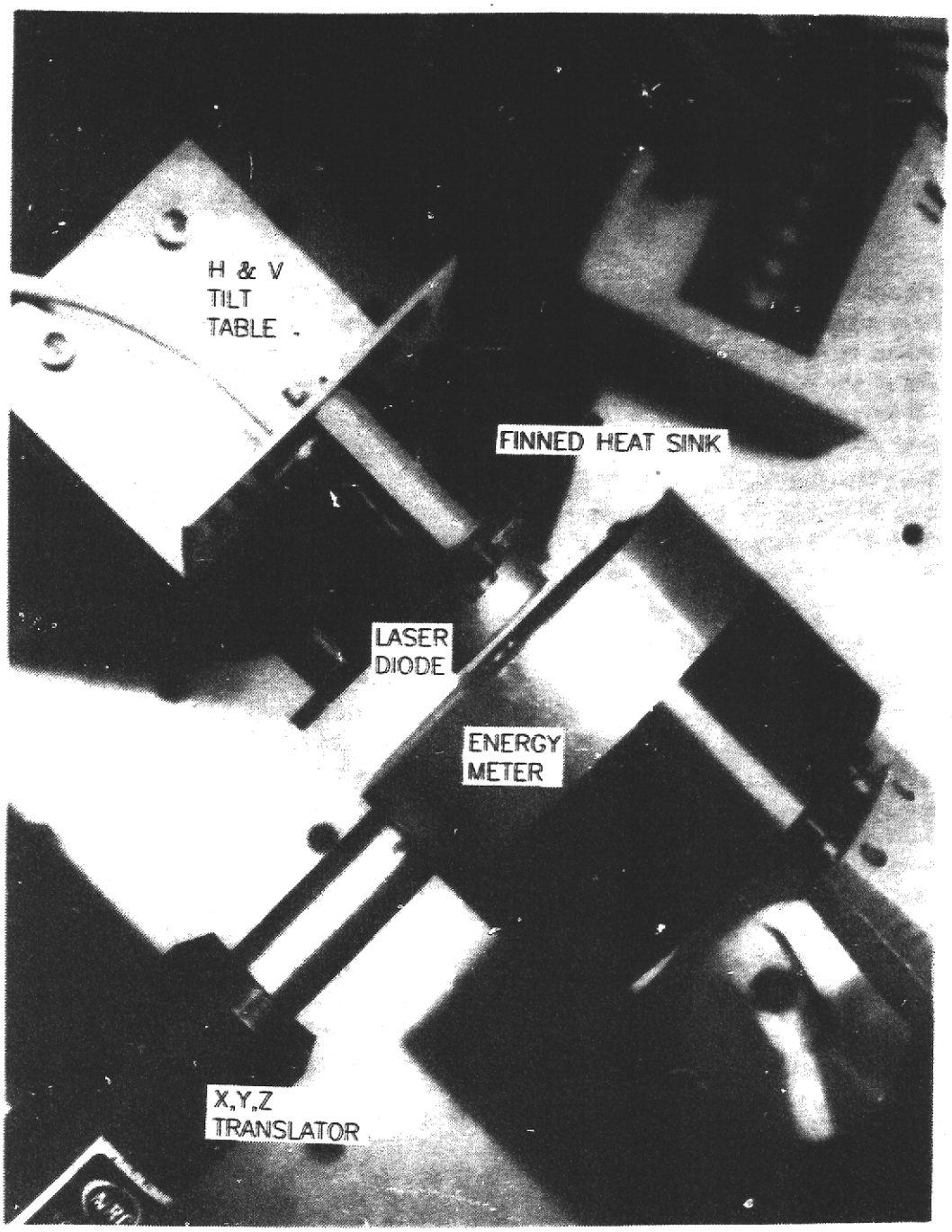

Figure 11. Photograph of Energy Meter in Front of SDL 100-mW LD

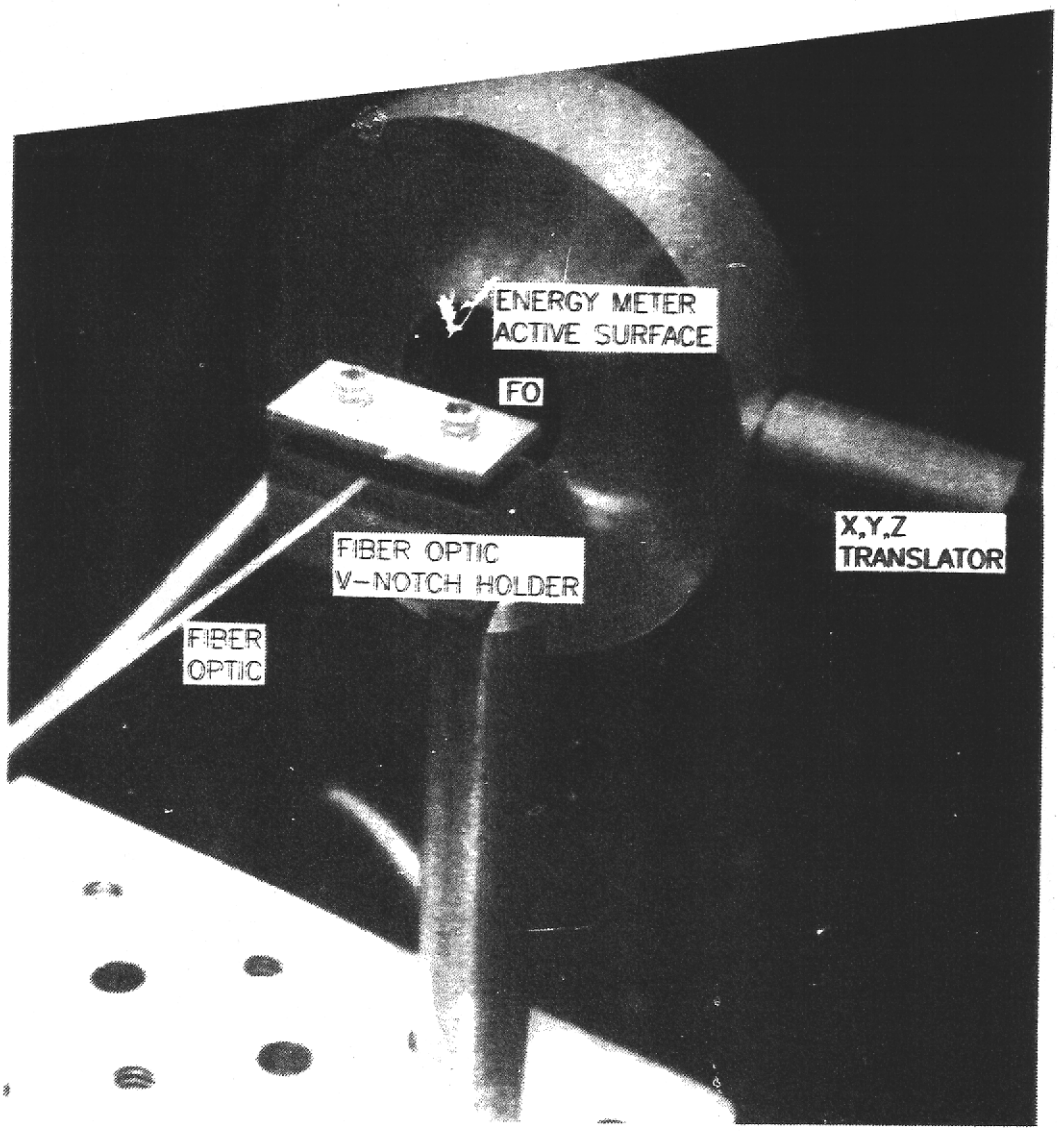

Figure 12. Photograph of Energy Meter in Front of 600-μm FO

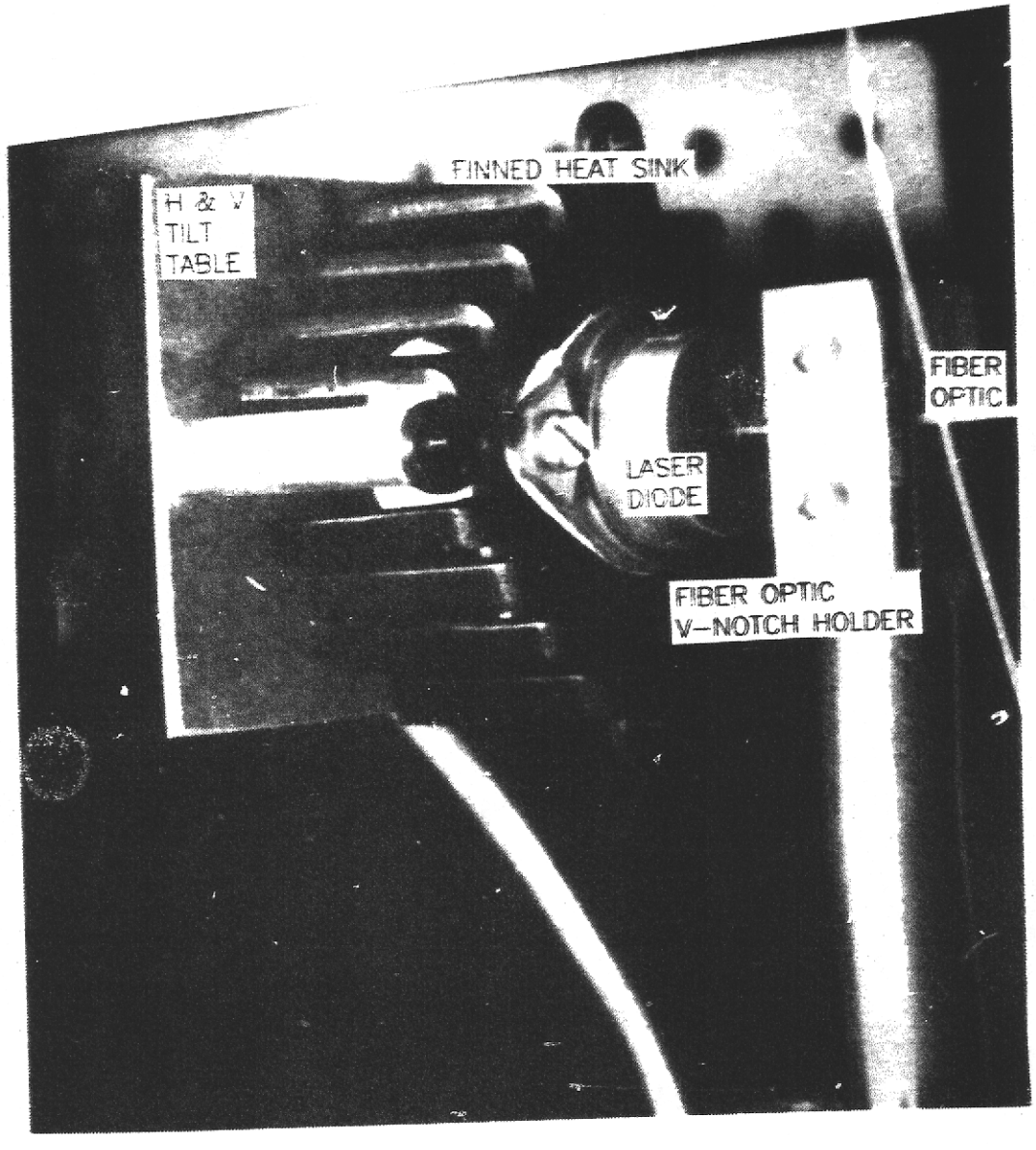

Figure 13. Photograph of FO Butt-Coupled to SDL 100-mW LD

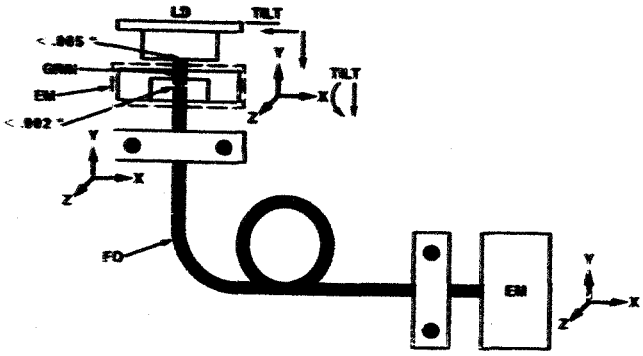

Figure 14. Setup Used to Measure Transmission of GRIN Lenses, GRIN Lenses and FO Combination, and FO

Figure 15 shows the setup used to measure the LD beam dimension out of the P-C lens that is coupled to a FO.

- The P-C lens is mounted on a small table mount, which allows X, Y, and Z translation and tilt about the H and V directions.
- The camera is mounted on an X, Y, and Z translation mount.
- Both lens and camera are placed on kinematic mounts.
- The energy meter and the camera are used in aligning the P-C lens. The P-C lens is aligned to the FO by scanning its input end in the X, Y, Z directions for maximum power. The FO is then scanned in the Z direction while monitoring the P-C lens output end with the camera for minimum diameter at a distance from the lens so that the image does not overfill the surface of the charge injection device (CID).

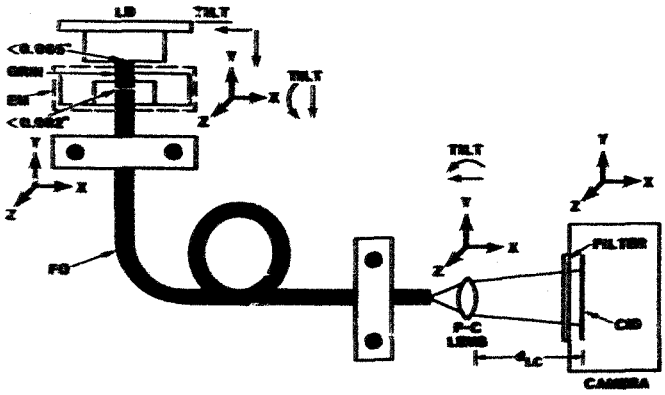

Figure 15. Setup Used to Measure the LD Beam Dimension Out of P-C Lens Coupled to a FO

Figure 16 shows the setup used to measure the transmission through a 3.8-mm aperture placed at different distance d_{LA} from the lens as the prism, P_1, is rotated about the optical axis, Z.

- Prism P_1 is secured to a gimble mount that allows small tilt about the H and V directions and rotation about the optical axis, Z. The resolution about the Z rotation is 0.5 min.
- The prism, aperture, camera, and energy meter are placed on kinematic mounts.
- The camera and energy meter are interchangeable.
- The prism is centered onto the optical axis using a helium-neon (HE-NE) laser and viewing the IR LD beam.
- The aperture is aligned in a manner similar to the lens.

The beam contours and profiles of the LDs and the optical couplers are recorded by a Laser Beam Diagnostic System made by Big Sky Software Corp.[28] The system consists of:

- **Camera.** The camera is a General Electric CID Model TN 2-509, capable of a full resolution of 256×256×8 (gray level) elements and a half resolution of 128×128×8 elements. Each pixel is 28×28 μm. Big Sky affixes its own high-resolution, low-distortion face plate on the input of the camera, which has about a 1% to 2% transmission at 800 nm.
- **Frame grabber.** The frame grabber is a Model-509 from Poynting Products, with color option for contour highlighting.
- **Computer.** The computer is an IBM AT with an Okidata Microline printer, Model 292, and two high-resolution monitors; an NEC video, Model JC-1401P3A; and a Princeton Graphic System Model HX-12E.
- **Software.** The software is Beamcode 4.0 from Big Sky.
- **Synchronizer.** Synchronization module for pulse synchronization of the frame grabbler to an outside pulse event, i.e., for Q-switch pulse-laser operation.

The computer is interfaced to the frame grabber through a 16-bit, parallel, digital-interface card for image-data acquisition and storage. For full resolution, one can select Frames 1 through 4; for half resolution, one can select Frames 1 through 16 with minimum-time resolution of 0.2 s for half and 0.8 s for full resolution between frames and a maximum of 999.9 s.

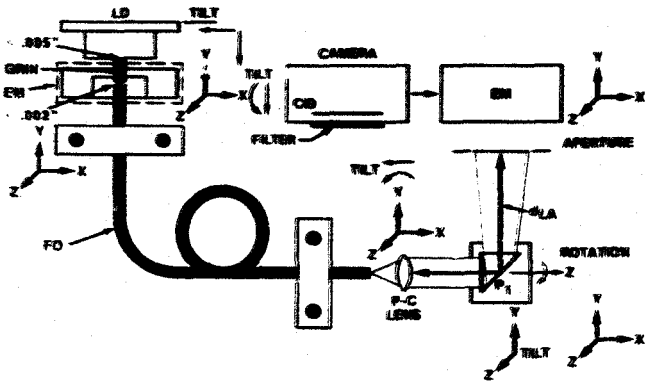

Figure 16. Setup Used to Measure the Transmission Through a 3.8-mm Aperture Located Different Distances From Prism as It Is Rotated

In use, we add neutral-density filters in front of the CID camera to keep it from saturating. The optical path length from the object to the active surface of the camera is such that the pattern emitted by the FO will be collected by the camera. For each setup, the camera is usually positioned at two points so that a divergence can be determined.

The Beamcode 4.0 software package allows contours of the laser beams to be recorded and their profiles in the X and Y directions through the centroid or any point designated by a mouse. The profiles can be compared to a Gaussian distribution with an estimate of the fit to $1/e^2$ points. A 3D rotatable isometric profile of the laser beam is also available.

In order to protect the operators from high voltage, the dc-dc converter, the high-voltage capacitor, and the resistor divider network are located inside a Lucite safety box (Figure 17). One oscilloscope (OSC) is calibrated using a known high voltage that is applied across the resistor divider network, R_2 and R_3. The network is connected in parallel with the HV capacitor. A 10× probe across R_3 is used to measure the voltage across the capacitor. This voltage trace is used to determine the charge time of the HV capacitor.

Another OSC, which is also calibrated with a known voltage source, is used to measure the voltage across the cell and the current into the dc-dc converter. A 1× probe across a known resistor, R_1 (in series with the cell) monitors the voltage. The current is then $I = V/R_1$.

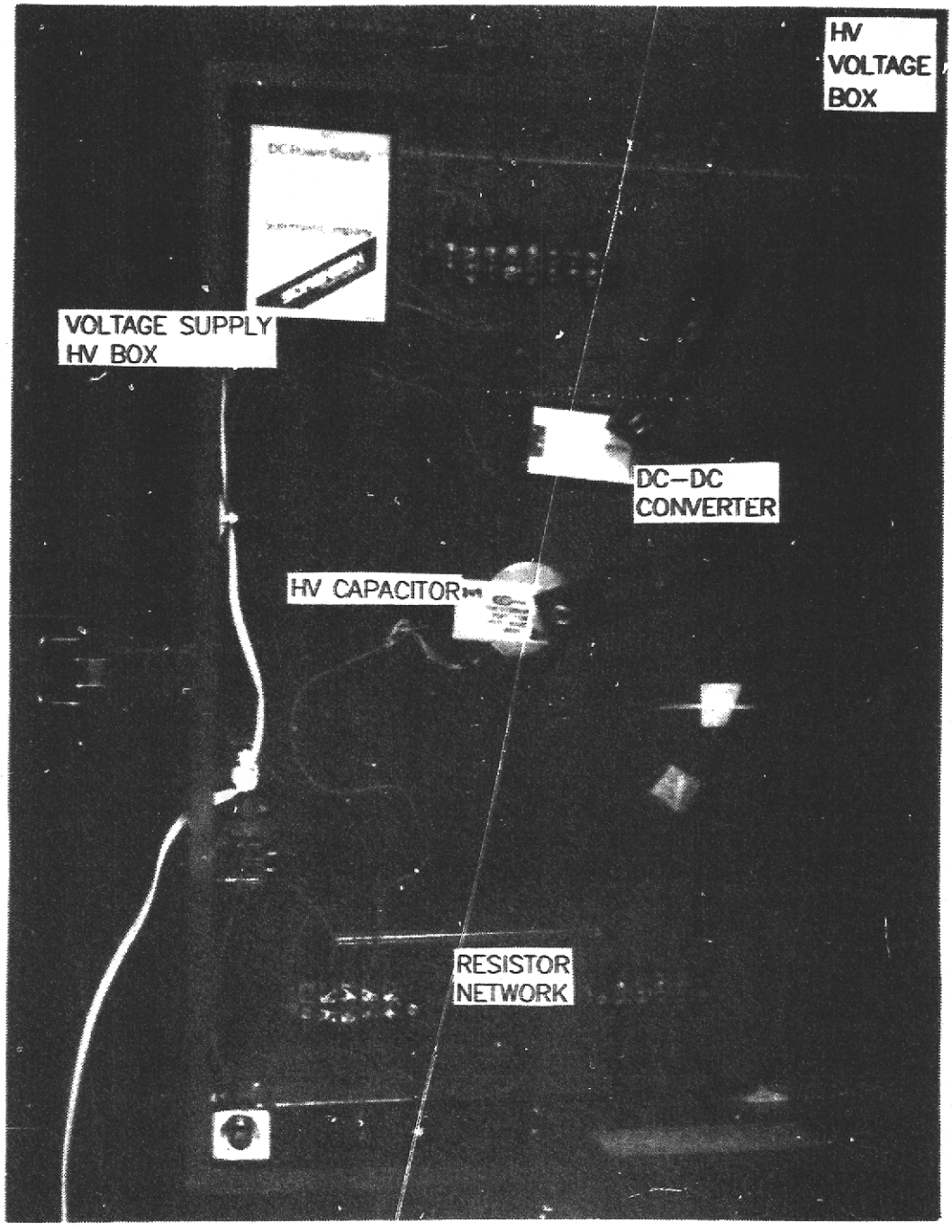

Figure 17. Photograph of Safety Box With High-Voltage Components. These components are the dc-to-dc converter, the HV capacitor, and resistor divider network.

4. Component Characteristics

The characteristics of the following four components were measured: the LDs, couplers, strong link, and PVA GaAs solar cells.

- **Laser Diodes.** The LD characteristics observed or measured include optical power as a function of current; efficiency as a function of LD optical power; degradation due to aging and thermal effects as a function of LD optical power; and beam intensity distribution as a function of LD optical power.
- **Couplers.** The characteristics of the couplers measured include the transmission of five GRIN lenses butt-coupled to LDs; the transmission of a GRIN lens as a function of distance from the lens; the transmission of 1000-, 600-, 400-, 200-, and 100-μm-dia FOs butt-coupled to SDL-100-mW, 500 mW, MDAC/OEC 1-W LDs as source; two different-diameter FOs butt-coupled to GRIN lenses with SDL 100- and 500-mW LDs as source, all as functions of incident LD optical power and beam profiles of a 0.23-pitch GRIN lens, 200-μm FO_2 #1 and 600-μm FO_3 #1 FOs, with 100-mW, 500 mW, and 4-W LDs as sources.
- **Strong Link.** The tolerance in the alignment of the elements of the strong link, which contain the prisms or mirrors, is determined as a function of energy collected at the same distance from the output of the lenses as that of the cell.
- **PVA GaAs Solar Cells.** The characteristics of 1-, 2-, 10-, and 16-V GaAs cells measured include output electrical power as a function of load resistance; and current as a function of voltage (I–V) curves for different-input LD optical powers. The characteristics also include optimum resistance R_p; efficiency; and fill factor as functions of LD optical power.

4.1 Laser Diodes

The LD optical power as a function of LD current and efficiency and degradation as functions of LD optical power were measured for different LDs along with their beam profiles.

The LD optical power as a function of current was measured for:

- Seven SDL 100-mW LDs
- Three SDL 500-mW LDs
- One SDL 1-W LD
- Three SDL 4-W LDs
- One SDL 8-W LD
- Six MDAC/OEC coated-cavity-reflector LDs
- Seven MDAC/OEC uncoated-cavity-reflector LDs.

4.1.1 Optical Power

Figure 18 shows the optical power as a function of current for six SDL 100-mW LDs operated to their rated 100-mW output levels. The slopes are comparable although the intercepts on the LD optical power axis, which are called threshold, vary. B126 (Curve 1) has the smallest threshold value, and A321 (Curve 6) has the largest threshold value.

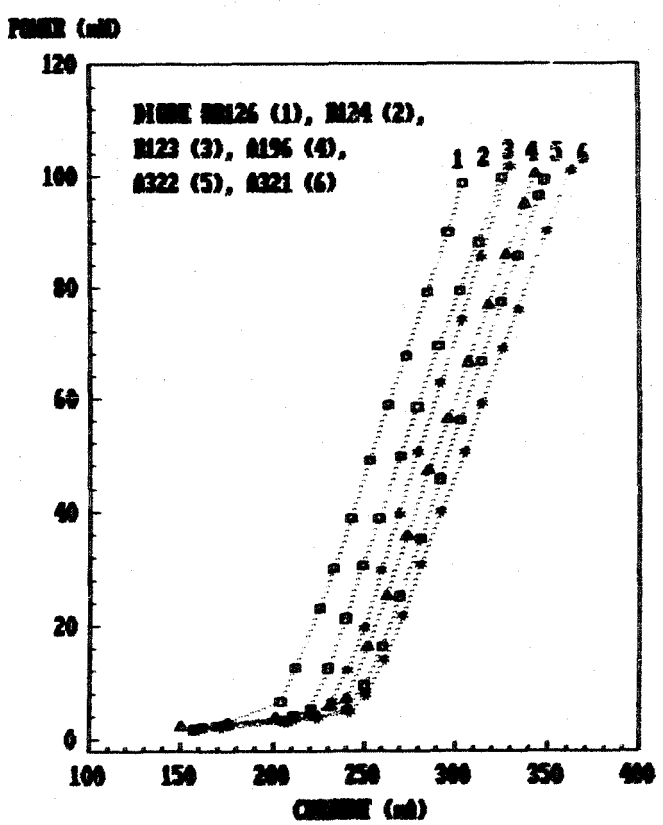

Figure 18. Optical Power vs. Current for Six SDL 100-MW LDs (B123, B124, B126, A196, A321, and A322) Operating Up to 100 mW

Figure 19 shows that as the current for two LDs (B126 and A321) increases, their slopes virtually stay the same, even when their optical power increases to greater than four times their rated power. The time interval between data shots is ~3 min.

Figure 20 shows the varying LD optical power as a function of current for SDL LD A195. The current has been greatly overdriven for a long time (exact time unknown) and the LD has experienced some damage (the extent of which is unknown). The initial threshold and slope efficiency is a specific value up to about 15 mW of output power, then suddenly the slope efficiency changes to a smaller value; finally it reestablishes to a new slope efficiency. The output of the LD continues to change from shot to shot as the LD continues to degrade, i.e., the slope continues to decrease.

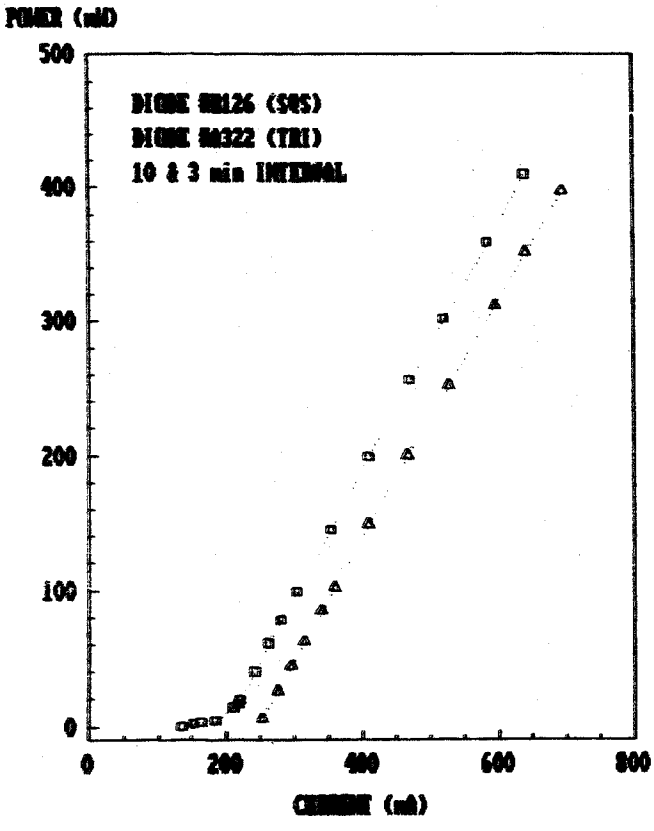

Figure 19. Optical Power vs. Current for Two SDL 100-mW LDs (A322 and B126) Operating up to 400 mW, Four Times Their Rated Power Levels

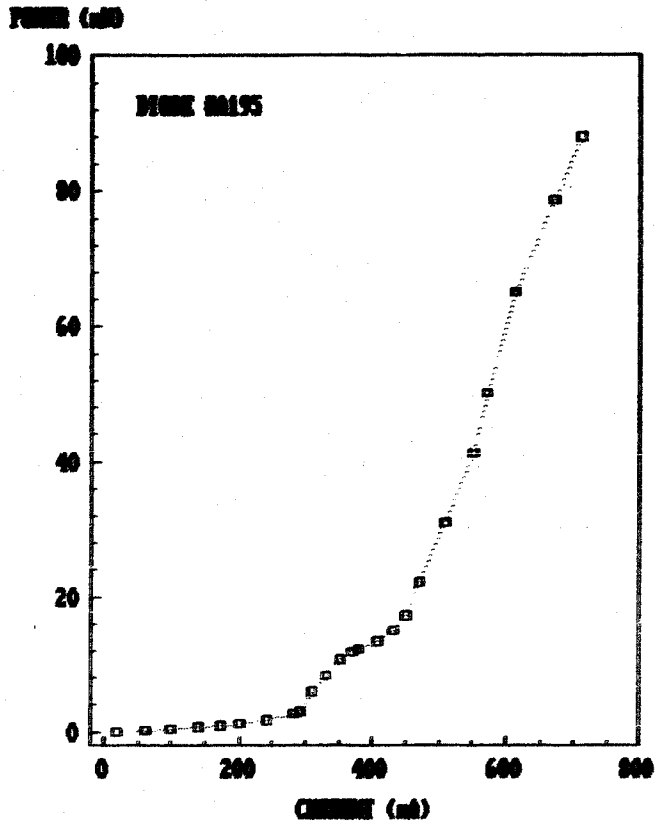

Figure 20. Erratic Behavior of SDL 100-mW LD A195 Undergoing Degradation

The slope changing is similar to the clear kinking described for LDs when modes are confined by a refractive index profile such as formed by the mode intensity profile itself.[29] This mode can easily move by slight asymmetry in the device structure. These trans- verse-mode instabilities in semiconductor LDs were reduced by introducing a stripe geometry[30] similar to SDL LDs like A195 using photon bombardment,[30] zinc diffusion,[31] and mesa structure.[32]

The optical powers as a function of current for two SDL 500-mW LDs (A841 and A840) are shown in Figures 21 and 22. The threshold and slopes of A841 and A840 are almost identical up to their rated power level (Figure 21) and also up to four times their rated power level (Figure 22). As the current increases in the LDs, their slopes decrease slightly as shown in Figure 22. The rollover at the larger LD optical power indicates a decrease in efficiency.

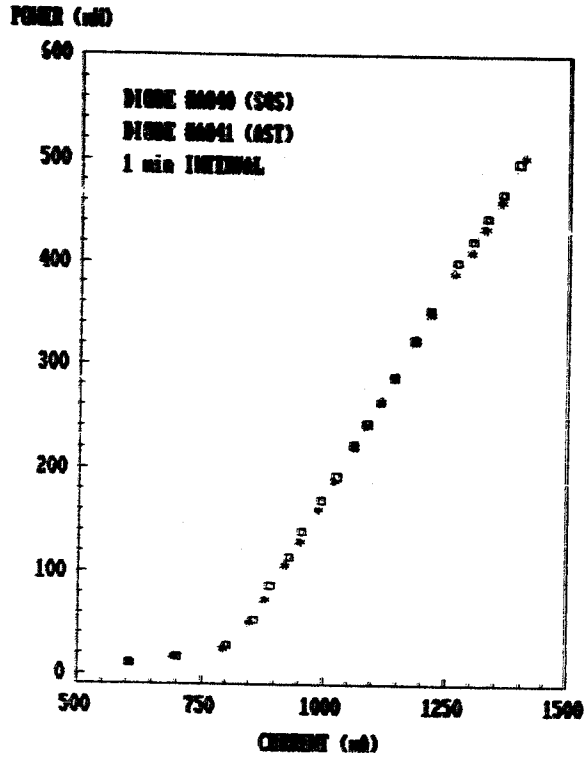

Figure 21. Optical Power vs. Current for Two SDL 500-mW LDs (A840 and A841) Operating up to 500 mW, at 1-min Intervals

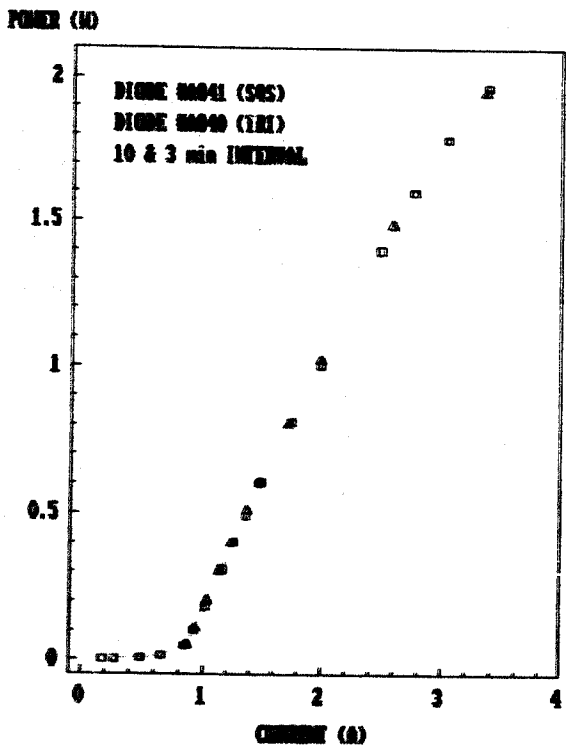

Figure 22. Optical Power vs. Current for Two SDL 500-mW LDs (A840 and A841) Operating up to 2 W, Four Times Their Rated Power Levels, at 3- and 10-min Intervals

Optical power as a function of current for SDL 500-mW C347 LD and SDL 1-W C338 LD is shown in Figures 23 and 24. The difference between these LDs and the SDL LDs previously tested is the lower threshold, which is about 190 mA for C347 and 430 mA for C338 versus about 820 mA for A840 and A841 LDs (Figure 22). LDs C347 and C338 have single-quantum wells instead of the multiple-quantum wells of A840 and A841. The 500-mW C347 LD has a 100-μm aperture compared to the 400-μm aperture of A840 and A841 LDs. LD C338 has the same aperture as A840 and A841. At rated power levels, the increase in brightness of C347 over A840 and A841 is 4 times, and C338 over A840 is 2 times. At operating power levels, the increase in brightness of A840 and A841 over C338 is 2 times, whereas C347, A840, and A841 are the same brightness.

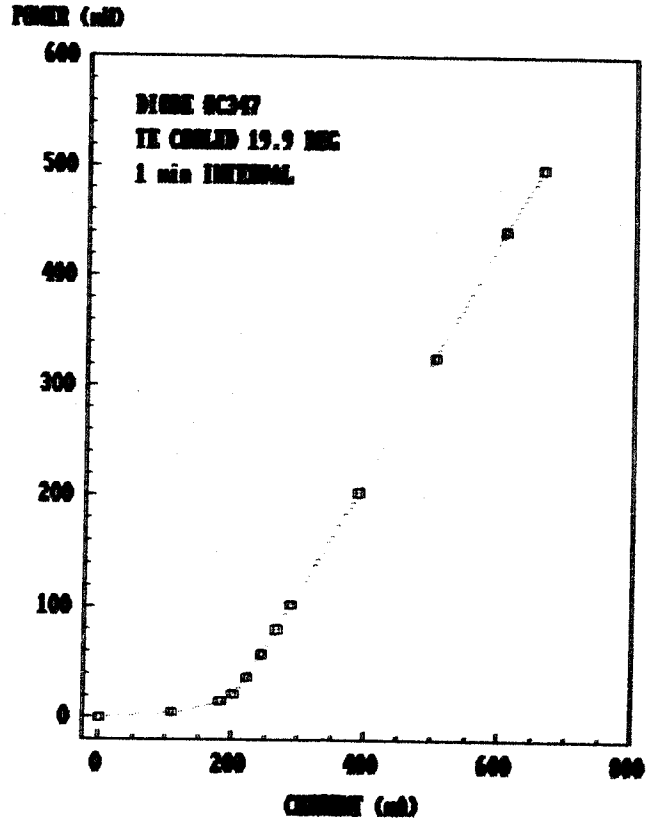

Figure 23. Optical Power vs. Current for SDL-500 mW LD C347 Operating up to 500 mW, TE-Cooled at 1-min Intervals

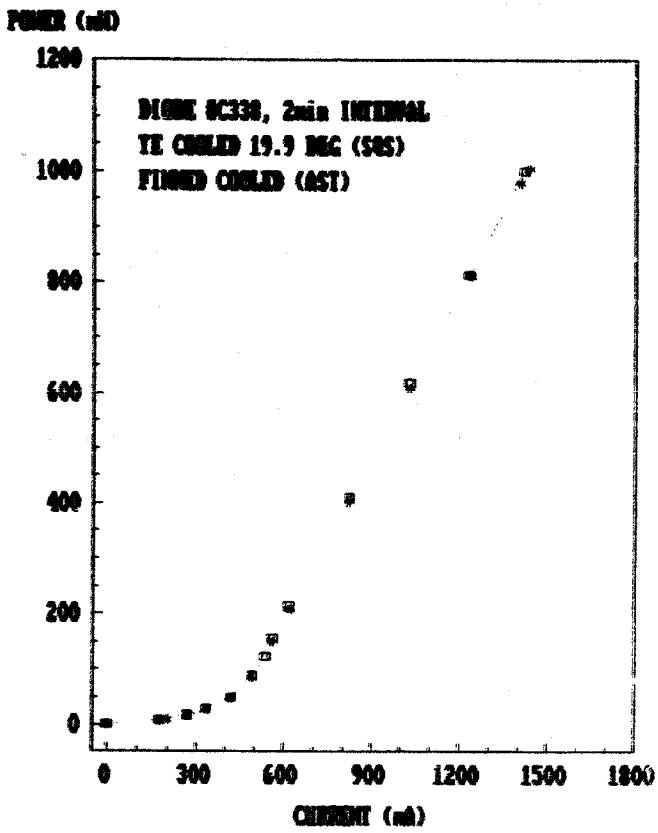

Figure 24. Optical Power vs. Current for SDL 1-W LD C338 Operating up to 1 W, TE- and Fin-Cooled at 2-min Intervals

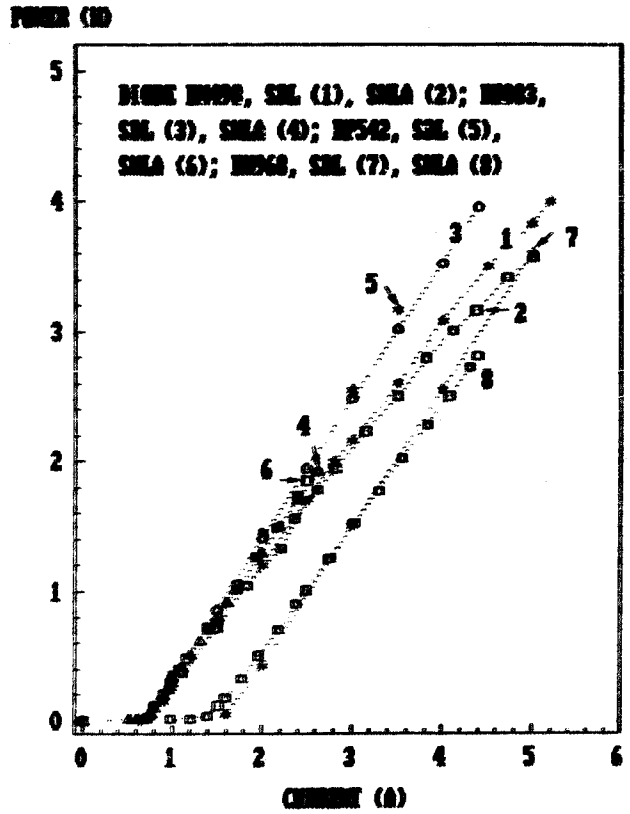

Figure 25. Optical Power vs. Current for Three 4-W and One 8-W Prototype SDL LDs: Three 4-W LDs (1 & 2) BM498, (3 & 4) RB883, and (5 & 6) RP542 and an 8-W LD (7 & 8) BN968 Operating to (1 & 2) 4 W at SDL and to Its Catastrophic Damage Level 3.57 W at SNLA, (3 & 4) 4-W at SDL and 2 W at SNLA, (5 & 6) 3.2 W at SDL and 2 W at SNLA, and (7 & 8) 3.6 W at SDL and 3 W at SNLA, all TE-Cooled at 3-min Intervals at SNLA

Figure 25 shows the optical power as a function of current for three SDL 4-W 100-μm-aperture LDs (BM498, RB883, and RP542). The figure also shows the optical power as a function of current for SDL 8-W 200-μm-aperture LD BN968. Curves 1, 3, 5, and 7 are produced by SDL data; Curves 2, 4, 6, and 8 are produced by SNLA data. Both sets of data for BM498 exhibit more erratic behavior than for RB883, RP542, BN968, A321, A322, B126, A840, or A841 tested previously.

When we compare the SDL data of BM498, RB883, and RP542 to the SNLA data at large LD optical power, it shows that a larger rollover is observed for the SNLA data:

- **SDL Test.** For the SDL test, the LD current is ramped to its maximum value in 0.2 to 0.3 s.
- **BM498.** For BM498, there is good agreement between the SDL and SNLA data until the LD emits about 1.6 W or when it draws 2.36 A. The SNLA test procedure for BM498 consists of four LD shots at a specific LD output optical power level, one shot through a FO, one shot through a FO to activate the HOFS system, and one shot through a FO while monitoring the output power. This test sequence is repeated in steps of 0.7 W, starting at 0.7 W. As the current in the LD increases above 2.36 A, the SNLA data show that less optical power is produced per incremental current increase than for the SDL data. Attempts to produce 3.7 W of optical power caused catastrophic damage to LD BM498.
- **RB883 and RP542.** The SNLA test for RB883 and RP542 is slightly different and consists of three, instead of five, LD shots prior to exciting the HOFS system. LD RP542 exhibits a larger slope efficiency than the other two 4-W LDs tested (Table 1). LDs RP542 and RB883 operate similarly to each other at both SDL and SNLA. At SNLA, they are not operated over 2 W. At the 2-W level, the optical power measured at SNLA is about 5% to 7% less than that measured at SDL. For the SNLA data on the three LDs, the large rollover is probably due to increased junction heating. The SNLA test sequence keeps the LDs on longer than does the SDL test sequence.
- **BN968.** The threshold of 8-W LD BN968 is less for the SNLA (1.32 A) than for the SDL data (1.48 A). The threshold of BN968 is more than two times larger than that of the 4-W LDs. The slope efficiency is larger for the SDL data (1.14 W/A) than for the SNLA data (0.95 W/A). The SNLA data do not roll over like that of the 4-W LDs. The LD current is limited to <5 A for the SDL data and <4.5 A for the SNLA data.

Figure 26 shows the plot of optical power as a function of current for four MDAC/OEC LDs with coated-cavity mirrors. The structure of these LDs is listed in Table 2. The specific doping and thickness of the layers are unknown. Each LD is operated until its catastrophic level is reached, i.e., when the slope of the LD changes or the LD ceases to emit light. Model E204A-6 had the best performance, producing 1.67 W of optical power. Model E220A-2 damaged at the lowest optical power of 0.6 W.

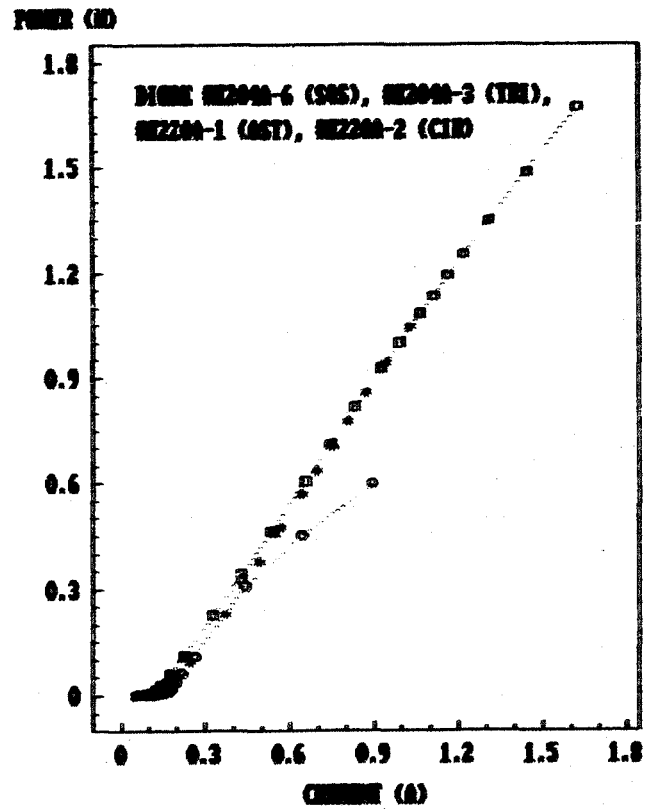

Figure 26. Optical Power vs. Current for Four Coated-Cavity-Mirror MDAC/OEC Developmental 1-W LDs Operating up to Their Catastrophic Levels: E204A-1 (1 W), E204A-2 (0.6 W), E204A-3 (0.7 W), and E204A-6 (1.67 W)

Figure 27 shows the optical power of seven MDAC/OEC uncoated-cavity-reflector LDs as a function of current. The structure of the LDs is listed in Table 2. The specific doping and thickness of the layers are unknown. Model E170R-1 produced the largest output optical power of 2.10 W before it damaged. E170T-5 produced the smallest output optical power, ~1.6 W. The coated-cavity-reflector LDs outperformed the uncoated-cavity-reflector LDs in that the coated-cavity LDs gave more output optical power at any specific current.

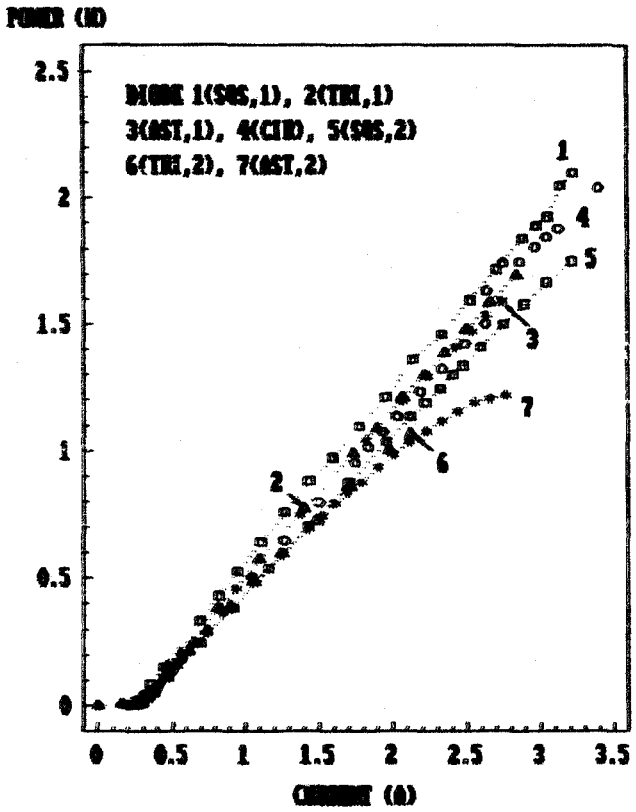

Figure 27. Optical Power vs. Current for Seven Uncoated-Cavity-Mirror MDAC/OEC Developmental 2-W LDs Operating up to Their Catastrophic Levels: Diode E170R-1 (2.1 W) of Curve 1 (1), E170T-4 (1.7 W) is 2, E170T-5 (1.6 W) is 3, E170R-4 (2 W) is 4, E204Q-1 (1.75 W) is 5, E170T-1 (1.1 W) is 6, and E170T-3 (1.2 W) is 7

Figure 28 shows the optical power of two MDAC/OEC coated-cavity-reflector LDs as a function of current. The structure of these LDs is shown in Table 2. These LDs have the longest cavity tested. LD E170T-2-10 (the AST data) was operated at a single shot at each level until the 2-W level. At this level, the LD was shot seven times. When the test was resumed, the first shot (which was at an elevated current in order to produce 2 W of optical power) damaged the LD. The LD continued to have reduced output for larger input currents. The other LD, E170T-2-9, was tested with each successive shot at elevated current until it emitted about 5 W. On the third shot at that level, catastrophic damage occurred.

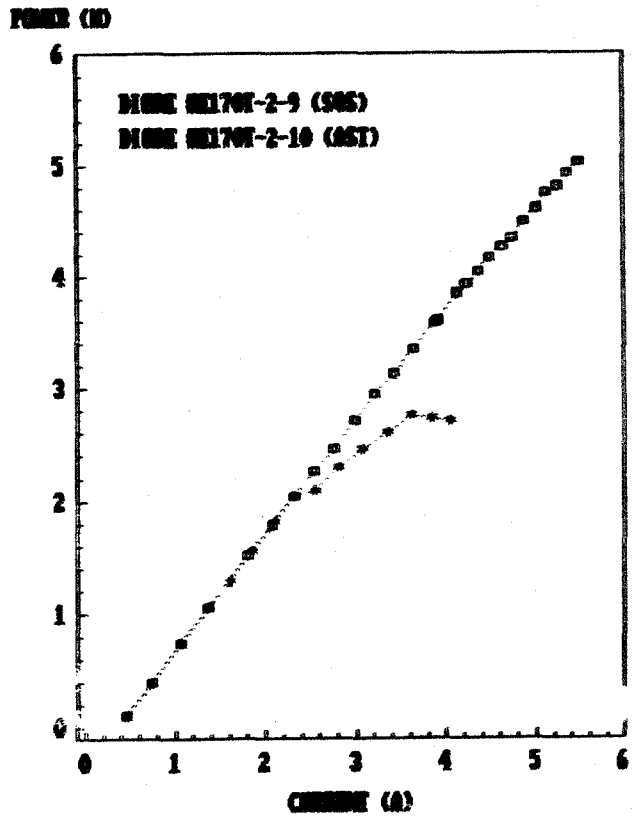

Figure 28. Optical Power vs. Current for Two Extra-Long Coated-Cavity-Mirror MDAC/OEC Developmental 5-W LDs Operating up to Their Catastrophic Levels: E170T-2-9 (5 W) and E170T-2-10 (2.1 W)

4.1.2 Efficiencies

The efficiencies as functions of LD optical power are measured for

- Six SDL 100-mW LDs
- Three SDL 500-mW LDs
- One SDL 1-W LD
- Three SDL 4-W LDs
- One SDL 8-W LD
- Six MDAC/OEC coated-cavity-reflector LDs
- Seven MDAC/OEC uncoated-cavity-reflector LDs.

Figure 29 illustrates the efficiencies of six SDL 100-mW LDs as functions of output optical power up to their rated power of 100 mW. The efficiency:

$$E_{LD} = (P_{LD}/P_e) \times 100 , \qquad (27)$$

where P_{LD} is the optical power out of the LD and P_e is the electrical power into the LD.

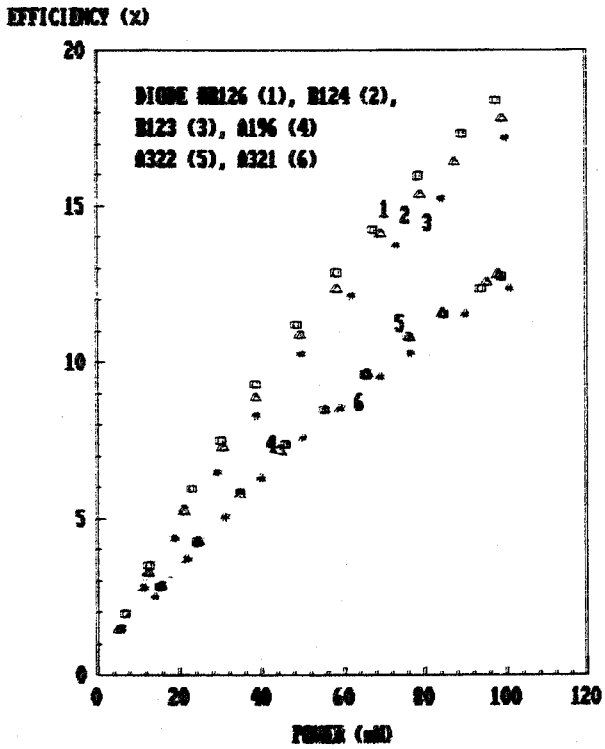

Figure 29. Efficiency vs. Optical Power for Six SDL 100-mW LDs (B123, B124, B126, A196, A321, and A322) Operating up to 100 mW

The LDs with the B-prefix serial numbers are more efficient by ~34% than those with the A prefixes. This is related to variations in LD fabrication, i.e., doping and possibly layer thickness.

Figure 30 shows that the efficiency of B126 at rated power of 100 mW is ~18%. As the LD input current increases above the rated current to produce 400 mW, the efficiency increases to ~33.5%, an increase of about 1.9 times. Similar results are observed for A322 and A321, where the 12.7% efficiency at rated conditions increases to ~24% at 400 mW; this is an increase of about 1.8 times. An apparent saturation is setting in at the upper levels, since an incremental increase in current does not produce as large an increase in efficiency.

Figure 31 shows that the efficiencies of the two SDL 500-mW LDs, A841 and A840, are almost identical. They increase to ~18.5% at rated output optical power of 500 mW.

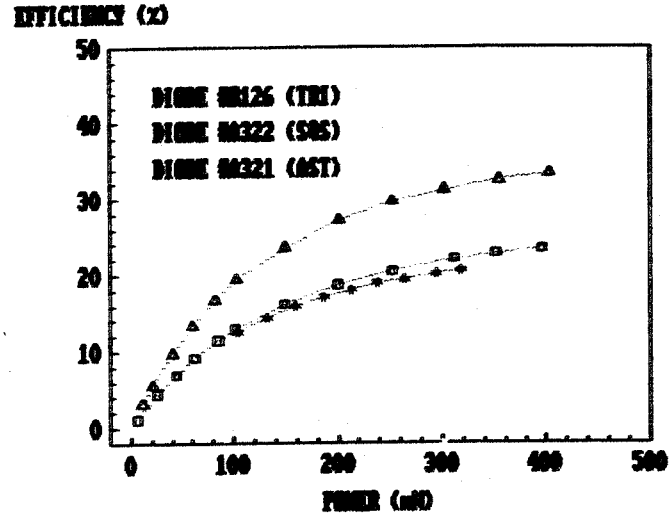

Figure 30. Efficiency vs. Optical Power for Three SDL 100-mW LDs (A321, A322, and B126) Operating up to 400 mW, Four Times Their Rated Power Levels

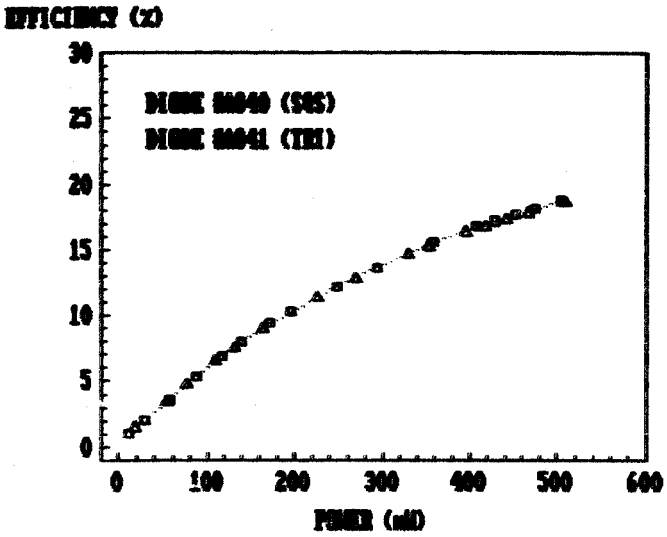

Figure 31. Efficiency vs. Optical Power for Two SDL 500-mW LDs (A840 and A841) Operating up to 500 mW

Figure 32 shows that the efficiencies of these LDs continue to track each other as the current is increased so as to produce 2 W of optical power. The maximum LD efficiencies of each LD of ~26% is reached at the LD level of 1.3 W. At the maximum LD optical power of 2 W, their efficiencies decrease to 25%.

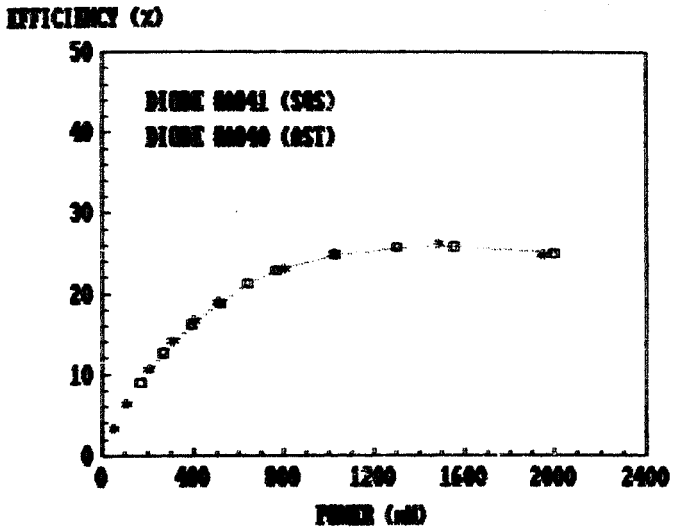

Figure 32. Efficiency vs. Optical Power for Two SDL 500-mW LDs (A840 and A841) Operating up to 2 W, Four Times Their Rated Power Levels

The efficiencies of SDL 500-mW LD C347 and the 1-W LD C338 are shown in Figures 33 and 34, respectively. For both the LDs operating up to their rated power, the efficiencies are still increasing. The maximum efficiency for C347 is almost 40%; for C338, the maximum efficiency is 38%. These are much greater than the efficiencies for either A840 or A841 (Figure 31). The increase in efficiencies is related to the decrease in the threshold described in Figures 23 and 24, and to LD structure architectural changes in the active region from multiple-quantum to single-quantum wells.

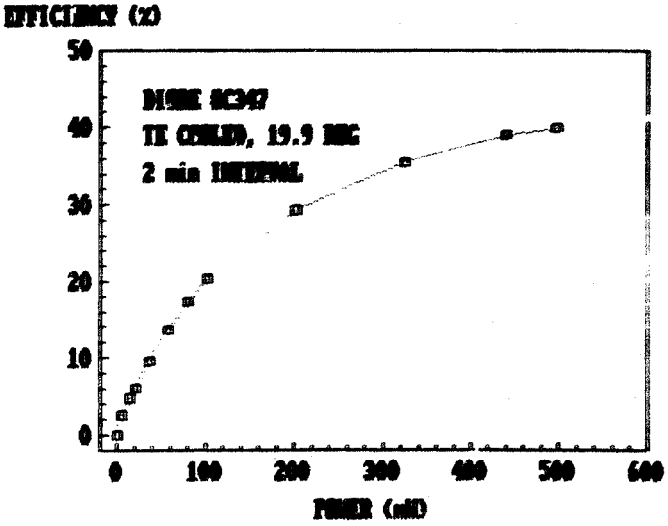

Figure 33. Efficiency vs. Optical Power Using SDL 500-mW LD C347 Operating up to 500 mW, TE-Cooled at 2-min Intervals

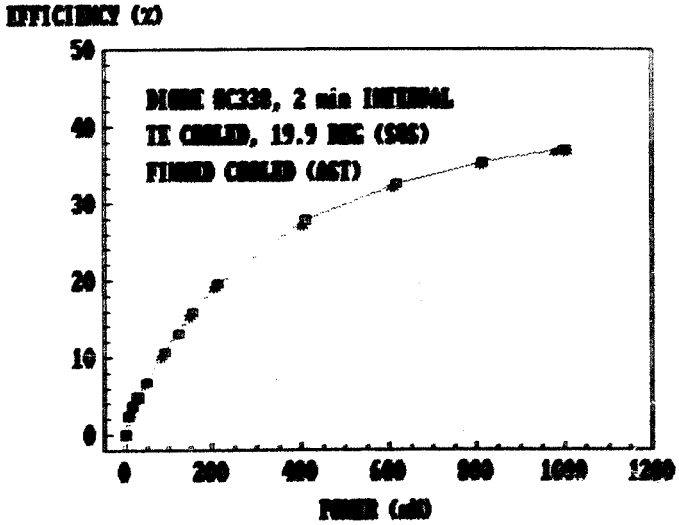

Figure 34. Efficiency vs. Optical Power Using SDL 1-W LD C338 Operating up to 1 W, TE-Cooled at 2-min Intervals

Figure 35 shows the efficiency of three SDL 4-W LDs (BM498, RB883, and RP542) and of an 8-W LD (BN968).

- **BM498.** The performance of the SDL LD BM498 was similar to the performances of the SDL A840 and A841; at about half its catastrophic damage level, the efficiency began to decrease. For A840 and A841, the maximum efficiency occurred at ~1.5 W (Figure 30), which is close to half the catastrophic damage level for this type of LD. The maximum efficiency for BM498 occurred at ~2.2 W, which is about half the catastrophic damage level for this type of LD.[32] The decrease in this maximum efficiency at the maximum LD optical power of 3.6 W is 8.8%. The rollover in efficiency is more severe for the BM498 than for A840. The maximum efficiency of 37.4% for BM498 is significantly larger than the 26.2% observed for A840 and A841.

- **LDs RB883, RP542, and BN968.** LDs RB883 and RP542 are operated up to 2 W, and BN968 is operated up to 2.8 W. The catastrophic level of both LDs, RB883 and RP542, should be the same as LD BM498. The 2.8-W operating level of LD BN968 is about 35% of its catastrophic 8-W level. For these three LDs, it is evident that we are below the rollover in efficiency. The maximum E_{LD} at 2 W is 40% for RB883 and 37.9% for RP542. This is slightly larger than that observed for BM498. For LD BN968, the maximum E_{LD} at 2.8 W is 33.7%, which is slightly less than the maximum for LD BM498.

Figure 36 illustrates the efficiency of the MDAC/OEC uncoated-cavity-mirror LDs. It varies from a maximum of ~35% at 0.9 W for the E170R-1 LD to ~25% at 0.9 to 1 W for the E204Q-1 LD. Two LDs showed irregular behavior, e.g., their efficiencies increased suddenly at the higher output power. (See E170R-1 at ~2 W and E170R-4 at ~1.6 W.)

Figure 37 illustrates the efficiency of four MDAC/OEC coated-cavity-reflector 1-W LDs. These LDs showed marked increases in efficiency over the uncoated LDs. The maximum efficiency of 50% was observed for E220A-1 at 1.05 W of output power. The efficiency was still increasing when the LD underwent catastrophic failure. The performance of LD E220A-2 was similar to that of E220A-1 until it damaged at ~0.7 W. At this time, there was a drastic change as shown by the plot of the AST data; the data deviate from the established trend for lower LD power.

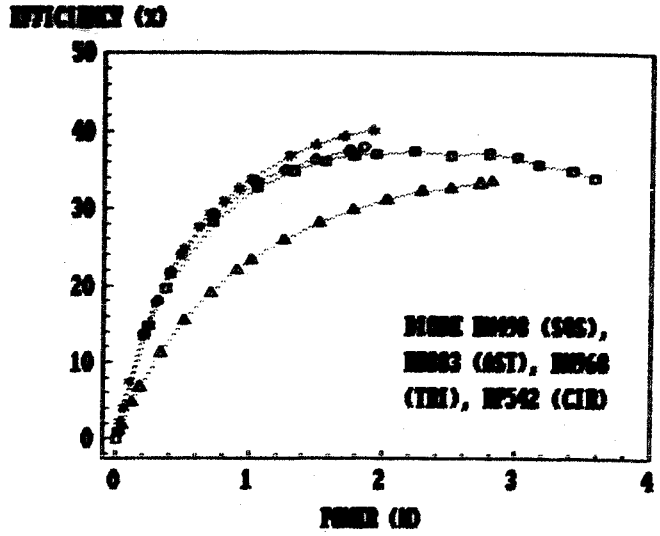

Figure 35. Efficiency vs. Optical Power for Three 4-W and One 8-W Prototype SDL LDs: Three 4-W LDs (SQS) BM498, (AST) RB883, and (CIR) RP542 and an 8-W LD (TRI) BN968 Operating (SQS) 4 W at SDL and to Its Catastrophic Damage Level 3.6 W at SNLA, (AST) 4 W at SDL and 2 W at SNLA, (CIR) 3.2 W at SDL and 2 W at SNLA, and (TRI) 3.6 W at SDL and 3 W at SNLA, all TE-Cooled at 3-min Intervals at SNLA

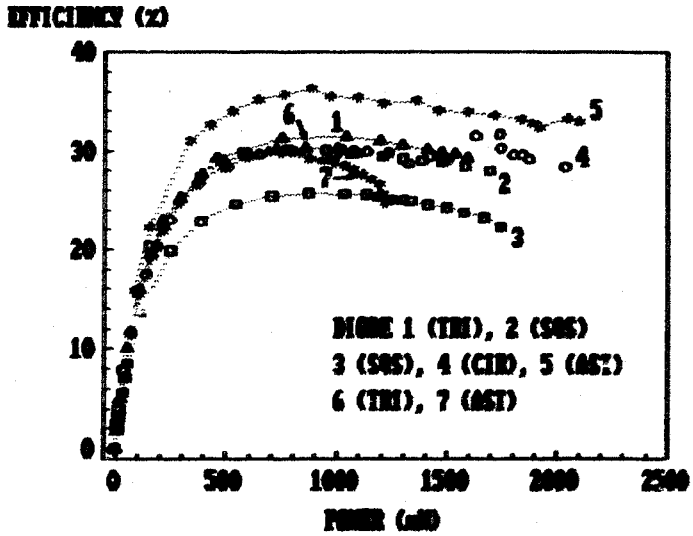

Figure 36. Efficiency vs. Optical Power for Seven Uncoated-Cavity-Mirror MDAC/OEC Developmental 2-W LDs Operating up to Their Catastrophic Levels: Diode E170T-5 (1.6 W) is Curve (1), E170T-4 (1.7 W) is 2, E204Q-1 (1.75 W) is 3, E170R-4 (2 W) is 4, E170R-1 (2.1 W) is 5, E170T-1 (1.1 W) is 6, and E170T-3 (1.2 W) is 7

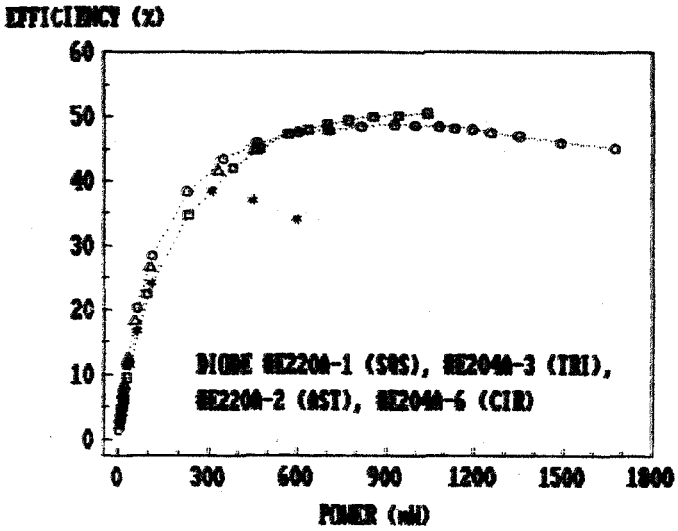

Figure 37. Efficiency vs. Optical Power for Four Coated-Cavity-Mirror MDAC/OEC Developmental 1-W LDs Operating up to Their Catastrophic Levels: E220A-1 (1 W), E220A-2 (0.6 W), E204A-3 (0.7 W), and E204A-6 (1.67 W)

Figure 38 depicts the efficiency of the long-cavity-mirror LDs E170T-2-9 and E170T-2-10. The efficiency of ~50% peaked at the output optical power of 2.4 and 2.0 W for each LD, respectively. The 50% efficiency and the 5 W of LD optical power are the largest observed for any SDL or MDAC/OEC LDs. LD E170T-2-9 had the largest decrease in efficiency prior to failure, with increase in LD optical power after the observed maximum of any LD measured. The efficiency ranged from a maximum of 50% to about 43%.

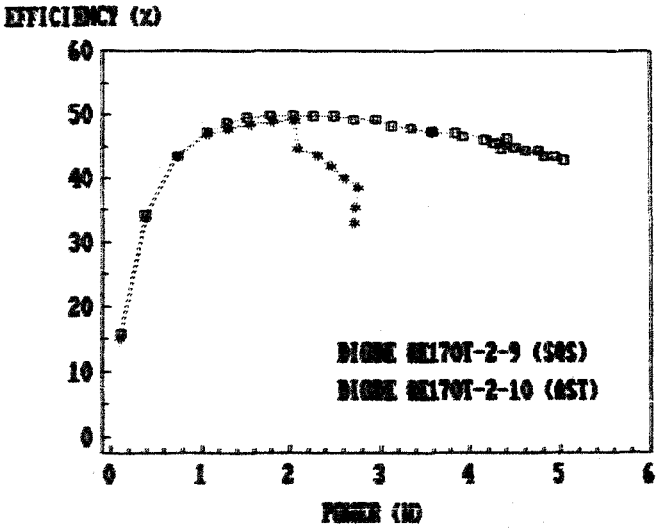

Figure 38. Efficiency vs. Optical Power for Two Extra-Long Coated-Cavity-Mirror MDAC/OEC Developmental 5-W LDs Operating up to Their Catastrophic Levels: E170T-2-9 (5 W) and E170T-2-10 (2.1 W)

4.1.3 Degradation

The degradation due to temperature was measured for

- SDL 100-mW LD B126
- SDL 500-mW LDs A840 and A841

The degradation due to aging[22] was measured for

- SDL 500-mW LD A841
- SDL 4-W LDs RB883 and RP542
- SDL 8-W LD BN968

Figure 39 illustrates the optical power vs. current for SDL LD B126. The LD is on a fin heatsink. As the shot interval changes from 10 min to 30 s, a slight decrease in LD output power is observed at the large LD levels.

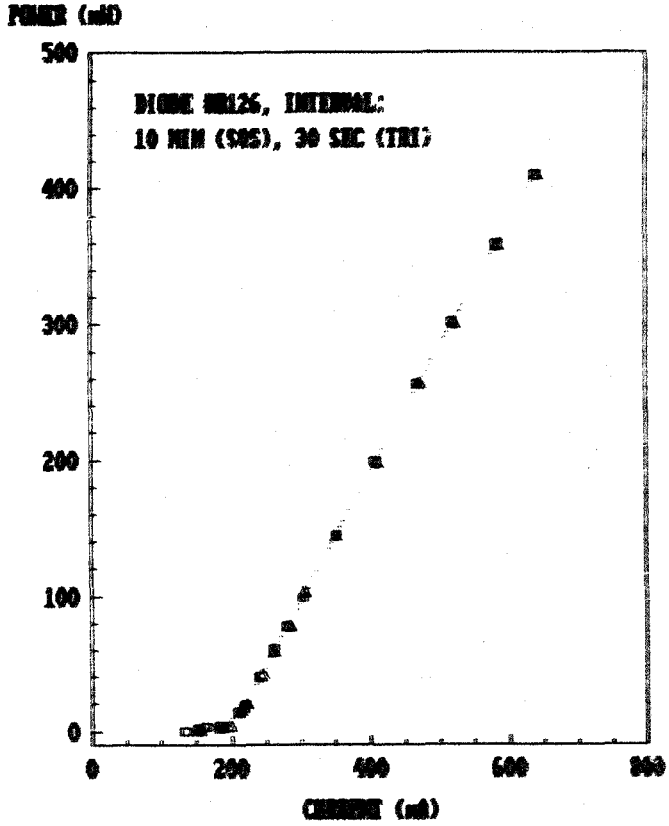

Figure 39. Degradation Due to Heating Illustrated by Optical Power vs. Current of SDL 100-mW LD B126 Operating up to 400 mW, Four Times Its Rated Power Level, at 10-min and 30-s Time Intervals

Figure 40 shows the optical power vs. current for SDL 500-mW LD A841. The effects due to the reduced time interval between LD shots are more pronounced for this LD than for LD B126. The same fin heatsink is used for all SDL LDs that are fin-heatsinked. This LD is fin-heatsinked. A rollover is

observed for LD A841 even at optical power levels near its 500-mW rated power level. At large output power and as the time interval between shots decreases or the repetition rate increases, the rollover is greater. At this LD power, the 30-s and 2-min-interval data are almost identical. At 2-W LD power, the 10-min-interval data show 4% less rollover than for the 30-s and 2-min-interval data. At this LD power, the thermal effects due to the reduced intervals also cause an increase in separation between the curves. The separation and increase in rollover are more apparent and larger at larger LD output optical power.

Figure 41 illustrates the optical power vs. current for SDL 500-mW LD A840 operating on a fin heatsink up to its 500-mW rated power level. At a 5-min interval between shots, the LD experiences minimum rollover. At the reduced 1-min interval between shots, the LD begins to roll over at the 200-mW output level. This rollover causes almost a 6% separation at the 500-mW level. This observed separation and rollover are undoubtedly due to the increase in LD junction heating caused by the increase in repetition rate.

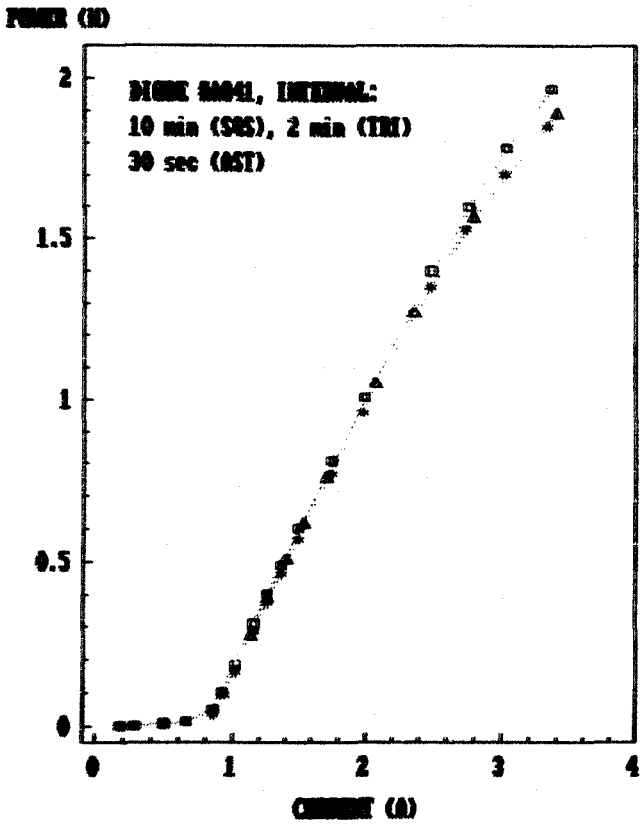

Figure 40. Degradation Due to Heating Illustrated by Optical Power vs. Current of SDL 500-mW LD A841 Operating up to 2 W, Four Times Its Rated Power Level, at 10-min, 2-min, and 30-s Time Intervals

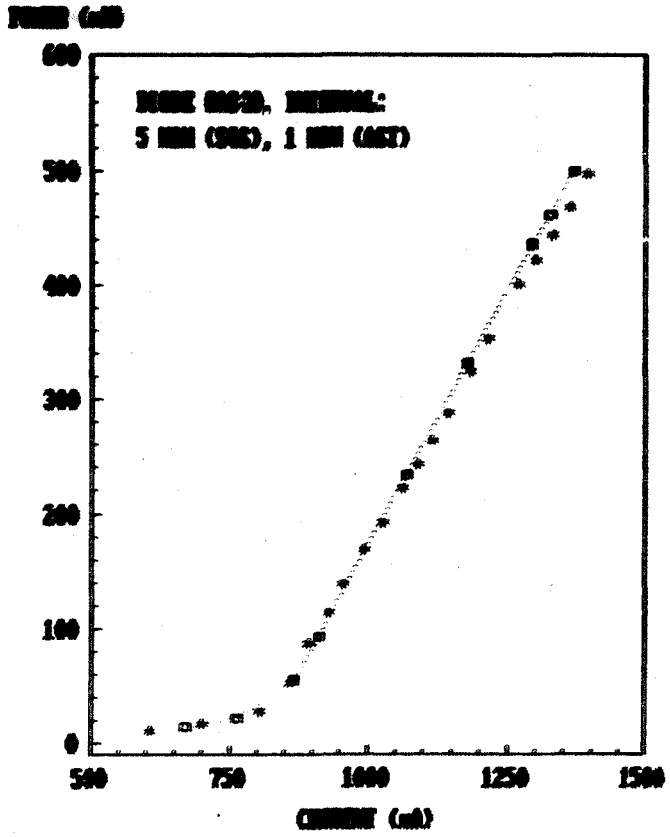

Figure 41. Degradation Due to Heating Illustrated by Optical Power vs. Current of SDL 500-mW LD A840 Operating up to 500 mW, Its Rated Power Level, at 1- and 5-min Time Intervals

Figure 42 shows the optical power vs. current of LD A840 operating on a TE heatsink cooled to 19.9°C. The optical power response at a different time interval between data shots is about the same, except at the 2-W level. At this level, only the 5-min-interval data show less heating effects. All the data show the same rollover from the 0- to 1.5-W output power.

Figure 43 illustrates the optical power vs. current for SDL 500-mW A840 on a fin heatsink and a TE-cooled heatsink. Both traces show a rollover of LD output power >500 mW, with increasing separation as LD output power increases. Heating appears to be more severe for the fin heatsink, even at low current. This is illustrated by the reduced LD output power for the fin compared to the TE-cooled heatsink with the same input current.

The rollover in LD optical power at large current and the increased separation indicate a decrease in efficiency in converting electrical energy to optical energy (Figure 44). The TE cooler data show that cooling improves the efficiency by ~10% at an output power >1 W.

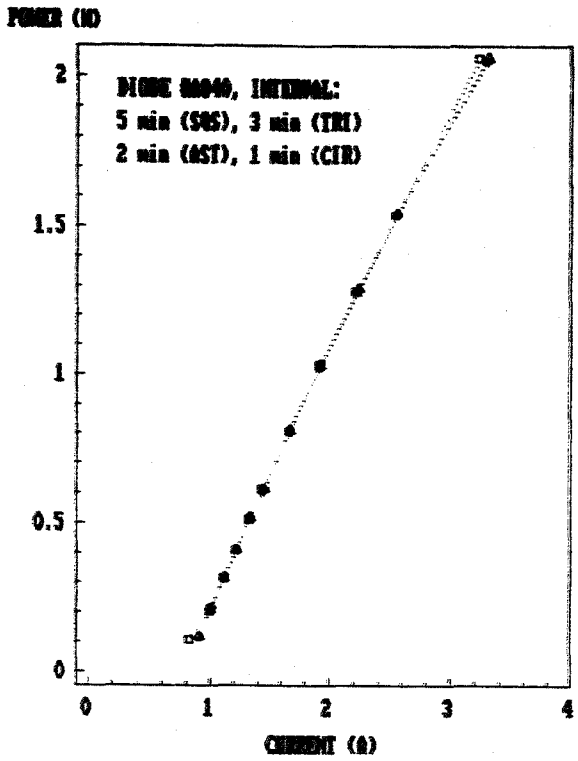

Figure 42. Degradation Due to Heating Illustrated by Optical Power vs. Current of SDL 500-mW LD A840, TE-Cooled, Operating up to 2 W. Four Times Its Rated Power Level, at 5-, 3-, and 1-min Intervals

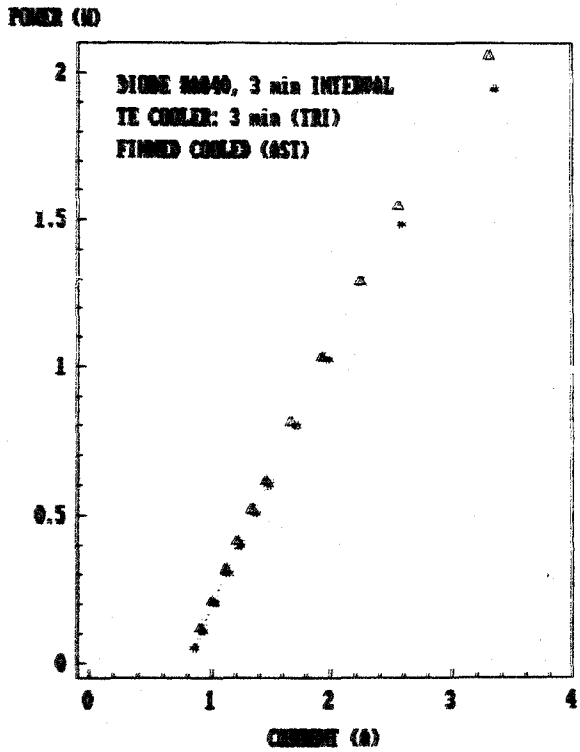

Figure 43. Degradation Due to Heating Illustrated by Optical Power vs. Current of SDL 500-mW LD A840, TE- and Fin-Cooled, Operating up to 2 W, Four Times Its Rated Power Level, at 3-min Intervals

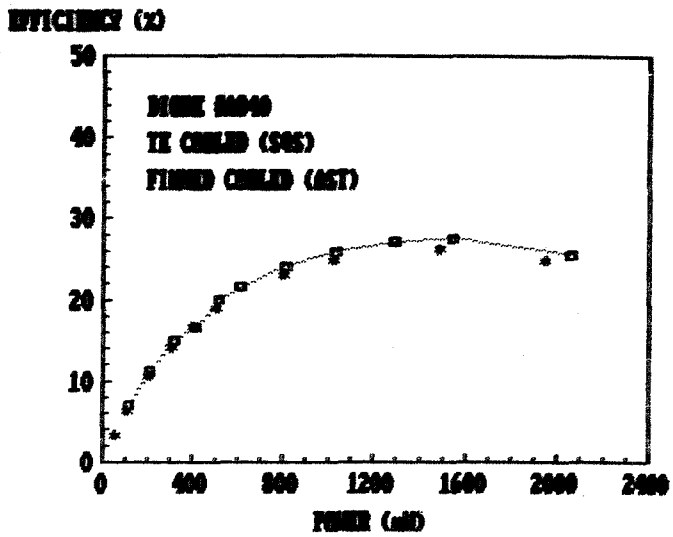

Figure 44. Degradation Due to Heating Illustrated by Efficiency vs. LD Optical Power of SDL 500-mW LD A840, TE- and Fin-Cooled, Operating up to 2 W, Four Times Its Rated Power Level, at 3-min Intervals

Aging is unrecoverable damage that produces less output optical power for the same LD current. Figure 45 shows optical power vs. current and Figure 46 shows efficiency vs. optical power for SDL LD A841 operating at different times during its life. Figure 20 described the initial slow degradation of SDL 100-mW LD A195 and then its more rapid degradation as aging[34] progressed. Figures 45 and 46 show that, at large LD output levels, apparent aging is taking place in LD A841. At the lower power level of up to 1 W, it appears that the efficiency of the LD increases after it has operated for a short period of time or after it is burned in. (Compare the SQS to the TRI data points.) After the LD is operated for longer periods of time, the decrease in efficiency at large-output optical power levels is apparent. (See the AST data points.) The late data (AST) were taken just before the LD quit operating. At that time, A841 had about 600 shots at ~5 s per shot, or a total operating time of ~50 min at elevated-output optical power levels.

The degradation of SDL 4-W LD BM498 has been described in Figure 25, Section 4.1.1.

Figure 47 shows the optical power vs. current for two SDL 4-W LDs, RB883 and RP542, and an 8-W LD, BN968. The degradation due to aging is apparent for LDs RB883 and BN968. There is little or no effect due to aging for LD RP542 (the AST close to CIR and TRI are later shots for LD RP542). LD efficiency vs. optical power for the same three LDs is shown in Figure 48. The degradation due to aging is also apparent in this plot for LDs RB883 and BN968 (the AST close to CIR are later shots for LD RP542). The early data shots were the first shots at each power level.

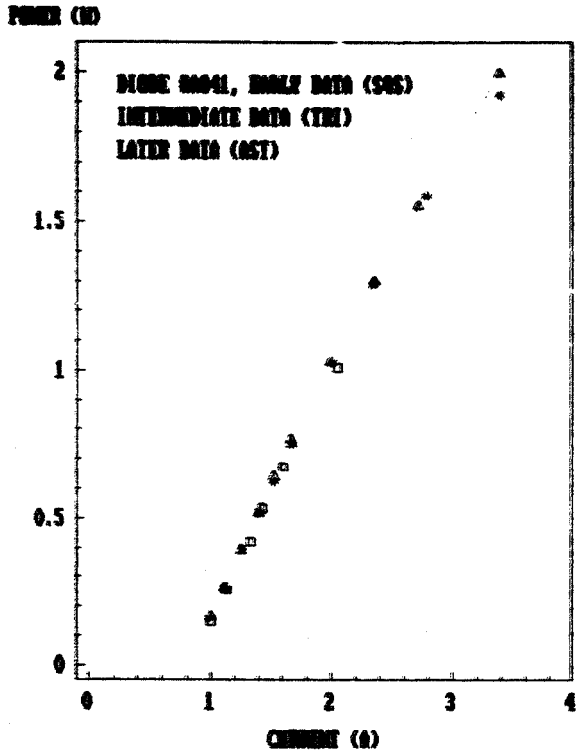

Figure 45. Aging Illustrated by Optical Power vs. Current of SDL 500-mW LD A841 Operating up to 2 W, Four Times Its Rated Power Level, at Different Times During Its Life

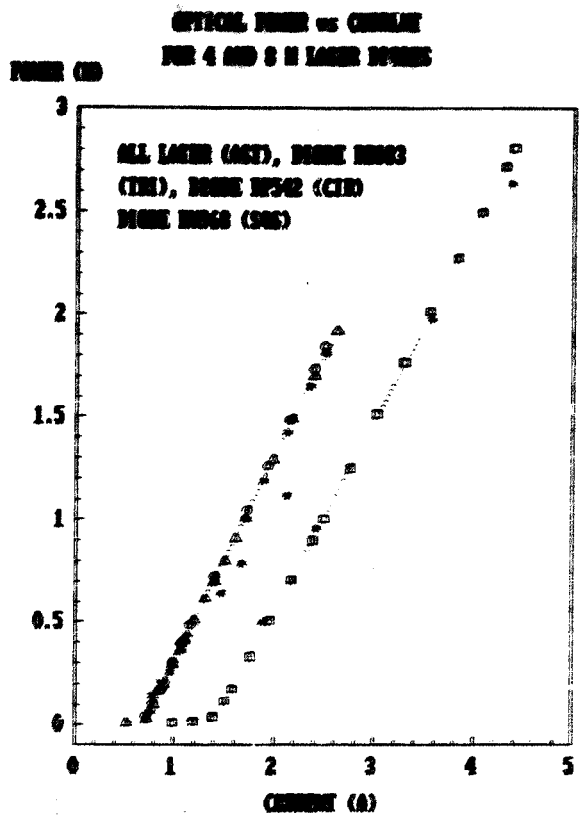

Figure 47. Aging Illustrated by Optical Power vs. Current of Four Prototype SDL LDs. Two 4-W LDs (RB883 and RP542) and an 8-W LD (BN968) Operating up to 2 and 2.8 W at Different Times During Their

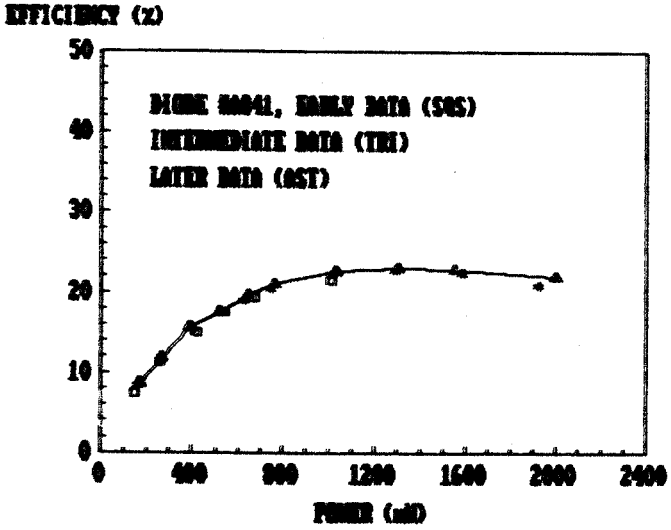

Figure 46. Aging Illustrated by Efficiency vs. Optical Power of SDL 500-mW LD A841 Operating up to 2 W, Four Times Its Rated Power Level, at Different Times During Its Life

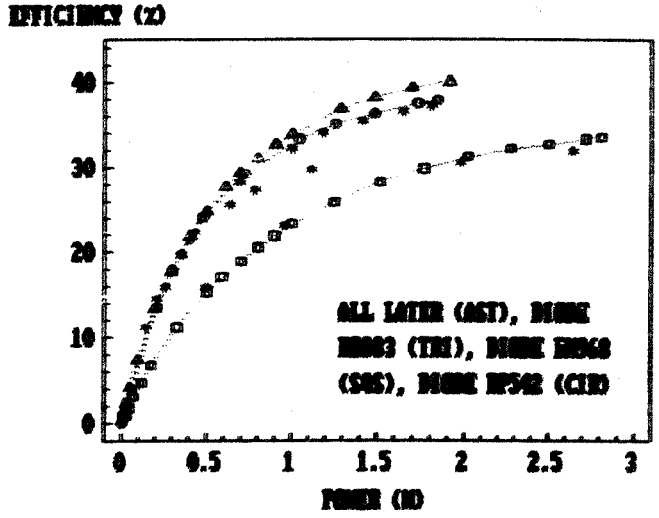

Figure 48. Aging Illustrated by Efficiency vs. Optical Power of Four Prototype SDL LDs: Two 4-W LDs (RB883 and RP542) and an 8-W LD (BN968) Operating up to 2 and 2.8 W at Different Times During Their Lives

For LD RB883, late AST data had

- 24 shots at 0.5 W
- 56 shots at 1 W
- 12 shots at 1.5 W
- 12 shots at 2 W

Aging causes LD RB883 at a current of 2.2 A to produce ~22% less P_{LD} than earlier in its life (TRI).

For LD BN968, late data had

- 142 shots at 0.5 W
- 94 shots at 1 W
- 17 shots at 1.5 W
- 98 shots at 2 W
- 14 shots at 2.5 W
- 62 shots at 3 W

At a current of 4.4 A, aging caused LD BN968 to produce 6% less P_{LD} than the early AST data.

Both LDs, RB883 and BN968, have a crossover region where the same amount of current before and after aging produces the same LD optical power. For LD RB883, the crossover is at 0.3 W for a current of 1 A. For LD BN968 the crossover is at 1.3 W for a current of 2.8 A. For currents below the crossover, less current produces more LD optical power after the LD ages (Figure 47).

Figure 48 shows the efficiency vs. optical power for LDs RB883, RP542, and BN968. The aged LD is more efficient below the crossover as described earlier. Above the crossover for RB883 operating at 1.2 W, the efficiency is decreased by 14.3%; for BN968 at 2.64 W, the efficiency is decreased by 5.1%.

4.1.4 Beam Intensity Distribution

The beam intensity distribution of four SDL LDs (A322, A840, BN968, and RP542) are described in this section. In particular, the beam intensity distributions of LDs BN968 and RP542 are studied at different times during their lives and after they are turned on. For LDs A322 and A840, Sections A and C of the figures are profiles in the X direction (perpendicular to the long dimension of the LD aperture) and in the Y direction (along the long dimension of the LD aperture) through the peak of the intensity distribution of the top and bottom lobes of the contours of the LD beam illustrated in Section B. The width of the frame from the right to left edge for the profiles in Sections A and C is 6.7 mm.

For LDs BN968 and RP542, Section A of the figures contains the contours (six equally spaced intensity (W/cm² levels) of the intensity distribution of the beam and Section B shows the profiles through the centroids of the LD beam in the X and Y directions. The dotted lines in the profiles of all figures are a Gaussian fit to the intensity distribution of the specific profile. When the correlation coefficient (CC) of the fit becomes unstable because the numbers used in the fitting equations are either too large or too small, the words "NO FIT" appear above the axis callout. A CC of 1 indicates a perfect Gaussian fit.

LDs A322 and A840

The beam intensity distributions of SDL 100-mW LD A322 operating at 99.8 and 395 mW are shown in Figure 49. The beam intensity distributions of SDL 500-mW LD A840 operating at 522 and 1952 mW are described in Figure 50. There are eight equally spaced intensity (W/cm²) contours in Figure 49 I and II, and in Figure 50 I, and ten contours in Figure 50 II. The optical distance from the active surface of the camera to the LD-emitting mirror is ~9.6 mm.

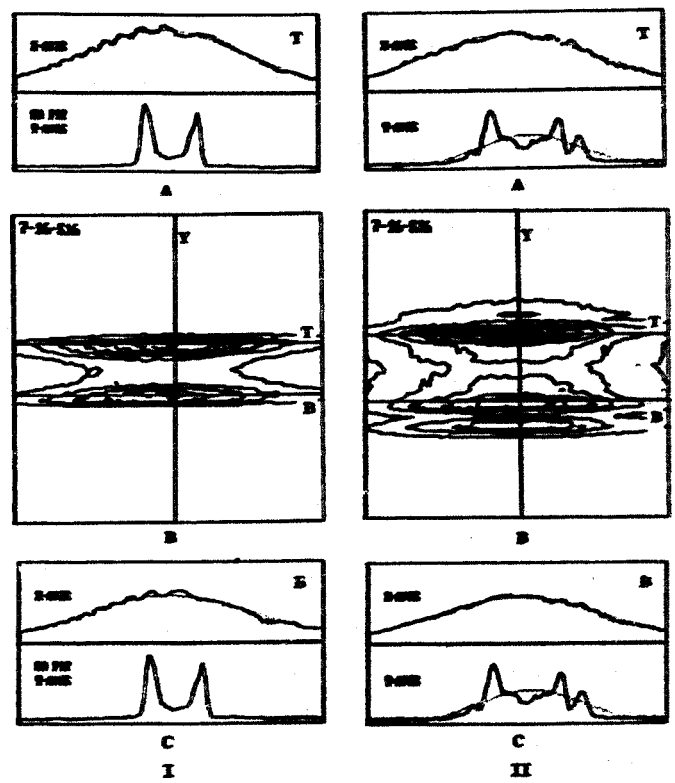

Figure 49. Contours and Profiles of Intensity Distribution of the Output Beam of SDL 100-mW LD A322 Operating at 99.8 mW (I) and 395 mW (II), Recorded 9.6 mm From the LD Mirror

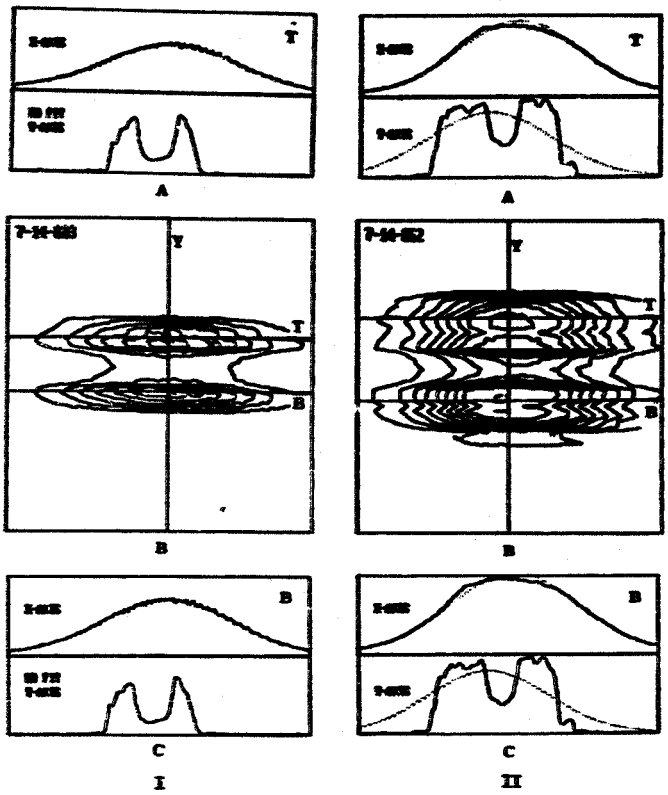

Figure 50. Contours and Profiles of Intensity Distribution of the Output Beam of SDL 500-mW LD A840 Operating at 522 mW (I) and 1952 mW (II), Recorded 9.6 mm From the LD Mirror

The Gaussian fits are generally good for the X axes; they are not as good for the Y axes due to the two lobes in the laser beam intensity distribution. The width, α_T, is the width of the intensity distribution to $1/e^2$ of the peak intensity of a Gaussian beam fit in the X and Y directions of the top lobes (marked "T" in the figures), and α_B is the width of the intensity distribution to $1/e^2$ of the peak intensity of a Gaussian beam fit in the X and Y directions of the bottom lobes (marked "B" in the figures). For Figure 49 I and II the α_T's are 7.40 mm (X) and NO FIT (nf) (Y) and 7.50 mm (X) and 4.50 mm (Y), respectively. For Figure 49 I and II the α_B's are 7.51 mm and nf and 7.58 mm and 4.50 mm, respectively. For Figure 50 I and II the α_T's are 5.97 mm and nf and 5.54 mm and 5.47 mm, respectively. For Figures 50 I and II the α_B's are 5.79 mm and nf and 5.77 mm and 5.39 mm, respectively. The LD intensity distribution record is taken 0.2 to 0.4 s after turn-on.

SDL 8-W LD BN968 Operating Early in Life

Figure 51 shows the contours and profiles of the intensity distribution of SDL 8-W LD BN968 beam. The LD operated at four output optical levels early in its life. The intensity distribution record is taken 0.2 to 0.4 s after turn-on. The optical distance from the LD output mirror to the camera active CID surface is 8.87 mm for Figure 51 I, II, III, and IV and is 10.87 mm for Figure 51 V, VI, VII, and VIII.

The LD emitting power and the number of accumulative LD shots prior to

- Figure 51 I and V are 0.47 W and 12 shots at 0.5 W
- Figure 51 II and VI are 1.0 W and 12 shots at 0.5 W and 5 shots at 1 W
- Figure 51 III and VII are 2.0 W and 12 shots at 0.5 W, 5 shots at 1 W, and 10 shots at 2 W
- Figure 51 IV and VIII are 2.8 W and 12 shots at 0.5 W, 5 shots at 11 W, 10 shots at 2 W, and 11 shots at 2.8 W, respectively.

After Shot 11-23-S39, the total number of LD shots at all levels is 38. The two lobes in the intensity distribution observed for LDs A322 and A840 in Figures 49 and 50 are observed for LD BN968 only at the 0.47-W level and then not as pronounced. At the close position (Figure 51 IV-A), the narrow divergence is in the V direction or the Y-axis of the LD or the X-axis of the camera instead of in the conventional H direction or the X-axis of the LD or Y-axis of the camera.

At the far position (Figure 51 VII and VIII), increased mode structure is observed at both the 1.99- and 2.84-W levels. The Gaussian fit is better for the H direction (Y-axis) or along the long direction of the LD aperture than for the V direction (X-axis).

The Gaussian fit is not very good for Figure 51 I and V along the Y-axis, IV and VII along the X-axis and Y-axis, and VIII along the X-axis.

SDL-8-W LD BN968 Operating Later in Life

Figure 52 shows the beam contours and profiles of the intensity distribution of SDL 8-W LD BN968 beam. The LD was operated at four output optical levels later in its life.

The optical distance from the LD output mirror to the camera active CID surface is 8.87 mm for Figure 52 I, II, III, and IV and is 10.87 mm for Figure 52 V, VI, VII, and VIII.

The LD emitting power and number of accumulative LD shots prior to

- Figure 52 I and V are 0.49 W and 27 at 0.5 W, 45 at 1.0 W, 38 at 2.0 W, and 51 at 2.8 W
- Figure 52 II and VI are 1.1 W and 27 at 0.5 W, 48 at 1.0 W, 38 at 2.0 W, and 51 at 2.8 W/
- Figure 52 III and VII are 2.0 W and 27 at 0.5 W, 48 at 1.0 W, 45 at 2.0 W, and 51 at 2.8 W
- Figure 52 IV and VIII are 2.8 W and 27 at 0.5 W, 48 at 1.0 W, 45 at 2.0 W, and 58 at 2.8 W, respectively.

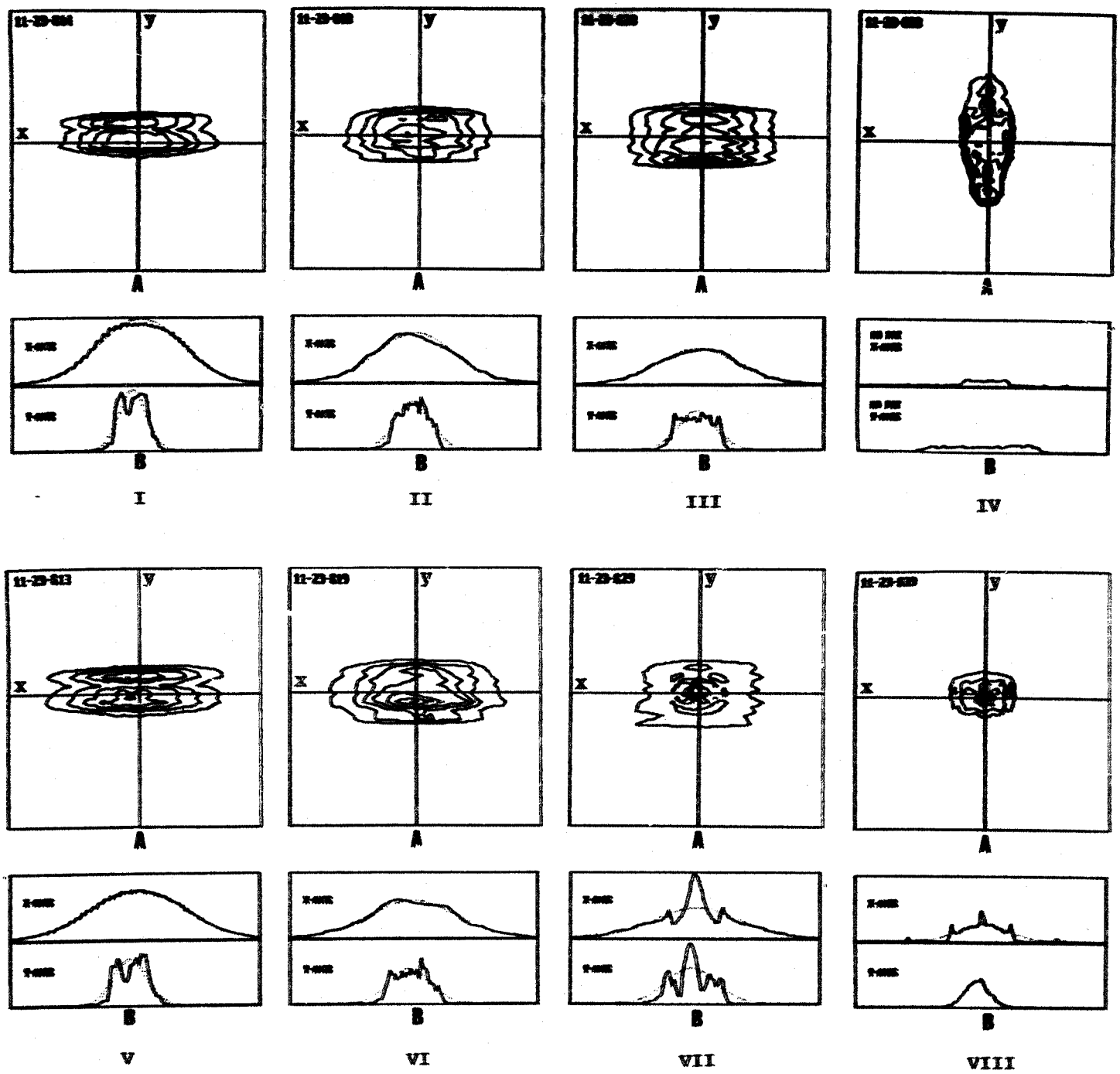

Figure 51. Contours and Profiles of Intensity Distribution of the Output Beam Early in the Life of SDL 8-W LD BN968. These operate at 0.47 W (I & V), 1 W (II & VI), 2 W (III & VII), and 2.84 W (IV & VIII).

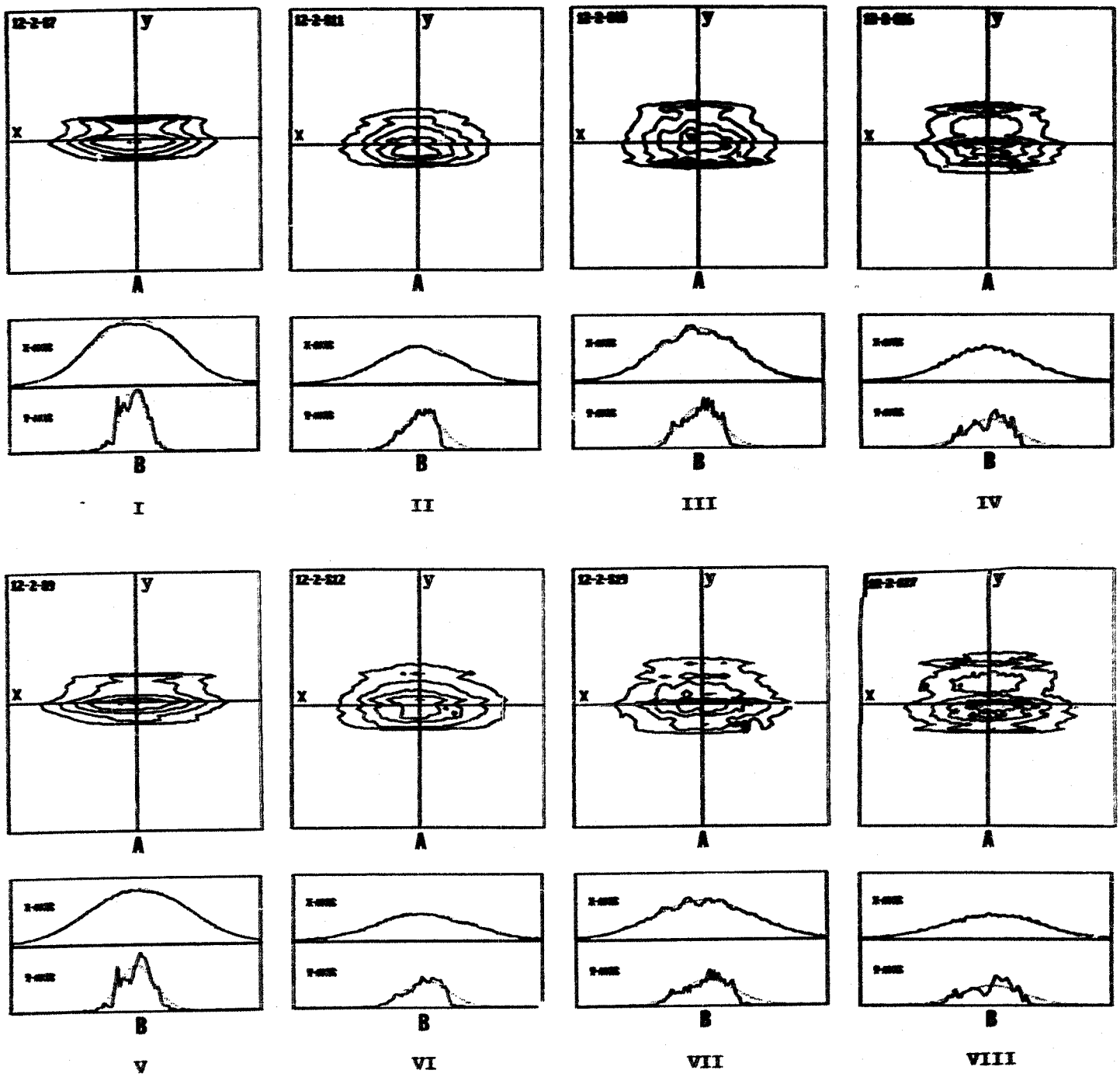

Figure 52. Contours and Profiles of Intensity Distribution of the Output Beam Later in the Life of SDL 8-W LD BN968. These operate at 0.49 W (I & V), 1.1 W (II & VI), 2 W (III & VII), and 2.84 W (IV & VIII).

After the last shot, 12-2-S27, the total number of LD shots at all levels is 178. The two lobes observed at the 0.5-W level earlier is all but gone. The mode structure observed earlier at the 2- and 2.8-W levels is also missing. The Gaussian fits are better for the X-axis than for the Y-axis. The Y-axis Gaussian fits of the Figure 52 data are better than those of Figure 51.

LD BN968 Operating at 1-W Accumulating Shots

Figure 53 shows LD beam contours and profiles of the intensity distribution of LD BN968 beam. The LD operated at 1 W as it accumulated shots. The optical distance from the LD output mirror to the camera's active CID surface is 8.87 mm for Figure 53 I, II, III, and IV and is 10.87 mm for Figure 53 V, VI, VII, and VIII.

The number of accumulative LD shots prior to

- Figure 53 I and V is 12 at 0.5 W and 5 at 1 W
- Figure 53 II and VI is 27 at 0.5 W, 48 at 1.0 W, 38 at 2.0 W, and 51 at 2.8 W
- Figure 53 III and VII is 42 at 0.5 W, 88 at 1.0 W, 80 at 2.0 W, and 74 at 2.8 W
- Figure 53 IV and VIII is 61 at 0.5 W, 118 at 1.0 W, 106 at 2.0 W, and 91 at 2.8 W.

The Gaussian fits improve with LD aging.

LD BN968 Operating at 2-W Accumulating Shots

Figure 54 shows LD beam contours and profiles of the intensity distribution of LD BN968 beam. The LD operated at 2 W as it accumulated shots. The optical distance from the LD output mirror to the camera active CID surface is 8.87 mm for Figure 54 I, II, III, and IV and 10.87 mm for Figure 54 V, VI, VII, and VIII. The number of LD shots at each output optical power level is as described for Figure 53. As mentioned earlier, the Gaussian fit improves with LD aging.

LD BN968 at Different Times After LD is Turned On

Figure 55 shows the contours and profiles of the intensity distribution of LD BN968 beam at different times after the LD is turned on.

- With the LD emitting 2.8 W, the number of LD shots prior to Figure 55 I, II, and III is 12 at 0.5 W, 5 at 1 W, 10 at 2 W, and 11 at 2.8 W.
- With the LD emitting 2.0 W, the number of shots prior to Figure 55 IV and V is 12 at 0.5 W, 5 at 1 W, and 10 at 2 W.

Figure 55 I, II, and III are for 0.218, 0.418, and 3.018 s after LD turn-on, whereas Figure 55 IV and V are 0.218 and 0.418 s after LD turn-on, respectively. For both LD levels, the beam contours and profiles change drastically in the X-axis and Y-axis during the time the LD operates.

Specifications for SDL 8-W LD BN968 Data

Table 4 lists specifications for SDL 8-W LD BN968, which include the shot number (#), LD output optical power (W), distance from the LD output mirror where the photographs are taken (mm), $1/e^2$ width (mm), divergence (degrees), CC, and the figure in which the contour or profile appears.

These data are for the contour and profile data in Figures 51 through 55. The records were taken at 8.87 and 10.87 mm from the LD's output mirror.

The divergence, a_x, (half-angle) is calculated using:

$$a_x = \tan^{-1}\left[\frac{(x_{13} - x_{14})}{2\,(z_{13} - z_{14})}\right], \qquad (26)$$

where x_{13} and x_{14} are the $1/e^2$ widths and z_{13} and z_{14} are the distances from the LD output mirror for Shots 11-23-S13 and 13-23-S14, respectively. The a_y divergence is calculated similarly, except that the x's are replaced by y's.

Previous to Shots 12-14-S6 through 12-14-S13, FO damage caused a white powder to be deposited on the LD mirrors. The divergence for these LD shots is not constant but erratic. After the FO damage, the divergence increased drastically.

If a trend appeared, it was the slight decrease in divergence with an increase in LD output optical power. The listings in Table 4 for Figures 53 and 54 show that there is also a trend for the divergence to increase with age at both the 1- and 2-W levels.

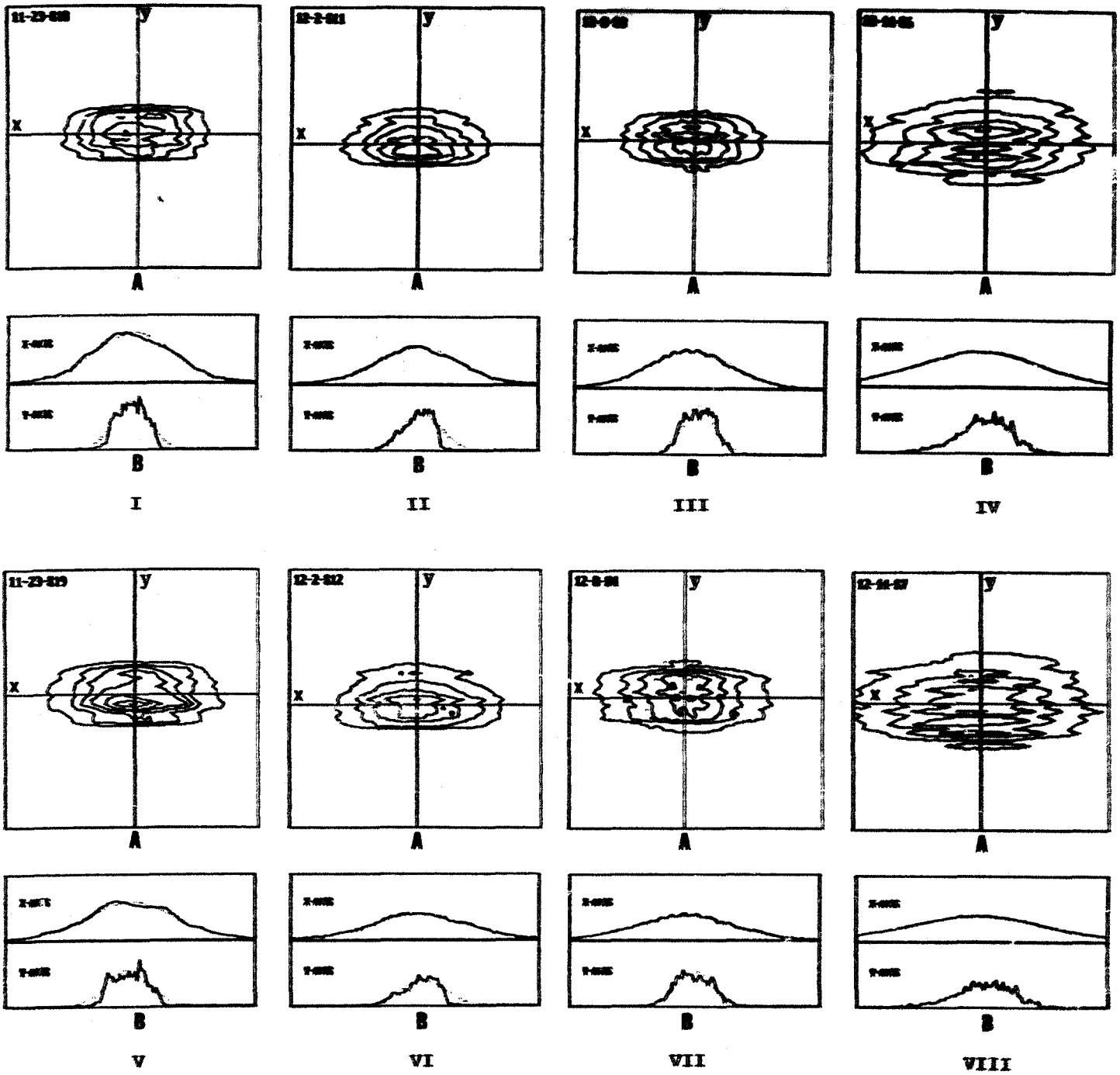

Figure 53. Contours and Profiles of Intensity Distribution of the Output Beam of SDL 8-W LD BN968 Operating at 1 W as Shots Accumulate

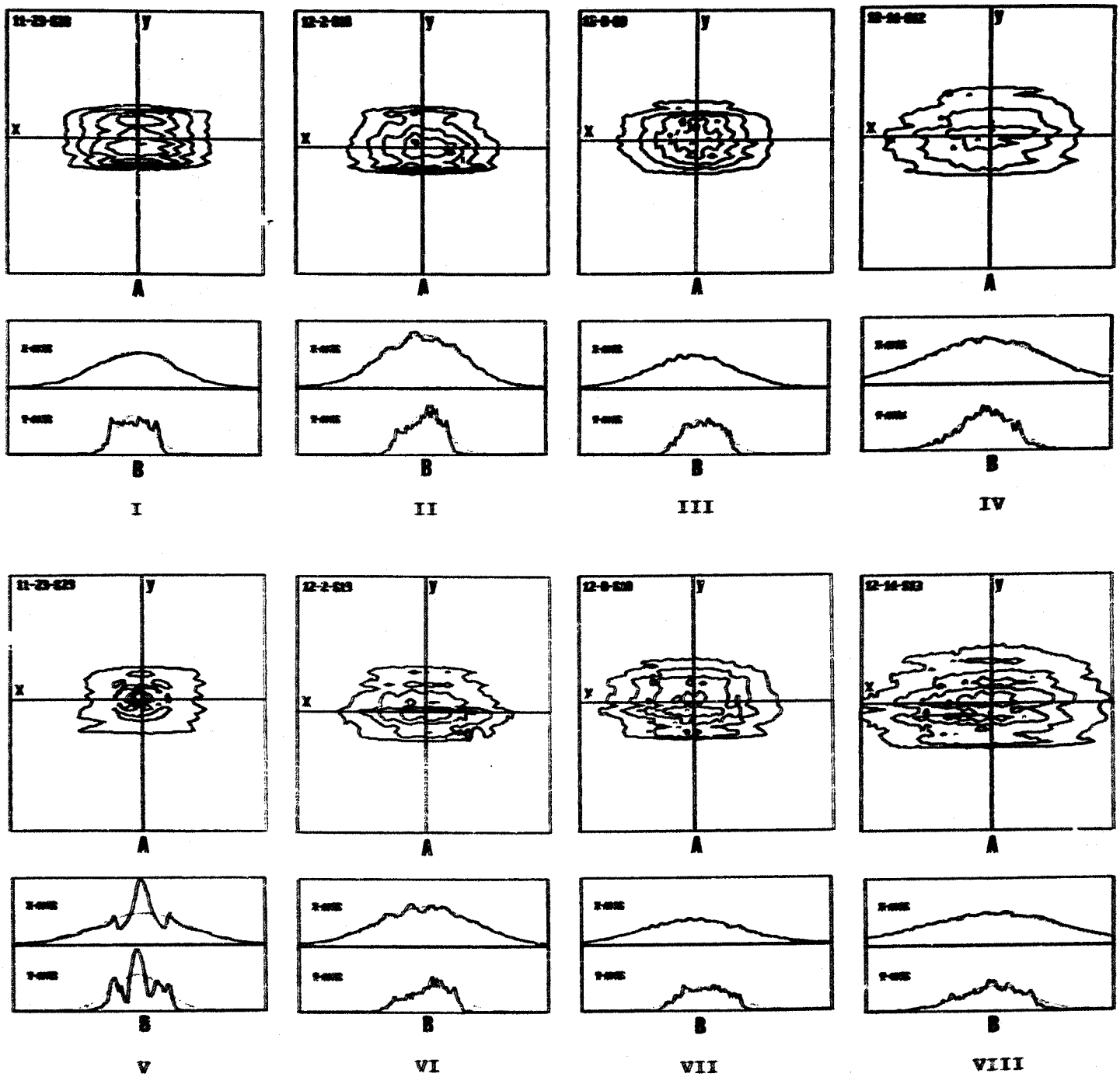

Figure 54. Contours and Profiles of Intensity Distribution of the Output Beam of SDL 8-W LD BN968 Operating at 2 W as Shots Accumulate

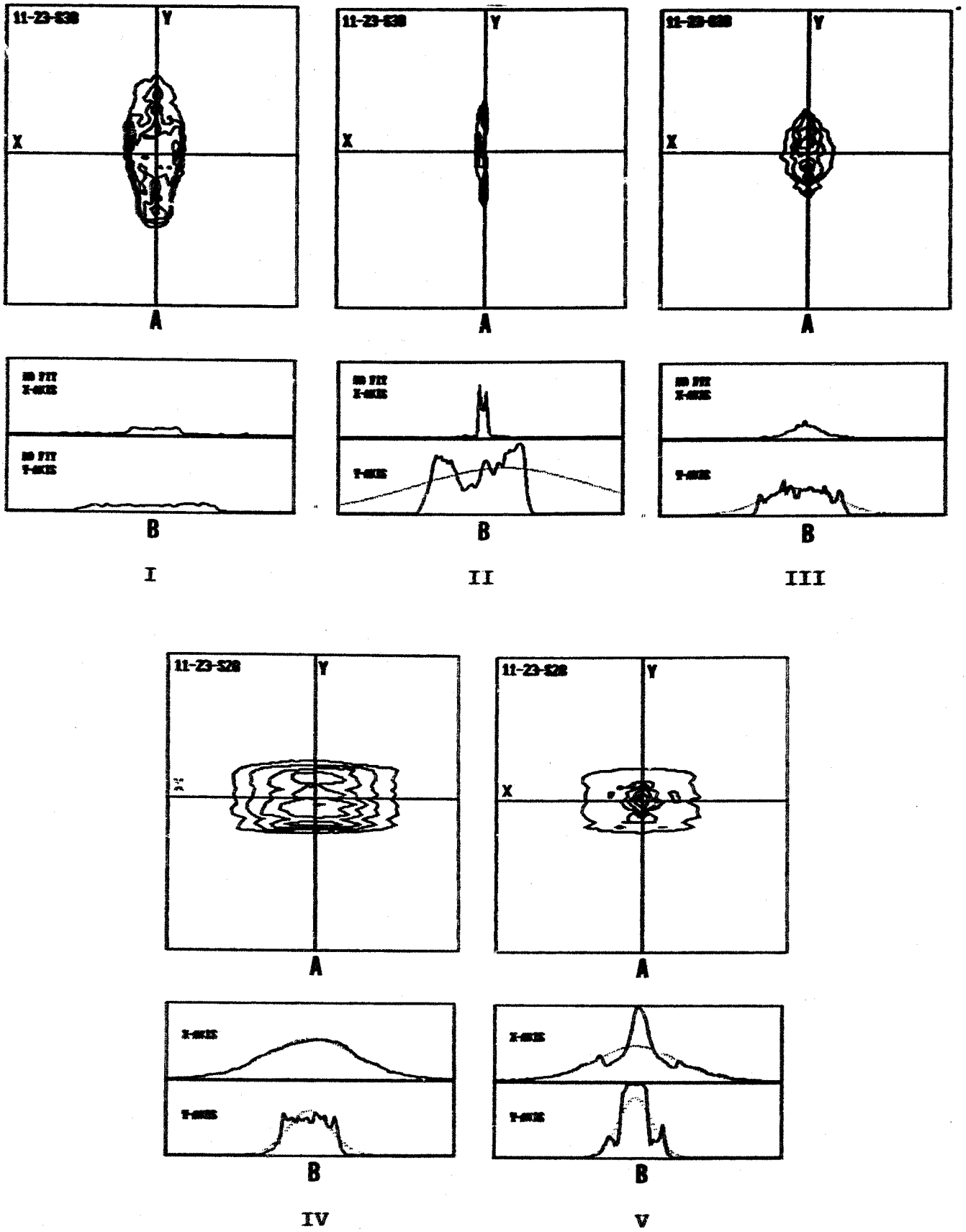

Figure 55. Contours and Profiles of Intensity Distribution of the Output Beam of SDL 8-W LD BN968 Taken at Different Times After LD Turn-On

Table 4. Beam Specifications for SDL 8-W LD [redacted] Data

SHOT	P_{LD}	CAMERA	$1/e^2$ WIDTH		DIVERGENCE		CORRELATION		FIG
		DIST	X	Y	X	Y	COEFFICIENT		
(#)	(W)	(mm)	(mm)	(mm)	(deg)	(deg)	(X)	(Y)	(#)
11-23-S14	0.47	8.87	4.47	1.42	–	–	.999891	.995880	51 I
11-23-S13	0.47	10.87	5.10	1.76	9.0	4.9	.999900	.995480	51 V
11-23-S18	1.0	8.87	4.16	1.87	–	–	.999787	.998949	51 II, 53 I
11-23-S19	1.0	10.87	4.74	2.19	8.3	4.6	.999611	.997799	51 VI, 53 V
11-23-S28	2.0	8.87	4.18	1.99	5.0	9.8	.999794	.995565	51 III, 53 I
									55 IV
11-23-S28	2.0	8.87	3.75	1.57	11.0	15.5	.993759	.990768	55 V,
11-23-S29	2.0	10.87	4.53	2.68	–	–	.995385	.992537	51 VII, 54 V
11-23-S38	2.8	8.87	–	–	–	–	–	–	51 IV. 55 I
11-23-S38	2.8	8.87	–	8.39	–	–	–	.992987	55 II
11-23-S38	2.8	8.87	–	3.29	–	–	–	.996363	55 III
11-23-S39	2.8	10.87	2.64	1.28	–	–	.995841	.999307	51 VIII
12-2-S7	0.49	8.87	4.55	1.41	–	–	.999894	.996811	52 I
12-2-S9	0.49	10.87	5.26	1.89	10.1	6.8	.999975	.997762	52 V
12-2-S11	1.1	8.87	4.31	2.05	–	–	.999907	.999072	52 II, 53 II
12-2-S12	1.1	10.87	4.97	2.37	9.4	4.6	.999738	.998056	52 VI, 53 VI
12-2-S18	2.0	8.87	4.42	2.20	–	–	.999798	.997519	52 III, 54 II
12-2-S19	2.0	10.87	5.18	2.86	10.8	9.4	.999756	.997083	52 VII, 54 VI
12-2-S26	2.8	8.87	4.30	2.60	–	–	.999797	.995862	52 IV
12-2-S27	2.8	10.87	4.93	3.24	9.0	9.1	.999666	.992936	52 VIII
12-8-S3	1.0	8.87	4.29	1.70	–	–	.999881	.998308	53 III
12-8-S4	1.0	10.87	5.17	1.97	12.4	3.9	.999738	.998006	53 VII
12-8-S9	2.0	8.87	4.60	2.25	–	–	.999838	.997955	54 III
12-8-S10	2.0	10.87	5.20	2.79	8.5	7.7	.999660	.997685	54 VIII
12-14-S6	1.0	8.87	6.57	2.77	–	–	.999956	,997656	53 IV
12-14-S7	1.0	10.87	7.32	3.12	10.6	5.0	.999928	.996214	53 VIII
12-14-S12	1.9	8.87	6.37	2.91	–	–	.999805	.997904	54 IV
12-14-S13	1.9	10.87	7.56	3.56	16.6	10.5	.999825	.997643	54 VIII

SDL 4-W LD RP542 Operating Early in Life

Figure 56 shows the contours and profiles of the intensity distribution of SDL 4-W LD RP542 beam. The LD operated at four levels. The optical distance from the LD output mirror to the camera active CID surface is 8.87 mm for Figure 56 I, II, III, and IV and 10.87 mm for Figure 56 V, VI, VII, and VIII, with the LD emitting:

- 0.49 W, the number of LD shots prior to Figure 56 I is 5 at 0.49 W, and 6 for Figure 56 V
- 1.1 W, the number of LD shots prior to Figure 56 II is 5 shots at 1 W plus the previous shots, and 6 for Figure 56 VI
- 1.5 W, the number of LD shots prior to Figure 56 III is 4 shots at 1.5 W plus the previous shots, and 5 for Figure 56 VII
- 1.8 W, the number of LD shots prior to Figure 56 IV is 5 shots plus the previous shots, and prior to Figure 56 VIII is 6 shots plus the previous shots.

After Shot 12-14-S53, the total number of LD shots at all levels is 23. Two weak lobes are observed at the 0.49-W level. The contours in (A) and the profiles in (B) are similar for all the remaining LD levels shown in Figure 56 II, III, IV, VI, VII, and VIII. The Gaussian fit is better for the X-axis of the profiles, which are perpendicular to the short direction of the LD aperture, than it is for the Y-axis.

SDL 4-W LD RP542 Operating Later in Life

Figure 57 shows the contours and profiles of the intensity distribution of SDL 4-W LD RP542 beam. The LD operated at four levels. The optical distance from the LD output mirror to the camera's active CID surface is 8.87 mm for Figure 57 I, II, II, and IV and 10.87 mm for V, VI, VII, and VIII.

For LDs emitting:

- 0.43 W, the number of shots prior to Figure 57 I is 220 at 0.5 W, 220 at 1 W, 6 at 1.5 W, and 85 at 2 W.
- 0.43 W, the number of shots prior to Figure 57 V is the same as Figure 57 I plus 1 at 5 W.
- 1.0 W, the number of shots prior to Figure 57 II is 221 at 0.05 W, 224 at 1W, 6 at 1.5 W, and 85 at 2 W.
- 1.0 W, the number of shots prior to Figure 57 VI is the same as Figure 57 II, plus 1 at 1 W.
- 1.4 W, the number of shots prior to Figure 57 III is 221 at 0.5 W, 225 at 1 W, 9 at 1.5 W, and 85 at 2 W.
- 1.4 W, the number of shots prior to Figure 57 VII is the same as Figure 57 III, plus 1 at 1.5 W.
- 1.8 W, the number of shots prior to Figure 57 IV is 221 at 0.5 W, 225 at 1 W, 10 at 1 W, and 88 at 2 W.
- 1.8 W, the number of shots prior to Figure 57 VIII is the same as Figure 57 IV, plus 1 at 2 W.

After Shot 1-13-531, the total number of LD shots at all levels is 545. The intensity distributions of the LD after all these shots look similar to those early in its life (Figure 56). The profile of the emission pattern is broadened slightly at the base, especially at the 1- and 1.5-W levels of operation. At the larger LD output levels (1.0, 1.4, and 1.8 W) the profiles vary. The two lobes are observed at the 0.43 level, but are absent at the elevated LD output power. As in the earlier operation (Figure 56), the Gaussian fit is better for the X-axis of the profile than it is for the Y-axis of the profile, which is the Y-axis or short dimension of the LD.

Specifications for SDL 4-W LD RP542 Data

Table 5 lists the specifications for SDL 4-W LD RP542. These include the shot number (#), P_{LD} LD output optical power (W), distance from the LD output mirror from where the photographs are taken (mm), $1/e^2$ width (mm), divergence (degrees), CC, and the figure in which the contour or profile appears.

The data in Table 5 are for the profile data in Figures 56 and 57. The records are taken at 8.867 and 10.867 mm from the output mirror of the LD. The LD divergences, a_x and a_y, are calculated as described in Eq (28) for the LD divergence in Table 4.

If a trend appears, it is a slight increase in divergence with an increase in LD output optical power for the three upper LD levels, both early and later in the life of LD RP542.

The Y-axis divergence is erratic because the Gaussian is not a good fit to the intensity distribution or profile in that direction, as is evident from the CC numbers.

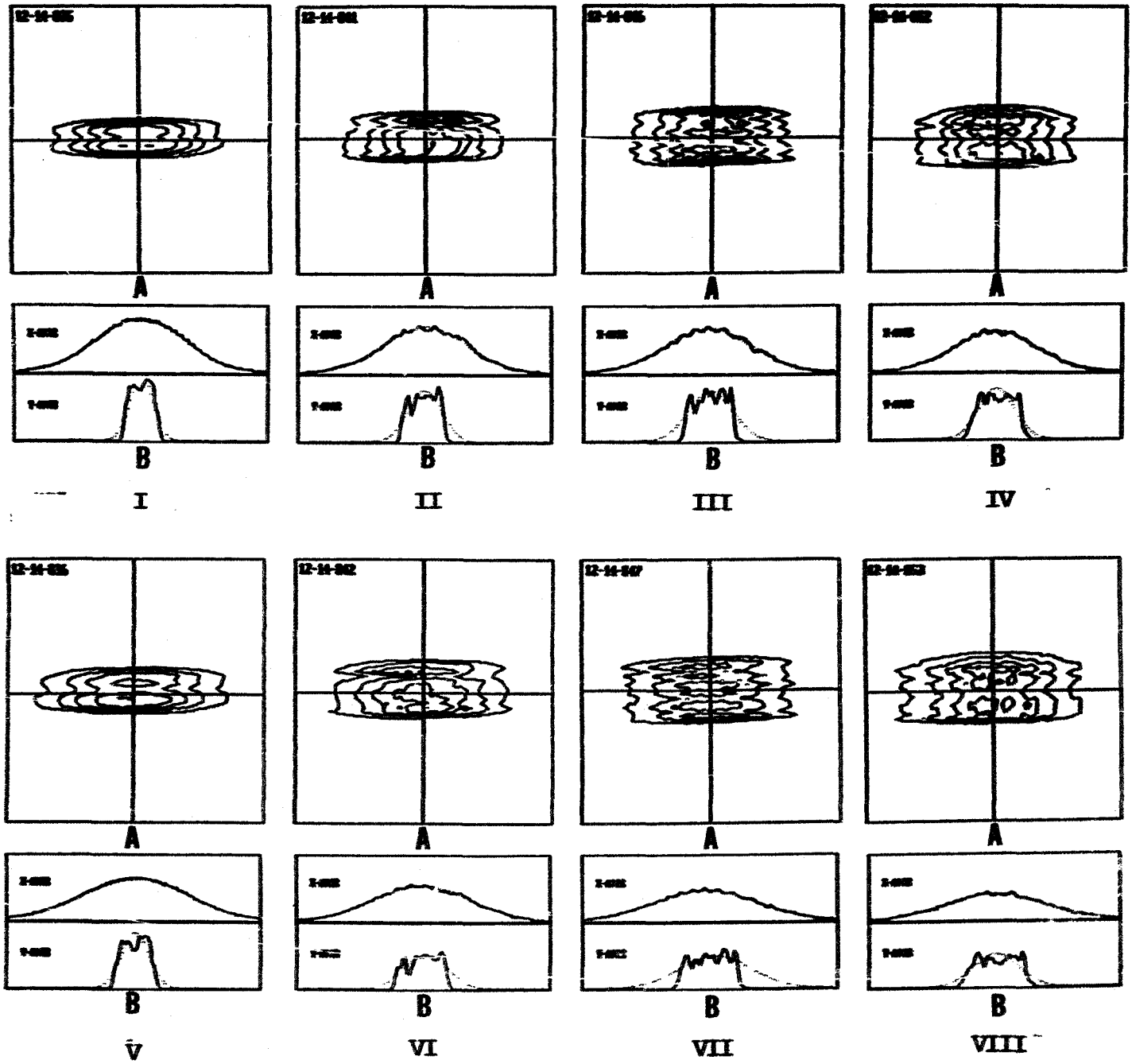

Figure 56. Contours and Profiles of Intensity Distribution of the Output Beam Early in the Life of SDL 4-W LD RP542. These operate at 0.49 W (I & V), 1.1 W (II & VI), 1.5 W (III & VII), and 1.8 W (IV & VIII).

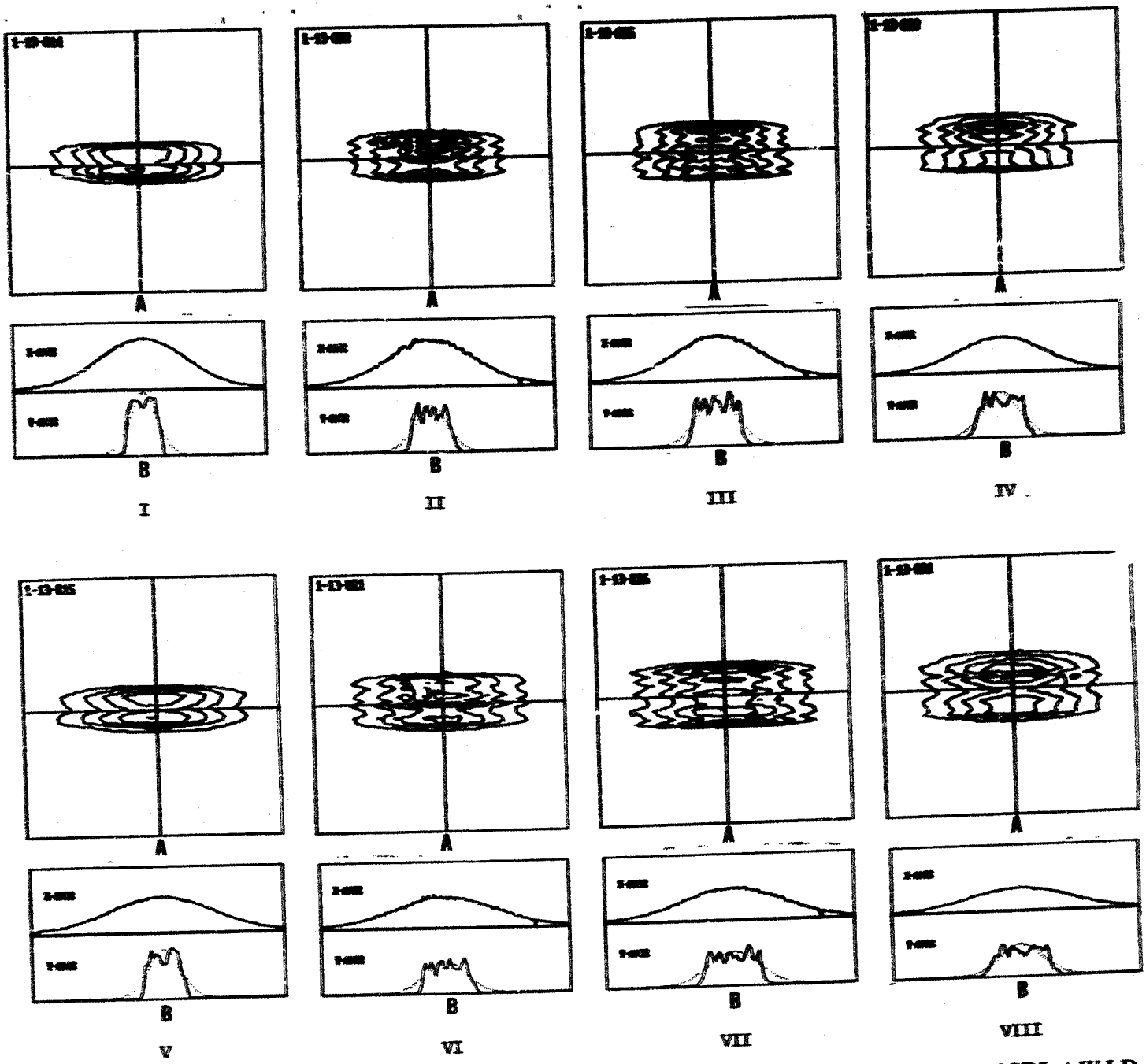

Figure 57. Contours and Profiles of Intensity Distribution of the Output Beam Later in the Life of SDL 4-W LD RP542. These operate at 0.43 W (I & V), 1.0 W (II & VI), 1.4 W (III & VII), and 1.8 W (IV & VIII).

Table 5. Beam Specifications for SDL 4-W LD RP542 Data

SHOT	P_{LD}	CAMERA	I/e^2 WIDTH		DIVERGENCE		CORRELATION		FIG
		DIST	X	Y	X	Y	COEFFICIENT		
(#)	(W)	(mm)	(mm)	(mm)	(deg)	(deg)	(X)	(Y)	(#)
12-14-S35	0.49	8.87	4.64	1.17			.999968	.997499	56 I
12-14-S36	0.49	10.87	5.50	1.44	12.4	3.9	.999941	.997259	56 V
12-14-S41	1.0	8.87	4.52	1.77			.999816	.996780	56 II
12-14-S42	1.0	10.87	5.03	2.31	7.4	7.7	.999874	.996212	56 VI
12-14-S46	1.5	8.87	4.64	2.36			.999818	.997282	56 III
12-14-S47	1.5	10.87	5.33	3.81	9.8	19.9	.999821	.998120	56 VII
12-14-S52	1.8	8.87	4.37	1.88			.999844	.996626	56 IV
12-14-S53	1.8	8.87	5.21	2.43	11.9	7.8	.999758	.994978	56 VIII
1-13-S14	0.43	8.87	4.62	1.42			.999979	.998131	57 I
1-14-S15	0.43	10.87	5.36	1.70	12.1	4.0	.999975	.997751	57 V
1-13-S20	1.0	8.87	4.56	1.73			.999889	.996967	57 II
1-13-S21	1.0	10.87	5.23	2.15	9.5	6.0	.999823	.995812	57 VI
1-13-S25	1.4	8.87	4.56	2.00			.999920	.995225	57 III
1-13-S26	1.4	10.87	5.25	2.64	9.8	9.1	.999901	.995051	57 VII
1-13-S30	1.8	8.87	4.45	1.95			.999951	.996261	57 IV
1-13-S31	1.8	10.87	5.17	2.26	10.2	4.4	.999927	.994527	57 VIII

LD RP542 Different Time After LD Turn-On

Figure 58 shows the contours and profiles of the intensity distribution of SDL 4-W LD RP542 beam at different times after the LD is turned on. The LD is emitting 1 W of optical power.

Unlike SDL 8-W LD BN968 (Figure 55), the beam contours and profiles are very stable after laser turn-on at the following recordings of:

- 0.22 s after turn-on in Figure 58 I
- 1.22 s after turn-on in Figure 58 II
- 2.22 s after turn-on in Figure 58 III
- 3.22 s after turn-on in Figure 58 IV.

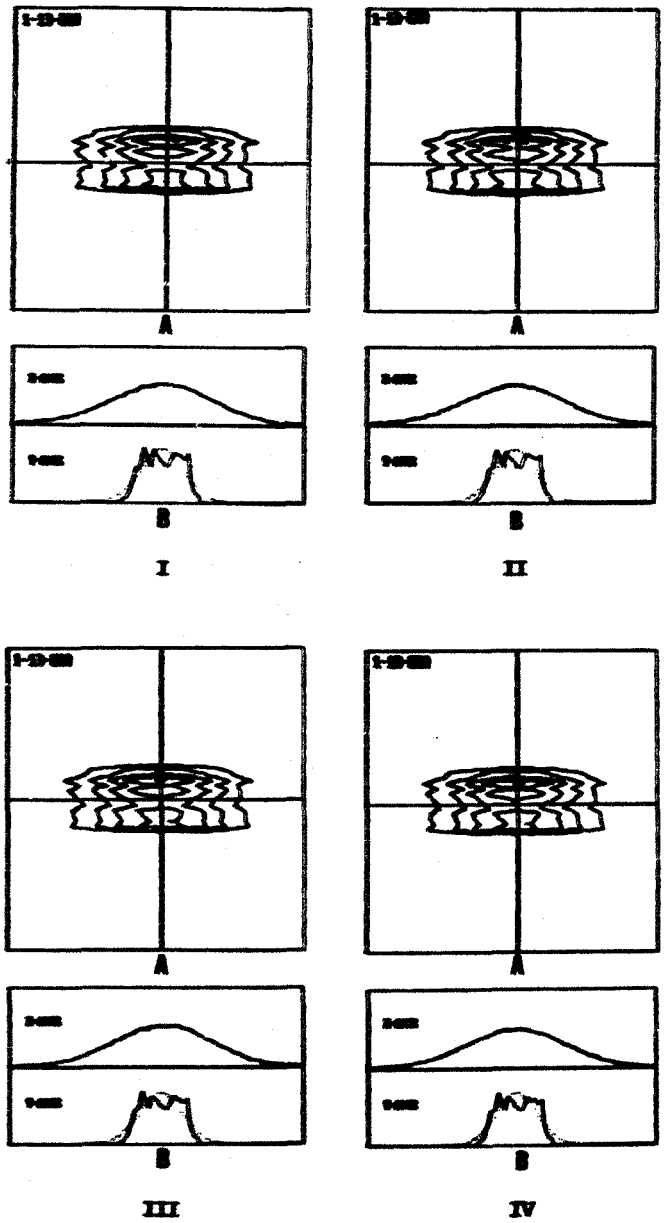

Figure 58. Contours and Profiles of Intensity Distribution of the Output Beam of SDL 4-W LD RP542 Taken at Different Times After LD Turn-On

4.1.5 Summary

SDL LDs vs. MDAC/OEC LDs

In Section 4.1 we have described the performances of high-power GaAlAs LDs manufactured by SDL and MDAC/OEC:

- The ***SDL LDs*** are constructed with multiple stripes containing single- and multiple-quantum wells. They are mounted in TO-3 cans or C-packages. All of these LDs have coated mirrors.
- The ***MDAC/OEC LDs*** have a single broad stripe with a single quantum well. They are mounted in TO-18 cans or LCB-packages. Six of these LDs have coated mirrors.
- ***SDL*** and ***MDAC/OEC LDs*** are fabricated using MOCVD technology.

SDL LDs

The six different SDL LDs—SDL-2410-H1 (A300 or B100 series), SDL-2430-H1 (C347), SDL-2450-H1 (A840 or A841), SDL-2460-H1 (C338), S7081 (BM498, RB833, or RP542), and S7086 (BN968)—have, respectively,

- Maximum thresholds of 0.24, 0.20, 0.82, 0.43, 0.60, and 1.3 A
- Maximum output optical power of 0.4, 0.5, 2.0, 1.0, 2.0 (except BM498 at 3.4 W), and 2.8 W
- Maximum efficiencies of 24% or 34%, 40%, 26%, 38%, 37% to 39%, and 33.6%
- Output cavity aperture dimensions of 100, 100, 400, 200, 100, and 200 μm by 1 μm.

Fin Heatsink Cooling

For fin heatsink:

- SDL-2430-H1 exhibited little or no decrease in output optical power as the interval of the LD shot changed from 30 s to 10 min.
- SDL-2450-H1 exhibited about 4% to 5.6% decrease in output optical power when its shot interval decreased from 5 or 10 min to 2 or 1 min.
- SDL-2450-H1 produced 5.8% more output optical power or 10% more efficiency when it was TE-cooled to 19.9°C compared to fin-heatsink-cooled to room temperture, 38°C (fin side).

Aging

- For SDL-2450-H1 0.5-W LD A841, aging, which results from operating the LDs at an elevated junction current, causes only a slight reduction in output optical power.

- For the SDL-S7081 4-W LD RB883, aging causes a 22% reduction in efficiency when emitting 1 W of power.
- For the SDL-S7086 8-W LD BN968, aging causes a 6% reduction in efficiency when emitting 2.8 W of power.
- For the SDL-7081 4-W LD RP542, aging causes only a slight reduction in efficiency when the LD emits 2 W of power.

Beam Intensity Distribution

- **LD A322 and A840.** The two well-defined, sharp-peaked lobes[30,31] in the Y direction (Y is along the long dimension of the LD aperture and X is perpendicular) of LD A322 beam, when the LD is emitting 0.1 W of power, develop into a three-lobed[32] beam with small roots as the LD power increases to 0.4 W. The two broad lobes of the LD A840 beam become broader as the LD emitted power is increased from 0.5 to 1.95 W. The beam profiles of both LDs in the X direction are smooth and approximate a Gaussian fit quite well.
- **LD BN968.** The two lobe-type LD beam patterns observed for LDs A322 and A840 are seen in LD BN968 only when it emits low power (0.47 W). The initial erratic beam profiles become more stable and Gaussian in shape in both the X and Y directions as the LD accumulates more shots. The LD divergence increases in both directions with the increase in LD emitting power and as the LD accumulates shots or ages. Early in LD life, its beam profile changes drastically as a function of time after the LD is turned on. The normal LD emitting pattern changes by 90°. The normal small divergence is that the Y direction becomes larger and the large divergence in the X direction becomes smaller. As it ages, the pattern stabilizes to large divergences in the X direction and small divergence in the Y direction.
- **LD RP542.** The two lobe-type LD beam patterns observed for LDs A322, A840, and BN968 are all but absent in the LD RP542, except at low power. The beam profiles are more stable than those of LD BN968. The LD beam divergence (half angle) is 14.5°, 19.6°, and 23.7° when LD RP542 emits 1.05, 1.49, and 1.85 W, respectively.

MDAC/OEC LDs

The thirteen different MDAC/OEC LDs—E204A-3, E204A-6, E220A-1, E220A-2, E204Q-1, E170T-1, E170T-3, E170T-4, and E170T-5, E170R-1, E170R-4, E170T-2-9, and E170T-2-10—have, respectively

- Thresholds of 80, 40, 80, 80, 80, 80, 140, 80, 80, 70, 80, 240, and 240 mA
- Catastrophic output optical power of 0.7, 1.67, 1.04, 0.6, 1.75, 1.07, 1.22, 1.69, 1.59, 2.1, 2.04, 5.03, and 2.05 W
- Efficiencies of 50%, 48%, 48%, 48.5%, 26%, 30%, 30%, 30%, 31.5%, 38%, 30%, 50%, and 49%
- Output cavity aperture dimensions (width by length) of 60×450 μm, 60×450 μm, 60×450 μm, 60×450 μm, 150×900 μm, 150×700 μm, 150×700 μm, 150×450 μm, 150×450 μm, 150×750 μm, 150×750 μm, 150×1200 μm, and 150×1200 μm.

All LDs have an aperture height of 1 μm.

Operation Levels of SDL and MDAC/OEC LDs

The catastrophic levels for different LDs are:

- 2 W for SDL-2450-H1-A841
- 3.4 W for SDL-S7081-BM498
- ~1 to 5 W for MDAC/OEC LDs.

The remaining SDL models—SDL-2410-H1, SDL-2430-H1, SDL-2460-H1—are operated up to their rated power or four times their rated power levels. The SDL-LD slope efficiencies vary from 0.80 to 1.14 W/A and the MDAC/OEC slope efficiencies vary from 0.60 to 1.10 W/A.

4.2 Couplers

The transmission data for five GRIN lenses are present. The decrease of the incident power on a solar cell with increase in distance between cell and GRIN lenses is measured.

The transmission data are presented for:

- A 1000- and 600-μm FO butt-coupled to 100- and 500-mW LDs
- A 1000- and 600-μm FO butt-coupled to two GRIN lenses butt-coupled to 100- and 500-mW LDs

- A 600-, 400-, 200-, and 100-μm FO butt-coupled to a 4-W LD
- A 200-μm FO butt-coupled to two 4-W LDs and an 8-W LD
- A P-C lens coupled to four FOs
- A 100-μm FO butt-coupled to four 1-W MDAC/OEC LDs.

The beam intensity distributions are presented for:

- A 1-m-long, 600-μm FO with a 100-mW LD as source
- Two 1-m-long and two 0.5-m-long 600-μm FOs with a 500-mW LD as source
- A 600-μm FO that begins 0.5 m long and is incrementedly reduced 0.0312 m long with a 500-mW LD as source
- A 1-m long, 200-μm FO with a 4-W LD as source
- A 200-μm FO that begins 0.5 m long and is incrementedly reduced 0.0422 m long with a 4-W LD as source.

The couplers are normally aligned by visually placing the center of the GRIN lens or FO in the center of the the emitting area of the LD. This is done with the help of a 20× eyepiece. The coupler is then fine-tune-aligned by turning the LD on continuous wave (CW) to emit ~100 mW, and then scanning the input end of the coupler in the X and Y directions for maximum optical power through the coupler output end.

4.2.1 GRIN Lenses

The transmission of five GRIN lenses with LDs A322 and A841 as sources are described. The decrease of incident power on the solar cell with the increase in distance between a 0.23-pitch GRIN lens and cell is measured.

SDL 100-mW LDA322 as Source

Figure 59 shows the transmission of GRIN lenses when the source is SDL 100 mW LD A322. The percent transmission is defined as the optical power out of the GRIN divided by the optical power into the GRIN × 100 . Data for the LD emitting 17, 100, and 400 mW show that the transmissions increase as LD optical power increases for all GRIN lenses except in the case of the 0.23-pitch for the optical power of 400 mW.

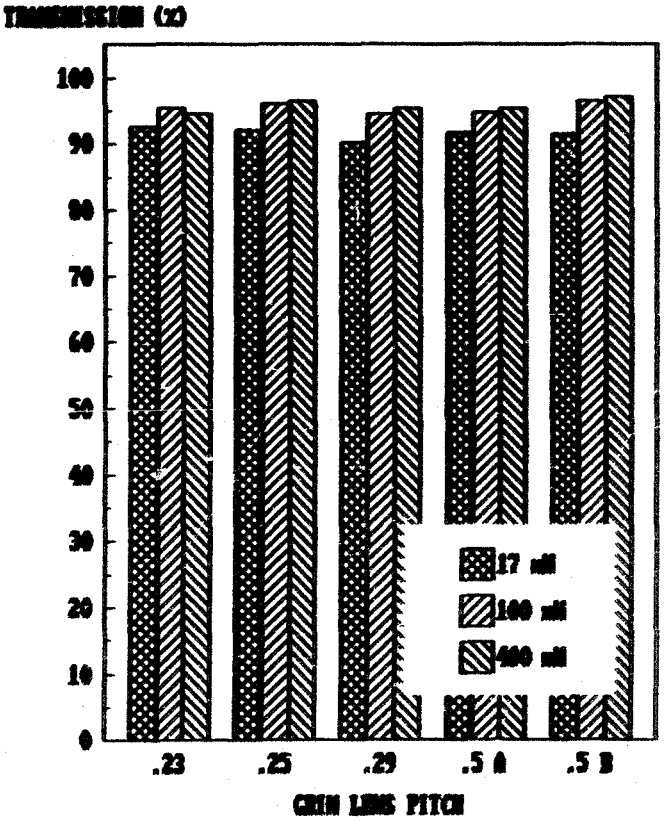

Figure 59. Transmission of Five GRIN Lenses With 0.23-, 0.25-, 0.29-, 0.5A-, and 0.5B-Pitch Using SDL 100-mW LD A322 as Source, Operating at 17-, 100-, and 400-mW Power Levels

SDL 500-mW LD A841 as Source

Figure 60 shows that the transmission of the GRIN lenses behaves similarly when the source is SDL 500 mW LD A841 instead of SDL 100 mW LD A322. The transmissions of the GRIN lenses increase as the LD optical power increases. In this case, the LD emits 60, 500, and 2000 mW. The transmissions of all the GRINs are quite high, >95% at the maximum optical power of the LDs. One drawback is that the GRIN lens, like a conventional lens, does not image the LD beam as a circular beam because of the different divergence in the X and Y directions. This causes the cell to be illuminated nonuniformly. (See Section 4.2.3.)

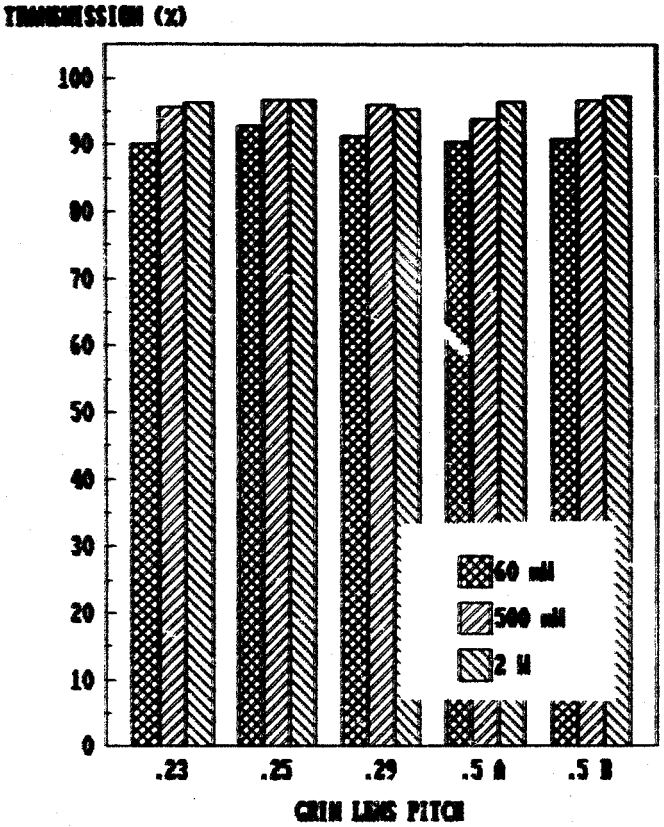

Figure 60. Transmission of Five GRIN Lenses With 0.23-, 0.25-, 0.29-, 0.5A-, and 0.5B-Pitch Using SDL 500-mW LD A841 as Source, Operating at 60-, 500-, and 2000-mW Power Levels

GRIN to Solar Cell Coupling

In order to reduce the data of the HOFS Systems 1′, 1, 2, and 3, it was necessary to determine the decrease of the optical power collected by the solar cell as a function of the distance between the cell it and the 0.23-pitch GRIN lens that is butt-coupled to the LD. The 1-V cell was simulated by a 0.368-cm aperture in front of the energy meter.

Figure 61 shows the LD optical power detected through a 0.368-mm aperture as a function of distance, d_{GA} between the GRIN lens output surface and the aperture located in front of the energy meter.

The power measured through the aperture, P_A, vs. distance, d_{GA}, obeys the relation:

$$P_A = C\, d_{GA}^{e}, \qquad (29)$$

where C is 107.4 for the d_{GA}^{e} and e is $-0.0878 > 2$ mm.

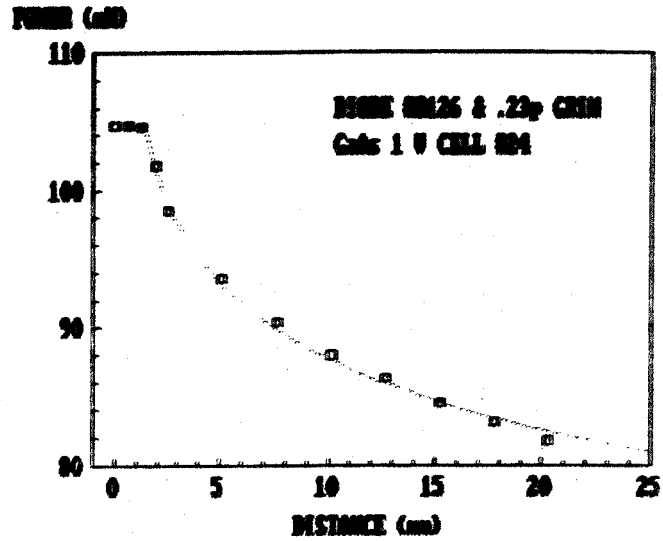

Figure 61. Optical Power Detected vs. Distance From Source Using SDL 100-mW LD B126 and 0.23-Pitch GRIN Lens as Source With 0.368-mm-dia Apertured Energy Meter

The falloff illustrates that the beam out of the GRIN lens is indeed not parallel. About 76.4% of the LD optical power enters the aperture at a distance of 20 mm, but the 23.6% that does not is accounted for in calculating the efficiency of the cell and the dc-dc converter combination in HOFS Systems 1′, 1, 2, and 3.

4.2.2 Fiber Optics

We present the transmission of:

- FO_4 #1 (1000 μm dia) and FO_3 #1 (600 μm dia) butt-coupled to LDs A322 and A841 as sources
- FO_4 #1 and FO_3 #2 (600 μm dia) butt-coupled to 0.5A-pitch and 0.5B-pitch GRIN lenses butt-coupled to LDs A322 and A841 as sources
- FO_2 #1 (200 μm dia) butt-coupled to LDs BM498, RB883, and BN968 as sources
- FO_5 #4 (400 μm dia), FO_3 #2, FO_2 #1, and FO_1 #1 (100 μm dia) butt-coupled to LD RP542.

We also describe the transmission of FO_2 #1 when aligned to the LD at each LD power level. The procedure to align FO_2 #1, is also described. For the beam profile measurements, the FOs Y direction is along the long dimension of the LD aperture, and its X direction is perpendicular to the long dimension of the LD aperture.

The dotted line, with the SQS data points in Figures 62 through 65, is the transmission of the FO labeled in each figure when it is butted against the LD window of the TO-3 can. The TRI and AST data are the transmission of the FO when 0.5A-pitch and 0.5B-pitch GRIN lenses, respectively, are in turn butted against the LD window and used as the light source to measure the transmission of the FO.

There are only three transmission data points (low, rated, and maximum LD power) for the FO when the GRIN lenses are used as the source. For the total efficiency of the GRIN-FO system, the GRIN efficiency must also be taken into account.

Transmission of FO_4 #1 and FO_3 #1 With 100-mW LD A322 as Source

Figure 62 illustrates the transmission vs. FO input optical power for FO_4 #1 butt-coupled to SDL 100-mW LD A322 and FO_4 #1 butt-coupled to 0.5A- and 0.5B-pitch GRIN lenses; each lens, in turn, is butt-coupled to the same LD. Figure 63 illustrates the transmission vs. FO input optical power for FO_3 #1 butt-coupled to SDL 100-mW LD A322 and FO_3 #1 butt-coupled to a 0.5A- and 0.5B-pitch GRIN lens; each lens, in turn, is butt-coupled to the same LD.

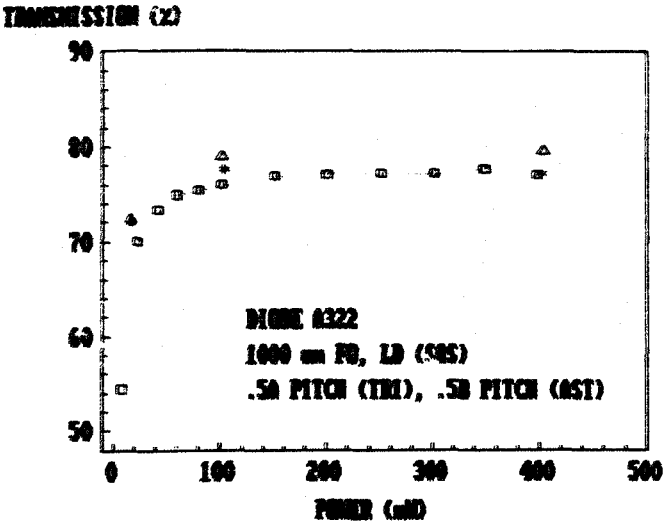

Figure 62. Transmission of 1000-μm FO_4 #1 vs. Optical Power Using SDL 100-mW LD A322, LD A322 and 0.5A-Pitch GRIN Lens, and LD A322 and 0.5B-Pitch GRIN Lens as Sources

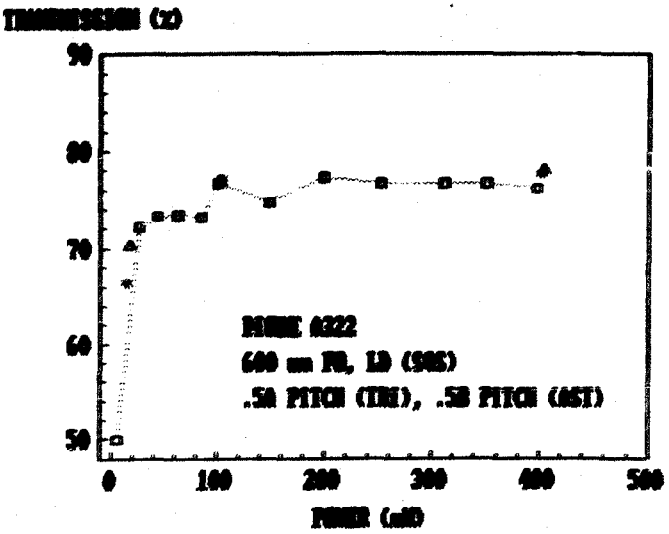

Figure 63. Transmission of 600-μm FO_3 #1 vs. Optical Power Using SDL 100-mW LD A322, LD A322 and 0.5A-Pitch GRIN Lens, and LD A322 and 0.5B-Pitch GRIN Lens as Sources

The transmission for the 1000- and 600-μm FOs, which are butted against the window of SDL 100-mW LD A322, is not maximum until the LD emits 150 and 100 mW, respectively (Figures 62 and 63). The diameter of both FOs is larger than the 100-μm-long emitting aperture of LD A322, but diameter is not the entire story; the NA of the FOs must also be considered.

When the 0.5A- and 0.5B-pitch GRIN lenses are butt-coupled to LD A322 and become the source for the FO, its transmission is always equal to or greater than the transmission measured when SDL 100-mW LD A322 is used directly as the illuminating source (see the dotted line in Figures 62 and 63).

For the 0.5A-pitch GRIN lens as source and the LD A322 emitting 100 mW of optical power, the transmission for FO_4 #1 and GRIN lens combined is 75.3% when transmission of the GRIN, which is about 95%, is considered. This is comparable to the transmission of 76% measured when the FO is butt-coupled to the window of the LD (Figure 62). The introduction of the GRIN lens caused about a 0.6% loss of energy out of the entire coupling train. The advantage of using the GRIN lens is that it provides an extra component in the optical train that facilitates beam manipulation in addressing the strong-link safety issue.

The results indicate that the LD divergence stabilizes relative to LD optical power at 150 and 100 mW. Since the NA of the FO is 0.37 (manufacturer specifications) to its 5% intensity level of a Gaussian beam profile fit, this corresponds to $\theta_a = 21.7°$ or a full angle of 43.4°. The specifications of the SDL LDs call out a divergence of 10°×35° to its FWHM level. Our data show that the NA of the FO limits transmission as the output optical power is increasing until the divergence of A322 stabilizes (as indicated by the plateau) at the higher-output optical power.

Transmission of FO_4 #1 With 500-mW LD A841 as Source

Figure 64 illustrates the transmission vs. FO input optical power for FO_4 #1 butt-coupled to SDL 500-mW LD A841 and FO_4 #1 butt-coupled to 0.5A- and 0.5B-pitch GRIN lenses; each lens is, in turn, butt-coupled to the same LD. Figure 65 illustrates the transmission vs. FO input optical power for FO_3 #1 butt-coupled to SDL 500-mW LD A841 and FO_3 #1 butt-coupled to 0.5A- and 0.5B-pitch GRIN lenses; each lens is, in turn, butt-coupled to the same LD.

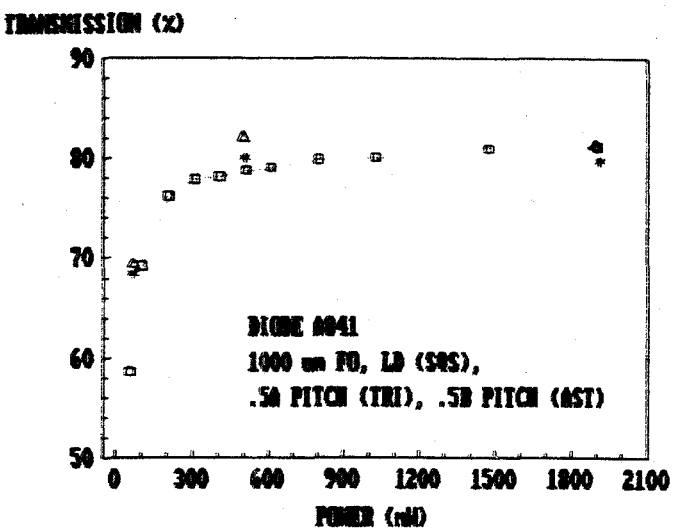

Figure 64. Transmission of 1000-μm FO_4 #1 vs. Optical Power Using SDL 500-mW LD A841, LD A841 and 0.5A-Pitch GRIN Lens, and LD A841 and 0.5B-Pitch GRIN Lens as Sources

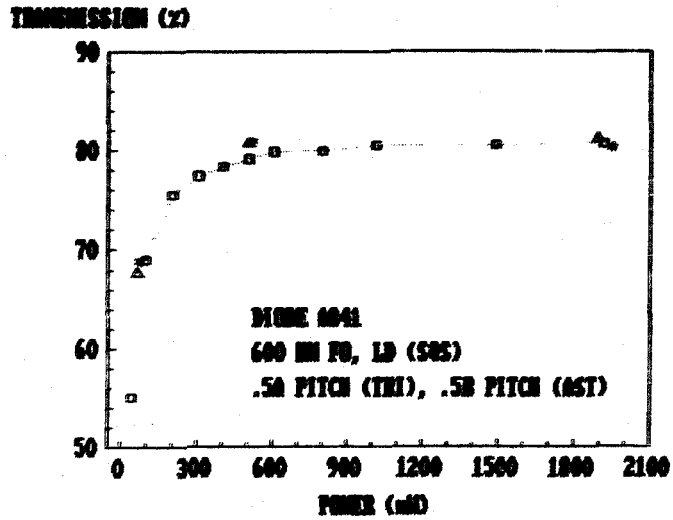

Figure 65. Transmission of 600-μm FO_3 #1 vs. Optical Power Using SDL 500-mW LD A841, LD A841 and 0.5A-Pitch GRIN Lens, and LD A841 and 0.5B-Pitch GRIN Lens as Sources

When the 0.5A- and 0.5B-pitch GRIN lenses are butt-coupled to LD A841 and become the source for the FO, its transmission is always equal to or greater than the transmission measured when LD A841 is used directly as the illuminating source (see dotted lines in Figures 64 and 65) for the 100- and 500-mW levels of operation, but this is not true at the maximum level of 1900 mW. At this level, the 0.5B-pitch GRIN lens as source produces a smaller transmission and the 0.5A-pitch GRIN lens as source produces about the same transmission for both FOs. In all cases, the 0.5A-pitch GRIN lens with the smaller NA of 0.46 produced the larger transmission for the FOs.

When SDL 500-mW LD A841 is the illuminating source, transmission for the FOs never reaches a plateau; rather, transmission continues to increase (dotted line in Figures 64 and 65). A significant change in transmission occurs at 300 mW for the 1000- and 600-μm FO. The diameter of both FOs is larger than the 400-μm-long emitting aperture of LD A841 but, again, diameter is not the entire story. The NA of the FOs must also be considered. The data in Figures 64 and 65 indicate that the divergence of SDL 500-mW LD A841 continues to decrease with increasing output power (no plateau is formed). In the future, we intend to verify this statement with divergence measurements of LDs A322 and A841.

Transmission of FO_3 #1 With 100-mW LDs Using LDs A322 and B126 as Sources

Figure 66 shows the transmission vs. FO input optical power for different LDs (A322 and B126) with the same SDL part number but with different serial numbers. The LDs are butt-coupled to the same 600-μm FO_3 #1. Figure 30 shows that LD B126 is more efficient than LD A322. The data in Figure 66 suggest that the divergence of B126 is greater than that of A322 since the transmission of the FO is smaller when B126 is the source. When the LDs emit ~100 mW, ~12% more energy is transmitted through the FO when A322 instead of B126 is the source.

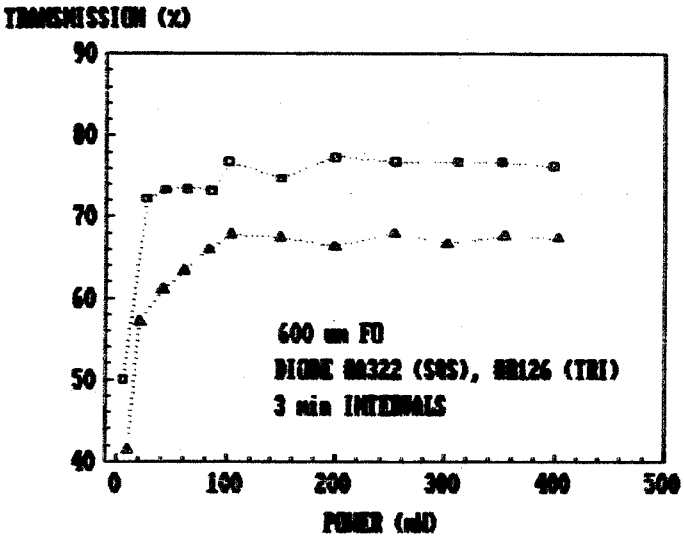

Figure 66. Transmission of 600-μm FO_3 #1 vs. Optical Power Using Two SDL 100-mW LDs (A322 and B126) as Sources

Transmission of FO_3 #1 With 500-mW LDs Using LDs A841 and A840 as Sources

Figure 67 illustrates the transmission vs. FO input optical power for FO_3 #1 when two 500-mW LDs (A841 and A840) are used as sources. The A840 LD data with the TRI data points are for the FO after the FO ends have been repolished. The AST data points are for the FO after it has been repolished a second time. After the second polishing of the FO, its transmission with A840 LD as the source was comparable to the transmission measured when A841 LD was the source (the SQS data). The different transmission of the FO for the same LD, namely A840 with the TRI and AST data, is related to the optical finish of the FO ends. The same transmission measured for the different LDs, namely the SQS and AST data points, indicates that the divergences of these two LDs are comparable.

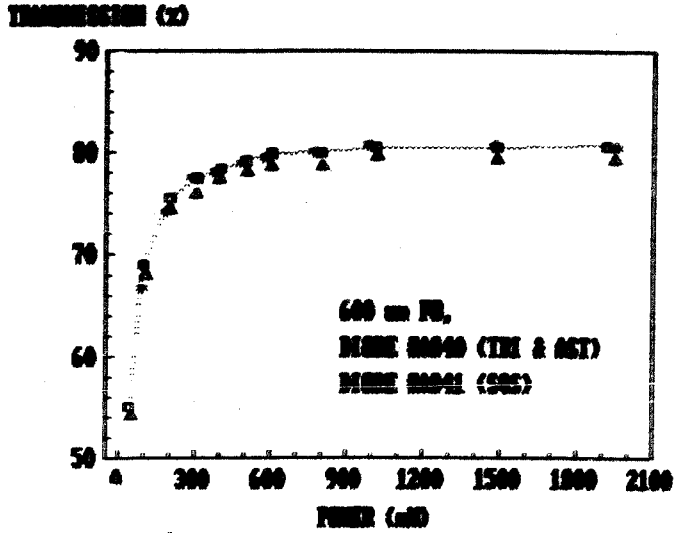

Figure 67. Transmission of 600-μm FO_3 #1 vs. Optical Power Using Two SDL 500-mW LDs (A840 and A841) as Sources, With FO Ends Repolished Twice

Transmission of FO_3 #1 and FO_4 #1 With LD A322 and A841 as Sources

Figure 68 illustrates the transmission vs. FO input optical power for FO_4 #1 and FO_3 #1 when SDL 100-mW LD A322 is the source. Figure 69 illustrates the transmission vs. input LD optical power for FO_4 #1 and FO_3 #1 when SDL 500-mW LD A841 is the source. Both FOs are labeled by the manufacturer as having the same NA. For both LDs, the larger-diameter FO appears to have a slightly larger transmission at large LD optical power. This is probably not real, since our measurements are good only to ~1.5%.

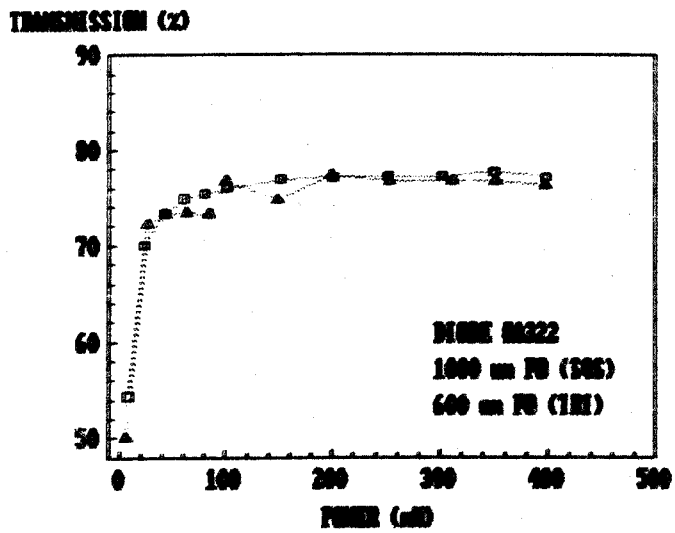

Figure 68. Transmission of 600-μm FO_3 #1 and 1000-μm FO_4 #1 vs. Optical Power Using SDL 100-mW LD A322 as Source

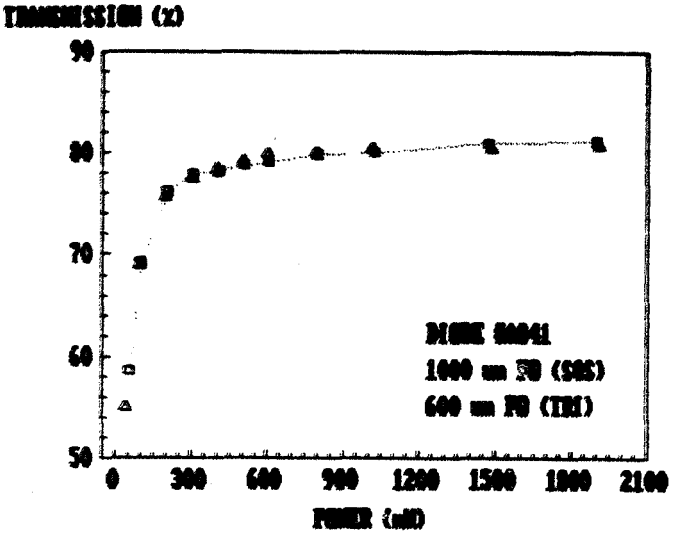

Figure 69. Transmission of 600-μm FO_2 #1 and 1000-μm FO_4 #1 vs. Optical Power Using SDL 500-mW LD A841 as Source

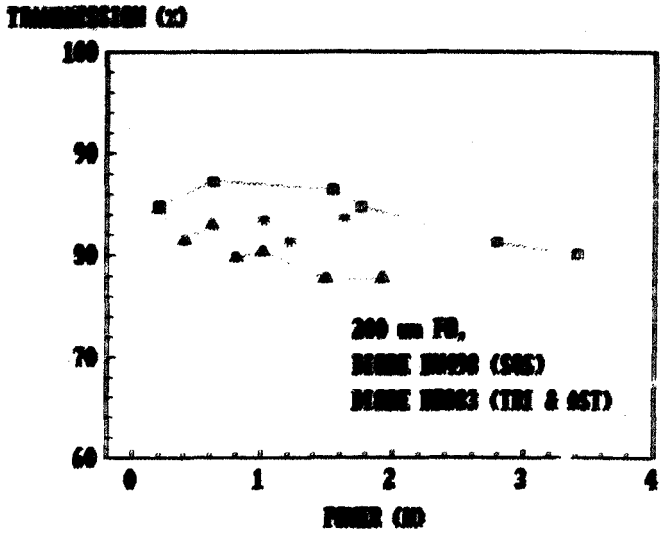

Figure 70. Transmission of 200-μm FO_2 #1 vs. Optical Power Using Two Prototype SDL 4-W LDs (BM498 and RB883) as Sources

Once the diameter of the FO is larger than the aperture of the LD (or, rather, larger than the diameter of the LD beam at the position in space where the FO intercepts the beam), it is the NA of the FO and the reflection losses at its ends that govern the transmission of the FO.

Transmission of FO_2 #1 With LDs BM498 and RB883 as Sources

Figure 70 illustrates the transmission vs. FO input optical power for FO_2 #1, a 200-μm-dia FO with two SDL 4-W LDs (BM498 and RB883) as sources. The FO is butt-coupled to within 25 to 50 μm of the LD's output cavity mirrors. Both 100-μm-dia aperture LDs are mounted on C-packages.

LD BM498 as Source

The SQS data of Figure 70 show the FO_2 #1 transmission with LD BM498 as the source. The shape of the transmission curve of the 200-μm FO differs from that of the 600- and 1000-μm FOs with LD A840 as the source (Figures 64 and 65). Until LD BM498 emits ~2.5 W, the transmission of the 200-μm FO is greater than either the 600- or 1000-μm FO. At higher-input optical power, the 200-μm FO decreases in transmission.

Possible Causes of the Decrease in Transmission. The NA of FO_2 #1 is reported to be the same as FO_3 #1 and FO_4 #1; the larger transmission for the 200-μm FO suggests that the LD divergence of BM498 (quoted to be 10°×17°) is smaller than the divergence of the A840 (quoted to be 10°×35°). The decrease in transmission at higher power could be caused by an increase in LD divergence or by beam steering. The increase in divergence can be caused by an increase in LD junction heating brought about by the increase in current required to produce the higher LD output optical powers. LD beam steering can be caused by modes changing with increasing LD output optical power. Mode changes are caused again by junction heating that causes changes in optical cavity configuration.

LD RB883 as Source

The TRI and AST data of Figure 70 show transmission of FO_2 #1 vs. FO input optical power with LD RB883 as source. Before LD RB883 was used, both FO ends were repolished. The FO was realigned between the two LD RB883 data runs. The alignment has been described before and is done while the LD is emitting ~100 mW. For both data runs, 1st (TRI) and 2nd (AST), the transmission, begins at the same level as when LD BM498 is the source (~84.6% at an LD optical power of ~0.2 W). At larger LD optical power, transmission decreases.

Erratic Transmission. The transmission of the FO is larger for the second data run (AST data), but is still more erratic than when LD BM498 is the source.

- *Reposition.* The large variations in transmission could be attributed to the alignment of the FO to the LD RB883. For each data shot, the FO is removed from the front of the LD in order to measure the FO input power; it is then repositioned in front of the LD.
- *Cantilevered.* The long, cantilevered, input FO end (~6.45 mm from the holder) could cause a misalignment. The FO is cleaned by rubbing it with a methanol-soaked cotton swab and blowing dust-free air on it. Once the cleaning has been done, the FO end may be realigned differently; it may not return to the same position relative to the kinematic base or, in turn, to the LD output mirror.

Transmission of FO_2 #1 With LD BN968 as Source

Figure 71 shows the transmission vs. FO input optical power for 200-μm-dia FO_2 #1, with LD BN968 as source. The emitting aperture of this laser is 200 μm × 1 μm.

- *Alignment With 0.11-W Input.* The initial alignment of the FO has been described previously.
- *Alignment With 0.5-W Input.* A second alignment is done with a CW FO input optical power of 0.5 W; the optical power emitted by the FO is checked and maximized by repositioning the FO relative to the LD. The FO position relative to the LD differs from the 100-mW alignment by 8 μm in the Y direction and by 30 μm in the X direction. The FO transmission for the data run at the 0.5-W level alignment is shown as SQS in Figure 71. The sudden increase in transmission between the 0.18- and 0.4-W P_{LD} levels is not too disturbing, but the sudden decrease in transmission from 65.4% to 45.6% between the 2- and 2.5-W levels and the sudden increase in transmission from 45.6% to 50.5% between the 2.5- and 2.8-W levels are disturbing. Something is causing large fluctuations in FO transmission.
- *Alignment With 2-W Input.* With an LD input optical power of 2 W, the optical power emitted by the FO is checked and maximized by repositioning the FO relative to the LD. In this case, the LD is not on CW but, rather, is pulsed on for 2 s every 3 min. The FO is aligned starting from the FO position determined by the 0.5-W alignment:

  1. The LD output optical power, which is the FO input optical power, is set at 2 W.
  2. The FO is scanned in the X direction to determine a maximum.
  3. The FO is positioned at the X determined for maximum power out of the FO.
  4. The FO is scanned in the Y direction to determine a maximum. (The FO transmission data collected during this scanning will be discussed shortly.)

  At the X and Y positions, the maximum transmission measured is 69%. With an LD input optical power of 2 W, the optical power emitted by the FO is checked and maximized by repositioning the FO relative to the LD. In this case, the LD is not on CW but, rather, is pulsed on for 2 s every 3 min. The FO transmission after realignment at the 2-W input optical power is represented by the circle.
- *Alignment With 2.8-W Input.* With 2.8 W of input optical power, the FO is realigned using the technique for aligning the FO with 2 W of input optical power just described above. The transmission increased from 50.2% for the 0.5-W alignment to 65.9% (AST). The FO is realigned with 0.1, 0.5, and 1 W of input optical power using the technique for aligning the FO with 0.5 W of input optical power described above. The FO transmission maxima measured for these alignments are shown as triangles in Figure 71.

  Are we seeing LD beam steering or is the LD divergence changing? The LD divergence was checked and found to be unchanged. While the FO input end was being cleaned, it broke about 1.5 mm from its input end. The erratic transmission data could have been caused by a cracked FO.

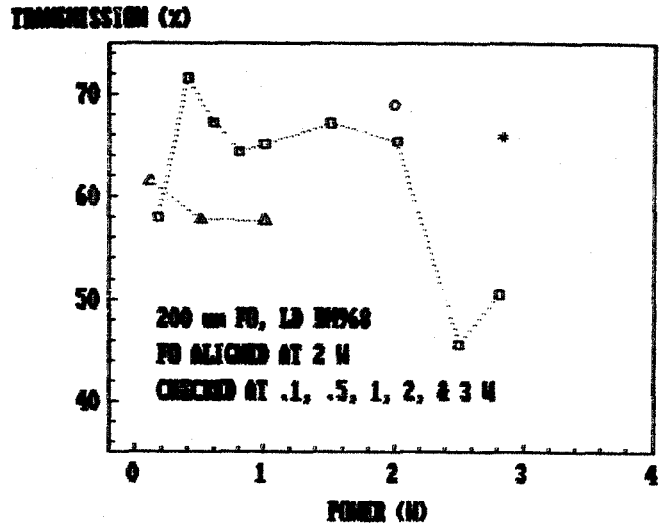

Figure 71. Transmission of 200-μm FO_2 #1 vs. Optical Power Using a Prototype SDL 8-W LD (BN968) as Source, FO Is Aligned When LD Is Emitting 2 W

Transmission of FO_2 #1 Aligned at Each Power Level

Figure 72 shows the transmission of FO_2 #1 vs. FO input optical power with LD BN968 as the source. The FO input end was repolished between the data described above in Figure 71 and the LD BN968 SQS data, and the LD BN968 AST data in Figure 72.

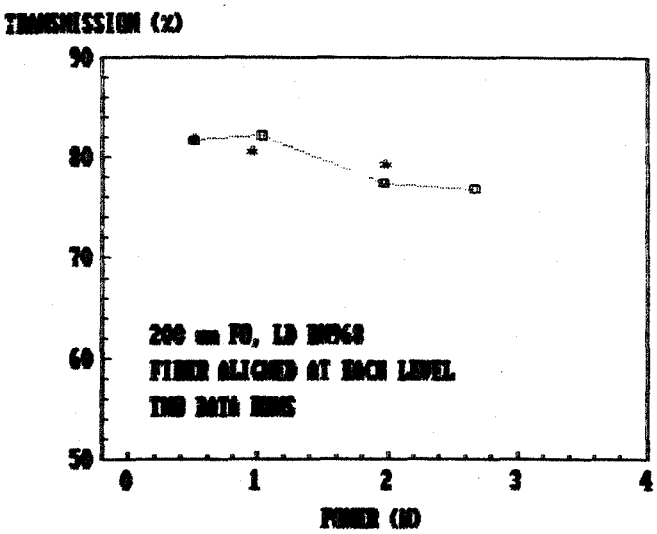

Figure 72. Transmission of 200-μm FO_2 #1 vs. Optical Power Using a Prototype SDL 8-W LD (BN968) as Source, FO Is Aligned at Each LD Optical Power Level

First Data Run

For the SQS data, FO is aligned to the LD with 0.13 W of CW LD output optical power as described earlier.

The FO was then aligned at each FO input optical power of 0.5, 1, 2, and 2.7 W. The LD is pulsed on for 3 s every 2 min for the 0.5- and 1-W data; every 3 min for the 2-W data; and every 5 min for the 3-W data.

The FO was aligned starting from the FO position determined for the 0.13-W alignment and proceeding as described for Figure 71. (The FO transmission data collected during this scanning will be discussed shortly in this section.)

The maxima determined during the scanning are plotted at each FO input optical power level as squares in Figure 72. With increased FO input optical power, the transmission remains high until the FO input optical power exceeds 2 W. On two occasions after the LD emitted more than 2 W, the FO transmission decreased for the next higher FO input optical power.

After the 2.7-W maximum determination, we were unable to reproduce the FO transmission of the original points. The divergence of the LD was checked and is shown in Table 4 in Shots 12-2-S7 through 12-2-S27. The half-angle divergence varies between ~9° to 11° or between 18° to 22° for full-angle divergence. This divergence is not large enough to overfill the NA=0.37 of the FO.

The FO input end breaks at the point where the jacket is removed from the FO cladding. The technique used to fabricate the FO input end comes in question. If cutting the jacket causes a tear in the cladding and a scratch mark on the FO core, then FO input optical power in excess of 2 W could relieve the stress in the core (caused by the scratch) by propagating a crack.

A closer look at the FO input end reveals that the jacket, which was initially 1.5 mm from the FO input end, is now 2 mm away from the end. A burnt ring is now visible on the cladding 1.5 mm from the FO input end and is also visible on the end of the jacket.

Second Data Run

For the AST data, the FO ends were repolished using the old method of polishing with the core, cladding, and jacket all flush with each other. The FO is aligned to the LD with 0.1 W of CW LD output optical power as described earlier.

The FO was then aligned at each FO input optical power of 0.5, 0.96, 2, and 2.6 W. The LD is pulsed on for 3 s every 2 min for the 0.5- and 0.96-W data; every 3 min for the 2-W data; and every 5 min for the 2.6-W data.

The FO was aligned starting from the FO position determined for the 0.1-W alignment and proceeding as described for Figure 71. (The FO transmission data collected during this scanning will be discussed shortly in this section.) The maxima determined during the scanning are plotted at each FO input optical power level as AST data in Figure 72.

At the 2.6-W FO input optical power level after the seventh LD shot into the FO, the initial FO transmission could not be repeated. A closer look at the FO input end revealed that the jacket was burned back from the end of the core and that a white, snow-like powder coated the FO, the FO holder, the LD BN968, and the C-package.

Upon examining the LD output optical power it was determined that, even with a 0.4% increase in LD current, the LD output optical power decreased 5.2% compared to what it had been before the FO damaged. After cooling, with a 1.1% increase in LD current, the LD output optical power decreased 7.2% compared to what it had been before the FO damaged. It appears that the white powder deposited on the LD cavity output mirrors is causing increasing LD damage.

FO_2 #1 Alignment Procedure For First Data Run

The alignment procedure used to generate the SQS data in Figure 71 results in transmission vs. FO position curves shown in Figure 73 for scanning in the X direction. It also results in transmission vs. FO position curves shown in Figure 74 for scanning in the Y direction.

The FO is aligned with 0.13 W of CW LD output optical power as described earlier. The FO was then aligned at each FO input optical power of 0.5, 1, 2, and 2.7 W. In these cases, the LD is not on CW but, rather, is pulsed on for 3 s every 2 min for the 0.5- and 1-W data; every 3 min for the 2-W data; and every 5 min for the 2.3-W data.

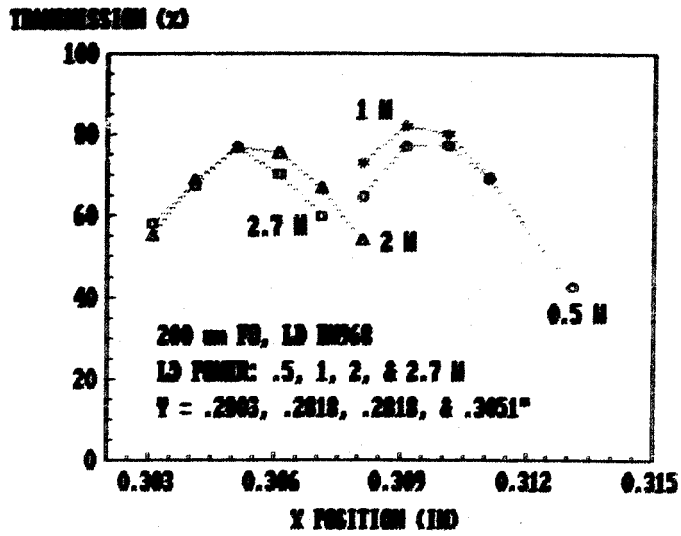

Figure 73. Transmission of 200-μm FO_2 #1 vs. X Position Using a Prototype SDL 8-W LD (BN968) as Source for Four Incident LD Optical Power Levels

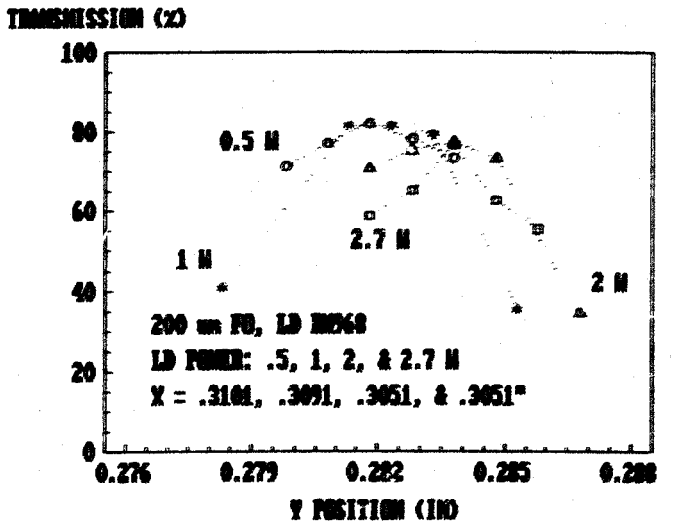

Figure 74. Transmission of 200-μm FO_2 #1 vs. Y Position Using a Prototype SDL 8-W LD (BN968) as Source for Four Incident LD Optical Power Levels

LD Beam Steering in X Direction

The FO was aligned starting from the FO position determined for the 0.13-W alignment labeled Y = 0.2803 in. in Figure 73.

1. The LD output optical power, which is the FO input optical power, was set at 0.5 W.
2. The FO was scanned in the X direction to determine a maximum.

These steps were repeated for FO input optical power levels of 1, 2, and 2.7 W, generating the curves in Figure 73.

For scanning in the X direction, with 0.5 and 1 W of LD output optical power incident onto the FO, the FO transmissions are maximum when the FO is at the same X position relative to the LD mirror. At the 2- and 2.7-W LD levels, the FO transmissions are maximum when the FO is at the same X position relative to the LD mirror, but 0.004 in. or 100 μm away (half a FO diameter) from the FO maximum transmission position when the incident LD optical power is 0.5 and 1 W. It appears that the LD beam steered about 100 μm between when the LD emitted 1 and 2 W.

LD Beam Steering in Y Direction

The FO is then positioned at the X determined in Figure 73 for maximum FO output power labeled X = 0.3101 in. in Figure 74. For 0.5 W of FO input optical power, the FO is scanned in the Y direction to determine a maximum. This procedure is repeated for FO input optical power levels of 1, 2, and 2.7 W, generating the curves in Figure 74.

For scanning in the Y direction, with 0.5 and 1 W of LD output optical power incident onto the FO, the FO transmissions are maximum when the FO is at the same Y position relative to the LD mirror. At the 2- and 2.7-W LD levels, the FO transmissions are maximum when the FO is at the same Y position relative to the LD mirror, but 0.002 in. or 50 μm away (one-fourth an FO diameter) from the FO maximum transmission position when the incident LD optical power is 0.5 and 1 W. It appears that the LD beam steered about 50 μm between the time that the LD emitted 1 and 2 W.

FO_2 #1 Alignment Procedure for Second Data Run

In a similar manner, the alignment used for the asterisked data in Figure 72 results in transmission vs. FO position curves shown in Figure 75 for scanning in the X direction and Figure 76 for scanning in the Y direction.

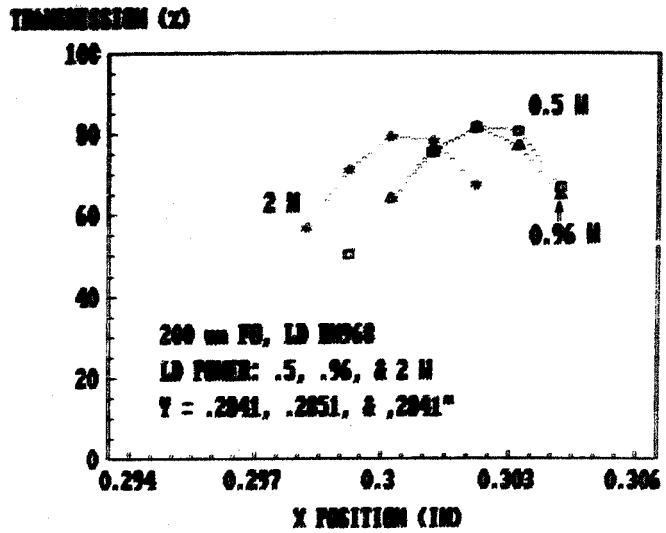

Figure 75. Transmission of 200-μm FO_2 #1 vs. X Position Using a Prototype SDL 8-W LD (BN968) as Source for Three Incident LD Optical Power Levels

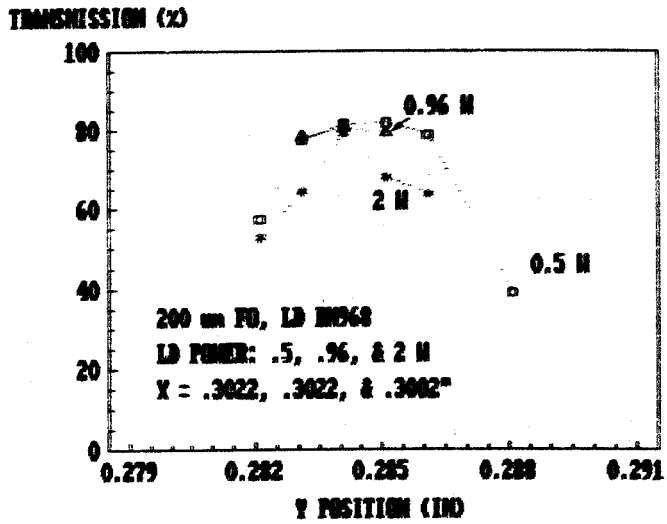

Figure 76. Transmission of 200-μm FO_2 #1 vs. Y Position Using a Prototype SDL 8-W LD (BN968) as Source for Three Incident LD Optical Power Levels

The FO is aligned with 0.1 W of CW LD output optical power as described earlier. The FO was then aligned at each FO input optical power of 0.5, 0.96, and 2 W. In these cases, the LD is not on CW but, rather, is pulsed on for 3 s every 2 min for the 0.5- and 0.96-W data and every 3 min for the 2-W data.

LD Beam Steering in X Direction

The FO was aligned starting from the FO position determined for the 0.1-W alignment labeled Y = 0.2841 in. in Figure 75.

1. The LD output optical power, which is the FO input optical power, was set at 0.5 W.
2. The FO was scanned in the X direction to determine a maximum.

This was repeated for FO input optical power levels of 0.96 and 2 W, generating the curves in Figure 75.

For scanning in the X direction with 0.5 and 1 W of LD output optical power incident onto the FO, the FO transmissions are maximum when the FO is at the same X position relative to the LD mirror. At the 2-W LD level, the FO transmission is maximum at an X position relative to the LD mirror, which is 0.002 in. or 50 μm away (half a FO diameter) from the FO maximum transmission position when the incident LD optical power is 0.5 and 1 W. It appears that the LD beam steered about 50 μm between when the LD emitted optical outputs of 1 and 2 W.

LD Beam Steering in Y Direction

The FO is then positioned at the X determined in Figure 73 for maximum FO output power labeled X = 0.3022 in. in Figure 76. For 0.5 W of FO input optical power, the FO is scanned in the Y direction to determine a maximum. This procedure is repeated for FO input optical power levels of 0.96 and 2 W, generating the curves in Figure 76.

For scanning in the Y direction with 1 and 2 W of LD output optical power incident onto the FO, the FO transmission is maximum when the FO is at the same Y position relative to the LD mirror. At the 0.5-W LD level, the FO transmission is maximum at a Y position relative to the LD cavity mirror, which is 0.0003 in. or 15 μm away from the maximum transmission position when the incident LD optical power is 1 and 2 W. It appears that the LD beam steered about 15 μm between when the LD emitted optical outputs of 0.5 and 1 W.

Transmission of Four FOs, LD RP542 as Source

Figure 77 shows the percent tramsmission vs. input LD optical power for four FOs with LD RP542 as source for a 600-μm FO_3 #4; a 400-μm FO_5 #1; a 200-μm FO_2 #1; and a 100-μm FO_1 #1.

The emitting aperture of the LD is 100×1 μm. The alignment of each FO is done with the LD emitting about 0.1 W CW and maximizing its transmission by scanning its input end in both the H and V directions.

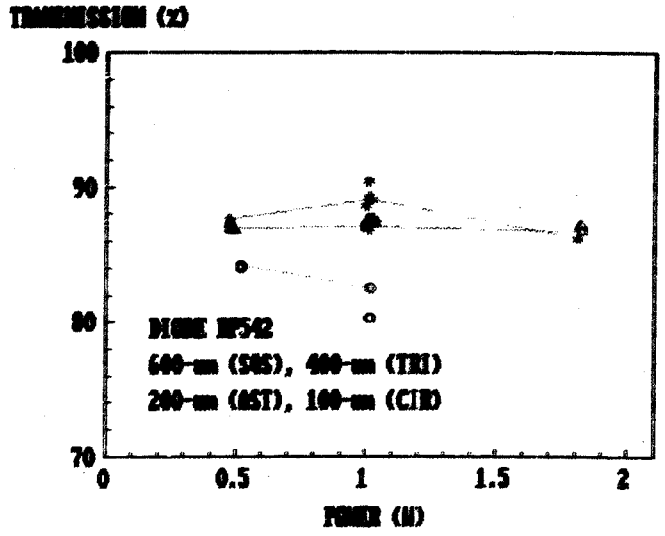

Figure 77. Transmission of 600-, 400-, 200-, and 100-μm FOs vs. Optical Power Using SDL 4-W LD (RP542) Operating at 0.5, 1, and 1.8 W of Output Optical Power

If all emitting levels are considered, the transmissions of FO_3 #4 and FO_5 #1 are 86.9% ± 0.3%. In all cases, the transmission at the beginning of the test is 0.3% less than those plotted.

The transmissions of FO_2 #1 and FO_1 #1 are not as constant. FO_2 #1 and FO_1 #1 have spreads of 3.5% and 2.7% at the 1-W level, respectively. For FO_1 #1 there is a definite decrease in transmission with an increase in LD output optical power. This type of change in transmission was observed for FO_2 #1, the 200-μm FO coupled to the 200-μm aperture LD BN968 as previously discussed. That decrease in transmission was attributed to LD beam steering. For this LD, the observed decrease in transmission with increase LD emitting power could likewise be due to LD beam steering. When the FO diameter approaches the LD aperture dimension, slight changes in LD beam direction can cause changes in FO transmission.

Transmission of P-C Lens

Figure 78 shows the percent transmission of P-C lens vs. LD output optical power with four FO sources. The lens transmissions for the different FOs with LD RP542 as the source are:

- 92.0% ± 0.1% for 600-μm FO_3 #4
- 91.6% ± 0.3% for 400-μm FO_5 #2
- 91.5% ± 0.8% for 200-μm FO_2 #1
- 91.9% ± 1% for 100-μm FO #1.

The trend is for the spread in the lens transmission and transmission to decrease to increase with an increase in LD output optical power.

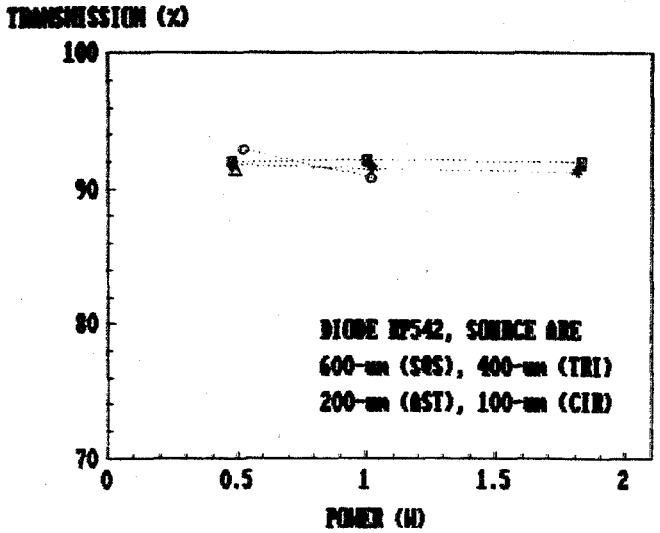

Figure 78. Transmission of P-C Lens vs. Optical Power Level Using Four FOs Coupled to SDL 4-W LD RP542 as Sources, With the LD Operating at 0.5, 1, and 1.8 W of Output Optical Power

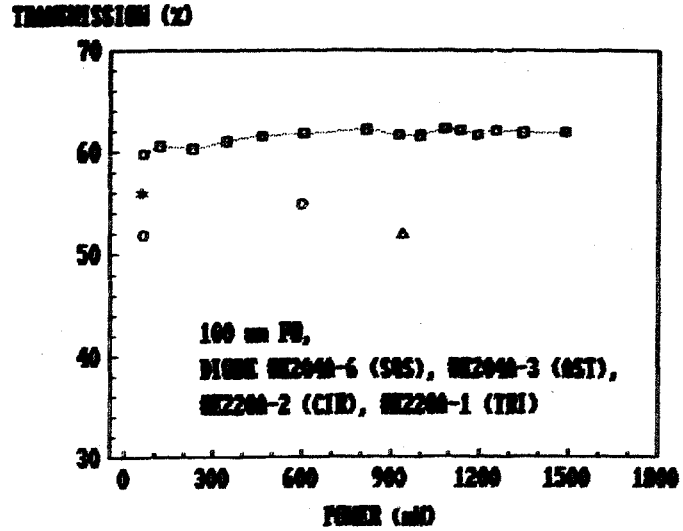

Figure 79. Transmission of 100-μm FO_1 #1 vs. Optical Power Using Four MDAC/OEC 1-W LDs: (AST) E204A-3, (SQS) E204A-6, (TRI) E220A-1, and (CIR) E220A-2 as Sources, Operating with (AST) 0.5 W, (SQS) up to 1.5 W, (TRI) 0.9 W, and (CIR) up to 0.6 W of Output Optical Power

Transmission of FO_1 #1 Using Four MDAC/OEC LDs as Source

Figure 79 shows the transmission vs. input LD optical power for FO_1 #1, a 100-μm-dia FO butt-coupled to four 60-μm aperture MDAC/OEC LDs. The variations in transmission for the same FO but different LDs are attributed to different LD divergences and possibly to the FO and LD alignments.

The 60-μm-wide emitting aperture of LD E204A-6 allows ~60% of the maximum output optical power of 1.5 W emitted by the LD to be transmitted through the FO. This corresponds to a power density (p) of

$$p = T\left(\frac{P_{FO}}{A_{FO}}\right) = 1.15 \times 10^4 \text{ W/cm}^2 . \qquad (30)$$

where

T = the transmission of FO
P_{FO} = power out of the FO
A_{FO} = the area of the FO core.

4.2.3 Beam Intensity Distribution

With LD A322 as the source, the LD beam intensity distribution transmitted by a 0.23-pitch GRIN lens and FO_3 #1 is described. With LD A840 as the source, the LD beam is described along with intensity distribution transmitted by

- FO_3 #1 and FO_3 #4 that are 1 m long
- FO_3 #1 and FO_3 #7 that are 0.5 m long
- FO_3 #7 that is 0.5 to 0.0312 m long.

With LD RB 883 as the source, the LD beam intensity distribution transmitted by FO_2 #1 and FO_2 #2, which are 100 cm long, are described. In each figure, Section A is the contour of the intensity distribution of the output beam of the particular coupler (i.e., GRIN lens or FOs) and Section B is a profile in the X and Y directions of the contour through its centroid.

Beam Contours and Profiles of 0.23-Pitch GRIN Lens and FO_3 #1

Figure 80 shows the beam contours and profiles of the 0.23-pitch GRIN lens with SDL 100-mW LD A322 operating as the source and emitting 400 mW.

Figure 81 shows the beam contours and profiles of 104.3-cm-long FO_3 #1 butt-coupled to SDL 100-mW LD A322 emitting 99.5 and 395 mW.

Figure 82 shows the beam contours and profiles of 104.3-cm-long FO_3 #1 butt-coupled to SDL 500-mW LD A840 emitting 515 and 1911 mW.

The camera is placed approximately the same distance away from the end of the couplers as the cells when they are used; the distance is ~20 mm for the 0.23-pitch GRIN lens and 9.9 mm for the FO.

There are eight equally spaced intensity (W/cm^2) contours in Figures 80 A and 81 I A and II A, and twelve contours in Figures 82 I A and II A. The bottoms (B) in each figure show the profile through the centroid in the X and Y directions. As was seen in Figures 50 and 51, the dotted line is a Gaussian fit to the profile of the intensity distribution at the maximum intensity.

Gaussian Beam Fit

For Figure 80 the $1/e^2$ widths of the Gaussian beam fits in the X and Y directions are 0.97 and 1.97 mm, respectively. The $1/e^2$ widths are 3.39 (X) and 2.89 mm (Y) for Figure 81 I B, and 4.81 and 4.18 mm for Figure 81 II B. The $1/e^2$ widths are 3.12 and 3.05 mm for Figure 82 I B, and 3.87 and 3.89 mm for Figure 82 II B.

- The Gaussian fit for the GRIN lens is not good in Figure 80. The two-lobe pattern of the LD described earlier is present in the X direction, whereas the intensity variations contain many peaks in the Y direction.
- The Gaussian fit is fairly good for the beam emitted by FO_3 #1 when the LDs are operated at their rated power (Figures 81 I and 82 I). On the other hand, when LDs are operated at levels of 395 and 1911 mW, the beam out of the FO is flatter at its peak relative to a Gaussian distribution (Figures 81 II and 82 II). It should be noted that the two lobes of the intensity distributions of the LDs shown in Figures 50 and 51 are absent from the output intensity distribution out of the FOs.

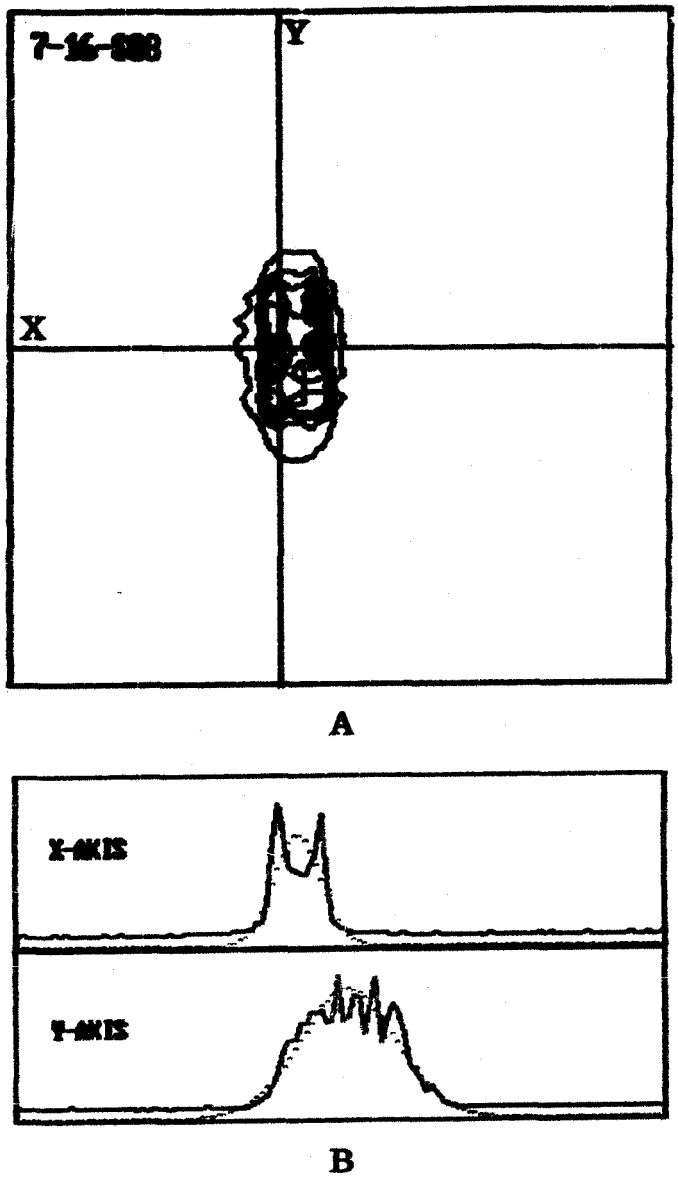

Figure 80. Contours and Profiles of Intensity Distribution of the Output of 0.23-Pitch GRIN Lens Butt-Coupled to SDL 100-mW LD (A322) Operating at 400 mW

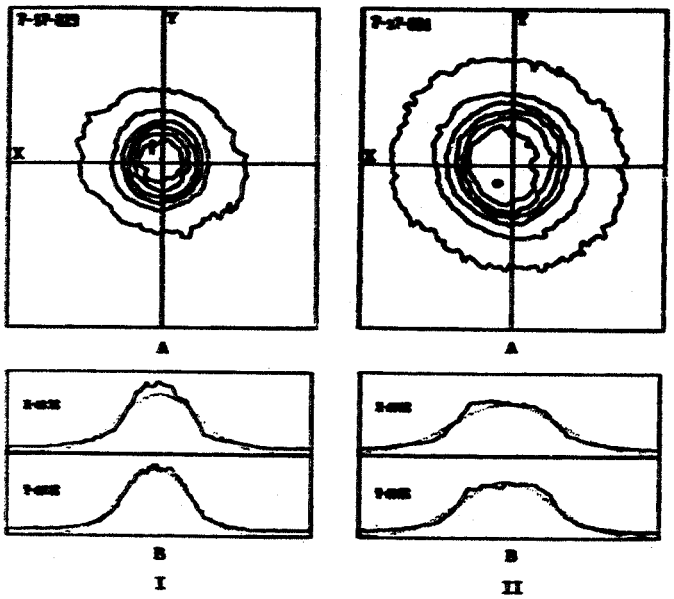

Figure 81. Contours and Profiles of Intensity Distribution of the Output of 600-μm FO_3 #1 Butt-Coupled to SDL 100-mW LD (A322) Operating at 99.5 mW (I) and 395 mW (II)

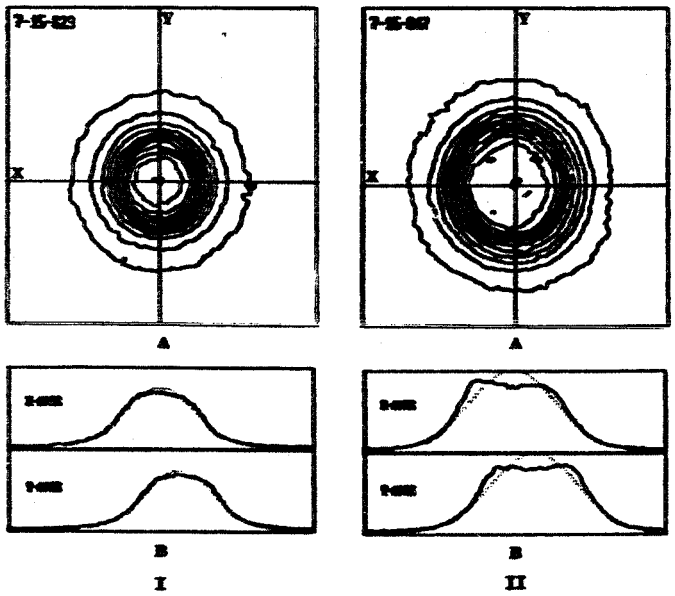

Figure 82. Contours and Profiles of Intensity Distribution of the Output of 600-μm FO_3 #1 Butt-Coupled to SDL 500-mW LD (A840) Operating at 515 mW (I) and 1911 mW (II)

Intensity Distribution of FO_3 #1, FO_3 #4, and FO_3 #7 With LD A840 as Source

The 600-μm FO beam intensity distribution data to be described are obtained using SDL 500-mW LD A840 emitting 600 mW, with the FO butt-coupled to the window of the LD. Three FOs are used:

- FO_3 #1 and FO_3 #4, each 104.3 cm long, are in a 15.2-cm × 21.6-cm loop configuration and a straight configuration, as can be seen in Figure 83.
- FO_3 #1 and FO_3 #7, each 49 cm long, are in a straight configuration, as can be seen in Figure 84.
- FO_3 #7 is 49.4 cm long, and is successively cut in half until the FO, which was 49.4 cm long, becomes 3.1 cm long. See Figures 85 and 86.

Intensity Distribution of FO_3 #1 and FO_3 #4

Figure 83 shows the beam contours and profiles of FO_3 #1 and FO_3 #4 under various conditions.

- Figure 83 I and IV, which shows the intensity distribution of 104.3-cm-long FO_3 #1 with a 15.2-cm × 21.6-cm loop (L), is recorded at a distance Z = 5.13 mm (close) and 7.13 mm (far) from the FO output ends, respectively.
- Figure 83 II and V, which shows the intensity distribution of 104.3-cm-long straight (S) FO_3 #1, is recorded 5.13 and 7.13 mm from the FO output ends, respectively.
- Figure 83 III and VI, which shows the intensity distribution of a 104.3-cm-long FO_3 #4 in a loop, is recorded 9.08 and 11.08 mm from the FO output ends, respectively.

The contours and profiles of FO_3 #1 recorded (1) close for the FO looped (I) and straight (II) are similar to one another and (2) far for the FO looped (IV) and straight are similar to each other.

A comparison of FO_3 #1 with FO_3 #4 both looped shows that the photographed profiles close (compare Figure 83 I with Figure 83 III) are quite different. This is also true of the far-recorded profiles (compare Figure 83 IV to Figure 83 VI). The Gaussian profile fit (the dotted line) is a better fit for the FO_3 #1 data than for the FO_3 #4 data.

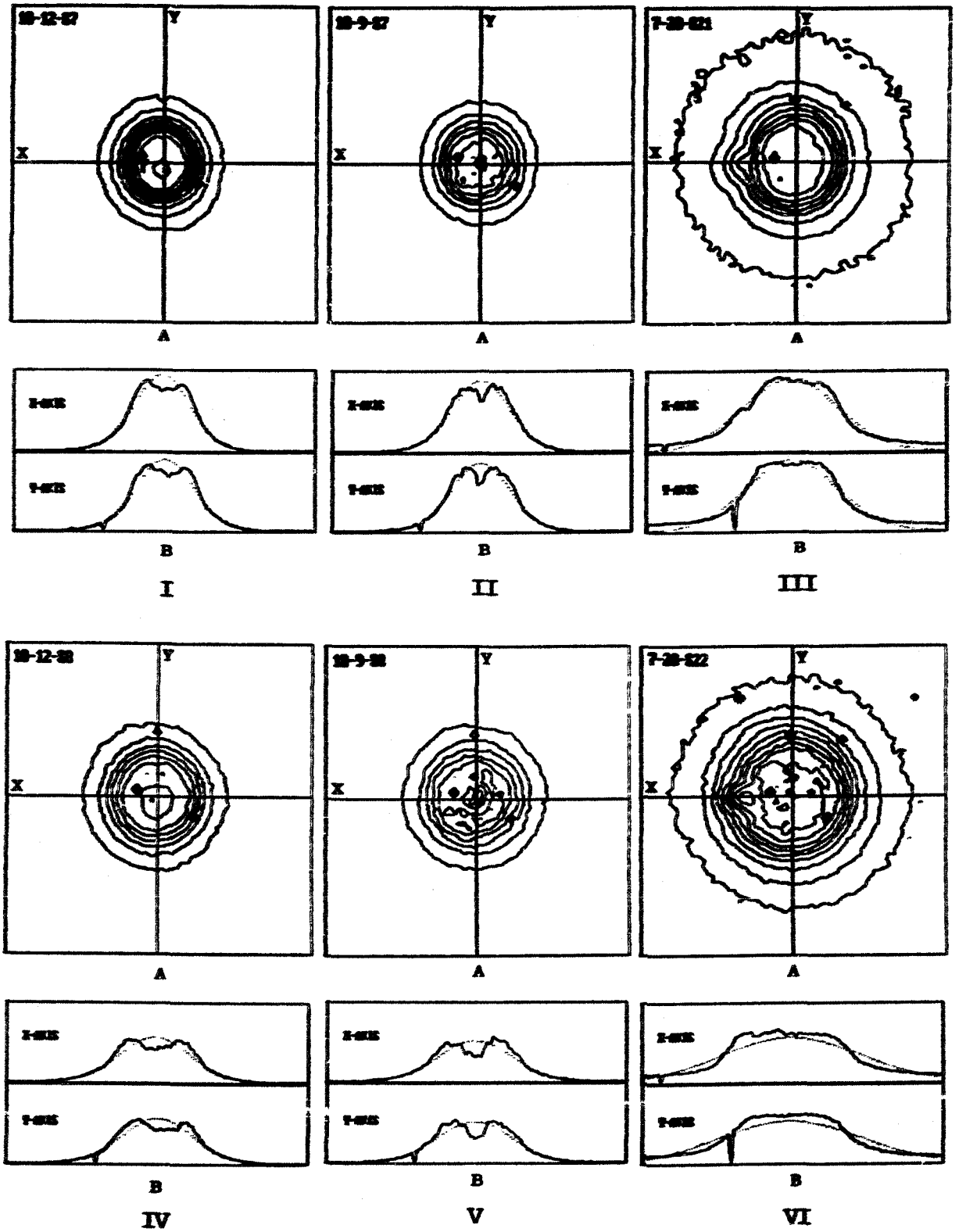

Figure 83. Contours and Profiles of Intensity Distribution of the Output of Two 104.3-cm-long 600-μm FO_3 #1 and FO_3 #4 Looped (I & IV FO_3 #1 and III & VI FO_3 #4) and Straight (II & V FO_3 #1), Recorded Close 5.13 mm (I & II) and Far 7.13 mm (IV & V) From FO Output End and 9.08 mm (III) and 11.08 mm (VI)

Intensity Distribution of FO_3 #1 and FO_3 #7

Figure 84 shows the beam contours and profiles of FO_3 #1 and FO_3 #7, 49.4 cm long. Figure 84 I through IV shows eight contours. For FO_3 #1 and FO_3 #7, Figure 84 I and II are recorded close and III and IV are recorded far, respectively. The close profiles of both FOs are similar to one another; this is also true for the far profiles. The Gaussian fit is best for the close profiles, and best for the X direction.

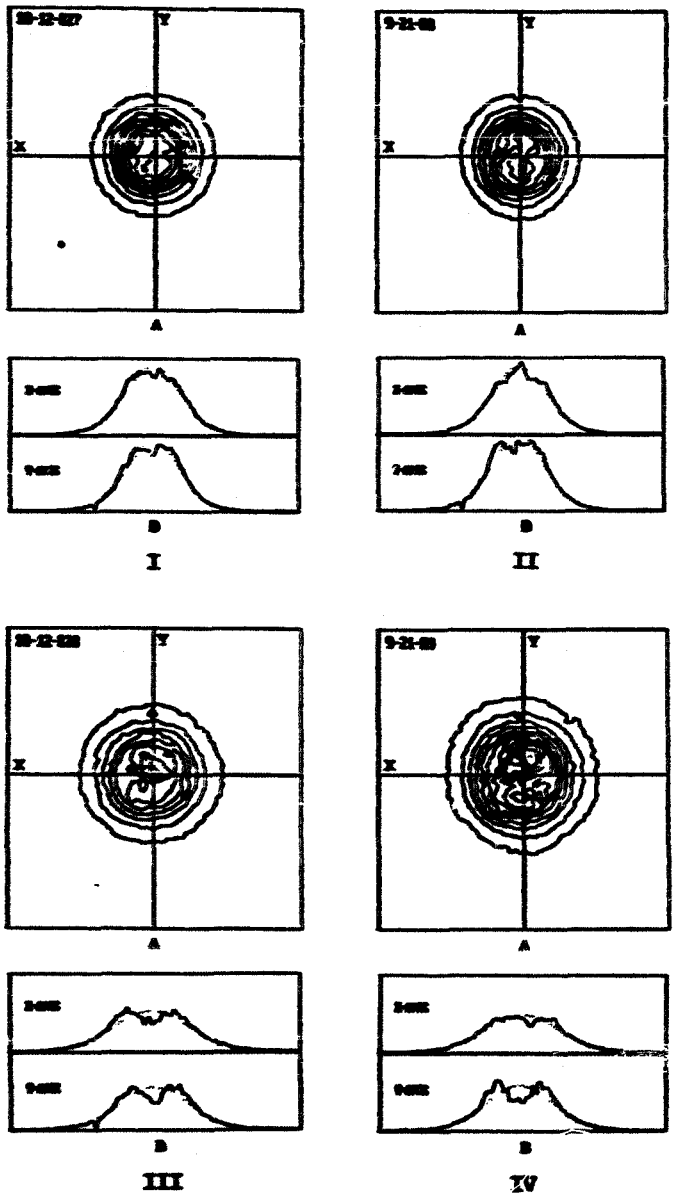

Figure 84. Contours and Profiles of Intensity Distribution of the Output of Two 49.4-cm-long 600-μm FO_3 #1 (I & III) and FO_3 #7 (II & IV) Straight, Recorded Close 5.13 mm (I & II) and Far 7.13 mm (III & IV) From FO Output End

Intensity Distribution of FO_3 #7

Figures 85 and 86 show the beam contours and profiles of FO_3 #7, which are successively cut in half starting with a 49.4-cm-long FO. Figure 85 consists of recordings close (5.13 mm) from the FO output end; Figure 86 consists of recordings far (7.13 mm) from the FO output end. The recordings are taken of FO length Z in Figure 85 I through V, where Z is 49.4 cm in I; 25.1 cm in II; 12.2 cm in III; 6.8 cm in IV; and 3.1 cm in V.

The FO Z lengths are the same for Figure 86. The beam contours and profiles of FO_3 #7 close and far change with the FO lengths. For both close and far positions, the intensity fluctuations in the profiles increase as the FO length decreases. The two lobes of the LD shown in Figure 50 are beginning to appear in the contours and the Y-axis profiles of Figures 85 III and 86 III; they become more pronounced as the FO is cut shorter (Figures 85 IV and V and Figure 86 IV and V).

Specification for Three 600-μm FOs With LD A840 as Source

Table 6 lists for three FO_3 600-μm FOs the shot numbers, the FO numbers, the distance from the FO end photographed, the FO length, $1/e^2$ width, the divergence, correlation coefficient (CC), the configuration of the FO, whether it is straight (S) or looped (L), and the figure in which the contour or profile appears.

The recordings of all the FOs are taken at 5.134 and 7.13 mm from the FO output ends, except for FO_3 #4 for which recordings are taken at 9.08 and 11.08 mm. The length of the FOs varies from 104.3 to 3.1 cm. The $1/e^2$ width is that of a Gaussian fit to the profile through the centroid of the intensity distribution. The FO divergences, a_x and a_y are calculated in Eq (28) for the LD divergence in Table 6:

$$a_x = \tan^{-1}\left[\frac{x_8 - x_7}{2\,(z_8 - z_7)}\right], \tag{31}$$

where x_8 and x_7 are the $1/e^2$ widths, and z_8 and z_7 are the distances from the FO output end for Shots 10-12-S8 and 10-12-S7, respectively.

The a_y divergence is calculated in a similar manner except that the x's are replaced by y's.

The "S" in the configuration column indicates that the FO is straight and in line with the emission from the LD, whereas an "L" indicates that the FO had a 15.2-cm × 21.6-cm loop halfway down the FO.

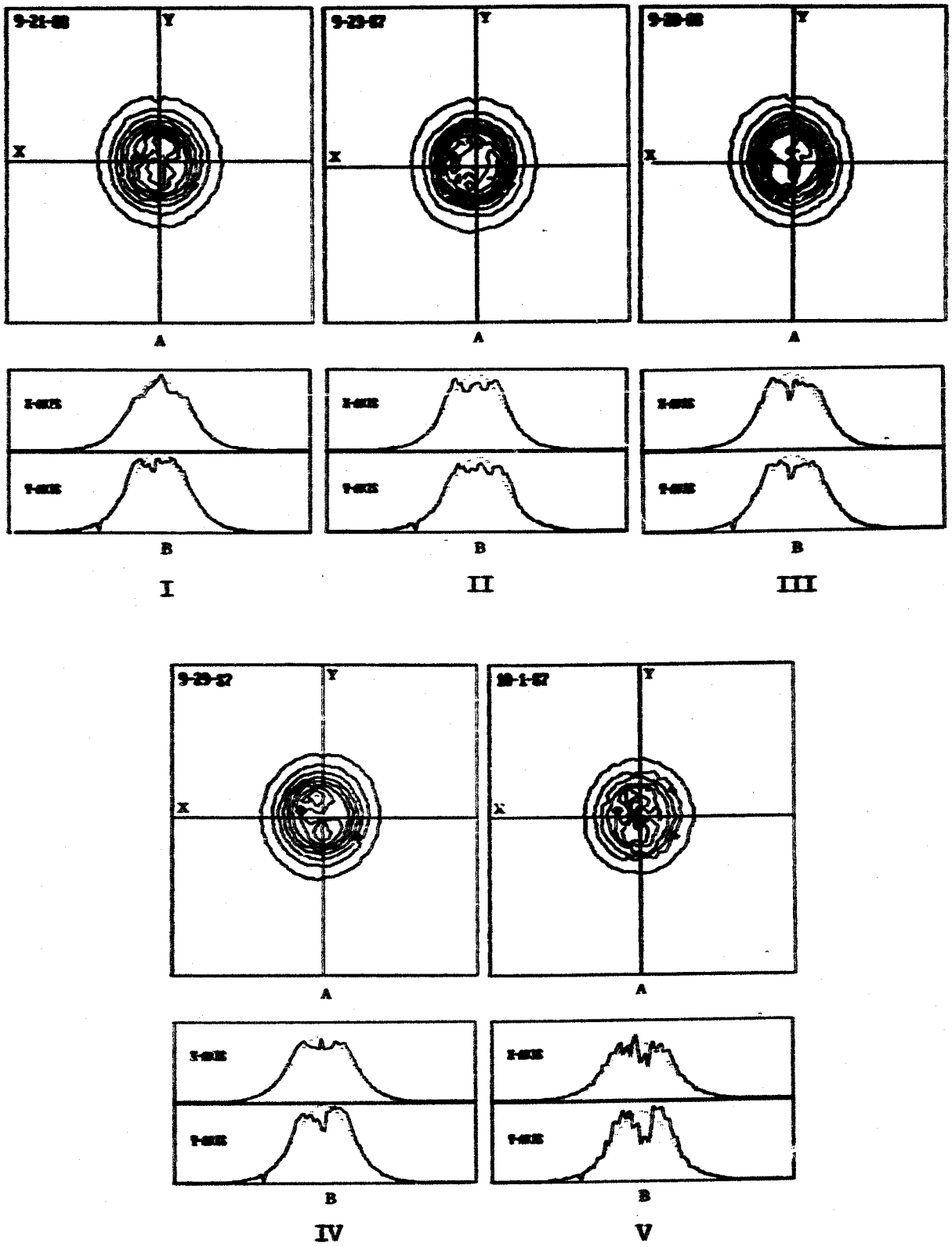

Figure 85. Contours and Profiles of Intensity Distribution of the Output of 600-μm FO_3 #7 Recorded 5.13 mm From FO Output End After Successively Cutting in Half Four Times. FO is 49.4 cm long in (I), 25.1 cm in (II), 12.2 cm in (III), 6.8 cm in (IV), and 3.1 cm in (V).

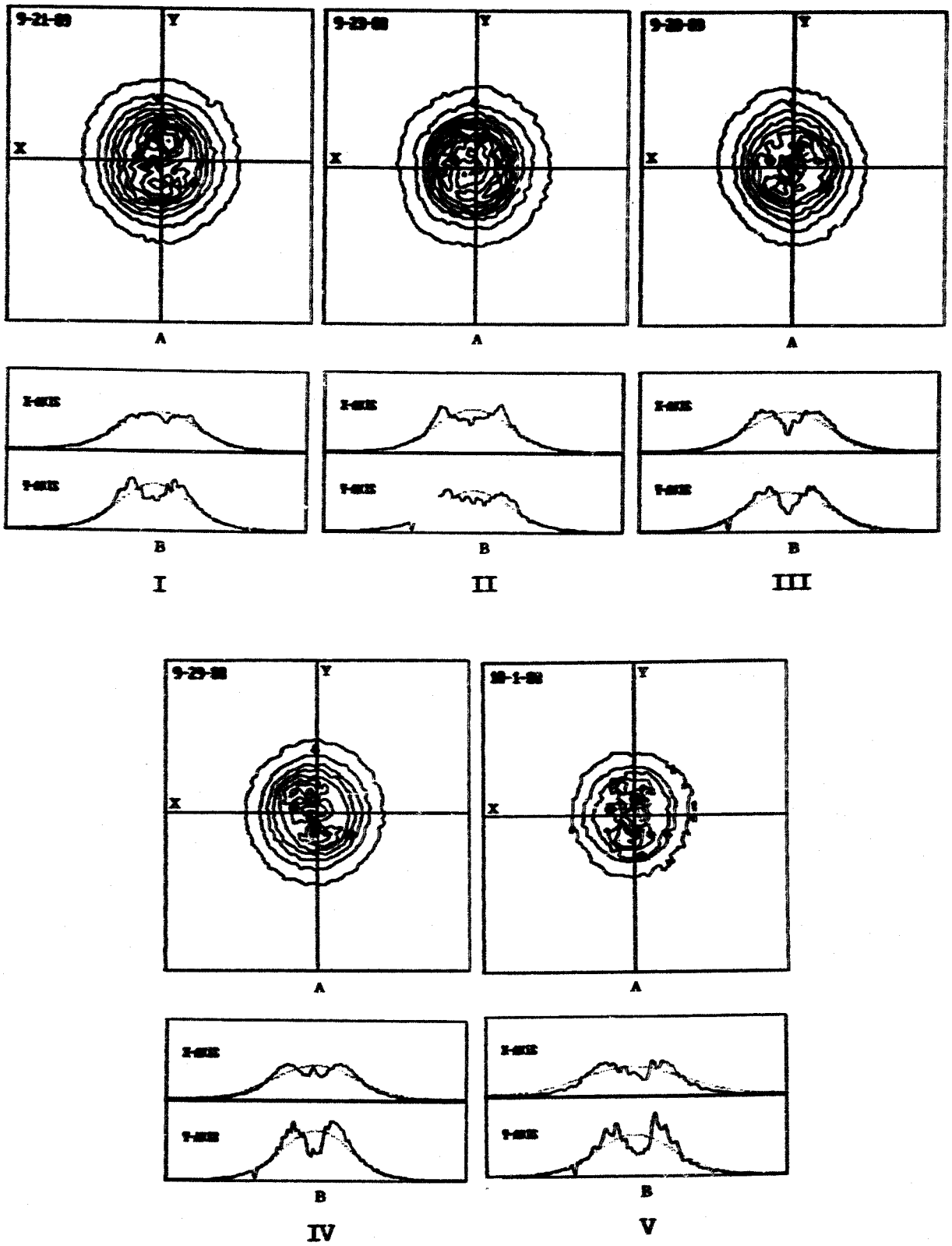

Figure 86. Contours and Profiles of Intensity Distribution of the Output of 600-μm FO_3 #7 Recorded 7.13 mm From FO Output End After Successively Cutting in Half Four Times. FO is 49.4 cm long in (I), 25.1 cm in (II), 12.2 cm in (III), 6.8 cm in (IV), and 3.1 cm in (V).

Table 6. Beam Specifications for Different 600-μm FOs and FO Lengths

SHOT (#)	FO (#)	FO DIST (mm)	FO LENGTH (cm)	I/e^2 WIDTH X (mm)	I/e^2 WIDTH Y (mm)	DIVERGENCE X (deg)	DIVERGENCE Y (deg)	CORRELATION COEFFICIENT (X)	CORRELATION COEFFICIENT (Y)	CONF	FIG (#)
10-12-S7	1	5.13	104.3	2.49	2.58			.999333	.999253	L	83 I
10-12-S8	1	7.13	104.3	3.22	3.19	10.3	8.7	.998411	.998529	L	83 IV
10-09-S7	1	5.13	104.4	2.58	2.62			.999419	.999273	S	83 II
10-09-S8	1	7.13	104.4	3.36	3.31	11.0	9.8	.997733	.997776	S	83 V
7-20-S21	4	9.08	104.4	4.15	3.39			.999328	.999184	L	83 III
7-20-S22	4	11.08	104.4	6.28	6.25	28.0	29.8	.996453	.996525	L	83 VI
10-12-S27	1	5.13	49.4	2.57	2.45			.999737	.999657	S	84 I
10-12-S28	1	7.13	49.4	3.42	3.17	12.0	10.2	.998578	.998214	S	84 III
9-21-S8	7	5.13	49.4	2.58	2.49			.999822	.999515	S	84 II
9-21-S9	7	7.13	49.4	3.41	3.24	11.7	10.6	.999247	.997842	S	84 IV
9-21-S8	7	5.13	49.4	2.58	2.49			.999822	.999515	S	85 I
9-21-S9	7	7.13	49.4	3.41	3.24	11.7	10.6	.999247	.997842	S	86 I
9-23-S7	7	5.13	25.1	2.53	2.56			.999301	.999284	S	85 II
9-23-S8	7	7.13	25.1	3.31	3.34	11.0	11.0	.997582	.997939	S	86 II
9-20-S8	7	5.13	12.2	2.58	2.67			.999315	.999319	S	85 III
9-20-S9	7	7.13	12.2	3.52	3.64	13.2	13.6	.996558	.996374	S	86 III
9-29-S7	7	5.13	6.8	2.62	2.58			.999423	.999233	S	85 IV
9-29-S8	7	7.13	6.8	3.63	3.89	14.2	18.1	.997684	.996441	S	86 IV
10-1-S7	7	5.13	3.1	2.78	2.53			.998541	.997480	S	85 V
10-1-S8	7	7.13	3.1	4.48	3.49	23.0	13.4	.995922	.994720	S	86 V

Divergence of FOs

For the same 104.3-cm-long FO_3 #1, the a's are comparable for both the "S" and "L" configurations. For the 104.3-cm-long FO_3 #1 and FO_3 #4, the a's are quite different; for the 49.4-cm-long FO_3 #1 and FO_3 #7, the a's are comparable.

Gaussian Fit of FO Beams

The beam of FO_3 #4 far away is not as good a fit to a Gaussian as FO_3 #1, as is indicated by the CC. As FO_3 #7 is cut shorter, the trend is for the divergences to increase and for CC to decrease, or for the intensity distribution to deviate further from a Gaussian for both the close and far shots.

Intensity Distribution at Different Distances From FO_3 #1 End

For 49.4-cm-long FO_3 #1, Figure 87 shows the intensity distribution recorded at different distances, Z_1, from the FO output end with LD A840 as source. Z_1 is 4.49 mm in I; 4.63 mm in II; 5.13 mm in III; 7.13 mm in IV; 9.13 mm in V; and 11.13 mm in VI.

The two closest distances show smooth contours and profiles compared to those farther away. As the distance from the FO output end increases (starting at 5.13 mm, but more pronounced at 7.13 mm), a hole develops in the center of the intensity distribution. This hole deepens as the distance from the FO increases.

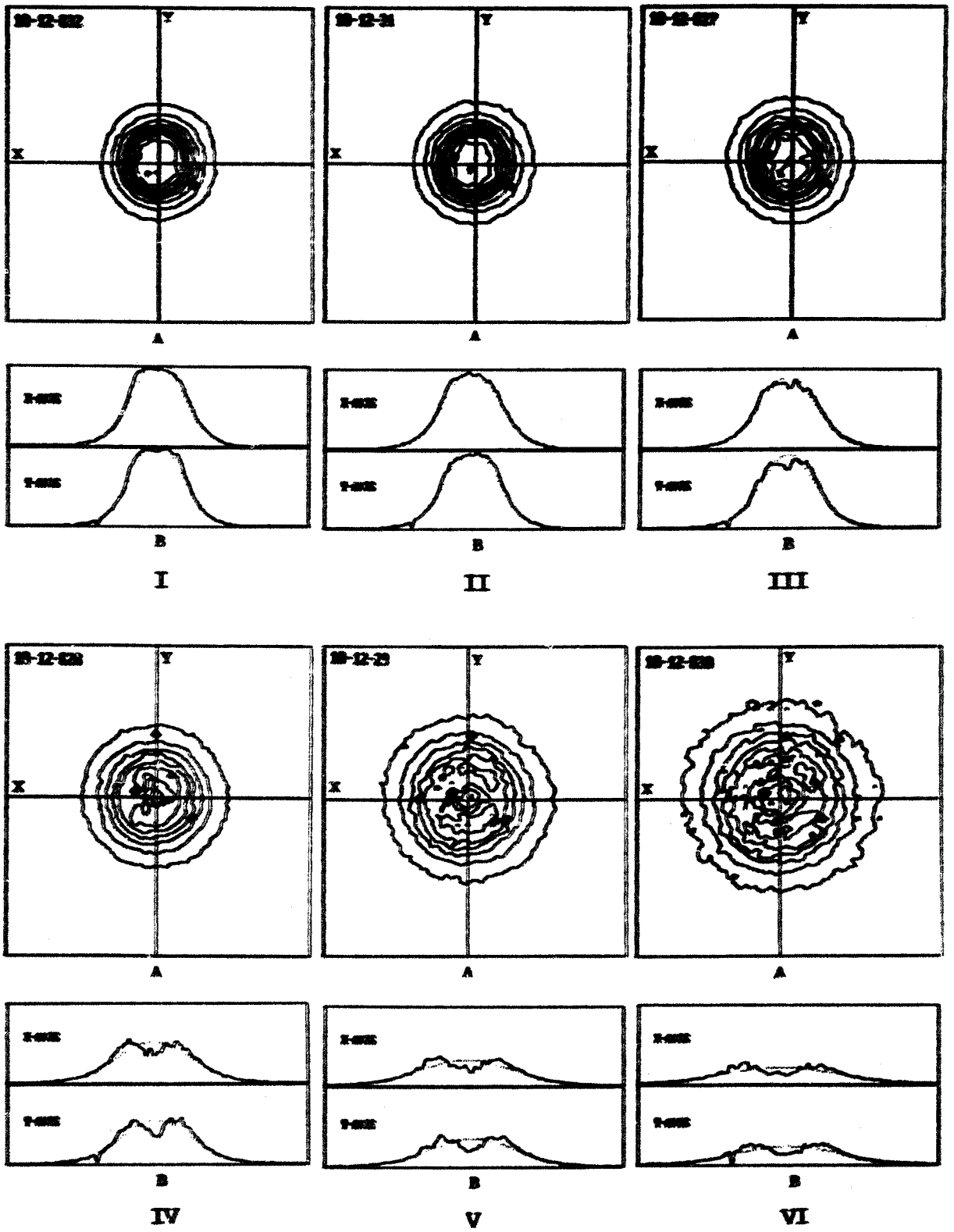

Figure 87. Contours and Profiles of Intensity Distribution of the Output of 49.4-cm-long 600-μm FO_3 #1 Recorded at Varying Distances From FO Output End: 4.48 mm (I), 4.63 mm (II), 5.13 mm (III), 7.13 mm (IV), 9.13 mm (V), and 11.13 mm (VI)

Intensity Distribution of 97.3-cm-long FO_2 #1 With LD RB883 as Source

Figure 88 shows the intensity distribution of a 97.3-cm-long FO_2 #1 200-μm FO with a loop. LD RB883 emitted 1 W of power into the FO that transmitted 0.82 W. The intensity distribution of the FO is recorded at four distances from its output end. The recordings are taken from the FO Output end at a distance of Z, where Z is 5.25 mm in I; 7.13 mm in II; 9.13 mm in III; and 11.13 mm in IV.

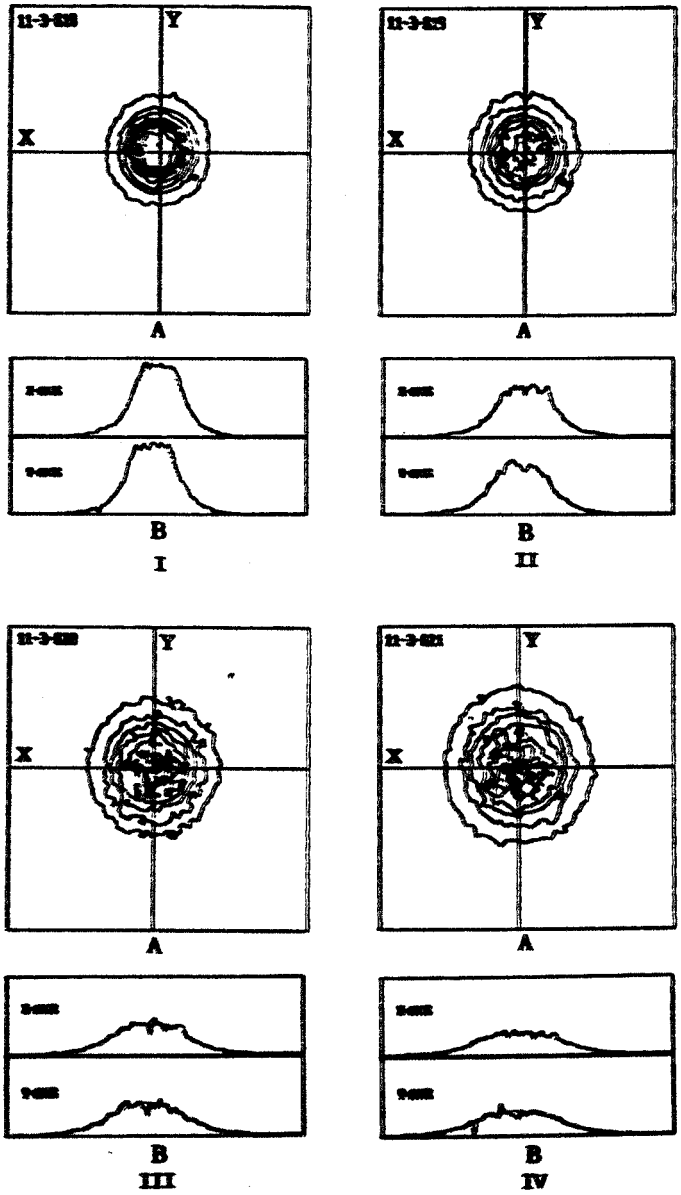

Figure 88. Contours and Profiles of Intensity Distribution of the Output of 97.3-cm-long 200-μm FO_2 #1 Recorded at Varying Distances From FO Output End: 5.25 mm (I), 7.13 mm (II), 9.13 mm (III), and 11.13 mm (IV)

The contours are relatively smooth at all distances. The intensity distributions of FO_2 #1 are smoother than those of FO_3 #1 (Figure 87) at each respective distance from the FO output ends (compare Figure 87 III to Figure 88 I; Figure 87 IV with Figure 88 II; Figure 87 V with Figure 88 III; and Figure 87 VI with Figure 88 IV). The intensity distributions of FO_2 #1 have no holes in their centers as do those of FO_3 #1 in Figure 87.

Specifications for FO_3 #1 and FO_2 #1

Table 7 lists specifications for FO_3 #1 with LD A840 as source and FO_2 #1 with LD RP883 as source. The specifications include the shot number, the distance from FO output end recorded, $1/e^2$ width, divergence, the correlation coefficient (CC), and the figure in which the contour and profile appear.

The results show:

- **Divergence.** Since the FO output beams are diverging, the $1/e^2$ widths increase as expected with increasing distance Z. Except for the first two divergences for FO_3 #1 and the first divergence for FO_2 #1, the FO divergences tend to stabilize at ~12° in the X direction and 10.3° in the Y direction for FO_3 #1, and ~7.5° in the X direction and 7.2° in the Y direction for FO_2 #1 (these are averages).

  If each of the profiles of FO_3 #1 at 5.13 mm and FO_2 #1 at 5.25 mm are compared to the respective FO profiles at 11.13 mm, the divergence for FO_3 #1 is 12° in the X, direction and 10.3° in the Y direction. The divergence for FO_2 #1 is 7.7° in both X and Y directions. The smallest divergence of the LD is in the Y direction.

- **Gaussian Fit of FO Beams.** For both FOs, CC decreases in value as Z increases except for the first distance. At all distances, the CCs are larger for the smaller-diameter-core FO_2 #1 than for FO_3 #1. The CC is larger for FO_2 #1, 4 mm farther from the end of the FO (at 11.13 mm) than for FO_3 #1 (at 7.13 mm). The smoother beam profiles and larger CC for the smaller-diameter core FO_2 #1 (Figure 88 and Table 7) over those of FO_3 #1 (Figure 87) are attributed to the increased number of bounces per unit length in the FO than the light makes in the smaller-diameter FO_2 #1.

Table 7. Beam Specifications for Two FOs at Different Positions From the End of Two FOs

SHOT	FO DIST	$1/e^2$ WIDTH X	$1/e^2$ WIDTH Y	DIVERGENCE X	DIVERGENCE Y	CORRELATION COEFFICIENT X	CORRELATION COEFFICIENT Y	FIG
(#)	(mm)	(mm)	(mm)	(deg)	(deg)			(#)
FO_3 #1 49.37 cm LONG								
10-12-S32	4.49	2.29	2.23			.999728	.999677	87 I
10-12-S31	4.63	2.44	2.34	26.6	20.1	.999837	.999779	87 II
10-12-S27	5.13	2.57	2.45	7.4	6.3	.999737	.999657	87 III
10-12-S28	7.13	3.42	3.17	12.0	10.2	.998578	.998214	87 IV
10-12-S29	9.13	4.28	3.92	12.1	10.6	.996457	.996611	87 V
10-12-S30	11.13	5.12	4.64	11.9	10.2	.993727	.994320	87 VI
FO_2 #1 100 cm LONG								
11-3-S18	5.25	2.00	2.08			.999686	.999684	88 I
11-3-S19	7.13	2.44	2.50	6.97	6.0	.999478	.999634	88 II
11-3-S20	9.13	3.09	3.20	9.23	9.9	.999005	.998805	88 III
11-3-S21	11.13	3.52	3.60	6.14	5.7	.998873	.998742	88 IV

Intensity Distribution of 101.2-cm-long FO_2 #2 With LD RP542 as Source

The intensity distribution of FO_2 #2, looped or straight, with varying length from 101.2 to 4.2 cm at different Z_1 distances from the FO output ends are shown in Figures 89 through 94. Correlation of the FO output intensity distribution is considered as the relative positions of the FO and LD outputs are changed (Figure 95).

Figures 89 and 90 show the beam contours and profiles of FO_2 #2 successively cut in half starting at 101.2 cm long. Figure 89 consists of recordings close (7.13 mm) from the FO output end; Figure 90 consists of recordings far (9.13 mm) from the FO output end. The recordings are taken of FO length Z in Figure 89 I through VI, where Z is 101.2 cm in I; 49.4 cm in II; 24.8 cm in III; 12.2 cm in IV; 6.8 cm in V; and 4.2 cm in VI.

The Z lengths are the same for Figure 90. The beam contours and profiles of FO_2 #2 close and far exhibit a hole in the center of the contour. The input ends of the FO in Figures 89 and 90 I and II were not moved relative to the LD outputs. The remaining four FO lengths in both figures are not correlated to each other or to the 101.2- and 49.4-cm-long FOs above because their inputs relative to the LD outputs were moved when the FOs were cut and polished. In general, the far profiles in Figure 90 have more high-frequency spatial components than the close profiles in Figure 89.

The correlations between the intensity distributions of the 101.2- and 49.4-cm-long FO_2 #2 are illustrated in Figures 91 and 92. The intensity distribution of the 101.2-cm-long FO is recorded at distance Z_1 from the FO output end with LD RP542 as source, where Z_1 in Figure 91 I is 5.74 cm; II is 7.13 cm; III is 9.13 cm; and IV is 11.13 cm.

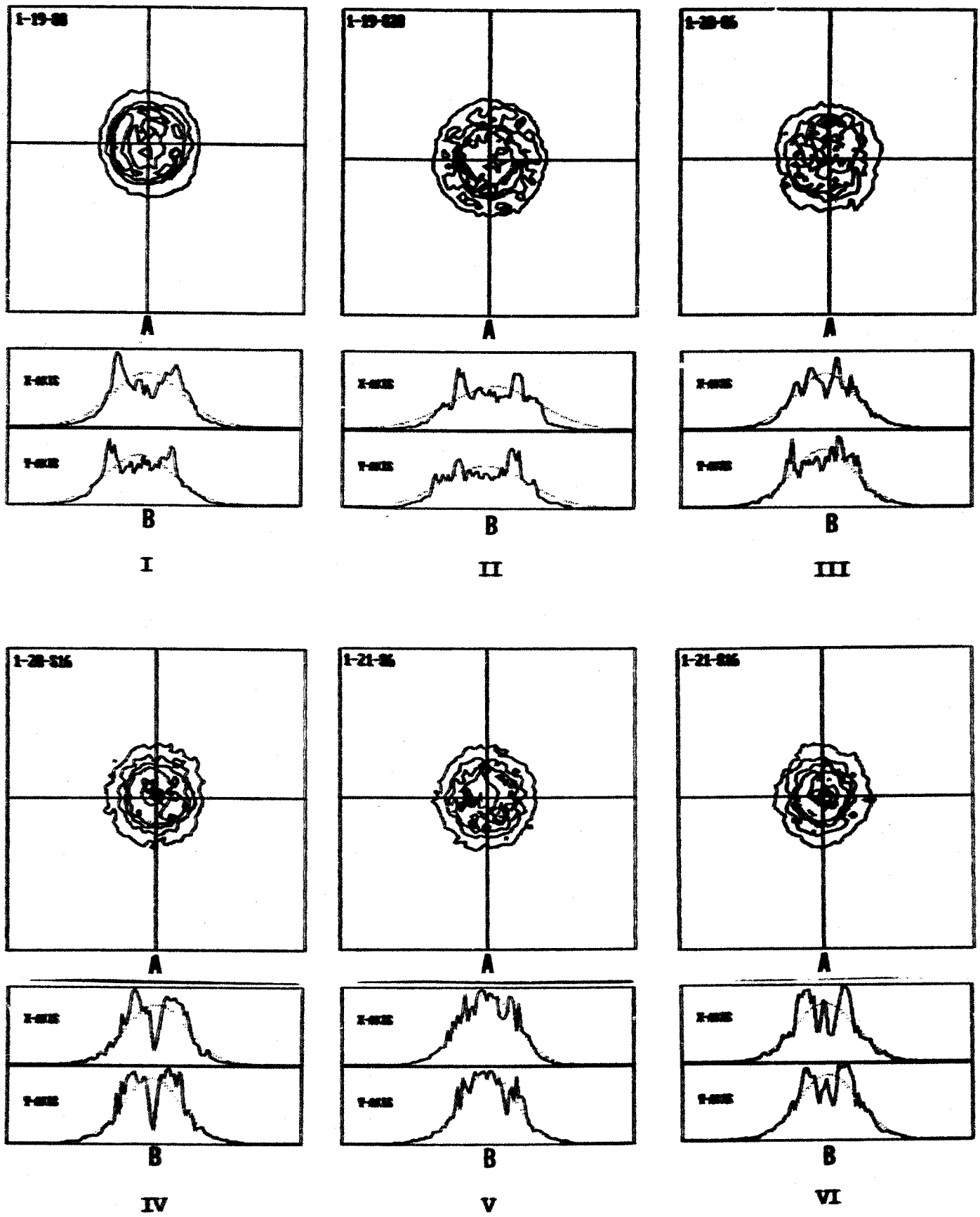

Figure 89. Contours and Profiles of Intensity Distribution of the Output of 101.2-cm-long 200-μm FO_2 #2 Recorded 7.13 mm From FO Output End After Successively Cutting in Half Five Times. FO is 101.2 cm long in (I), 49.4 cm (II), 24.8 cm (III), 12.22 cm (IV), 6.8 cm (V), and 4.2 cm (VI).

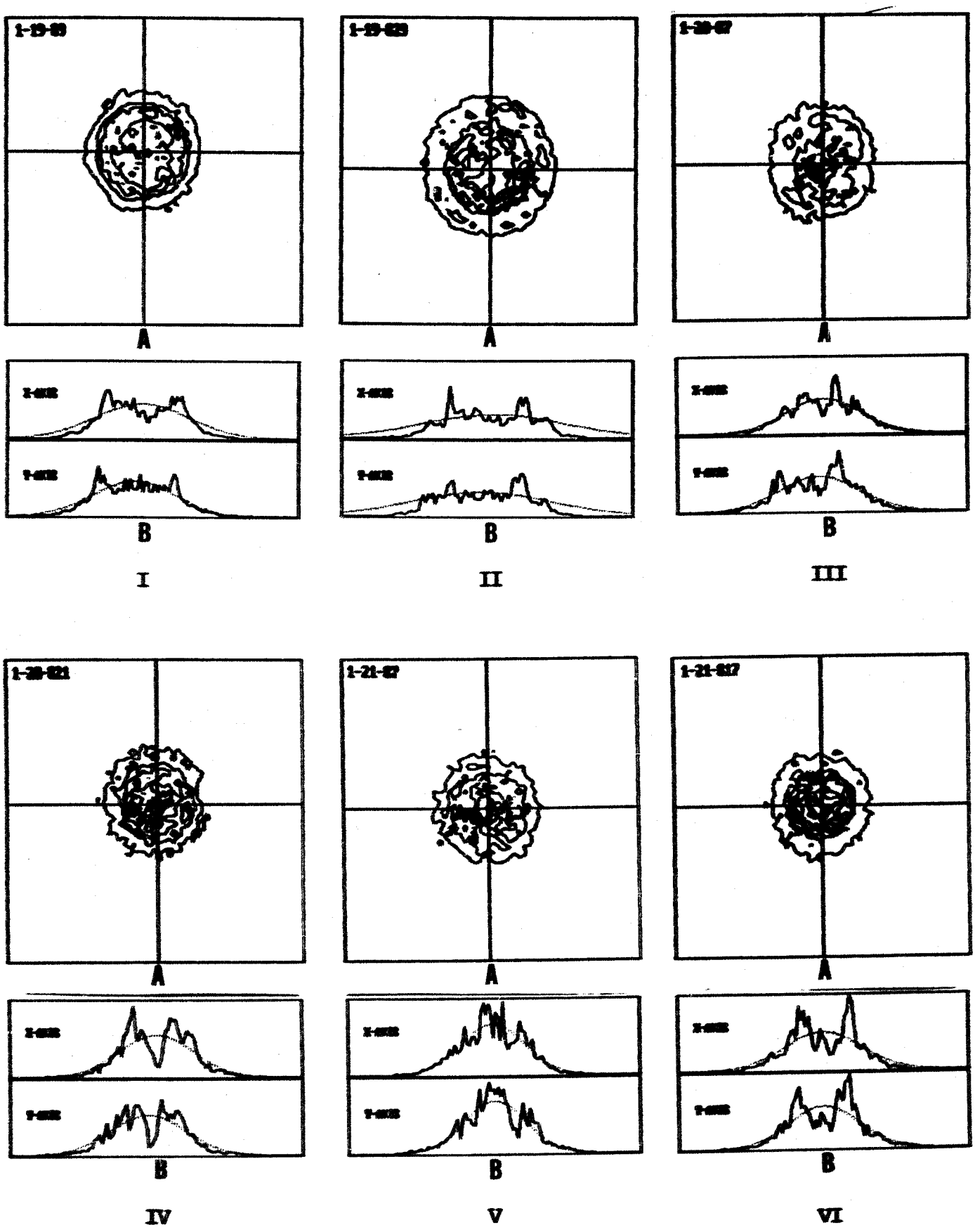

Figure 90. Contours and Profiles of Intensity Distribution of the Output of 101.2-cm-long 200-μm FO_2 #2 Recorded 9.13 mm From FO Output End After Successively Cutting in Half Five Times. FO is 101.2 cm long in (I), 49.4 cm (II), 24.8 cm (III), 12.2 cm (IV), 6.8 cm (V), and 4.2 cm (VI).

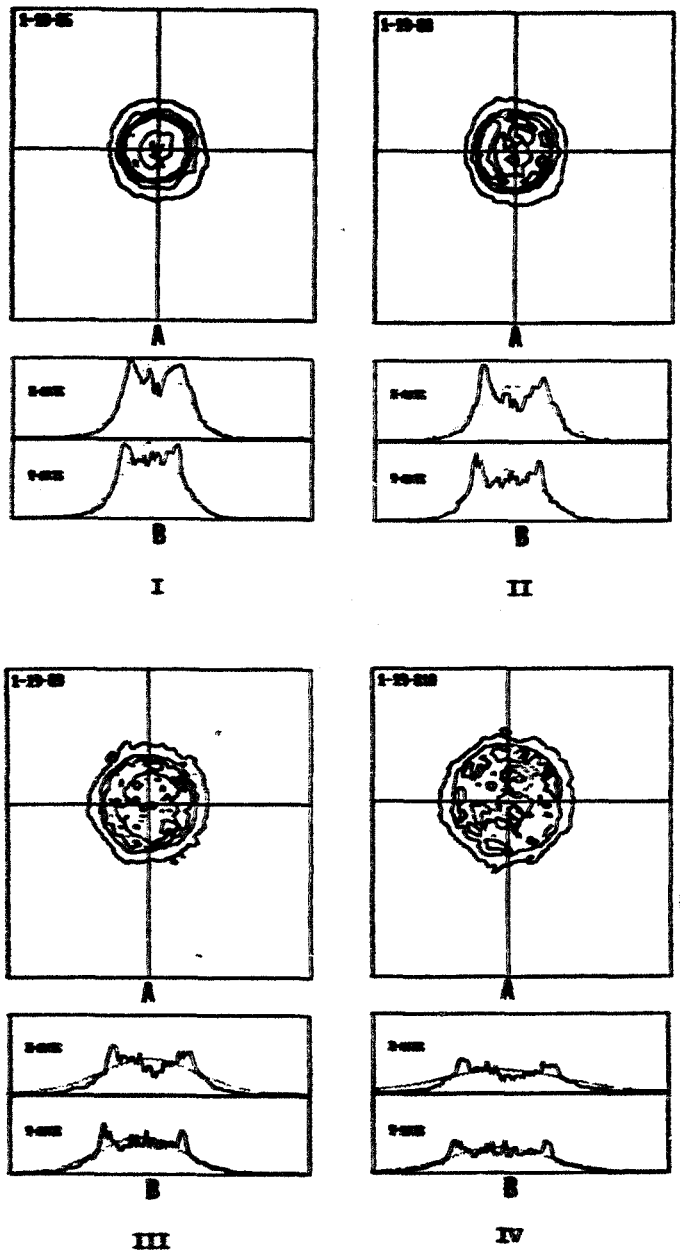

Figure 91. Contours and Profiles of Intensity Distribution of the Output of 101.2-cm-long 200-μm FO_2 #2 Recorded at Varying Distances From FO Output End: 5.74 mm (I), 7.13 mm (II), 9.13 mm (III), and 11.13 mm (IV)

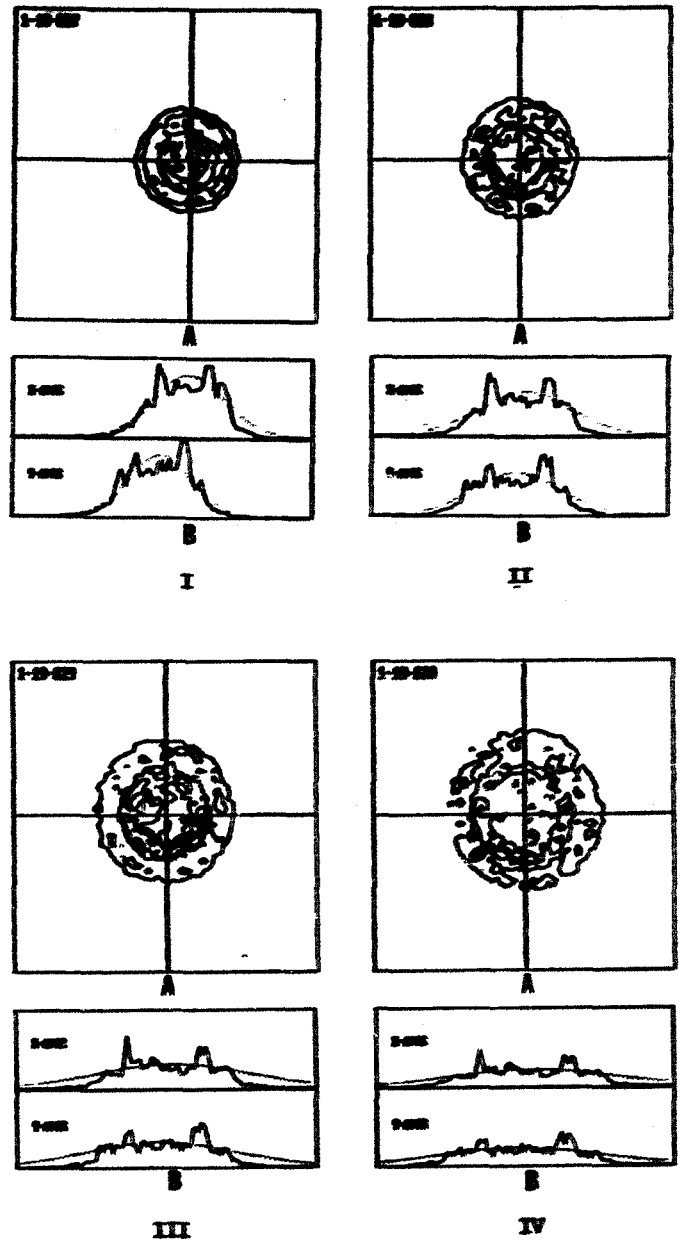

Figure 92. Contours and Profiles of Intensity Distribution of the Output of 49.4-cm-long 200-μm FO_2 #2 Recorded at Varying Distances From FO Output End: 5.74 mm (I), 7.13 mm (II), 9.13 mm (III), and 11.13 mm (IV)

For 49.4-cm-long FO_2 #2, Z_1 in Figure 92 I is 5.74 cm; II is 7.13 cm; III is 9.13 cm; and IV is 11.13 cm.

The depression in the center of the intensity distribution is evident at all Z directions for both FO lengths. The depth of the depression decreases with an increase in the Z_1 direction. The peaks in the intensity distribution of the corresponding record at the same Z_1 distance are somewhat similar.

Figure 93 shows the intensity distribution of the 24.8-cm-long FO_2 #2 recorded at distance Z_1 from the FO output end, where Z is the same as in Figures 91 and 92: 5.74 cm in I; 7.13 cm in II; 9.13 cm in III; and 11.13 cm in IV.

During the cutting and repolishing of the output end of FO_2 #2, the position of the input end of the F relative to LD output was changed. It is evident that the intensity distribution of the 24.8-cm-long FO does not correlate to those at the corresponding Z positions of the 49.4- or 101.2-cm-long FOs.

Figure 94 shows the intensity distributions of FO_2 #2 101.2 cm long, looped and straight, and 4.2 cm long recorded at distance Z_1 from the FO output end. The Z_1 distance is:

- 7 mm in I and 9 mm in IV for the 101.2-cm-long FO looped
- 7.13 mm in II and 9.13 mm in V for the 101.2-cm-long FO straight
- 7.13 mm in III and 9.13 mm in VI for the 4.2-cm-long FO straight.

The Gaussian fit is much better for the looped FO than for the two straight FOs. The short straight FO had higher spatial frequency than the two long straight FOs.

Figure 95 shows the effect of small motion of the input end of the FO_2 #2 relative to LD RP542 output on the intensity distribution out of FO_2 #2 at a Z distance of 7.13 mm from the FO output end. In Figure 95, the FO input is aligned in I; moved 8.5 μm in X direction in II; realigned in III; moved 8.5 μm in Y direction in IV; and realigned in V relative to the LD output.

A 8.5-μm motion of the FO input relative to the LD output in Figure 95 I when compared to II shows that large-scale structure is the same; this is shown by a depression in the center of the intensity distribution. The finer, high spatial frequencies are different. Realigning the FO does not reestablish the contours and profiles out of the FO.

A motion of 8.5 μm in the Y direction (Figure 95 IV) and repositioning the FO (Figure 95 V) as shown in Figure 95 III fails to reestablish the fine structure of the contours or profiles out of the FO.

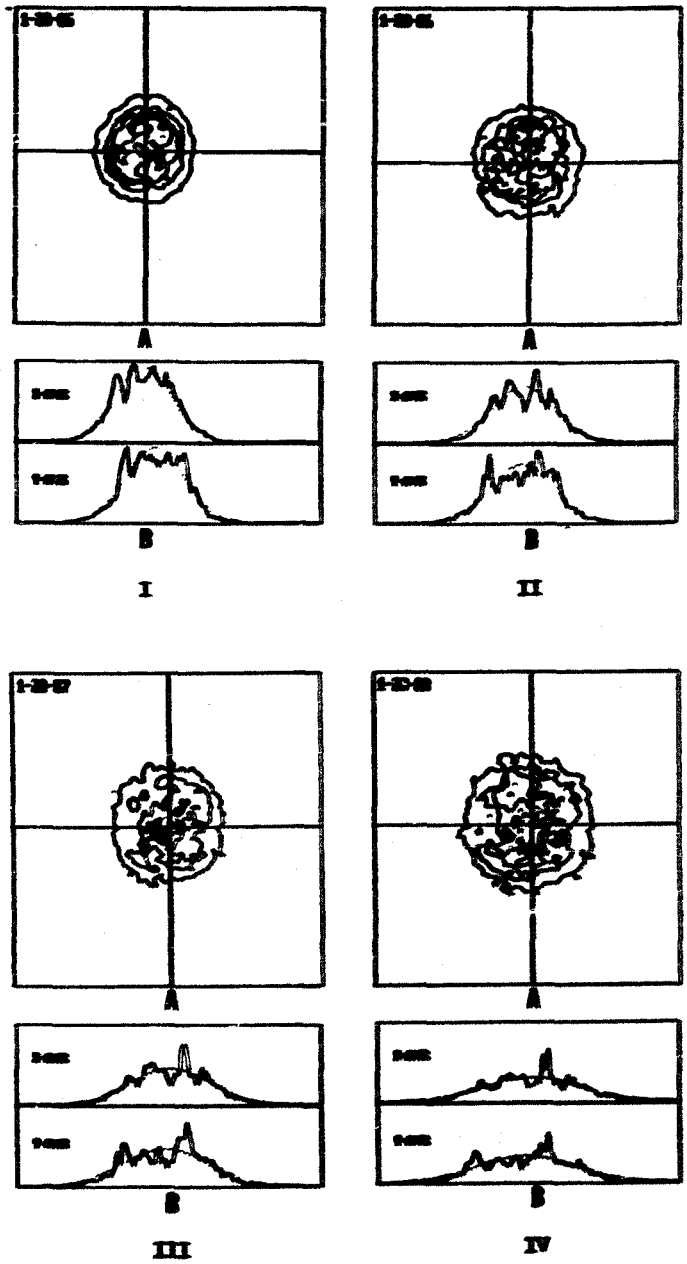

Figure 93. Contours and Profiles of Intensity Distribution of the Output of 24.8-cm-long 200-μm FO_2 #2 Recorded at Varying Distances From FO Output End: 5.74 mm (I), 7.13 mm (II), 9.13 mm (III), and 11.13 mm (IV)

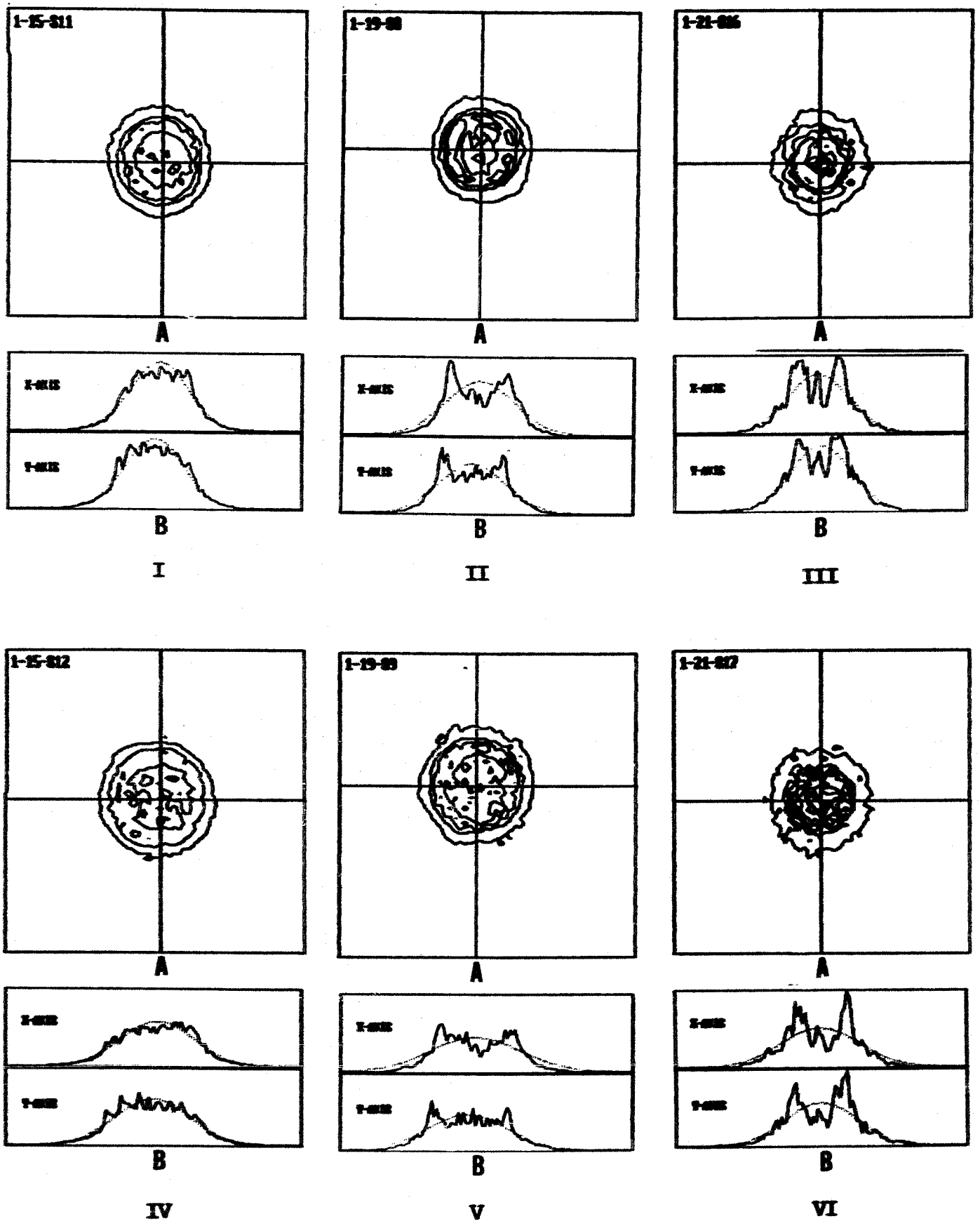

Figure 94. Contours and Profiles of Intensity Distribution of the Output of 101.2-cm-long 200-μm FO_2 #2 Looped (I & IV) and Straight (II & V) and 4.2-cm-long Straight (III & IV) Recorded Close at 7.13 mm (I, II, & III) From FO Output End

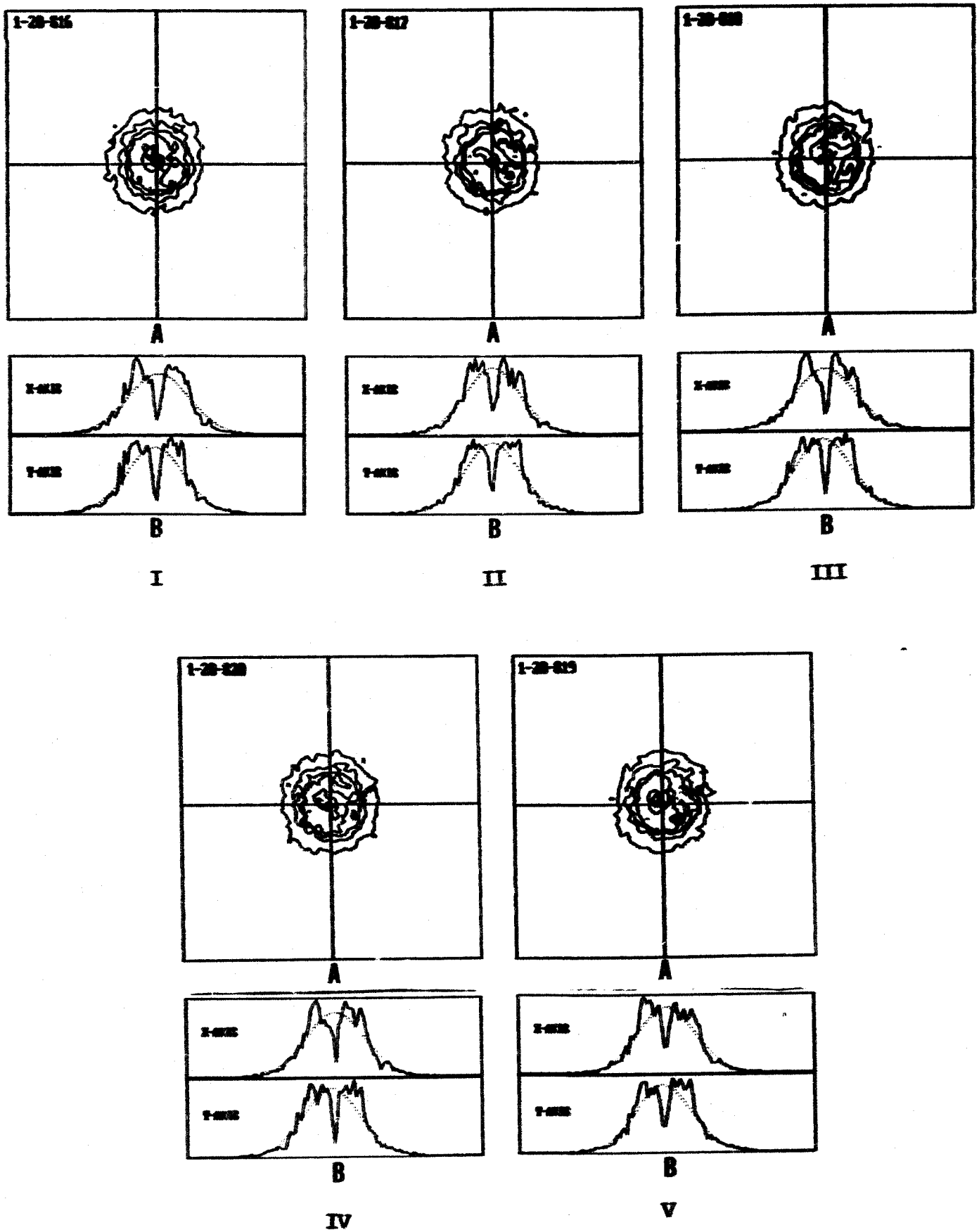

Figure 95. Contours and Profiles of Intensity Distribution of the Output of 12.2-cm-long 200-μm FO_2 #2 Aligned to SDL RP542 and Then Misaligned in Both X and Y Axes: Aligned in (I), 8.5 μm Misaligned in X Axis in (II), Aligned in (III), 8.5 μm Misaligned in Y Axis in (IV), and Aligned in (V)

Specifications for FO_2 #2

Table 8 lists specifications for FO_2 #2 that include the shot number, the FO length, the distance from FO output end recorded, $1/e^2$ widths, divergences, CC, and the figure in which the contours and profiles appear.

For Shots 1-15-S11 and 1-15-S11, the FO is looped; for all remaining shots, the FO is straight.

The divergences of the 101.2-cm-long FO_2 #2 looped and straight at $Z_1 = 9$ and 9.134 mm (Z_1 is the distance from FO output end) are comparable (compare Shot 1-15-S13 with Shot 1-19-S9). As the Z_1 increases to 11.134 mm, the divergences increase and the Gaussian fit CC decreases. The divergences of the 49.4-, 24.8-, 12.2-, 6.8- and 4.2-cm-long FOs are erratic. The profiles do not fit a Gaussian very well (see figure numbers listed in Table 8). All these shots show large peaks that are far removed from the best Gaussian fit.

Figure 96 shows the intensity distribution of a 9.04-mm-long 100-μm-dia FO stub recorded at different distances from the FO output end with LD RP542 emitting 1 W. Table 9 and Figure 96 I through IV show the specifics of the FO stub.

The 100-μm-dia FO used in the stub is a Spec Tran #420 FO with the following specifications:

- NA is 0.27 to 0.3
- Step index
- Glass on glass
- Attenuation: 3 to 5 dB/km

Section A of Figure 96 I through IV shows that the intensity contours are not smooth; they look like speckled patterns. The X and Y profiles in Section B also show large intensity fluctuations of the beam that can vary by a factor of 3 times over very short lateral displacement across the FO stub.

The low (68.2%) transmission of the stub suggests that its NA is less than the NA of the Ensign-Bickford FOs; however, the divergence to $1/e^2$ widths listed in Table 9 at 7.13 and 11.13 mm from the FO output end is $>22°$. This gives an NA of >0.37. Table 9 shows that CC is not large; this indicates that the Gaussian fit is not very good.

4.2.4 Summary

In Section 4.2 the performance of couplers, which include GRIN lenses, FOs, FO and GRIN lens combinations, and FO and spherical lens combination, were described.

GRIN Lens Transmission

The 0.23-, 0.25-, 0.29-, 0.5A-, and 0.5B-pitch GRIN lenses transmitted 95%, 97%, 95.5%, 95.5%, and 97.5% when LD A322 was emitting 400 mW as the source, and 97%, 97%, 96%, 97%, and 98% when LD A841 was emitting 2 W as the source, respectively. For a 0.23-pitch GRIN lens, the energy collected by a 0.368-cm-dia aperture was down by 76.4% when the aperture was 20 mm from the GRIN lens.

FOs Transmission

FO_4 #1 and FO_3 #1, SDL LDs Sources

The 1000-μm-dia FO_4 #1 and 600-μm-dia FO_3 #1 butt-coupled to:

- LD A322 emitting 0.4 W, transmits 77% and 76.4%, respectively
- LD A841 emitting 1.9 W, transmits 82% and 81.5%, respectively
- 0.5A-pitch GRIN lens in front of LD A322 emitting 0.4 W, transmits 79% and 78%, respectively
- 0.5A-pitch GRIN lens in front of LD A841 emitting 1.9 W, transmits 82% and 81.5%, respectively
- 0.5B-pitch GRIN lens in front of LD A322 emitting 0.4 W, transmits 77% and 78%, respectively
- 0.5B-pitch GRIN lens in front of LD A841 emitting 1.9 W, transmits 80% and 80%, repsectively

The 600-μm FO_3 #1 transmits 10% more LD power when SDL-2410-H1 A322 is the source vs. when the same model number SDL-2410-H1 B126 LD is the source. The transmissions of the FOs are limited because their NAs are smaller than the divergence of the LDs.

FO_5 #1, FO_3 #4, FO_2 #1, and FO_1 #1

For LD RP542 butt-coupled to within 25 μm of the LD output mirror and emitting

- 1 and 2 W, the transmissions of FO_3 #4 are 86.9% ± 0.3%
- 1 and 2 W, the transmissions of FO_5 #1 are 86.9% ± 0.3%
- 1 and 2 W, the transmissions of FO_2 #1 are 86.9% to 90.2% and 86%, respectively
- 1 W, the transmissions of FO_1 #1 are 80% to 82.5%, respectively.

Table 8. Beam Specifications for 200-μm FO_2 #2 of Different Lengths

SHOT (#)	FO DIST (mm)	FO LENGTH (cm)	I/e^2 WIDTH X (mm)	I/e^2 WIDTH Y (mm)	DIVERGENCE X (deg)	DIVERGENCE Y (deg)	CORRELATION COEFFICIENT (X)	CORRELATION COEFFICIENT (Y)	FIG (#)
1-15-S11	7.00	101.2	2.65	2.68	-	-	.998962	.998889	94 I LOOP
1-15-S12	9.00	101.2	3.32	3.35	9.5	9.5	.998594	.990385	94 IV LOOP
1-19-S5	5.74	101.2	2.50	2.45	-	-	.998962	.998889	91 I
1-19-S8	7.13	101.2	3.18	3.06	9.7	8.7	.995097	.996498	89 I 91 II 94 II
1-19-S9	9.13	101.2	4.29	3.71	9.7	9.2	.994603	.996174	90 I 91 III 94 IV
1-19-S10	11.13	101.2	5.58	4.43	17.9	10.2	.993538	.994444	91 IV
1-19-S27	5.74	49.4	3.16	2.83	-	-	.997472	.996809	92 I
1-19-S28	7.13	49.4	4.09	3.07	13.1	3.4	.997033	.996058	89 II 92 II
1-19-S29	9.13	49.4	6.72	6.61	33.3	41.5	.994611	.995036	90 II 92 III
1-19-S30	11.13	49.4	7.36	7.47	9.1	12.4	.992552	.993417	92 IV
1-20-S5	5.74	24.8	2.48	2.54	-	-	.998721	.998215	93 I
1-20-S6	7.13	24.8	2.00	2.08	-	-	.998098	.997368	89 III 93 II
1-20-S7	9.13	24.8	3.50	3.72	20.6	22.3	.996828	.995076	90 III 93 III
1-20-S8	11.13	24.8	4.35	4.37	12.0	9.2	.995634	.994719	93 II
1-20-S16	7.13	12.2	2.01	2.63	-	-	.993888	.993389	89 IV 95 I
1-20-S21	9.13	12.2	3.40	3.43	19.2	11.3	.990560	.993661	90 IV
1-20-S22	11.13	12.2	4.15	4.33	10.6	12.7	.992976	.993284	
1-21-S6	7.13	6.8	2.54	2.46	-	-	.998476	.998055	89 V
1-21-S7	9.13	6.8	3.01	2.05	6.7	-	.997187	.996025	90 V
1-21-S8	11.13	6.8	3.57	3.27	8.0	17.0	.994849	.994126	
1-21-S16	7.13	4.2	2.75	2.76	-	-	.994622	.997354	89 VI 94 III
1-21-S17	9.13	4.2	3.62	3.25	12.3	7.0	.991884	.992742	90 VI 94 VI
1-21-S18	11.13	4.2	5.93	4.39	30.0	15.9	.985742	.990206	
1-20-S17	7.13	12.2	2.51	2.54	-	-	.995703	.996097	95 II
1-20-S18	7.13	12.2	2.66	2.52	-	-	.993949	.995126	95 III
1-20-S19	7.13	12.2	2.62	2.56	-	-	.996134	.996018	95 IV
1-20-S20	7.13	12.2	2.66	2.58	-	-	.995747	.994889	95 V

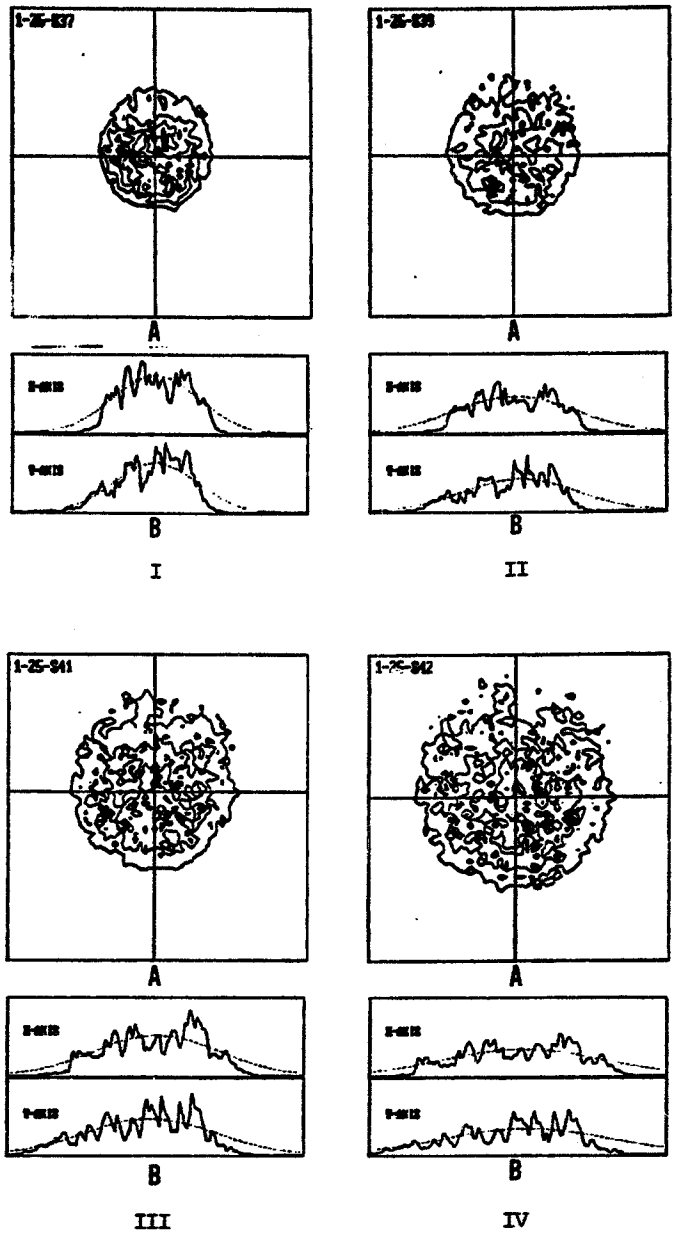

Figure 96. Contours and Profiles of Intensity Distribution of the Output of 9.04-mm-long SDL 100-μm FO Stub Recorded at Varying Distances From FO Output End: 5.74 mm (I), 7.13 mm (II), 9.13 mm (III), and 11.13 mm (IV)

Table 9. Beam Specifications for 9.0-mm-long, 100-μm FO Stub at Different Distances From Its Output End

SHOT	FO DIST	$1/e^2$ WIDTH X	$1/e^2$ WIDTH Y	DIVERGENCE X	DIVERGENCE Y	CORRELATION COEFFICIENT (X)	CORRELATION COEFFICIENT (Y)	FIG
(#)	(mm)	(mm)	(mm)	(deg)	(deg)			(#)
1-25-S37	5.74	3.84	3.72			.997499	.995572	96 I
1-25-S39	7.13	5.32	5.11	28.0	26.5	.997168	.994898	96 II
1-25-S41	9.13	5.68	5.97	5.1	12.1	.995628	.994010	96 III
1-25-S42	11.13	7.36	7.75	22.8	24.0	.994610	.993158	96 IV

For a 200-μm FO_2 #1 butt-coupled to within 25 μm of the output mirror of

- LD BM498 emitting 0.2, 1, and 3.4 W, the transmissions are 85%, 87.4%, and 80%, respectively
- LD RB883 emitting 0.2 and 1.6 W, the transmissions are 85% and 81.8%, respectively
- LD BN968 emitting 1 and 2 W, the transmissions are 82% and 79%, respectively.

FO_1 #1, MDAC/OEC as Sources

With MDAC/OEC LDs E204A-3, E204A-6, E220A-1, and E220A-2 as sources, the transmissions of a 100-μm-dia FO_1 #1 are 56%, 62%, 52%, and 55%, respectively. The low transmission is attributed to large LD divergence.

LD Beam Steering

LD beam steering with the 200-μm aperture LD BN968 emitting 1 and 2 W is monitored by measuring the transmission of a 200-μm FO_2 #1. The beam steered 15 μm in the Y direction perpendicular to the 200-μm LD aperture, and 50 μm in the X direction along the 200-μm LD aperture.

P-C Spherical Lens

With LD BN968 as source, the transmissions of the P-C spherical lenses coupled to 600-, 400-, 200-, and 100-μm FOs are 92% ± 0.1%, 91.6% ± 0.3 %, 91.5% ± 0.8 %, and 91.9% ± 1%, respectively.

Beam Intensity Distribution

GRIN Lens

With LD A322 emitting 0.4 W of power, the beam profile transmitted through the 0.23-pitch GRIN lens at a distance of 20 mm exhibits two well-defined, sharp-peaked lobes in the X direction (perpendicular to the long LD aperture) and seven not-too-well-defined peaks in the Y direction (along the long LD aperture). In other words, the beam profile is not smooth.

Fiber Optics

With LD A840 emitting 0.6 W of power into several 100-mm-long, 600-μm-dia FOs, a dip in the center of the intensity distribution is observed. Structure in the beam varies as to whether the FO is straight or in a 15.2-cm × 21.6-cm loop. Different FOs exhibit similar and unique structures in the transmitted beam. The similar structure is attributed to originating in the LD; the unique structure is attributed to the FO modifying the LD profile.

With LD RB883 as source, the beam transmitted through 200-μm-dia FO_2 #1:

- Has less structure
- Is more uniform
- Fits a Gaussian better
- Has smaller divergence (between 12° and 18° full $1/e^2$ width at 7.1 and 9.1 mm) than the 600-μm FO_3 #1.

Divergence

With LD A840 emitting 0.6 W of power into 1-m-long, 600-μm FO, the divergence in the X direction (perpendiclar to the long LD aperture) is 14.8° at 5.13 mm from the FO end and stabilizes to ~22.0° at 7.13 mm. As the 49.4-cm-long, 600-μm-dia FO_3 #7 is cut shorter, the full-width angle to $1/e^2$ width divergence increases from 23.4° to 46° at FO lengths of 49.4 cm and 3.12 mm.

The divergence of a 1-m-long, 200-μm FO with a 15.2-cm × 21.6-cm loop positioned at mid-distance is comparable to that of the straight FO.

4.3 Beam Interrupter-Coupler

In this section, the X and Y dimensions of the LD beam transmitted through four different-diameter FOs coupled to Lens P-C is determined. The LD optical power transmitted through a 3.8-mm aperture as a function of angular rotation of an in-line prism is measured.

4.3.1 P-C Lens Collimation for Different FOs as Input

Figures 97, 99, and 101 show the X dimensions of the LD beams with LD RP542 emitting 0.5, 1, and 1.8 W, respectively, transmitted through different-diameter FOs and then through a collimating P-C lens plotted as functions of distance from the lens surface. Figures 98, 100, and 102 show the Y dimension of the LD beam emitting 0.5, 1, and 1.8 W, respectively, transmitted through different-diameter FOs and then through a collimating P-C lens plotted as functions of distance from the lens surface. Both directions are perpendicular to the optical axis of Lens P-C.

The Gaussian fit of the intensity of the LD beam transmitted by Lens P-C is given by:

$$I = I_o e^{\frac{-2r^2}{w^2}}, \tag{32}$$

where

I_o = intensity at r = 0
r = radial dimension
w = LD beam waist through Lens P-C.

The radial dimension is given as:

$$r = w\left[-\frac{(\ln I/I_o)}{2}\right]^{1/2}. \tag{33}$$

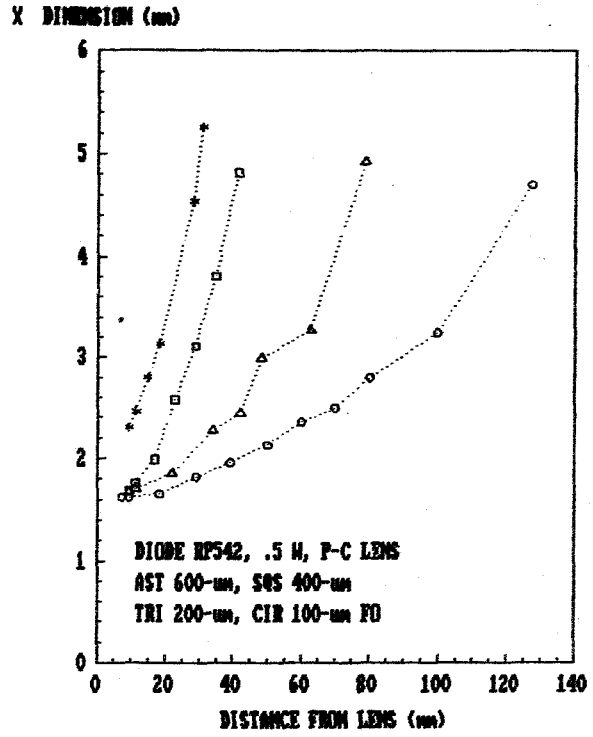

Figure 97. X Dimension of LD Beam Emitting 0.5 W Transmitted Through 600-, 400-, 200-, and 100-μm FOs vs. Distance From the P-C Lens

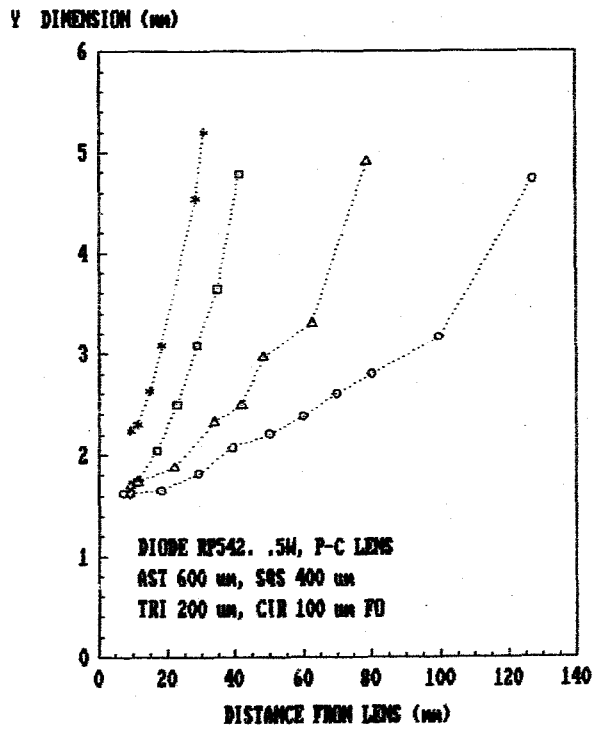

Figure 98. Y Dimension of LD Beam Emitting 0.5 W Transmitted Through 600-, 400-, 200-, and 100-μm FOs vs. Distance From the P-C Lens

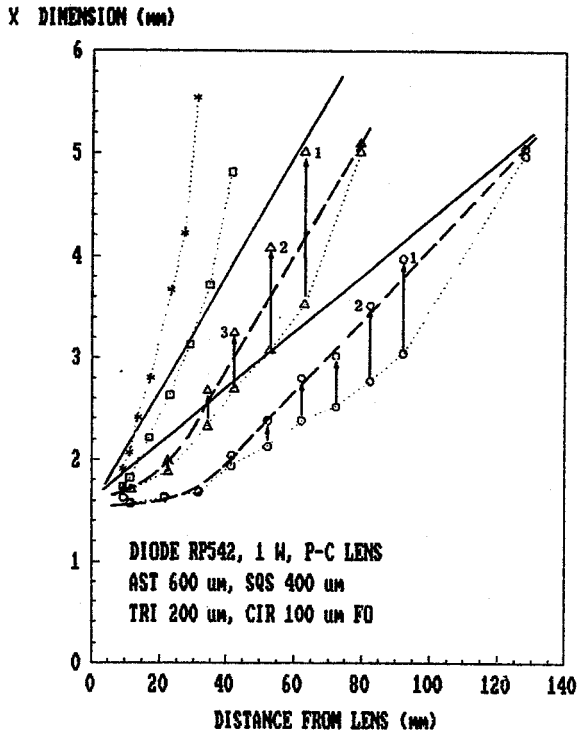

Figure 99. X Dimension of LD Beam Emitting 1 W Transmitted Through 600-, 400-, 200-, and 100-μm FOs vs. Distance From the P-C Lens

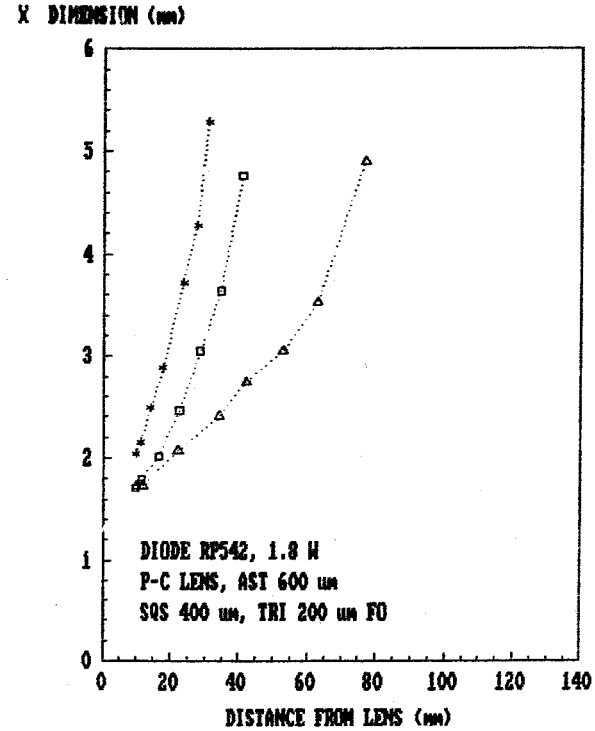

Figure 101. X Dimension of LD Beam Fmitting 1.8 W Transmitted Through 600-, 400-, 200-, and 100-μm FOs vs. Distance From the P-C Lens

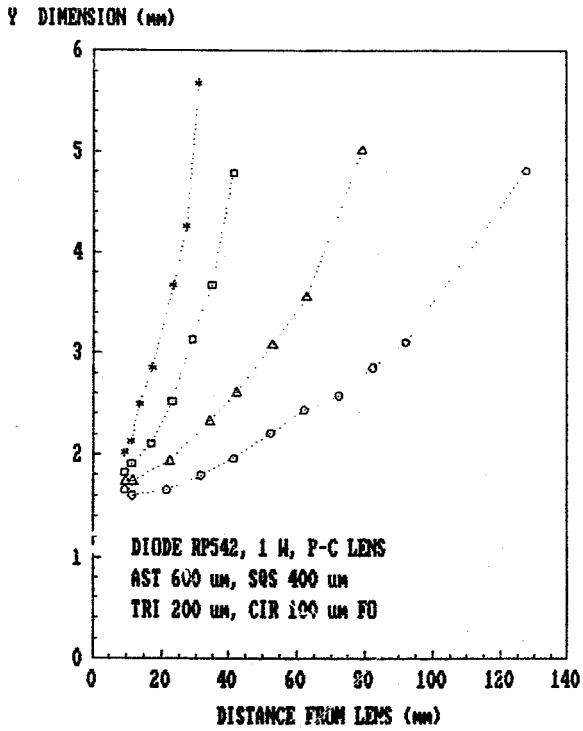

Figure 100. Y Dimension of LD Beam Emitting 1 W Transmitted Through 600-, 400-, 200-, and 100-μm FOs vs. Distance From the P-C Lens

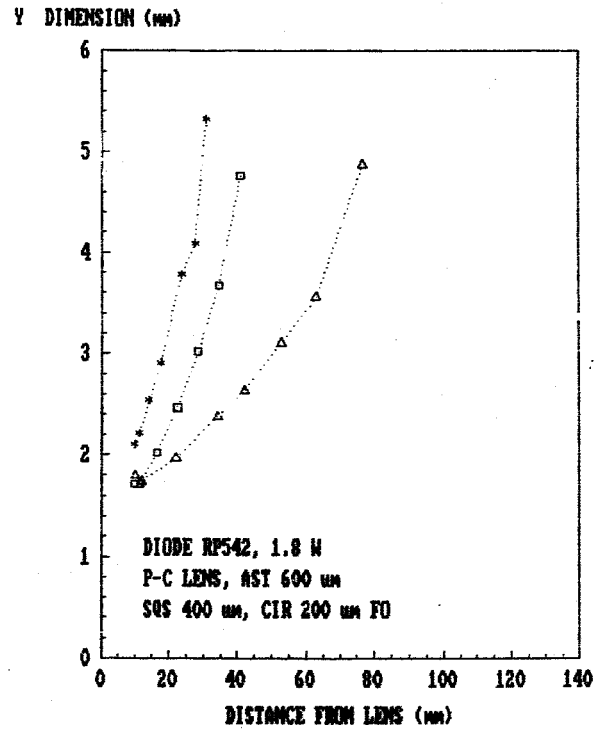

Figure 102. Y Dimension of LD Beam Emitting 1.8 W Transmitted Through 600-, 400-, 200-, and 100-μm FOs vs. Distance From the P-C Lens

The X and Y dimensions are determined by locating the first pixel on either side of beam maximum, which reads zero output intensity of the profile through the centroid of the intensity output of the P-C lens. The X or Y dimension is the number of pixels between the two pixel recording zero intensity times 28 μm/pixel. For the camera at d_{LC} minimum, its response is adjusted using neutral-density filters in front of the camera until its response is 100%. As d_{LC} increases, the intensity $I_o(d_{LC})$ decreases; this causes a bias in the X or Y dimension. Since I_o decreases with increasing d_{LC}, the first pixels to record zero on either side of $I_o(d_{LC})$ are at larger intensities relative to $I_o(d_{LC})$ taken at a closer position. The bias is removed by determining $r(d_{LC})$ at each d_{LC} and ratioing $r(d_{LC})$ to the r value of 1.67 W when the camera is 100% [using $I_o = 256$ and $I = 1$ in Eq (33)].

The smaller the I_o, the larger the correction factor. Since the P-C lens intensity distribution curves do not approximate a Gaussian very well, larger errors in the correction factor exist for the intensity distribution with the smaller I_o.

For the 100- and 200-μm FOs, the new unbiased X values in Figure 99 are the CIR and TRI to which the arrows point. The long dashed lines are through the corrected X values with Points 1, 2, and 3 (TRIs) and Points 1 and 2 (CIRs) discriminated against because of their low I_o values. The corrected X values have a limiting P-C lens full-angle divergence of 2.0° and 3.3° for the 100- and 200-μm FOs. The corrected values for X are larger for the 200-μm FO than for the 100-μm FO, especially at Points 1 and 2.

The solid lines in Figure 99 are for θ_a of 12.8° and 13.7° [obtained from $d_{LC} = 0$ in Eq (17)] out of the 100- and 200-μm FOs at an X of 1.79 and 2.05 mm for $d_{LC} = 10$ mm in Eq (17). The limiting full-angle divergence is 1.64° and 3.27° for the 100- and the 200-μm FOs and P-C lens combination. This approximation predicts a 19.6% and 0.3% smaller divergence for the 100- and the 200-μm FOs, respectively. The main difference in the results is that there is more disagreement in the X dimension at the largest d_{LC} measured for the 200-μm FO than for the 100-μm FO. At very large distances, it appears that the approximation is best for the larger-diameter FO.

For a specific FO, the shape of the beam in the X and Y dimensions is independent of the LD output optical power level. The slopes of the beam X and Y dimensions vs. distance d_{LC} from the lens decrease with the decrease in FO diameter.

For a 4-mm-dia cell diameter, the working distance between the cell and the FO for the cell to collect all the energy increases with the decrease in FO diameter as follows: from nominally 25, 35, 68, and 110 mm for the 600-, 400-, 200-, and 100-μm-dia FOs, respectively.

4.3.2 Transmission Through Aperture as Prism Rotates

Figure 103 shows the percent of LD optical power transmission through a 3.8-mm-dia aperture for three distances d_{LA} between the P-C lens and aperture as a function of prism P_1 (Figure 16) angular displacement. The LD RP542 is emitting 1 W of power. With the prism aligned, the aperture transmits 96.1% of the LD power at the shortest distance $d_{LA} = 52.0$ mm. A rotation of 85 min or 1.42° reduces the power by 16.8%, or to 80% (see SQS data in Figure 103).

With the prism aligned, the aperture transmits 91.7% of the LD power at the intermediate distance $d_{LA} = 67.8$ mm. A rotation of 32 min or 0.53° reduces the power by 12.8%, or to 80% (see AST data in Figure 103).

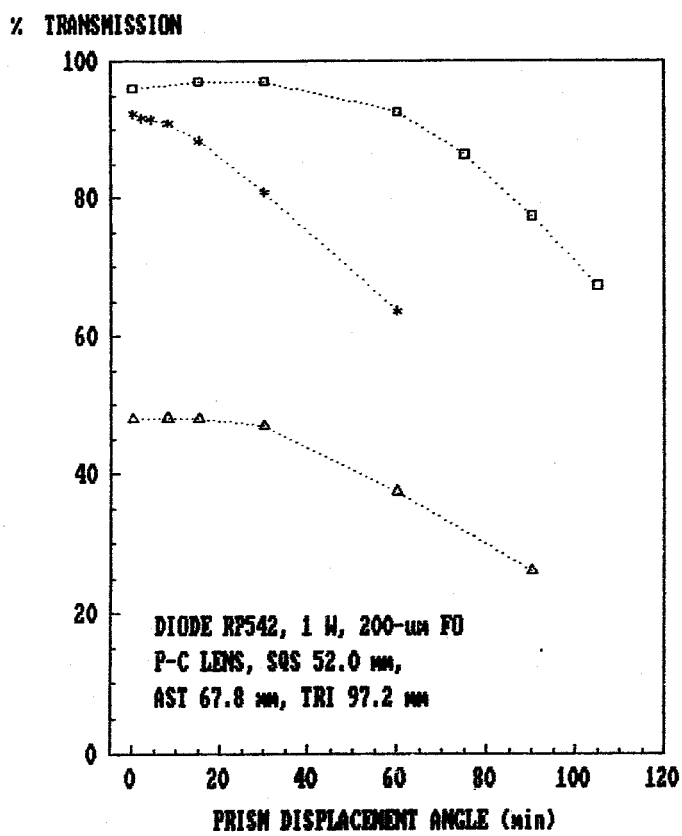

Figure 103. Transmitted LD Output Optical Power Through 3.8-mm Aperture vs. Prism Angular Displacement for LD Beam Collimated by 94.5-cm-long, 200-μm-dia FO_2 #1 and P-C Lens Combination With Aperture at 52.0-, 67.8-, and 97.2-mm Distance From the P-C Lens

With the prism aligned, the aperture transmits 47.8% of the LD power at the longest distance d_{LA} = 97.2 mm. A rotation of 32 min or 0.53° reduces the power by 3.3%, or to 46.2% (see TRI data in Figure 103). A rotation of ~50 min or 0.83° reduces the power by 16.8%, to 39.8%. A larger rotational tolerance exists for the shortest distance d_{LA} from the lens = 52 mm (SQS data in Figure 103).

4.4 PVA GaAs Cells

The data of the 1-V monolithic cell and the 2-, 10-, and 16-V hybrid PVA GaAs cells to be presented in this section include:

- Electrical power vs. resistance curves for different LD optical power
- I vs. V curves for different LD optical power
- Optimum R_P vs. LD optical power
- Efficiency vs. LD optical power
- Fill factor vs. LD optical power.

The measurements are made with a 600-μm-dia FO_3 #1, butt-coupled to an SDL-2450-H1 500-mW LD. The cell is positioned at a distance d_1 from the FO output end. The distance d_1 is such that the diameter of the cell matches the diameter D of the cone of light defined by the FO NA (0.37) specified by the manufacturer to its 5% level relative to zero, i.e., 95% of the light emitted by the FO is in diameter D.

4.4.1 Electrical Power

The electrical power generated by 1-, 2-, 10-, and 16-V PVA GaAs cells as a function of load resistance will be described for different LD optical power transmitted through 600-μm FO_3 #1 incident on the cells.

1-V Cell #10

Figure 104 shows the electrical power generated by the 1-V cell #10 as a function of load resistance for eight input LD optical powers. For this measurement, the voltage across the cell is taken at the cell pin interface, and the resistance value of the load is measured from one pin of the cell external to the cell to the other pin; this takes into account the resistance of the resistor and all the lead wire.

The erratic variations in the data are attributed to inaccurate resistance determinations. For the 1-V cell, the total resistance is very low. There is a decrease in the resistance R_P at the maximum cell electrical power P_m from ~5.5 to 1.2 Ω as the input LD optical power is increased from 300 to 1500 mW. The width of the curves near 90% of the peak value decreases from ~2.4 to 0.75 Ω in a monotonic manner as the input LD optical power increases from 300 to 1500 mW.

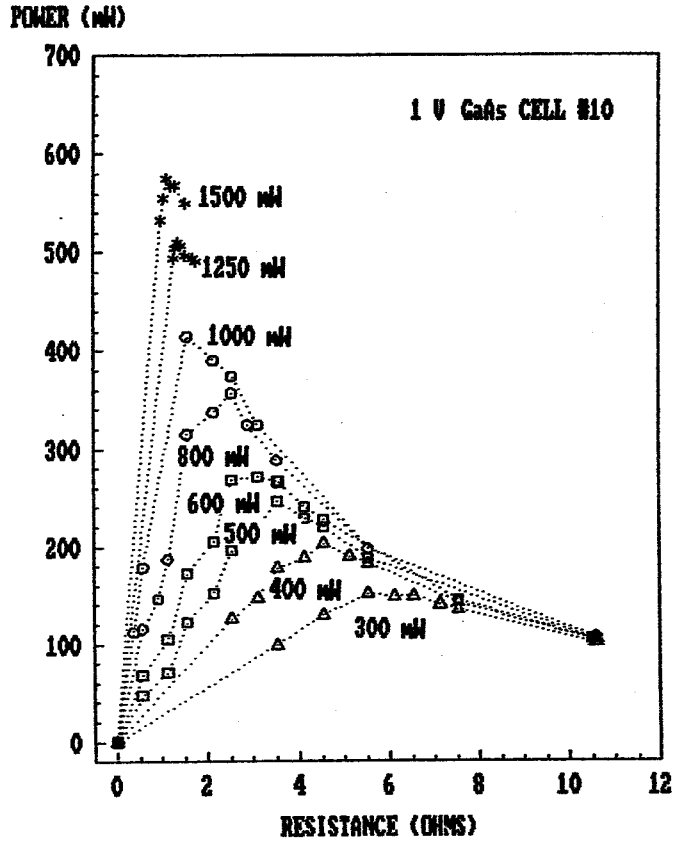

Figure 104. Electrical Power Generated by 1-V PVA GaAs Cell #10 vs. Load Resistance for 300, 400, 500, 600, 800, 1000, 1250, and 1500 mW of Optical Power Incident on the Cell Using SDL 500-mW LD A841 Coupled to 600-μm FO_3 #1 as Source

2-V Cell #12

Figure 105 shows the electrical power generated by the 2-V hybrid cell #12 as a function of load resistance for seven input LD optical powers. Similar behavior is observed for the 2-V cell as was observed in the 1-V cell, i.e., a decrease in R_P and a narrowing of the width at the 90% point of the power vs. resistance curve with increasing input LD optical power. The maximum electrical power generated external to the cell is less at each input optical power for the 2-V cell compared with the 1-V cell. The R_P value is larger at each input LD optical power for the 2-V cell, compared to the 1-V cell.

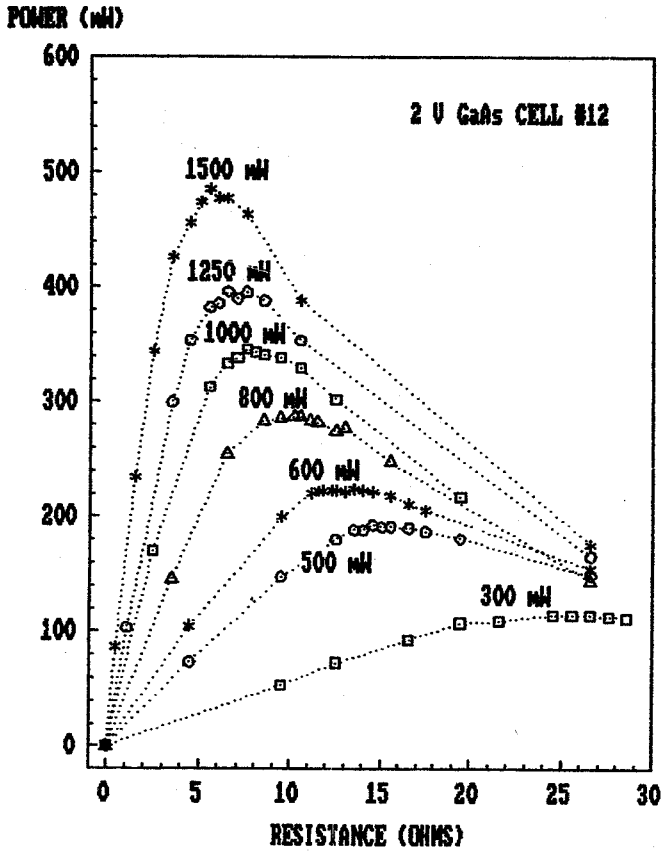

Figure 105. Electrical Power Generated by 2-V PVA GaAs Cell #12 vs. Load Resistance for 300, 500, 600, 800, 1000, 1250, and 1500 mW of Optical Power Incident on the Cell Using SDL 500-mW LD A841 Coupled to 600-μm FO_3 #1 as Source

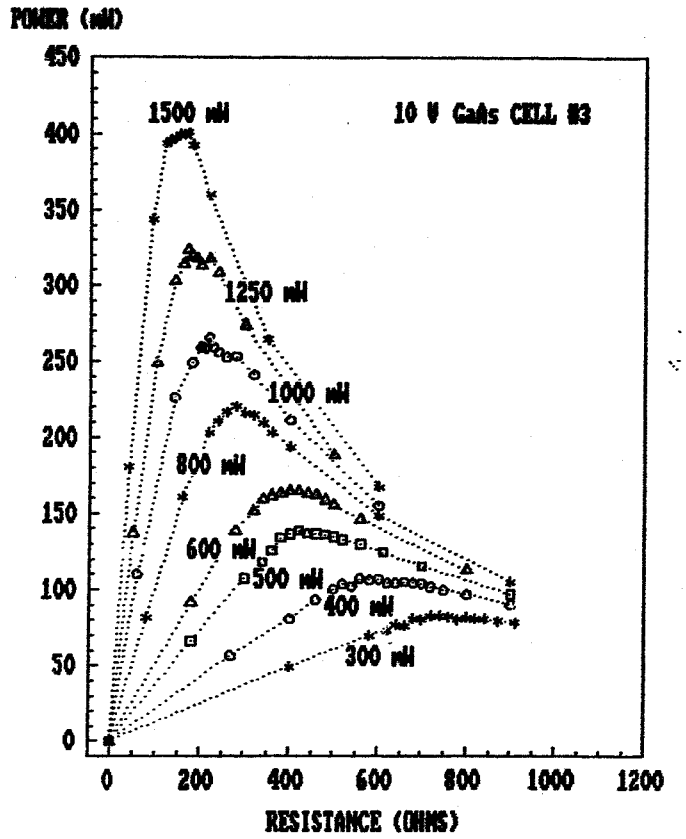

Figure 106. Electrical Power Generated by 10-V PVA GaAs Cell #3 vs. Load Resistance for 300, 400, 500, 600, 800, 1000, 1250, and 1500 mW of Optical Power Incident on the Cell Using SDL 500-mW LD A841 Coupled to 600-μm FO_3 #1 as Source

10-V Cell #3

Figure 106 shows the electrical power generated by the 10-V hybrid cell #3 as a function of load resistance for eight input LD optical powers. The behavior of the 10-V cell is similar to that of the 2- and 1-V cells. A decrease in R_P and a narrowing of the width at the 90% point of each curve is observed as the input LD optical power increases. The P_m generated by the 10-V cell at each optical power level is less than for the 2- and 1-V cells. R_P is larger for the 10-V cell than for the other two cells.

16-V Cell #3

Figure 107 shows the electrical power generated by the 16-V hybrid cell #39 as a function of load resistance for three input LD optical powers. A decrease in R_P and a narrowing of the width at the 90% point of each curve is observed as the input LD optical power increases. The P_m generated by the 16-V cell at each input LD optical power is about half that generated by the 10-V cell. R_P is larger for the 16-V cell than for the other cells. When the input LD optical power is 1500 mW, the 16-V cell's R_P value is about three times larger than that of the 10-V cell.

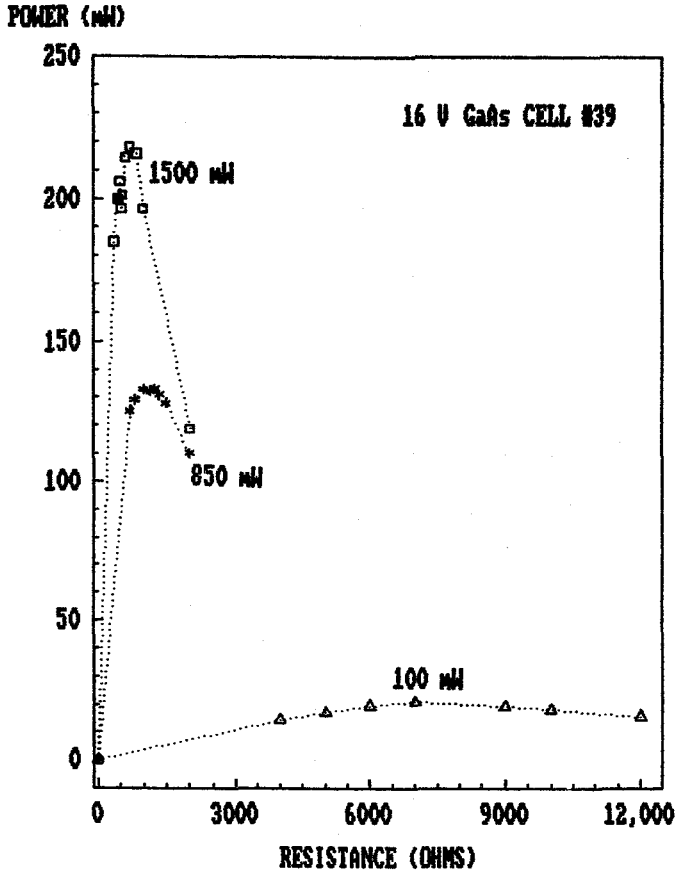

Figure 107. Electrical Power Generated by 16-V PVA GaAs Cell #39 vs. Load Resistance for 100, 850, and 1500 mW of Optical Power Incident on the Cell Using SDL 500-mW LD A841 Coupled to 600-μm FO_3 #1 as Source

The decrease in R_P for the lower-voltage rated cells indicates that they would be more difficult to match to a specific dc- dc converter, i.e., the 1-V cell at 1500 mW has an R_P of <1.1 Ω, whereas the 10-V cell has an R_P of ~175 Ω. Tolerance in impedance-matching would also be tighter because the lower-voltage rated cells have narrower curves at the 90% value of R_P.

It is much more difficult to fabricate 10- and 16-V cells than the 2-V cells because so many more solder connections must be made. It is also hard for 10- and 16-V cells to retain their integrity once fabricated because of these connections. The operation of the hybrid cells is affected by the solder connections made between the segments, especially if the solder connections yield.

10-V Cell #5

Tests were run on another 10-V cell, #5. The results are shown in Figure 108. The incremental increase in electrical power with increase in incident optical power observed for cell #3 is not observed for cell #5. It is evident that the response of this cell is not as predictable as the response of the previous 10-V cell, #3.

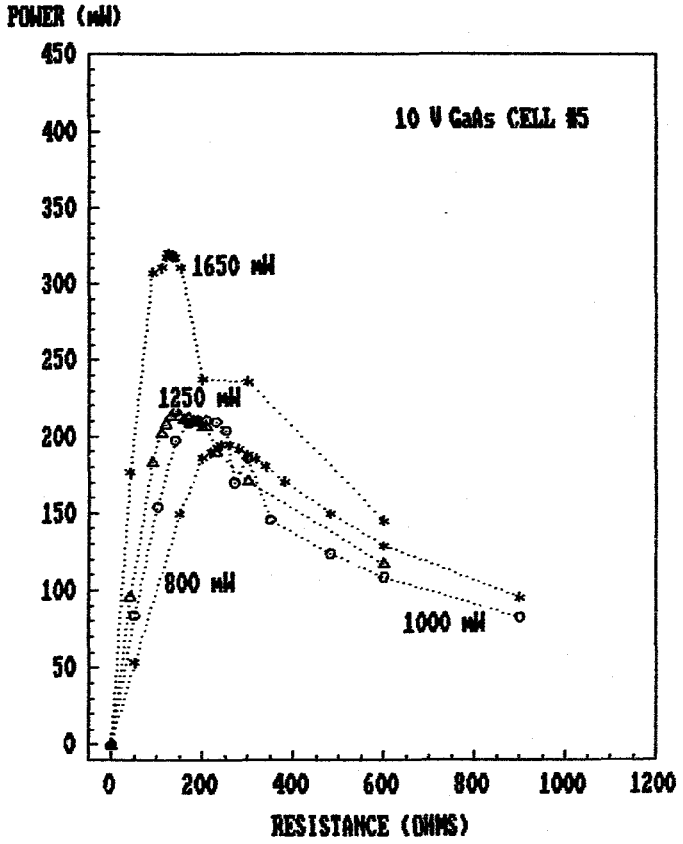

Figure 108. Electrical Power Generated by 10-V PVA GaAs Cell #5 vs. Load Resistance for 800, 1000, 1250, and 1650 mW of Optical Power Incident on the Cell Using SDL 500-mW LD A841 Coupled to 600-μm FO_3 #1 as Source

4.4.2 Optimum R_P

For the 1-, 2-, 10-, and 16-V cells the optimum resistance (R_p), which is the resistance that yields the maximum cell output power (P_m), is described for different LD optical power.

Figure 109 shows the R_P value corresponding to P_m for the 1-, 2-, 10-, and 16-V cells as a function of input LD optical power. The data points for each cell lie on a power curve that adheres to:

$$R_P = a P_m^b . \quad (34)$$

The constants, a and b, are different for the different cells. Table 10 gives the a and b for each cell. At constant LD power, R_P increases with the increase in cell voltage rating, i.e., R_P value is the smallest for the 1-V cell and increases to the largest for the 16-V cell. Maximum power is transferred to a load if the coupling resistor is the R_P value. Equation (34) is used to predict R_P values for larger-incident LD powers than those measured. These predicted R_P values are listed in Table 11.

At 1.5 W of incident power,

- The P_m generated by 1-, 2-, 10-, and 16-V cells is 0.58, 0.49, 0.40, and 0.22 W, respectively.
- The voltage is 0.799, 1.62, 8.26, and 12.35 V, respectively.
- The current is 720, 298, 50, and 17.7 mA through R_p of 1.11, 5.47, 160, and 699 Ω, respectively.

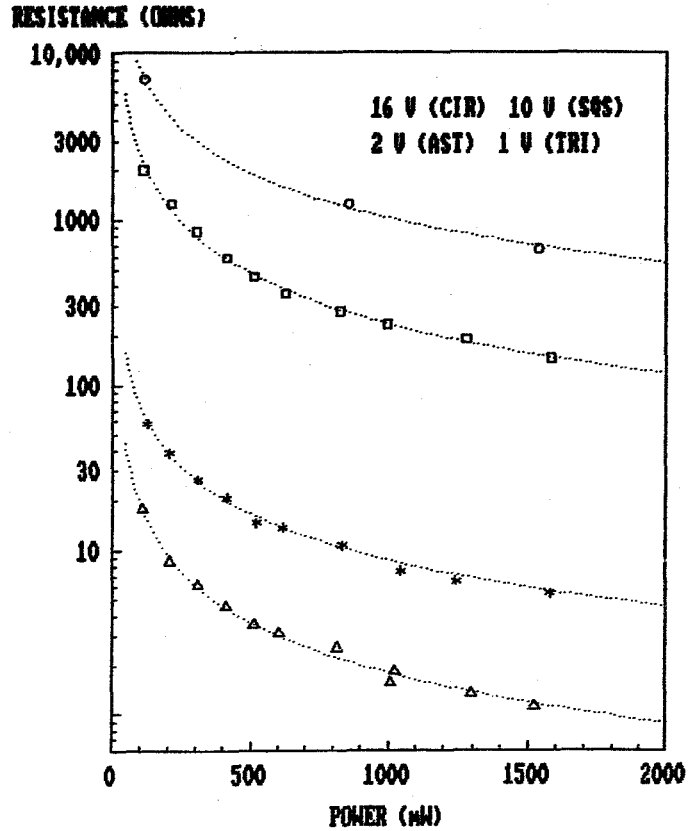

Figure 109. Optimum Load Resistance for 1-, 2-, 10-, and 16-V PVA GaAs Cells vs. Incident LD Optical Power Using SDL 500-mW LD A841 Coupled to 600-μm FO_3 #1 as Source

Table 10. a and b Coefficients for Equation 34

CELL (V)	a	b
1	2082.5	-1.022
2	5206.1	-0.926
10	206.8	-1.016
16	408.9	-0.890

Table 11. Predicted R_p Values of Four GaAs Cells for Different Optical Powers

LASER POWER (W)	R_p FOR_ 1 V CELL (ohms)	2 V CELL (ohms)	10 V CELL (ohms)	16 V CELL (ohms)
2	0.879	4.55	115.8	553.5
3	0.581	3.13	76.7	385.8
4	0.433	2.39	57.3	298.6
5	0.345	1.95	45.7	244.8
10	0.170	1.02	22.6	132.1
20	0.084	0.539	11.2	71.3
50	0.033	0.231	4.4	31.5
100	0.016	0.I21	2.1	17.0

4.4.3 Efficiency

The efficiency for the maximum power generated by 1-, 2-, 10-, and 16-V cells is described for different LD optical powers.

Figure 110 is a plot of the maximum efficiency (E_m) of the 1-, 2-, 10-, and 16-V GaAs cells as a function of input LD optical power (P_{LD}). The actual efficiency in percentage is given by the following relationship:

$$E_m = \left(\frac{P_e}{P_{LD}}\right) 100, \qquad (35)$$

where P_e is the cell output electrical power for maximum power transferred to R_P. The value of E_m is not corrected for contact area masking, reflection losses, series, and shunt resistance.

1-V Cell

As shown, E_m is largest for the 1-V cell. For this cell, E_m is essentially a constant value of 49% for $P_{LD} \leq 500$ mW. For larger LD power, E_m decreases monotonically with increasing P_{LD}. E_m varies from 49% to 38% as P_{LD} varies from 100 to 1500 mW.

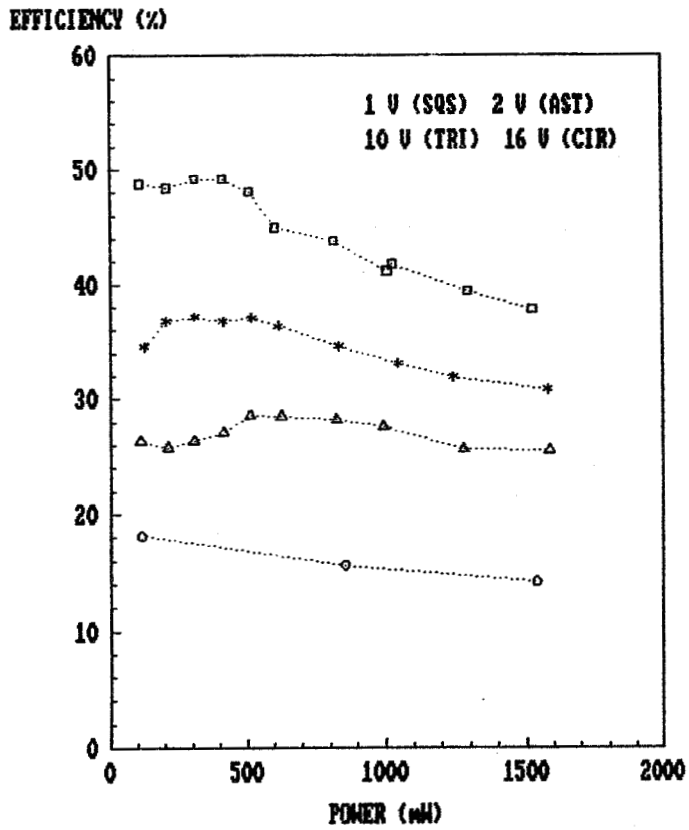

Figure 110. Maximum Efficiency for 1-, 2-, 10-, and 16-V PVA GaAs Cells vs. Incident LD Optical Power Using SDL 500-mW LD A841 Coupled to 600-μm FO_3 #1 as Source

2-V Cell

The hybrid 2-, 10-, and 16-V cells have lower efficiencies. The higher the cell voltage rating, the lower the E_m for all P_{LD} values. The 2-V cell behaves similarly to the 1-V cell except that P_{LD} = 100 mW has a reduced efficiency. For P_{LD} values between 200 and 500 mW, E_m is ~37%, which is ~76% of the 1-V cell's E_m values. E_m varies from 37% to 30% as P_{LD} varies from 100 to 1500 mW.

10-V Cell

For the 10-V cell, E_m is almost constant. It varies from 25.5% to 28.5% as P_{LD} varies from 100 to 1500 mW.

16-V Cell

There are only three data points for the 16-V cell. E_m decreases monotonically from 18% to 14% as P_{LD} varies from 100 to 1500 mW.

The cells with the higher voltage rating have lower efficiency because:

- Series cell resistance increases with increasing cell voltage rating.
- Cell performance is limited by the segment with the worst response. As cell voltage rating increases, the probability of perfectly matching all segment decreases.

The peak of each curve is determined by the grid pattern designed to accommodate the proposed input optical power level and the series resistance of the cell.

4.4.4 I vs. V Curves

Figures 111-114 show the family of current vs. voltage (I to V) curves, tested at different P_{LD} levels, for the 1-, 2-, 10-, and 16-V cells, respectively.

I_{SC} Values

At the maximum LD power of 1500 mW, the short-circuit current (I_{sc}) decreases with the increase in cell voltage rating. The I_{sc} is 850 mA for the 1-V cell; 410 mA for the 2-V cell; 67 mA for the 10-V cell; and 30.6 mA for the 16-V cell.

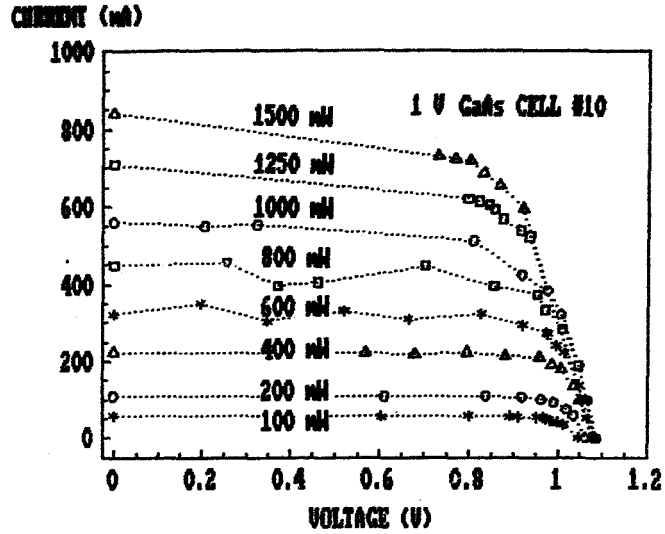

Figure 111. Current for 1-V PVA GaAs Cell #10 vs. Voltage for 100, 200, 400, 600, 800, 1000, 1250, and 1500 mW of Optical Power Incident on the Cell Using SDL 500-mW LD A841 Coupled to 600-μm FO_3 #1 as Source

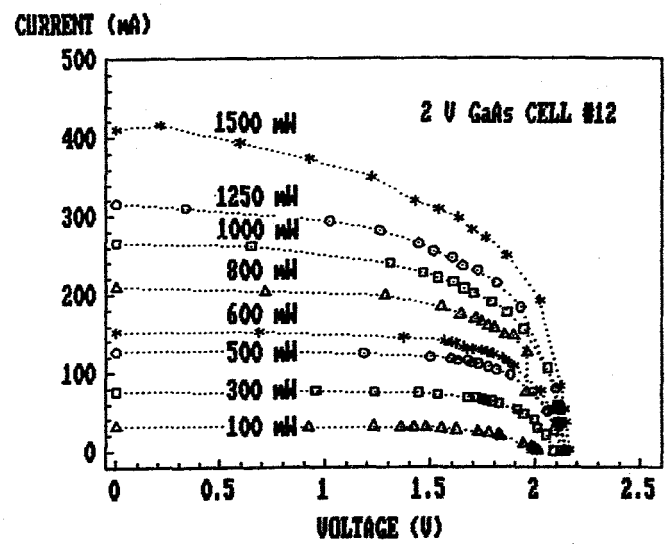

Figure 112. Current for 2-V PVA GaAs Cell #12 vs. Voltage for 100, 300, 500, 600, 800, 1000, 1250, and 1500 mW of Optical Power Incident on the Cell Using SDL 500-mW LD A841 Coupled to 600-μm FO_3 #1 as Source

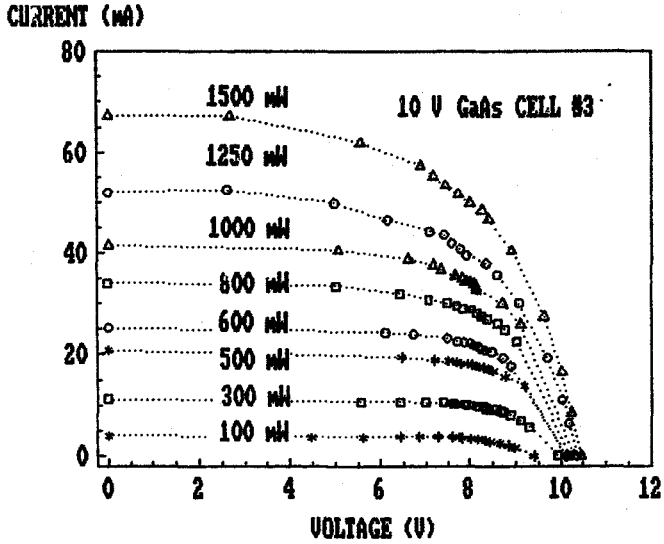

Figure 113. Current for 10-V PVA GaAs Cell #3 vs. Voltage for 100, 300, 400, 500, 600, 800, 1000, 1250, and 1500 mW of Optical Power Incident on the Cell Using SDL 500-mW LD A841 Coupled to 600-μm FO_3 #1 as Source

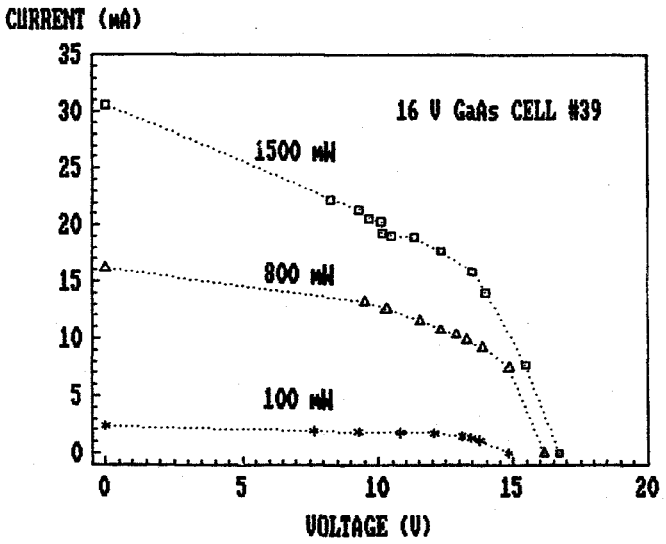

Figure 114. Current for 16-V PVA GaAs Cell #39 vs. Voltage for 100, 800, and 1500 mW of Optical Power Incident on the Cell Using SDL 500-mW LD A841 Coupled to 600-μm FO_3 #1 as Source

V_{oc} Values

The V_{oc} of the cells is 1.08 V for the 1-V cell; 2.16 V for the 2-V cell; 10.5 V for the 10-V cell; and 16.7 V for the 16-V cell.

For specific P_{LD} values, as the cell voltage rating increases, the cell current at P_m decreases. Therefore, what is gained in increased voltage for the higher-voltage cells is lost in current.

Figure 115 shows the effect of the short-circuit current of the 2-V cell #12 with 0.83 W of LD optical power leaving the FO and incident on the cell as the distance is varied between the output of the FO and the cell. Our operational distance of 4.78 mm or power density of 49.9 W/cm^2 (the common point to both curves) is close to the optimum, i.e., the short-circuit plateau between 3.3 and 4.3 mm and the corresponding power density of 90.8 to 59.8 W/cm^2. The optical power density, p, is calculated using:

$$p = \frac{P_{FO}}{\pi}(r_{FO} + d \tan a)^2 , \qquad (36)$$

where

d = the distance between the FO and the cell
a = the divergence out of the FO given by Eq (31).

The divergence value to calculate p is taken from Table 7 for FO_2 #1 $1/e^2$ points. It is the average X direction divergence 7.45° (the last three divergences are used).

The implication of Figure 115 is that the I–V curves of Figures 111 to 114 would change as the distance between the FO and the cell changed. For the different FOs used, the illumination from the FO, which is the input to the cells, was not uniform but, rather, approached a Gaussian. The optical power density for the same LD optical power onto the 2-V cell #12 using FO_3 #1 was about 18.0 W/cm^2, less than half that produced by FO_2 #1. The reduced power density for FO_3 #1 (600 μm FO) was due to slightly larger divergence (average 12° from Table 7) and the larger-diameter FO_3 #1. The short-circuit current produced by FO_3 #1 (600 μm FO) for 800 mW of incident LD power was ~210 mA (Figure 112), whereas for FO_2 #1 (200 μm FO) it was 187 mA. The larger optical power density incident onto cell #12 by FO_2 #1 produced slightly less short-circuit current than FO_3 #1.

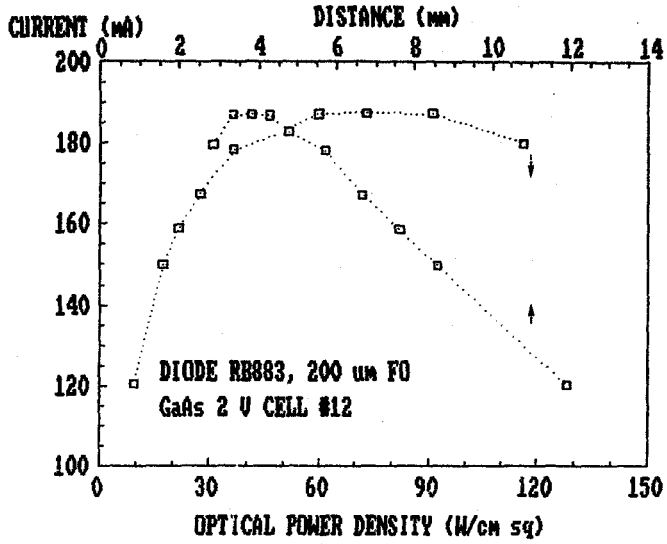

Figure 115. Short-Circuit Current for 2-V Cell #12 vs. Incident Optical Power Density and Distance Between 200-μm FO_2 #1 and Cell, With LD RB883 Emitting 1 W Into the FO and FO Transmitting 0.83 W Onto the Cell

4.4.5 Fill Factor

The fill factor (FF) [defined in Eq (25)] is largest for the 1-V cell for all incident LD optical powers, as shown in Figure 116. The break in the 1-V cell curve is because data were taken at two different times using slightly different setups.

The maximum FF values of the 1-, 2-, 10-, and 16-V cells are 0.854, 0.743, 0.773, and 0.594, and occur at 0.3, 0.2, 0.1, and 0.1 W of incident optical power. An increase in incident optical power to 1.5 W causes a decrease in FF to 0.636, 0.548, 0.585 (at 1.0 W), and 0.426, respectively. These decreases in FF values with increasing incident optical power are related to the grid pattern of the cell being designed for different incident optical power density.

Large bridges in the grid pattern lead to low cell series resistances (R_S), which lead to high FF values.[35] The obscuration caused by the large bridges decrease the E_m value. A low obscuration produces large I_{SC} values and possibly large E_m values if R_S is low. This trade-off results in a cell with large E_m values at large incident optical power. This task and the development of monolithic >1-V cells[36] at large-incident LD optical power are under consideration by Org. 6224 at SNLA.

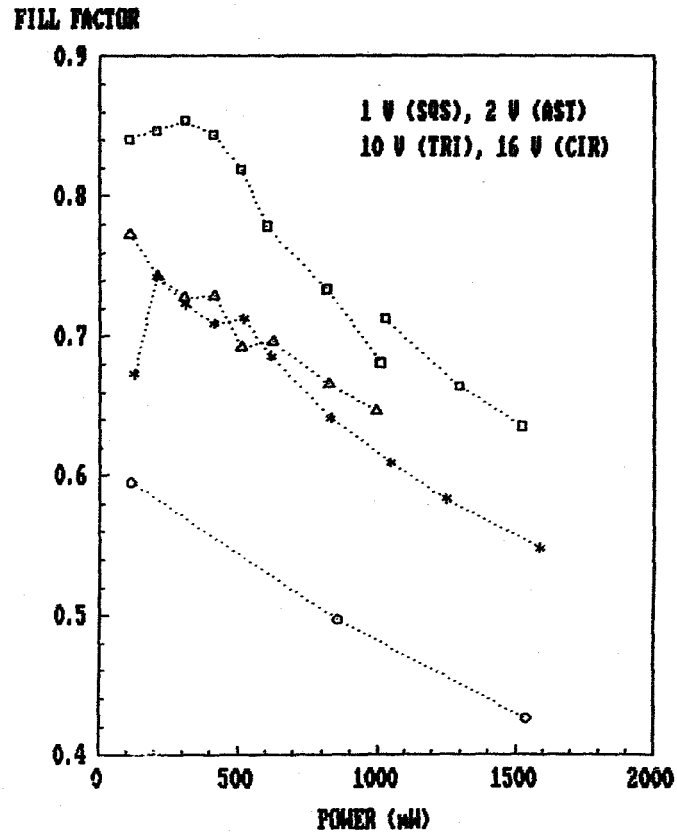

Figure 116. Fill Factor for 1-, 2-, 10-, and 16-V GaAs Cells vs. Incident Optical Power Using SDL 500-mW LD A841 Coupled to 600-μm FO_3 #1 as Source

The decrease in the FF for the hybrid 2-, 10-, and 16-V cells compared to the monolithic 1-V cell at the low illuminating optical power could be caused by:

- Hybrid cells that are not designed for the level of LD optical power incident onto the cell
- Unmatched segments
- Large cell resistance due to contact resistance at the solder junctions between the individual segments.

As the cell voltage rating increases, the number of segments also increases. This increases solder junction resistance, series resistance, and the cell segment-matching problem.

4.4.6 Summary

The PVA cell characteristics measured included

- Electrical power vs. cell resistance for different incident LD power (P_{LD})

- Current vs. voltage for different P_{LD}
- Optimum resistance vs. P_{LD}
- Efficiency vs. P_{LD}
- Fill factor vs. P_{LD}.

Characteristics of PVA GaAs Cells Measured With LD Optical Power

Table 12 summarizes the characteristics of the cells measured using LD light transmitted through 600-μm FO_3 #1.

Cell Electrical Power

For a specific cell, the electrical output power increases with increasing P_{LD}. The P_m and I_m listed in Table 12 decrease with increasing cell voltage rating, whereas R_P and V_m increase with increasing cell voltage rating. As the LD power is decreased by 15 times (from 1.5 to 0.1 W), the electrical power generated by the 1-, 2-, 10-, and 16-V cells decreases 11.6, 10.8, 14.3, and 9.5 times, respectively.

Optimum R_p

When P_{LD} decreases from 1.5 to 0.1 W, R_P values increase to 17.5, 55.6, 2000, and 7000 Ω for the 1-, 2-, 10-, and 16-V cells, respectively.

I-V Curves

For all incident optical power, the cell output electrical power decreases with increased voltage cell rating. At a specific output voltage, the cell current is found to increase with increasing P_{LD} values. Table 12 lists the short-circuit currents and the open-circuit voltages of the cells tested.

Maximum Efficiency

The maximum efficiency E_c listed in Table 12 is for 0.3, 0.3, 0.5, and 0.1 W of incident LD optical power for the 1-, 2-, 10-, and 16-V cells, respectively. The higher the cell voltage rating, the lower its efficiency for all incident LD optical power levels.

Fill Factor

The maximum fill factors are listed in Table 12 along with the FF at 1.5 W of incident optical power. For nonuniform LD light transmitted through an FO and uniform white light with comparable incident power levels, the fill factor of the 2- and 16-V cells (nominally 0.7 and 0.6 W for 0.1 W of LD light) differ by 2.3% and 0.4%, respectively. When P_{LD} increases from 1 to 1.5 W, the 1-, 2-, and 16-V cell FF (nominally 0.7, 0.6, and 0.5 W for 1 W of LD light) decreases by 6.5%, 11.0%, and 11.1%, respectively.

Table 12. Characteristics of PVA GaAs Cells Measured With 1.5 W of Incident LD Optical Power

SER #	SEG V	P_{LD} (W)	P_{FO} (W)	P_m (W)	I_m (mA)	R_p (ohm)	V_m (V)	I_{sc} (mA)	V_{oc} (V)	E_c (%)	FF max / LD	V_{oc}/I_{sc} (V/A)	I_m/I_{sc}
10	1	1.90	1.52	.575	720.0	1.11	0.80	850.0	1.08	38	.854/.636	1.29	0.86
12	2	2.00	1.61	.486	298.0	5.47	1.63	410.0	2.16	30	.743/.548	5.26	0.73
3	10	1.97	1.58	.400	50.0	160.0	8.26	67.2	10.5	26	.773/.585	156.0	0.74
39	16	1.96	1.57	.218	17.7	690.0	12.34	30.6	16.7	14	.595/.426	547.0	0.58
5	10	1.59	1.27	.298	40.7	180.0	7.32	52.5	10.5	19	.534/	199.0	0.78

5. HOFS Systems Configurations

Fifteen different HOFS systems were tested. The first generation of testing included nine HOFS systems (HOFS 1′, 1 through 8); the second generation, six HOFS systems (HOFS 9 through 14). The poor performance of any component of the HOFS system directly affects total system performance. One component, the dc-dc converter, could not be tested individually as could the other components; therefore, the converter was tested as an assembly with the cell. Converter performance depends greatly on the input impedance of the GaAs cell and of the output load, the capacitor. Attempts were made to keep the output voltage of the converter (i.e., the capacitor charge voltage) between 2 and 3 kV. In order to store sufficient energy in the capacitor to perform the desired function, different values of capacitance, depending on the output voltage of the converter, were used in different HOFS systems.

5.1 HOFS Systems Configuration Summarized

Table 13 summarizes the HOFS systems configurations described below. The specific components of HOFS Systems 1′, 1 through 14, and 14′ include the HOFS number, LD part numbers, electrical power, optical power, and percent efficiency, the coupler type and percent transmission (T), the PVA cell number, voltage, and percent efficiency, the dc-dc converter model number, and the capacitor value.

All efficiencies are measured at maximum output LD optical power.

HOFS 1–14

HOFS 1 through 14 and 14′ uses basically the same test setup shown in Figure 117, but has different LDs, cells, converters, and capacitors. HOFS 1 through 3 use two LDs, GRIN lens couplers, and cells. The cells are connected in series and are then input to the converter.

HOFS Test Setup

The following equipment is common to the setup used to test HOFS 1 through 14 and 14′:

- The LD current driver described in Section 2.1
- A resistor network, which includes resistors:
  R_2 = 10 gigaohms
  R_3 = 1 megaohms
- Oscilloscopes:

  OSC 1 (Model 7844). OSC 1 measures the voltage across the cell and the current delivered to the dc-dc converter by measuring the voltage across $R_1 = 0.465\ \Omega$.

  OSC 2 (Tektronics Model 7633). OSC 2 measures the voltage across the calibrated resistor divider network, R_2 and R_3, that is used to determine the capacitor charge time.
- An electrostatic voltmeter, Sensitivity Research Model ED V24436.

HOFS 1 through 14 and 14′ use a different LD current driver than HOFS 1′ and have a variable current control for more flexible operation. HOFS 1′, 1, 2, and 3 use two of the same type of SDL 100-mW LDs, optically coupled through GRIN lenses onto two 1-V PVA GaAs cells. These cells are connected in series to a dc-dc voltage converter to charge a 0.0524-μF capacitor. HOFS 1′, 1, and 2 use the same dc-dc voltage converter; HOFS 3 uses a different converter. HOFS 4 through 8 use different LDs, FO couplers, cells, converters, and capacitors than do HOFS 1′, 1 through 3. HOFS 6 and 7 are the same as HOFS 4 and 5, respectively, except that their capacitors are larger.

Table 13. Components of the Hybrid Optical Firing Set Systems

HOFS SYS (#)	LD (#)	LD POWER ELECT (W)	LD POWER OPT (W)	LD POWER E_{LD} (%)	COUPLER type/%T	PVA CELL (#)	PVA CELL (V)	PVA CELL (%)	DC-DC CONVERTER MODEL #	CAP (uF)
1st GENERATION										
1′	A194	1.9	0.16	8.2	G_1/95.9*	19	1	-		
	A200	1.7	0.18	10.2	G_1/95.9*	18	1	-		
	TOTAL	3.6	0.34	9.4					ST-10N[1]	0.05
1	A194	4.2	0.18	4.1	G_1/95.9*	24	1	-		
	A200	2.2	0.18	8.0	G_1/95.9*	10	1	24 49+		
	TOTAL	6.4	0.35	5.5					ST-10N	0.0524
2	A321	1.5	0.32	20.5	G_1/96.8	10	1	49+		
	B126	1.0	0.32	31.6	G_1/95.4	24	1	-		
	TOTAL	2.6	0.64	24.9					ST-10N	0.0524
3	A321	1.7	0.41	23.5	G_1/96.8	10	1	44		
	B126	1.2	0.40	33.3	G_1/95.4	24	1	-		
	TOTAL	2.9	0.81	27.6					MC-10N-M[2]	0.0524
4	A841	8.2	1.9	23.1	FO_3/80	12	2	31	MC-10N-M	0.0524
5	A841	8.1	1.9	23.3	FO_3/80	3	10	26	Q-30[3]	0.0353
6	A841	8.0	1.9	24.3	FO_3/80	12	2	31	MC-10N-M	0.1089
7	A841	8.1	1.9	23.3	FO_3/80	3	10	26	Q-30	0.0859
8	A840	7.7	1.9	24.6	FO_3/80	39	16	14	Q-30	0.0231
2nd GENERATION										
9	A840	7.7	2.0	24.6	FO_3/80	12	2	31	MC25/M143[4]	0.0524
10	A840	7.7	2.0	24.6	FO_3/80	12	2	31	MC25/M143	0.1089
11	A840	8.1	2.0	24.6	FO_3/80	10	1	44	MC25/M142[5]	0.0524
12	BM498	9.9	3.4	39.4	FO_2/80	12	2	31	MC25/M143	0.0524
13	BM498	9.9	3.4	39.4	FO_2/80	12	2	31	MC25/M143	0.1089
14	RB883	4.8	2.0	40.4	FO_2/84	12	2	31	MC25/M143	0.0524
14′	RB883	3.0	1.0	33.8	FO_2/84	12	2	31	MC25/M143	0.0524

G_1 is a .23 pitch GRIN LENS

A841 & A840 @ 500 mW

BM498 @ 3.4 W

RB883 @ 2 W others at 100 mW

* measured with A198 & GRIN at 0.17 W

\+ measured with FO_3 coupler

1 = Venus #1747

2 = Gamma #081186D (modified)

3 = Venus #3899

4 = Gamma #03-0587B-1

5 = Gamma #03-0587A-2

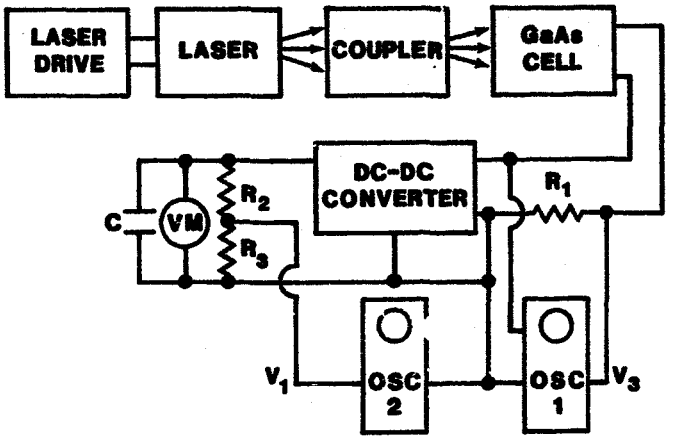

Figure 117. Basic Block Diagram of Setup Used to Test HOFS Systems 1 Through 14 and 14′

5.2 First-Generation HOFS 1′ and 1–8

HOFS 1′

HOFS 1′ was assembled at SNLA in 1985 by R. P. Roberts. The system was tested by Roberts and retested in this study. Figure 118 shows the block diagram of HOFS 1′. The LD driver is a breadboard-mounted circuit with 10-V input and is capable of delivering ~700 mA for 5.3 s; after this, it delivers ~ 360 mA to three SDL 100-mW LDs connected in series.

The couplers are Melles Griot 0.23-pitch GRIN lenses butt-coupled against the LD window with their output ends positioned a distance d_1 = 20.81 mm from the cells. The three 1-V PVA GaAs cells have a 4-mm-dia active area. Two cells are connected in series to a dc-dc voltage converter. The third cell is used as a triggering source. The voltage converter is a Venus Scientific Corp. Vidicon Power Supply, Model ST-10N. When this converter is operated with a positive 2- to 10-V input, it produces a negative 2-kV to 10-kV output. A Dearborn 0.0524-μF capacitor, rated at 4 kV, is charged to ~2.0 kV.

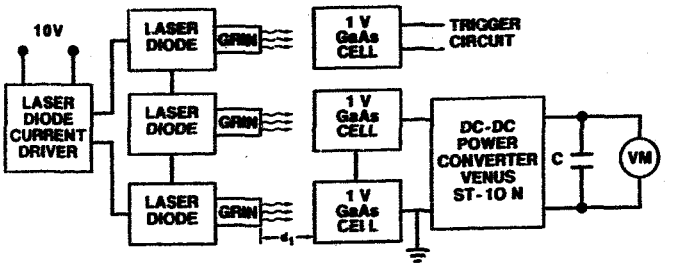

Figure 118. Block Diagram of Setup Used to Test HOFS System 1′ Using the Breadboard LD Driver

HOFS 1

The diagram of the components used in HOFS 1 is shown in Figure 119. The components of HOFS 1 are the same as those of HOFS 1′ except that the LDs, GRIN lenses, and cells are aligned optically for maximum output. This entails unmounting the components from their breadboard and providing special mounts. The distance, d_1, is 20.81 mm.

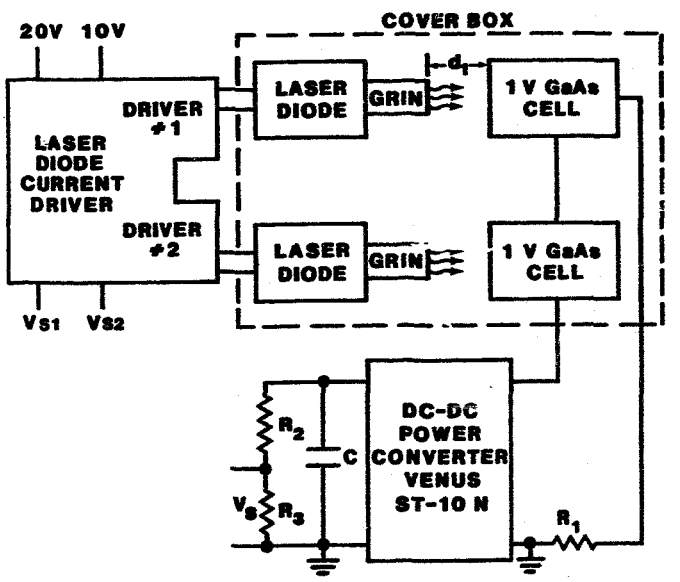

Figure 119. Block Diagram of Setup Used to Test HOFS System 1

HOFS 2

HOFS 2 uses the same type components (the LDs, coupler, cell, dc-dc converter, and capacitor used in HOFS 1′ and 1) except that they are new. The LDs used in HOFS 1′ and 1 had degraded due to age. Figure 120 is a photograph of HOFS 2 with its components labeled. The components in the HV box are the same shown in Figure 17. Distance, d_1, is reduced to 5.08 mm. During testing, a cover is placed over the LDs and cells to eliminate background light and air currents, which cause signal variations.

HOFS 3

The components used in HOFS 3 are identical to those used in HOFS 2 except that the dc-dc voltage converter is changed to a Gamma High-Voltage Research, Inc. Model MC-10N-MOD. For this modified converter, a 1.75- to 12-V dc input produces negative 1- to 10-kV output; a limited 400-mA input current yields a 100-μA output current. The converter was modified in order to reduce the input voltage required to turn on the oscillator input transistor.

HOFS 4

The diagram of the components used in HOFS 4 is shown in Figure 121. A single SDL 500-mW LD A841 replaces the two SDL 100-mW LDs and a 2-V GaAs cell replaces the two 1-V cells used in HOFS 1′, 1 through 3. The GRIN lens couplers are replaced by 600-μm-dia FO_3 #1. A FO is used because the segmented hybrid cells are more efficient with uniform illumination.

In an attempt to optimize the coupling between the cell and the FO cable, the FO is placed at a distance d_1 = 4.27 mm from the 4-mm-dia cell. The dc-dc converter and capacitor are the same as those used in the HOFS 3.

Figure 122 is a photograph of HOFS 4; the components have been labeled. The components in the HV box were shown in Figure 17.

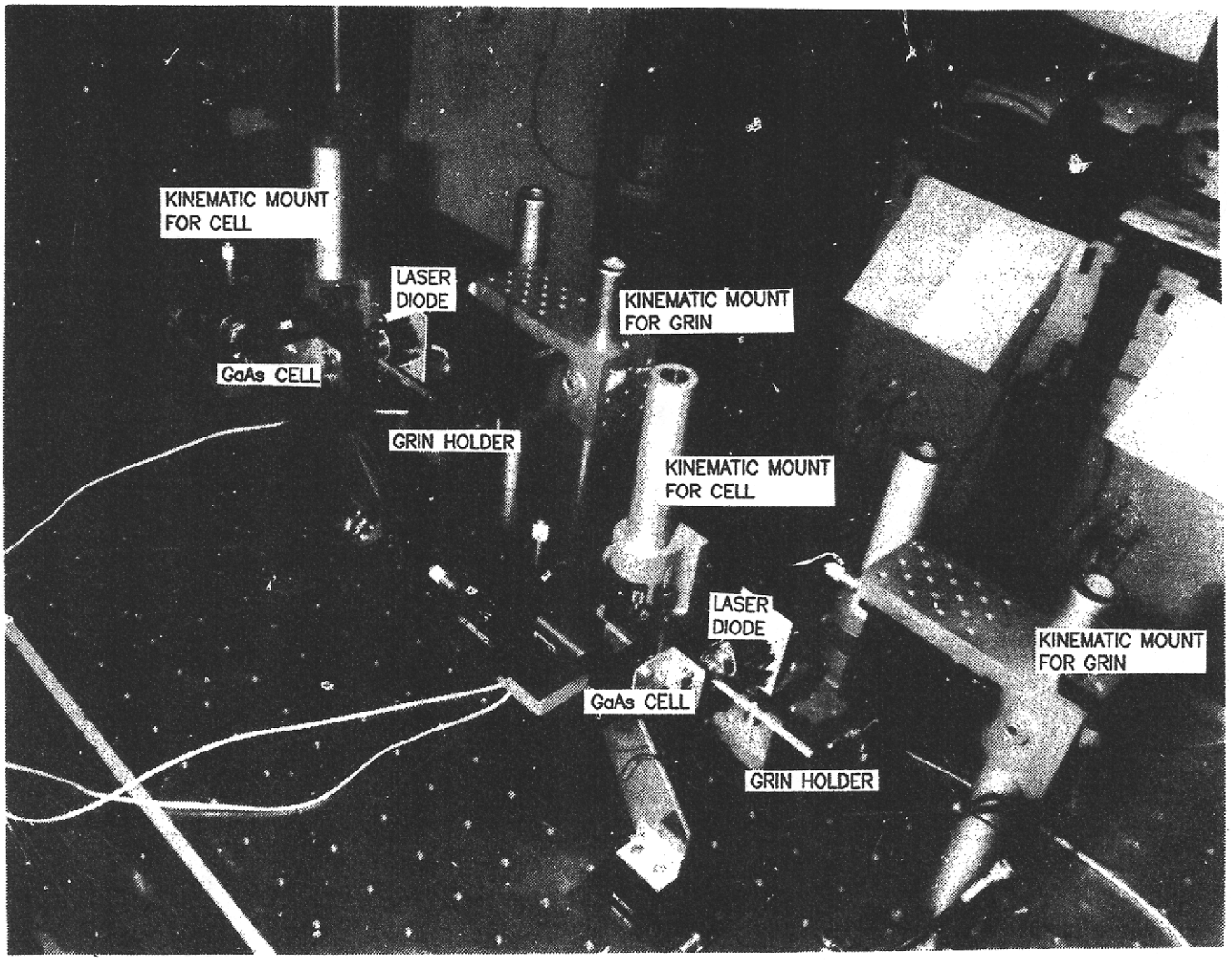

Figure 120. Photograph of HOFS 2 Showing Components Mounted Onto Kinematic Mounts, Allowing for X, Y, and Z Motions

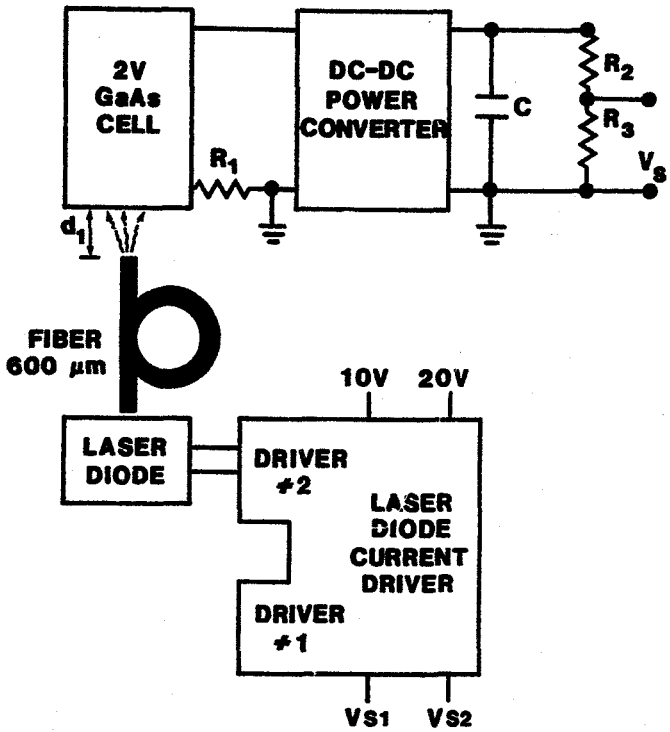

Figure 121. Block Diagram of Setup Used to Test HOFS System 4

HOFS 5

The diagram of the components used in HOFS 5 is similar to that of HOFS 4 shown in Figure 121. The LD, FO coupler, and test equipment are described for HOFS 4. The remaining components are changed as follows:

- The 2-V cell is replaced by a 10-V PVA GaAs cell.
- The Gamma dc-dc converter is replaced by an off-the-shelf Venus Model Q-30 converter.
- The 0.0524-μF capacitor is replaced by a Dearborn 0.0353-μF capacitor rated at 3.2 kV.
- The coupling is optimized by making $d_1 = 9.91$ mm. This distance is larger than for the 2-V cell because the 10-V cell is 10 mm in diameter instead of 4 mm.

HOFS 6 and 7

HOFS 6 and 7 are the same as HOFS 4 and 5, respectively, except that the capacitors are replaced with larger ones in order to store more energy. A 0.1089-μF capacitor, rated at 6 kV, is used in HOFS 6; a 0.0859-μF capacitor, rated at 3.2 kV, is used in HOFS 7.

HOFS 8

HOFS 8 uses the same dc-dc converter as HOFS 5 and 7. The remaining components are changed:

- The SDL 500-mW LD A841 is replaced by another SDL 500-mW LD A840.
- The 10-V cell is replaced by a 16-V cell.
- The capacitor is replaced by a 0.0231-μF capacitor rated at 3.2 kV. The diameters of the 10- and 16-V cells are the same; therefore, d_1 is still 9.91 mm.

5.3 Second-Generation HOFS, 9–14 and 14′

The second generation of new components for the HOFS system includes:

- improved dc-dc converters for 1- and 2-V GaAs cells
- 4- and 8-W LDs
- 200-μm core-diameter FOs.

HOFS 9 and 10

HOFS 9 and 10 use the same components as HOFS 4 and 6 except that the Gamma Model MC-10N-M dc-dc converter is replaced by a Gamma Model MC25/M143 and LD A841 is replaced with A840.

HOFS 11

HOFS 11 uses the same components as HOFS 9 except that the 2-V cell is replaced with the 1-V GaAs cell, and the Gamma Model MC25/M143 dc-dc converter is replaced with Model MC25/M142.

HOFS 12 and 13

HOFS 12 and 13 use the same components as HOFS 9 and 10 except that LD A840 is replaced by SDL 4-W experimental prototype SDL LD BM498, and the 600-μm FO_3 #1 is replaced by 200-μm FO_2 #1. The distance, d_1, is also changed to 4.78 mm.

HOFS 14

HOFS 14 uses the same components as HOFS 12 except that LD BM498 is replaced by LD RB883.

HOFS 14′

HOFS 14′ uses the same components as HOFS 14. The distance, d_1, is varied from 4.78 to 12 mm.

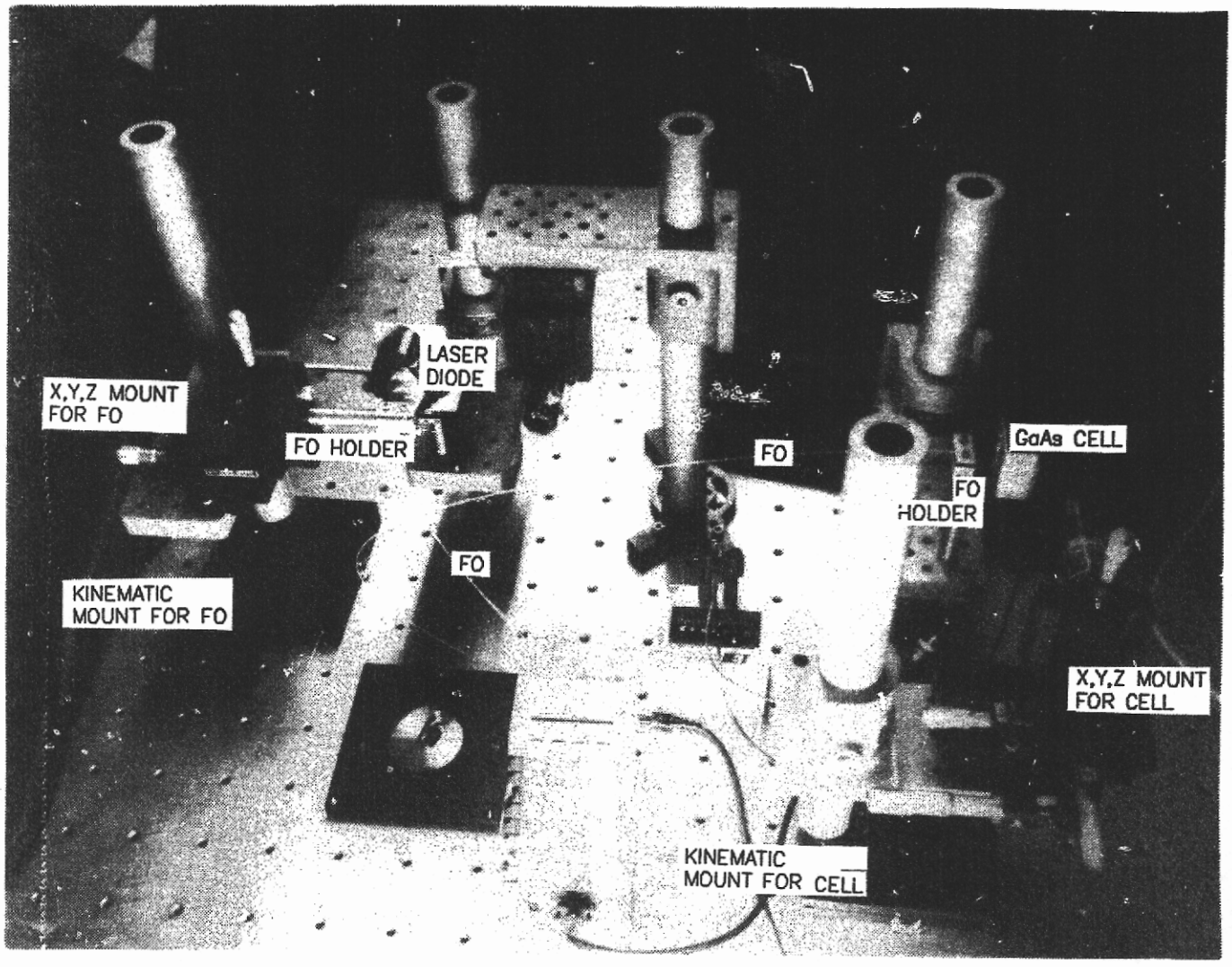

Figure 122. Photograph of HOFS System 4 Showing Components Mounted Onto Kinematic Mounts, Allowing for X, Y, and Z Motions

6. Characteristics of the HOFS Systems Measured

The following characteristics of the HOFS systems were measured as functions of LD optical power for the 1/e of maximum voltage (V_m), 100- or 220-mJ charge, and 90% of V_m of the HOFS capacitor:

- The efficiency of the combination PVA GaAs cell and dc-dc converter (E_{cc})
- The overall system efficiency (E_s)
- System charge time (T_s).

The individual component characteristics were described in Section 4 but will be discussed again relative to the HOFS system performance.

The data were taken using the techniques described in Section 3. Figure 123 shows a typical voltage trace recorded by OSC 2 for the voltage across R_3 of the resistor network, which is across the capacitor. This record is for HOFS 1 with a total of 200 mW of LD optical power. Figure 124 shows a change in charge rate after 5 s. Initially, each LD emitted 100 mW into each cell. After 5 s, the output of each LD decreased to 25 mW, or a total of 50 mW to keep the capacitor charged to a 62.2-mJ level.

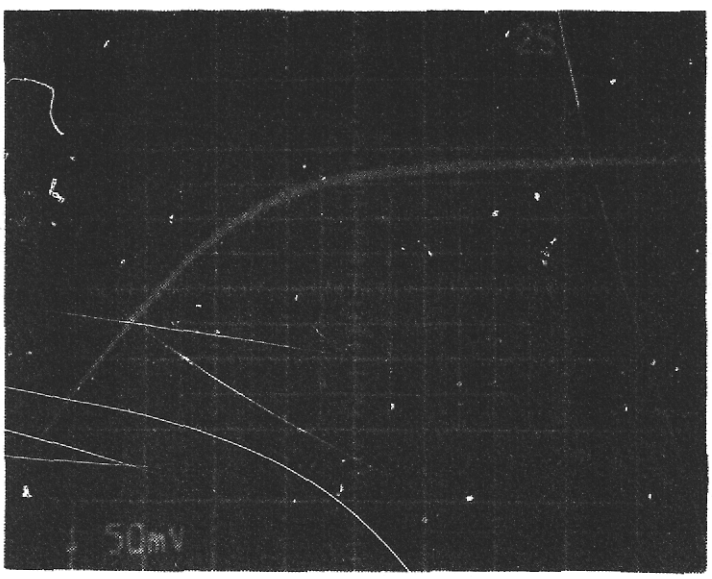

Figure 123 Voltage Trace Recorded by OSC #2 of the Voltage Across R_3 of the Resistor Network Across the HV Capacitor of HOFS System 1. Each LD emits 100 mW onto the surface of the cells.

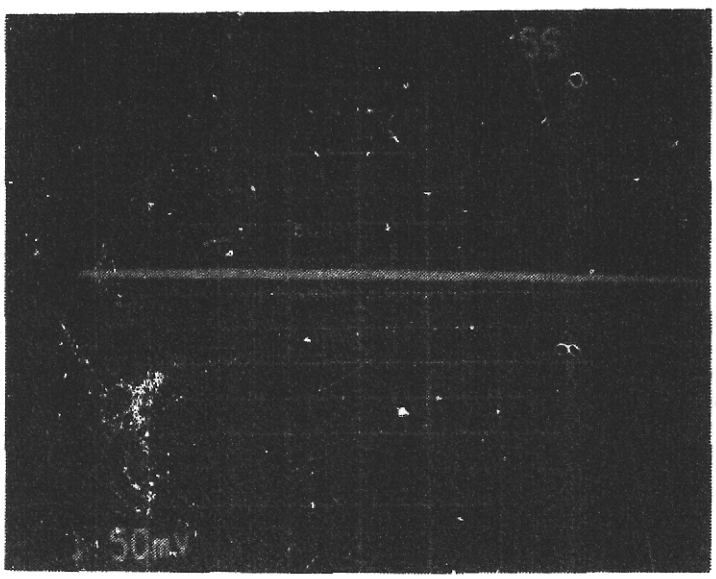

Figure 124. Voltage Trace Recorded by OSC #2 of Voltage Across R_3 of the Resistor Network Across the HV Capacitor of HOFS System 1 Kept Constant After 5 s of Charge. Each LD emitted 25 mW onto the surface of the cells after 5s.

6.1 Cell and Converter Efficiencies

The cell and converter efficiency (E_{cc}) in percent is given by:

$$E_{cc} = \left(\frac{e_{cap}}{e_{cell}}\right) 100 , \qquad (37)$$

where e_{cap} is the energy stored in the capacitor and is given by:

$$e_{cap} = \frac{1}{2} C V^2 , \qquad (38)$$

where C is the capacitance and V is the voltage at the specific charge level of 1/e of V_m, 100 or 220 mJ, or 90% of V_m. The energy incident on the cell is given by:

$$e_{cell} = (P_{LD})\ T_c , \qquad (39)$$

where P_{LD} is the LD optical power collected by the cell and T_c is the time it takes to charge the capacitor to the specific energy level.

6.1.1 First-Generation HOFS, 1–8

The efficiencies of the cell and converter used to charge the capacitors of HOFS 1 through 8 are shown in Figures 125 through 127 for 1/e of V_m, about 100 mJ (104 mJ) or 220 mJ (217.7 mJ), and 90% of V_m.

HOFS Systems 1–4, and 6

As expected, E_{cc} decreases as the level of charge increases from 1/e, 100 mJ, or 220 mJ to the 90% of full charge. E_{cc} values for HOFS 1 and 2 are similar. They use the same type of cells, converter, and capacitor.

The GRIN lenses are better aligned for HOFS 2 than for HOFS 1. The converter used in HOFS 1 and 2 saturates at high optical power levels; therefore, a different converter is used in HOFS 3. E_{cc} changed drastically for the different charge levels in HOFS 3.

In HOFS 4 and 6, the same converter was used as in HOFS 3. The increase in the efficiency of HOFS 4 and HOFS 6 over that of HOFS 3 is probably because:

- The 2-V cell provides a better impedance match (discussed below) to the converter than do the two 1-V cells connected in series.
- The FO provides more uniform illumination to the cell than do the GRIN lenses.

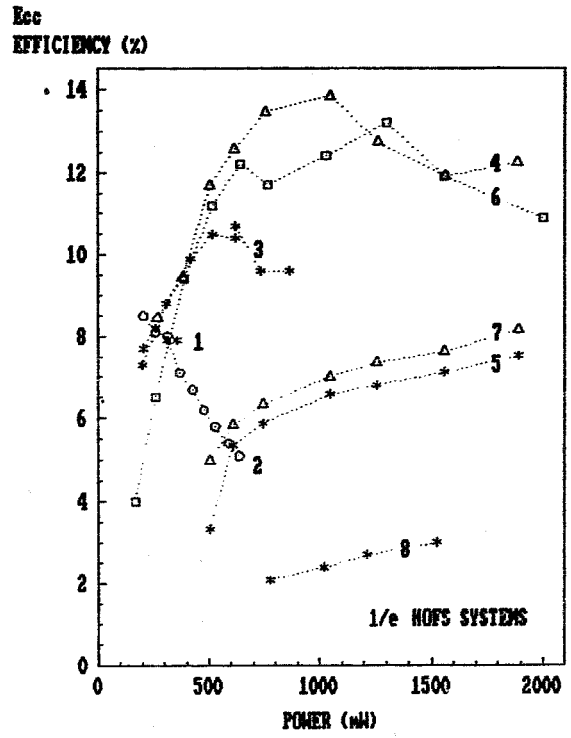

Figure 125 Efficiency of the Combination PVA GaAs Cell and dc-to-dc Converter vs. LD Output Optical Power for 1/e of V_m for Eight HOFS Systems (1 Through 8) Described in Table 13

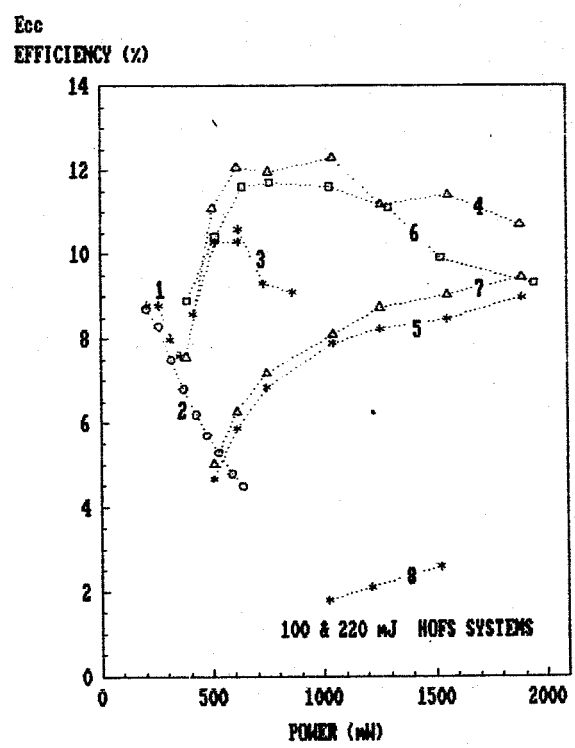

Figure 126. Efficiency of the Combination PVA GaAs Cell and dc-to-dc Converter vs. LD Output Optical Power for 100 and 220 mJ of Energy Charge for Eight HOFS Systems (1 Through 8) Described in Table 13

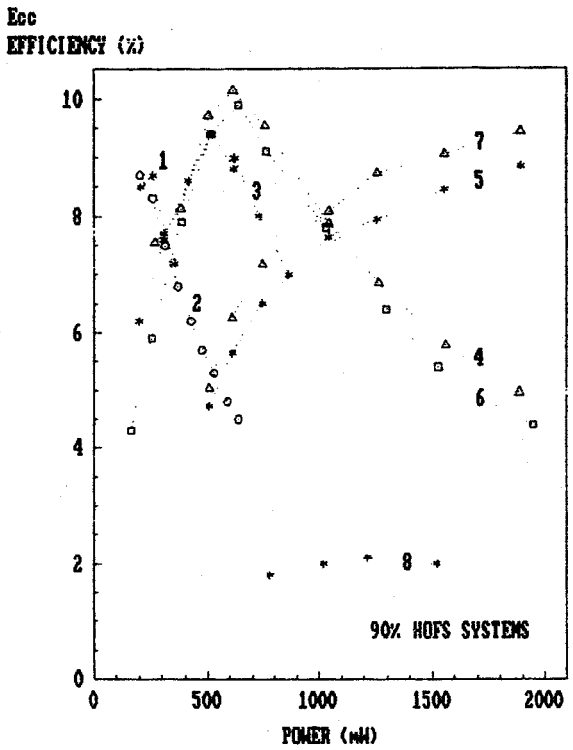

Figure 127. Efficiency of the Combination PVA GaAs Cell and dc-to-dc Converter vs. LD Output Optical Power for 90% of V_m for Eight HOFS Systems (1 Through 8) Described in Table 13

The change in efficiency of a cell with the intensity distribution on the cell was discussed in Section 4.4.4. The general shape of the E_{cc} curves are similar for each specific HOFS system at different charge levels, except for HOFS 4 and 6 at the 90% level where they are more peaked at the lower LD power.

Argument for Better Impedance Match of 2-V Cell

The argument for better impedance match of the 2-V cell over the two 1-V cells connected in series to Gamma Model MC-10N-M follows.

HOFS System 3 uses two 1-V cells connected in series to provide the 2-V input into the dc-dc converter. HOFS 4 and 6 use a single 2-V cell to provide the 2-V input into the dc-dc converter. The area, geometry, grid pattern, series resistance, and in particular the R_P values of the two cells are different.

The R_P of a 1-V cell is ~1.2 Ω. The R_P of two 1-V cells connected in series, though not measured, would probably be slightly larger than two times the R_P of a single cell due to line and contact resistance of the cells in series. However, the two cells would probably still be less than the 5.2-Ω R_P of the 2-V cell. The larger R_P of the 2-V cell provides a better impedance match to the dc-dc converter in HOFS 4 and 6 than does the 1-V cell connected to the same dc-dc converter in HOFS 3.

HOFS Systems 5, 7, and 8

The different shapes of the E_{cc} for HOFS 5, 7, and 8 relative to the other HOFS systems are due to the changes in the converter (to a Q-30) and to the cells (to 10-V cells for HOFS 5 and 7 and to a 16-V cell for HOFS 8).

The reduced efficiency E_c of the 16-V cell compared with the 10-V cell (Figure 110) could almost account for the reduced E_{cc} of HOFS 8 compared with 5 and 7. The reduced E_{cc} of HOFS 8 is not as much as the reduced E_c shown in Figure 110, because the increase in R_P of the 16-V cell over the 10-V cell (Figure 109) could help increase E_{cc} through a better impedance match between the 16-V cell and the converter.

6.1.2 Second-Generation HOFS, 9–14

The efficiencies of the cell and converter used to charge the capacitor in the second generation of components for HOFS 9 through 14 are shown in Figures 128 through 130 for 1/e of V_m, about 100 or 220 mJ, and 90% of V_m. For HOFS 9 and 10, the main difference between these data and the HOFS 4 and 6 data in Figures 125 through 127 is that E_{cc} does not peak but, rather, continues to increase at the 2-W P_{LD} level. In all cases, the peak E_{cc} for HOFS 9 and 10 is larger than for HOFS 4 and 6. The differences in E_{cc} are attributed to the converter.

The E_{cc} of HOFS 9 and 10 is greater than for HOFS 12 through 14 for any specific P_{LD}. The lower E_{cc} for HOFS 12 through 14 is attributed to the 200-μm-dia FO_3 #1 used in the systems. The smaller-diameter FO illuminates a smaller diameter on the 2-V cell than the larger-diameter 600-μm FO_3 #1 used in HOFS 9 and 10. The larger optical power density incident on the cell causes increased local currents that, in turn, cause a decrease in the conversion efficiency due to the increased voltage drop across the internal resistance of the cell.

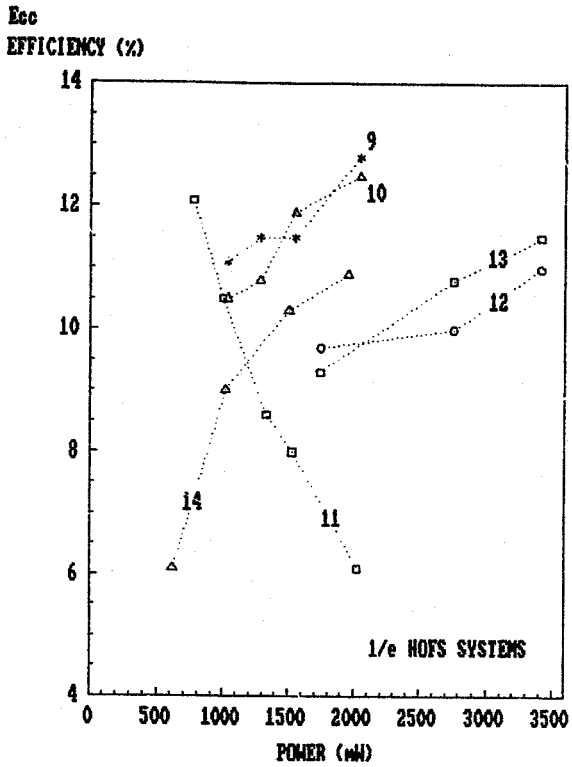

Figure 128. Efficiency of the Combination PVA GaAs Cell and dc-to-dc Converter vs. LD Output Optical Power for 1/e of V_m for Six HOFS Systems (9 Through 14) Described in Table 13

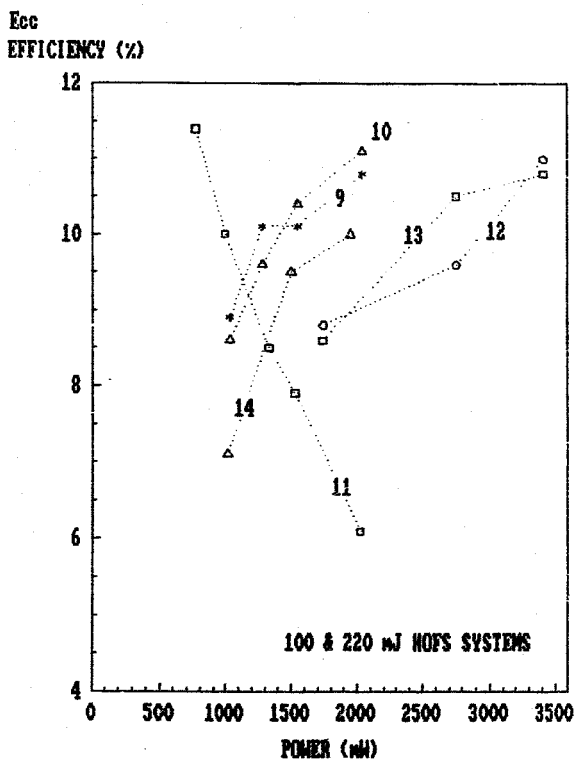

Figure 129. Efficiency of the Combination PVA GaAs Cell and dc-to-dc Conveter vs. LD Output Optical Power for 100 and 220 mJ of Energy Charge for Six HOFS Systems (9 Through 14) Described in Table 13

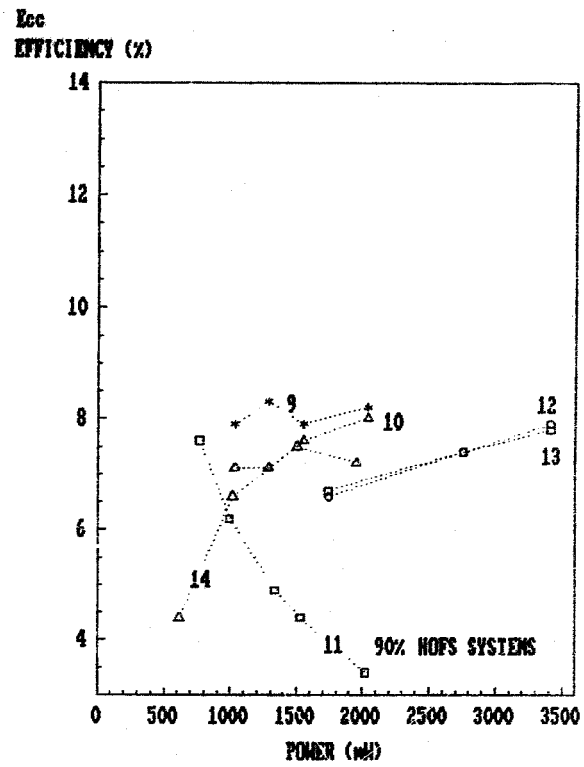

Figure 130. Efficiency of the Combination PVA GaAs Cell and dc-to-dc Converter vs. LD Output Optical Power for 90% of V_m for Six HOFS Systems (9 Through 14) Described in Table 13

HOFS 11 cannot be compared to any other system because it is the only system that uses a single 1-V cell. The converter built by Gamma uses germanium transistors, which have lower turn-on voltages than the silicon transistors so as to have more voltage available to up-convert to the large output voltage of the dc-dc converter after the oscillator turns on. The decrease in E_{cc} with increasing P_{LD} is attributed to the reduction in performance of the dc-dc converter. This reduction in performance is caused by the mismatch in impedance between the cell and the dc-dc converter at larger P_{LD}. Figure 109 shows, and Eq (34) predicts, a decrease in R_P with increasing P_{LD} values; therefore, the mismatch increases with increasing P_{LD} values. The E_{cell} of HOFS 11 does not decrease significantly with increasing P_{LD} to cause the noted decrease in E_{cc}.

6.2 HOFS System Efficiencies

The total HOFS system efficiency (E_s)—which includes the efficiency of the LD, the coupler, the PVA cell, the dc-dc converter, and capacitor—is given by:

$$E_s = \left(\frac{e_{cap}}{e_e}\right) 100 , \qquad (40)$$

where e_e, the electrical input LD energy, is given by:

$$e_e = V_{LD} \times I_{LD} \times T_c, \quad (41)$$

where V_{LD} is the voltage across the LD, I_{LD} is the current through the LD, and T_c is the time to the specific capacitor charge level.

6.2.1 First-Generation HOFS, 1–8

The shapes of the E_s curves for first-generation HOFS Systems 1 through 8 shown in Figures 131 through 133 for 1/e of V_m, 100 or 220 mJ, and 90% of V_m, differ from the E_{cc} curves of Figures 125 through 127 because the E_{LD} of the LDs and the transmission of the couplers must be folded into the E_{cc} curves in order to produce the E_s curves.

HOFS 1, 2, and 3

The E_s of HOFS 1 is much less than that of HOFS 2 because the LDs used in HOFS 1 are old and their E_{LD} was about 2.4 times less than those used in HOFS 2. The larger E_s for HOFS 3 over HOFS 2 is attributed to the change in the converter, since E_{LD} for the LDs used in HOFS 2 and 3 is comparable (24% vs. 29%).

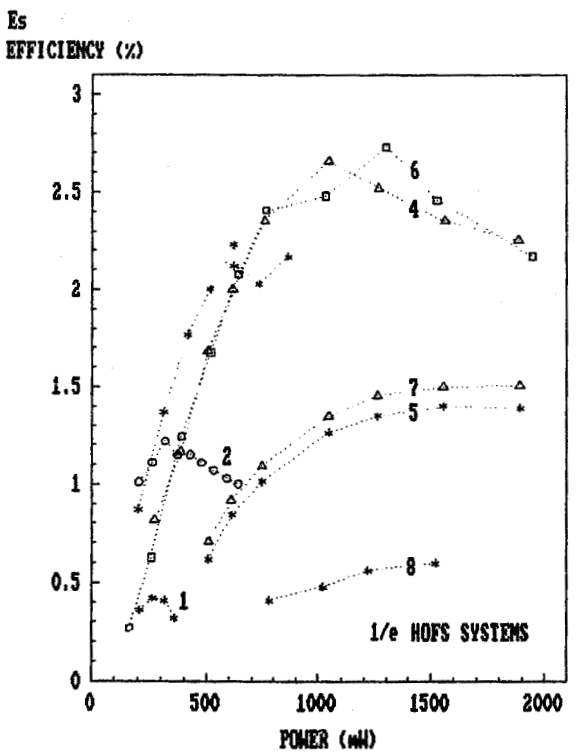

Figure 131. Total System Efficiency vs. LD Output Optical Power for 1/e of V_m for Eight HOFS Systems (1 Through 8) Described in Table 13

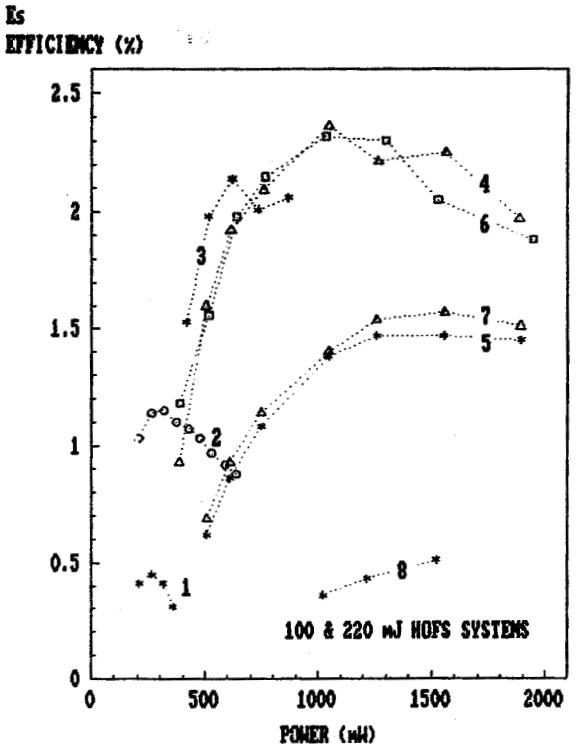

Figure 132. Total System Efficiency vs. LD Output Optical Power for 100 and 220 mJ of Charge for Eight HOFS Systems (1 Through 8) Described in Table 13

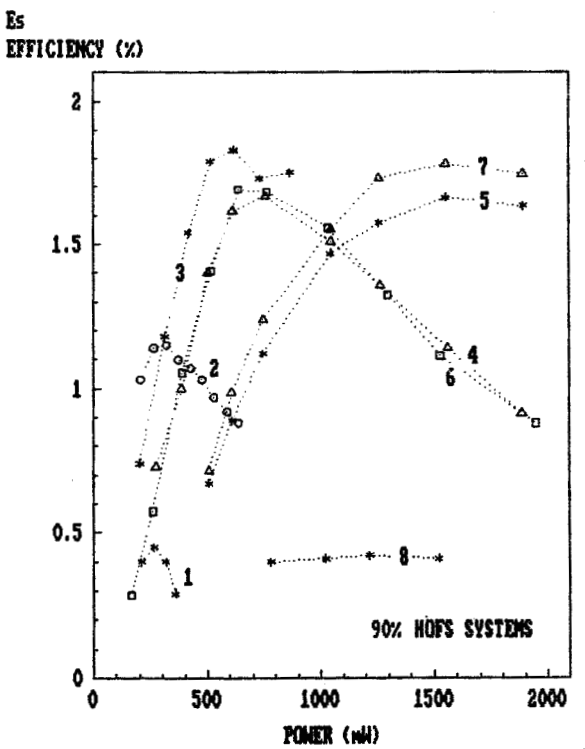

Figure 133. Total System Efficiency vs. LD Output Optical Power for 90% of V_m for Eight HOFS Systems (1 Through 8) Described in Table 13

HOFS 4 Through 7

The large increase in E_{cc} observed for HOFS 4 and 6, compared to HOFS 3, is reduced for the E_s because E_{LD} for LD A841, which is used in HOFS 4 and 6, is less than the E_{LD} for LDs A322 and B126, which are used in HOFS 3.

The shapes of the E_s curves for HOFS 4 through 7 are similar to the respective E_{cc} curves of Figures 125 through 127. The LDs and couplers are the same for these systems. The cell and converter, which are responsible for the shape of the E_{cc} curves, still control the general shape of the E_s curves for all HOFS systems except HOFS 5 and 7.

The steep increase in the slopes of HOFS 4 through 7 at low P_{LD} (~500 mW) is related to the increase in E_{LD} of LD A841 (Figure 32) at the low P_{LD} and the increase in the efficiency of the cell and dc-dc converter combination at low P_{LD} shown in Figures 125 through 127. The decrease in the slope of HOFS 4 through 7 at higher P_{LD} is controlled by the leveling-off of E_{LD} at the higher P_{LD} seen in Figure 32.

The difference in E_s for HOFS 5, 7, and 8 for the 1/e and the 100- or 220-mJ charge curves of Figures 131 and 132 is about 2.4 times at P_{LD} of 1500 mW, which is about the same difference in the E_{cc} curves shown in Figures 125 and 126.

The E_s curve for HOFS 3 at the 90% level (Figure 133) differs from the respective E_{cc} curves (Figure 127). It is evident that the increase in E_{LD} and not the shape of the E_{cc} curves causes the increase in E_s. Of all the HOFS systems tested, only HOFS 5, 7, and 8 show a continuing increase in E_s at large P_{LD}, even though HOFS 5 and 7 are beginning to exhibit saturation at the 220-mJ and the 90% levels for P_{LD} of 2.0 W.

6.2.2 Second-Generation HOFS, 9–14 and 14′

The shapes of the E_s curves used to charge the capacitor with the second-generation components for HOFS Systems 9 through 14, shown in Figures 134 through 136 for 1/e of V_m, 100, or 220 mJ, and 90% of V_m differ from the corresponding E_{cc} curves in Figures 128 through 130. The E_s curves result from the E_{cc} curves only after E_{LD} and the transmission of the couplers have been considered.

The peaks in E_s observed for HOFS 4 and 6 at P_{LD} of ~700 mW for the 90% level, 1100 mW for the 100- or 220-mJ level, and 1300 mW for the 1/e level are not observed for HOFS 9 and 10, or for HOFS 12 through 14. The maximum E_s for HOFS 9 and 10 and for HOFS 12 through 14 are all greater than the peaks mentioned above for HOFS 4 and 6.

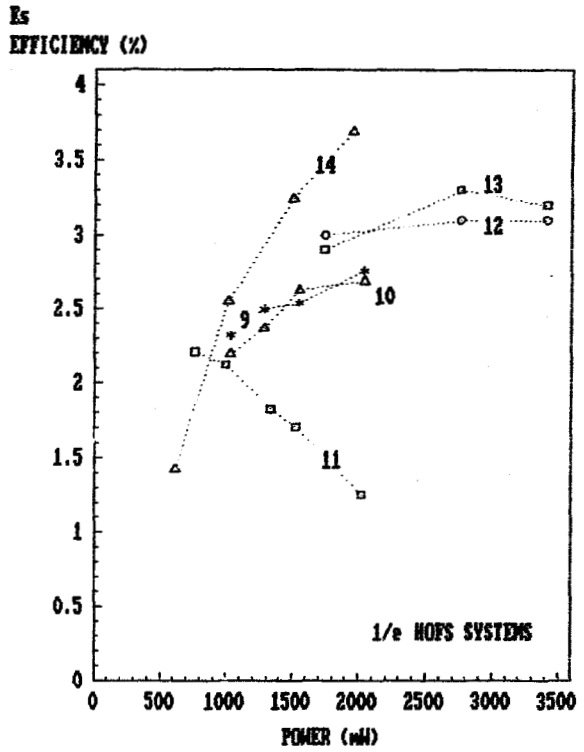

Figure 134. Total System Efficiency vs. LD Output Optical Power for 1/e of V_m for Six HOFS Systems (9 Through 14) Described in Table 13

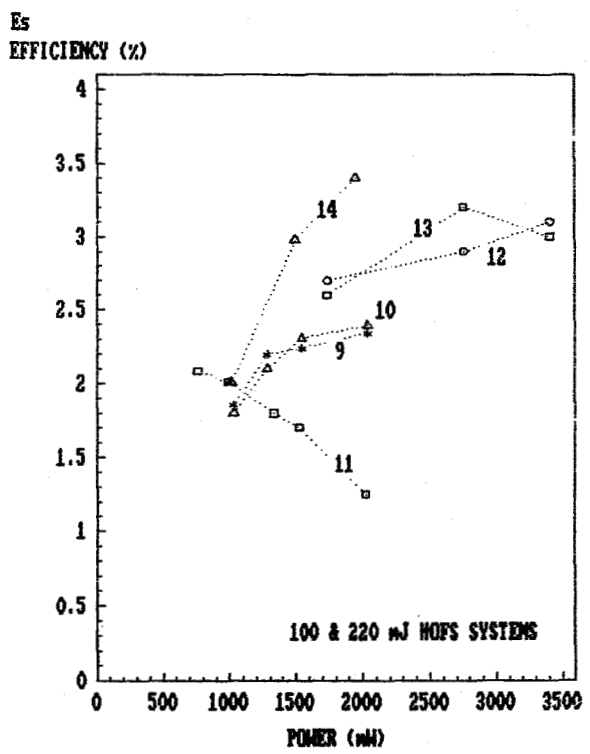

Figure 135. Total System Efficiency vs. LD Output Optical Power for 100 and 220 mJ of Charge on Six HOFS Systems (9 Through 14) Described in Table 13

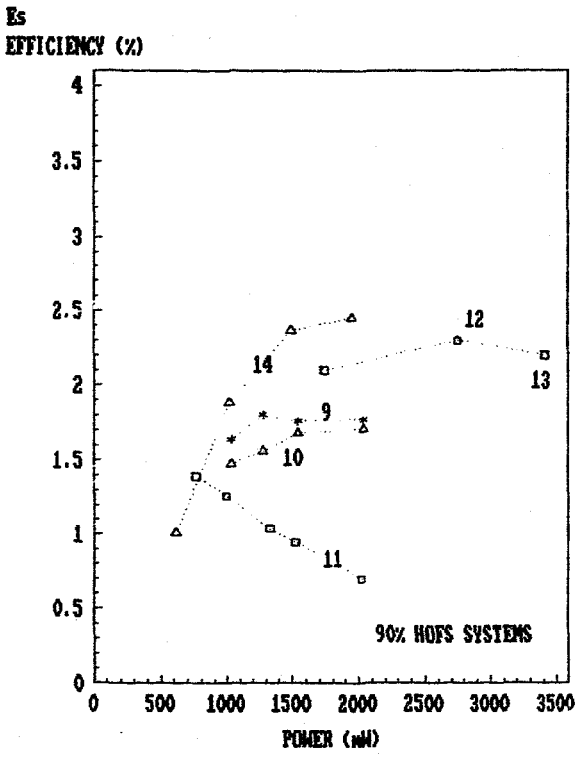

Figure 136. Total System Efficiency vs. LD Output Optical Power for 90% of V_m for Six HOFS Systems (9 Through 14) Described in Table 13

The slopes of the E_s curves for HOFS 12 through 14 are less than the slopes of the corresponding E_{cc} curves due to the slight decrease in E_{LD} (Figure 35) and the decrease in transmission of the 200-μm FO_2 #1 (Figure 70) as P_{LD} increases. Both these factors cause the slopes of HOFS 12 and 13 to be almost zero; they also cause a marked decrease in the slopes of HOFS 9 and 10. The behavior of HOFS 14, which is different than HOFS 12 and 13, is attributed to the slight increase in E_{LD} of LD RB883 over LD BM498 and the increase in transmission of FO_2 #1 when LD RB883 is used instead of BM498.

For HOFS 12 and 13, the at E_s at 1/e and 90% level of full charge (Figures 134 and 136) appear to have peaked at a P_{LD} of ~2700 mW. The E_{LD} of LD BM498 begins to decrease at ~2700 mW (Figure 35). The E_s of the 100-mJ charge level for HOFS 12 (Figure 135) has not peaked at a P_{LD} of 3400 mW. HOFS 14 has E_s values of 3.69%, 3.40%, and 2.45% for the 1/e, 100-mJ, and 90% level of full charge. These values are larger than for any other HOFS system at these E_{LD} levels. E_s for HOFS 14 has also not peaked up to the P_{LD} value of 1950 mW.

The decrease in E_s for HOFS 11 with increase in P_{LD} shown in Figures 134 through 136 follow the general trends of the corresponding E_{cc} curves of Figures 128 through 130. This correspondence is due to the converter and cell controlling the HOFS system performance.

The E_s values for HOFS 14′ are shown in Figure 137 for 100-mJ charge as the distance between the FO and the PVA cell (D_c) is varied. The 200-μm FO_2 #1 used in HOFS 14′ was repolished before it was used in HOFS 14. For LD RB883 emitting 1 W, the transmission increased from 80.3% to 83.7% after polishing. The normal distance D_c = 0.188 in. is the first data to the left of the plot. The maximum efficiency of 1.87% is measured as D_c = 0.226 in. with LD RB883 emitting 1 W. This value is 19.9% larger than the 1.57% measured for the normal D_c = 0.188-in. distance. The E_s of 1.57% for HOFS 14′ is lower than E_s of 2.01% for HOFS 14 due to the different FO transmission. The implication is that the E_s of HOFS 14 at the 1-W LD power would increase to 2.5% if the cell were in position at 0.226 in. (5.74 mm) instead of at 0.188 in. (4.78 mm). Some increase would also be observed at larger LD output power, but the amount would be less than at the 1-W level due to the beginning of saturation.

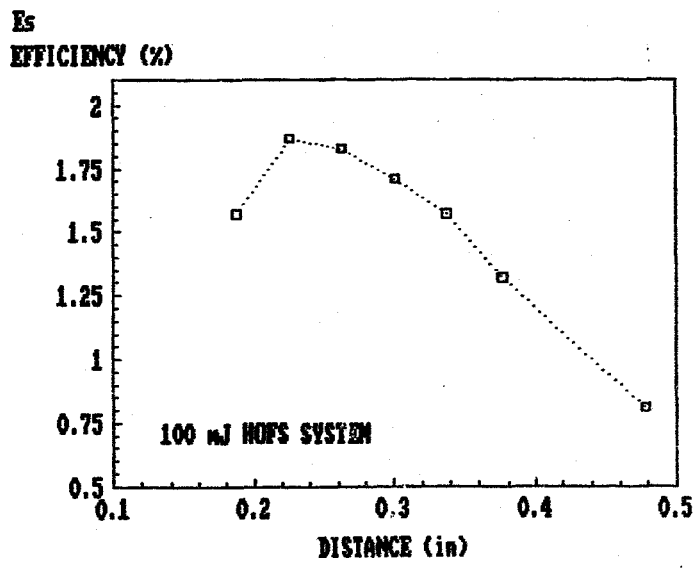

Figure 137. Total System Efficiency vs. FO to Cell Distance From 0.19 in. (4.78 mm) to 0.48 in. (12.14 mm) for 100 mJ of Charge for HOFS 14′ Described in Table 13

6.3 HOFS System Charge Times

The charge time (T_s) is first determined by measuring the maximum displacement of the voltage trace (V_m) recorded across resistor R_3, which is in parallel with the HOFS capacitor. The time on the voltage trace is measured to:

(a) 1/e of V_m

(b) 100 mJ of full charge is the time to $V_{100\,mJ} = \left(\frac{0.2}{C}\right)^{1/2}$ or for 220 mJ is $\left(\frac{0.44}{C}\right)^{1/2}$

(c) 90% of V_m.

6.3.1 First-Generation HOFS, 1–8

The charge times (T_s) for the capacitors of HOFS 1 through 8 are depicted in Figures 138 through 140 for 1/e of V_m, 100 or 220 mJ, and 90% of V_m.

1/e vs. 100-mJ Charge

For 1/e (Figure 138) and the 100- and 200-mJ (Figure 139), HOFS 4 through 7 produced the smallest T_s in decreasing order, followed by HOFS 3, 8, 2, and 1.

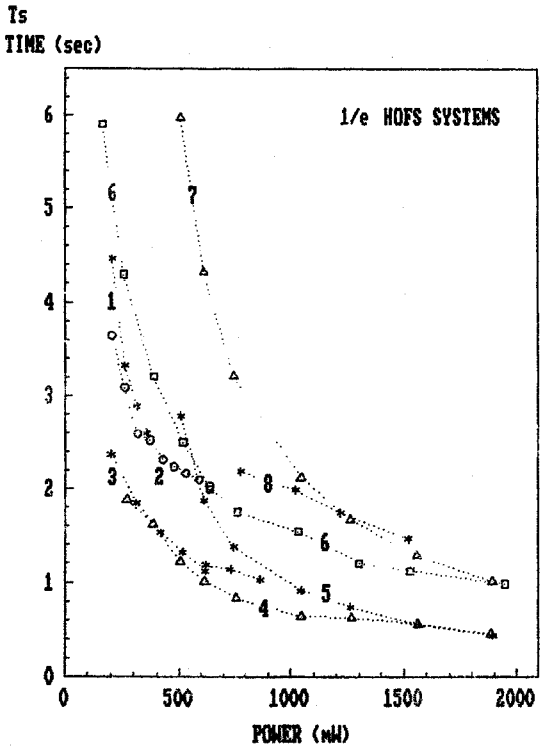

Figure 138. Charge Time for HOFS Capacitor vs. LD Output Optical Power for 1/e of V_m for Eight HOFS Systems (1 Through 8) Described in Table 13

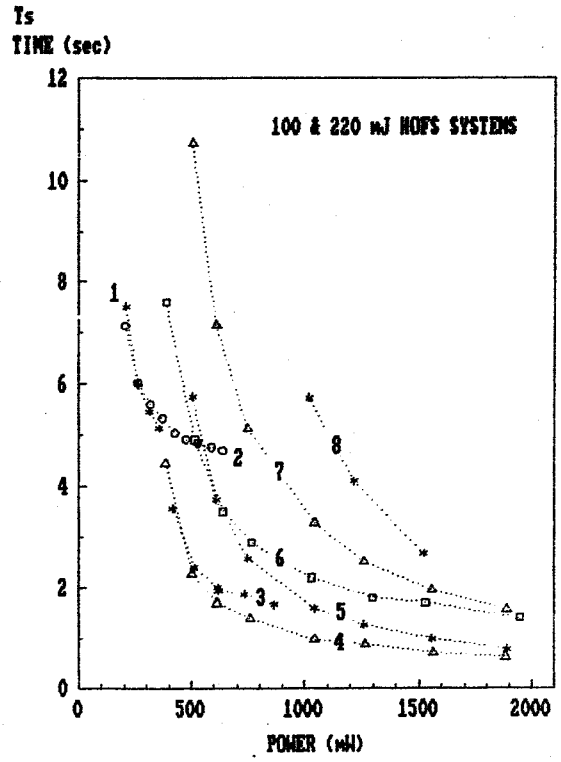

Figure 139. Charge Time of HOFS Capacitor vs. LD Output Optical Power for 100 and 220 mJ of Charge for Eight HOFS Systems (1 Through 8) Described in Table 13

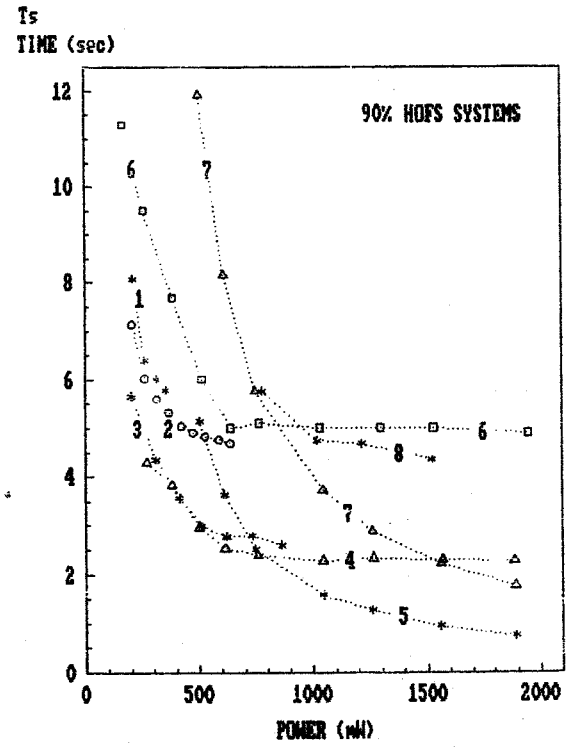

Figure 140. Charge Time of HOFS Capacitor vs. LD Output Optical Power for 90% of V_m for Eight HOFS Systems (1 Through 8) Described in Table 13

For 1/e (Figure 138), HOFS 4 and 5 have almost the same T_s value (0.45 and 0.49 s, respectively); and HOFS 6 and 7 have almost the same T_s value (0.98 s and 1.01 s, respectively) at the maximum P_{LD}. As the charge level increases, both these times separate, as shown in Figures 139 and 140. It should be noted that HOFS 5 and 7 have not leveled off at the maximum input P_{LD} onto the cell, and that T_s could still decrease if more P_{LD} were available.

90% vs. 100-mJ Charge

For HOFS 4 and 6, the abrupt leveling off of T_s for the 90% charge level at the low P_{LD} of 600 mW is believed to be converter-related. It is expected that, had HOFS 8 been operated at larger-input P_{LD} levels, it would have produced shorter T_ss, maybe even shorter than for HOFS 4 and 5 at the 100-mJ charge level. On the other hand, HOFS 2 illustrates a leveling off at large P_{LD} for all charge levels. This leveling off does not allow for any large reduction in the T_ss with increasing P_{LD}.

6.3.2 Second-Generation HOFS, 9–14 and 14′

The T_s curves for the capacitor of the second-generation components of HOFS 9 through 14 are shown in Figures 141 through 143 for 1/e of V_m, 100 or 220 mJ, and 90% of V_m. The higher E_s values for HOFS 12 through 14 compared to HOFS 9 and 10 in Figures 134 and 136 lead us initially to expect lower T_s values for HOFS 12 through 14 than observed for HOFS 9 and 10 (HOFS 9 compared to 12 and 14, and HOFS 10 compared to 13) at the same P_{LD} level. However, this does not occur. The reason is that we are plotting against LD output optical power and not input power LD used in HOFS 9 and 10 (A840) is less efficient than the LDs used in HOFS 12 through 14 (BM498 and RB883). Plotting vs. input power would move curves 9 and 10 to the right.

The T_s becomes smaller at the large P_{LD} value of 3.4 W for HOFS 12 and 13 than for the maximum P_{LD} values of HOFS 9 and 10. The T_s for HOFS 9 and 10 is unknown at P_{LD} = 3.4 W. HOFS 12 exhibits the smallest T_s value at all capacitor charge levels measured for any HOFS system for maximum P_{LD} (0.26 s for the 1/e level, 0.35 s for the 100-mJ level, and 0.73 s for the 90% level).

For all charge levels, the slope for HOFS 9 indicates that, had more P_{LD} had been available, the T_s would have continued to decrease. HOFS 4 and 9 share common components, except for the dc-dc converter and the LD. For 1/e of V_m, 100-mJ charge level, and 90% of V_m, the minimum T_s values are 0.34, 0.56, and 1.07 s for HOFS 9 compared to 0.46, 0.62, and 2.28 s for HOFS 4, respectively (Figures 138 to 140).

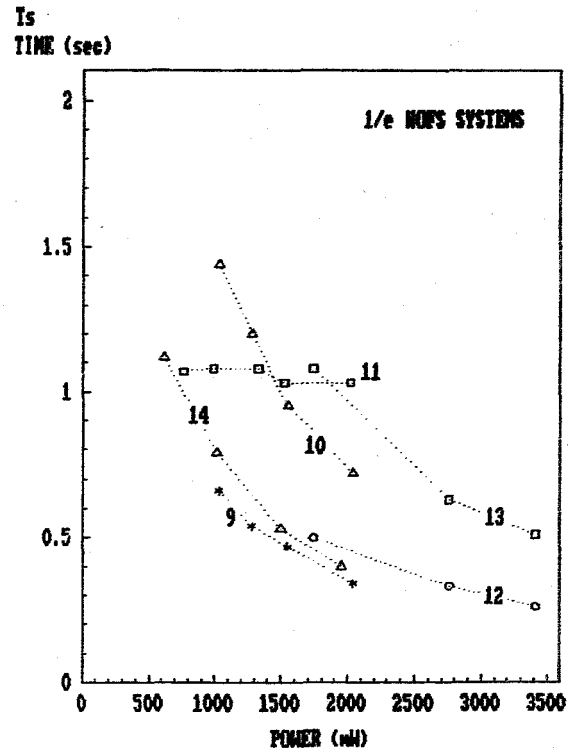

Figure 141. Charge Time of HOFS Capacitor vs. LD Output Optical Power for 1/e of V_m for Six HOFS Systems (9 Through 14) Described in Table 13

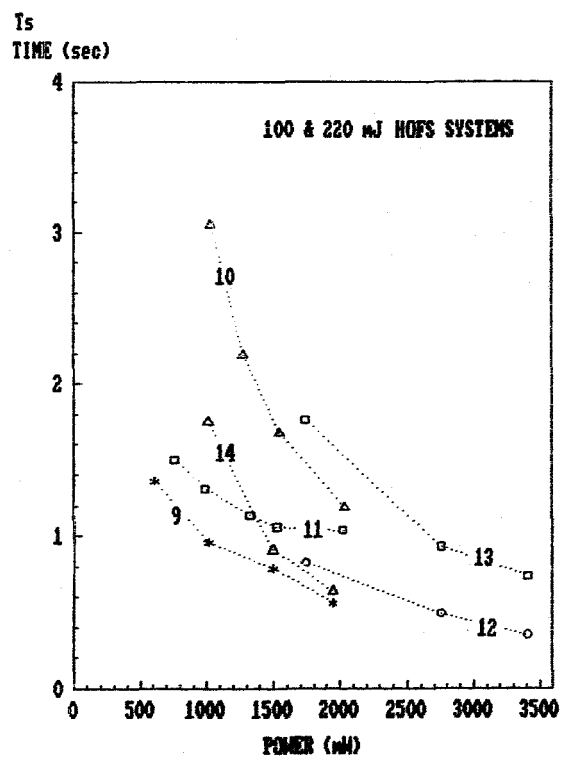

Figure 142. Charge Time of HOFS Capacitor vs. LD Output Optical Power for 100 and 220 mJ of Charge for Six HOFS Systems (9 Through 14) Described in Table 13

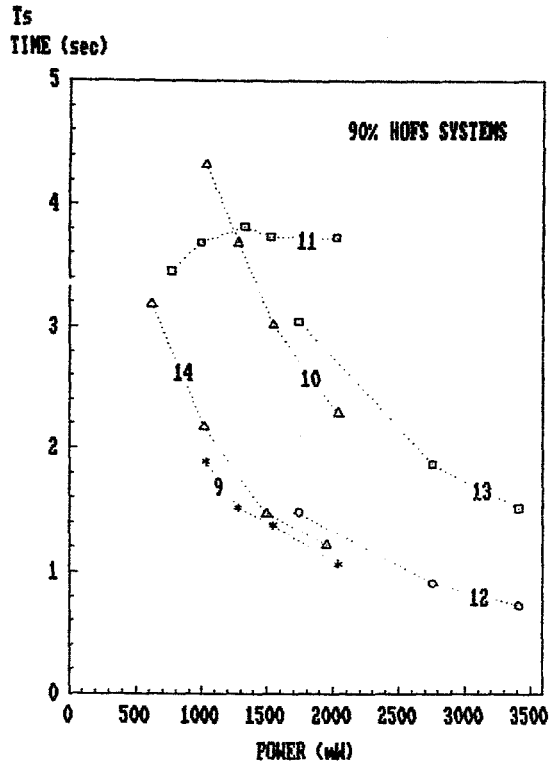

Figure 143. Charge Time of HOFS Capacitor vs. LD Output Optical Power for 90% of V_m for Six HOFS Systems (9 Through 14) Described in Table 13

For HOFS 9 and 12, the decreases in T_s over HOFS 4 are attributed to the improved performance of Gamma Model MC25/M143 over the Model MC-10N-M dc-dc converter. For HOFS 12, another improved component is the LD, which has a smaller divergence than the NA of the 200-μm FO_2 #1. This smaller LD divergence allows more P_{LD} to be coupled into the FO than is possible with other LDs. This decrease in divergence produces an increase in E_s and also causes T_s to decrease even further than observed for HOFS 9 compared to HOFS 4 where only the dc-dc converter is different.

For HOFS 14, LD RB883 is similar to LD BM498 used in HOFS 12 but is slightly more efficient. The smaller divergence of LD RB883 allows better coupling into FO_2 #1 than LD BM498. These produce larger E_s's for HOFS 14 than for HOFS 12, and also cause the T_s for HOFS 14 to be less than the T_s for HOFS 12 at the E_{LD} values tested. It is expected that, had HOFS 14 been operated at the 3.4-W level, the T_s values measured would have been less than the those observed for HOFS 12.

Similar arguments can be made for HOFS 10 and 13 (capacitor is 0.1089 μF), which differ from HOFS 9 and 12 only in their capacitor values (capacitor is 0.0524 μF).

HOFS 10 vs. HOFS 9

As expected, the T_s values essentially doubled for HOFS 10 relative to HOFS 9. The minimum T_s values for HOFS 10 compared to HOFS 9 are:

0.72 s vs. 0.34 s for the 1/e level
1.19 s vs. 0.56 s for the 100-mJ level
2.29 s vs. 1.07 s for the 90% level.

HOFS 13 vs. HOFS 12

As expected, the T_s values essentially doubled for HOFS 13 relative to HOFS 12. The minimum T_s values for HOFS 13 compared to HOFS 12 are:

0.51 s vs. 0.26 s for the 1/e level
0.74 s vs. 0.35 s for the 100 mJ level
1.52 s vs. 0.73 s for the 90% level.

HOFS 11

The T_s values for HOFS 11 are a constant of about:

1.06 s for the 1/e of V_m level
3.70 s for the 90% of V_m level.

At the 100-mJ charge level, a slight decrease from 1.5 to 1.06 s is observed, with an increase in P_{LD} from ~800 to 2000 mW.

HOFS 14′

The T_s for the capacitor of HOFS 14′ with LD emitting 1 W is shown in Figure 144, which illustrates how the 100-mJ charge changes as D_c changes. The normal operation distance D_c = 0.188 in. is the first data point to the left in the figure. The minimum charge time of 1.88 s is measured at D_c = 0.226 in. This value is 6.9% smaller than the 1.75 s measured for the normal D_c = 0.188-in. distance used in HOFS 14. The 2.24 s of HOFS 14′ is larger than the 1.75 s observed for HOFS 14 (Figure 142) for LD RB883 emitting 1.0 W at D_c = 0.188 in. The implication is that the T_s of 1.75 s of HOFS 14 at the 1-W LD power would be reduced to 1.47 s. Some decrease would occur at the larger LD power, but the amount would be less due to the leveling off of the HOFS 14 T_s curve.

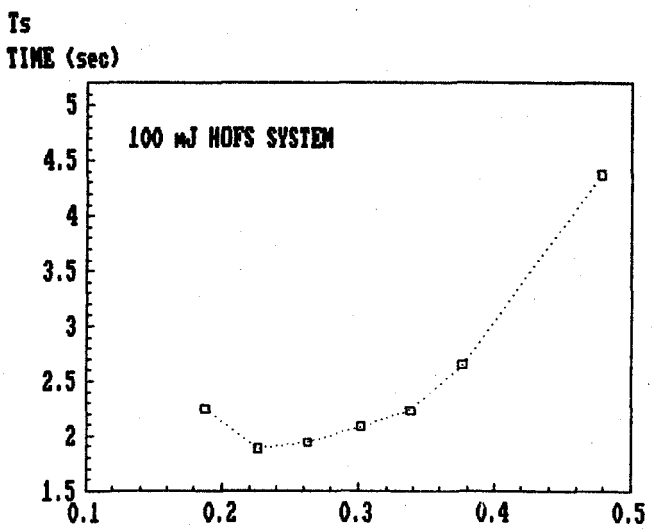

Figure 144. Charge Time of HOFS Capacitor vs. FO to Cell Distance From 0.188 in. (4.78 mm) to 0.478 in. (12.14 mm) for 100 mJ of Charge on HOFS System 14′ Described in Table 13

6.4 Summary of HOFS 1′, 1–14, and 14′

Table 14, which summarizes the 16 HOFS systems, lists the HOFS system number; laser diode number; HOFS E_{cc} in percent; HOFS E_s in percent measured and predicted; and HOFS T_s in percent for 100- and 220-mJ charge levels. The predicted values are for all components optimized.

All listings are for the largest-input P_{LD} listed in Table 13. The two system-performance identifiers are system efficiency, E_s, and system charge time, T_s.

6.4.1 First-Generation HOFS 1′, 1–8

HOFS 3 is the most efficient system in the first generation, although it is not the fastest charger. HOFS 4, charging to 100 mJ, is the fastest at 0.62 s.

The high E_{cell} values for the 1-V cell at the low input, P_{LD} (Figure 110), along with the increasing E_{LD} values at low P_{LD} values (Figure 30), helped make the HOFS 3 E_s the largest, even though E_{cc} is decreasing with increasing P_{LD} as shown in Figures 125 through 127.

For the larger capacitor storing about twice more energy (220 mJ), HOFS 7 charged in ~1.6 s. For the maximum P_{LD} value of 1.9 W, the E_s values for HOFS 4 through 7 vary from 1.5% to 2%, since E_{LD} and E_{cc} are different for these HOFS systems.

6.4.2 Second-Generation HOFS 9–14 and 14′

HOFS 14 is the most efficient of the second-generation systems tested for 100-mJ charge; it is also the most efficient 100-mJ-charged HOFS system tested. The E_s of 3.4% is certain to increase if the distance between the cell and the FO is increased from 4.78 to 5.74 mm as for HOFS 14′. HOFS 12 charges to 100 mJ in 0.35 s. It is the fastest second-generation HOFS system tested and the fastest HOFS system tested.

The high E_{cc} and P_{LD} of HOFS 12 relative to HOFS 14 helps make HOFS 12 charge faster. IF HOFS 14 could be charged with comparable $P_{LD} = 3.4$ W, it is expected that it would charge faster.

HOFS 13 is the most efficient and the fastest of the second generation systems tested for the 220-mJ charge; it is also the most efficient and fastest 220-mJ-charged HOFS system tested. The E_s is 3.0% and the T_s is 0.74 s. The E_s could increase and the T_s could decrease if the cell-to-FO distance were increased from 4.78 to 5.74 mm as was done for the HOFS 14′.

6.4.3 Best HOFS System Efficiency

The projected best HOFS system efficiency for 100-mJ charge on HOFS capacitors (listed in the last column of Table 14) is calculated using the following assumptions:

- E_{LD} could be increased to 50%, as is true for the MDAC/OEC LDs.
- The reflection losses at the end of the FO could be eliminated. This would increase the transmission for the 600-, 200-, and 100-μm FOs to 96%.
- Transmission for the 0.23-pitch GRINs would be ~95%, whereas coupling of the GRIN to the cells would be about 82% for HOFS 1′ and 1, and ~93.6% for HOFS 2 and 3.
- E_{cc} could be increased to 40% by increasing the E_{cell} to 50% and increasing the $E_{converter}$ to 80%.

The calculated E_s is between 15.6% and 19.2% for HOFS 1′ through 14.

Table 14. Performance Characteristics of the Hybrid Optical Firing Set Systems

HOFS SYS (#)	LASER DIODE (#)	PWR (W)	HOFS SYSTEM PARAMETERS MEASURED E_{CC} (%)	E_S (%) 100 mJ	E_S (%) 220 mJ	T_S (s) 100 mJ	T_S (s) 220 mJ	PROJECT E_S* (%)
1st GENERATION								
1'	A194,A200	0.34	-	0.39	-	5.5**	-	15.6
1	A194,A200	0.35	7.6	0.31	-	5.1	-	15.6
2	A321,B126	0.64	4.5	0.88	-	4.7	-	17.8
3	A321,B126	0.81	9.1	2.1	-	1.7	-	17.8
4	A841"	1.9	10.7	2.0	-	0.62	-	19.2
5	A841	1.9	9.0	1.5	-	0.78	-	19.2
6	A841	1.9	9.3	-	1.9	-	1.4	19.2
7	A841	1.9	9.3	-	1.5	-	1.6	19.2
8	A840"	1.9	2.6	0.51	-	2.6	-	19.2
2nd GENERATION								
9	A840	2.0	10.8	2.34	-	.56	-	19.2
10	A840	2.0	11.1	-	2.4	-	1.2	19.2
11	A840	2.0	6.1	1.25	-	1.04	-	19.2
12	BM498+	3.4	11.0	3.1	-	.35	-	19.2
13	BM498	3.4	10.8	-	3.0	-	0.74	19.2
14	RB883++	2.0	10.0	3.4	-	.64	-	19.2
14'	RB883	1.0	-	1.87	-	2.4	-	19.2

* If E_{LD} = 50 % E_{CC} = 40 % (E_{cell} = 50 % and $E_{converter}$ = 80 %)

** MEAS. 77 mJ LDs: " 500 mW, ++ 2 W, + 4 W, OTHERS 100 mW

7. Conclusions

The performance of the HOFS systems and their respective components have been studied in this report. The components include:

- **The laser driver.** The laser driver is capable of delivering up to 8 A of current.
- **Laser diodes.** SDL-2410-H1, SDL-2450-H1, SDL-2430-H1, SDL-2460-H1, SDL-S7081, and SDL-S7086 laser diodes delivered from 0.4 to 3.4 W of output optical power; their best efficiencies were 33%, 26%, 40%, 38%, 40%, and 37.9%, respectively.

  MDAC/OEC LDs produced efficiencies of up to 50% at the 5-W optical power level, but were unreliable.

  See Summary Section 4.1.5
- **Couplers.** These include SELFOC GRIN lenses, a P-C lens, and Ensign-Bickford FOs. Their best transmissions were greater than 95%, 92.9%, and 90.4% of the power incident on them, respectively.

  See Summary Section 4.2.4
- **GaAs cells.** The 1-, 2-, 10-, and 16-V GaAs cells had maximum efficiencies of converting optical to electrical energy of 49%, 37%, 28.5%, and 18%, respectively, when they were illuminated with a 600-μm-dia FO_3 #1 butt-coupled to an SDL-2450-H1 500-mW laser diode that emitted up to 2 W of optical power.

  See Summary Section 4.4.6.

7.1 Efficiencies of Dc-Dc Converters and GaAs Cell Combination

The efficiencies of the dc-dc converters were not measured directly but were evaluated in combination with GaAs cells; they were measured while charging the HOFS capacitor. The best cell/converter combination efficiencies (E_{cc}) for the HOFS capacitor charged to

- 100 mJ was 10.7% for HOFS 4 and 11% for HOFS 12 in the first- and second-generation HOFS systems, respectively
- 220 mJ was 9.3% for HOFS 6 and 7 and 11.1% for HOFS 10 in the first- and second-generation HOFS systems, respectively.

HOFS System Efficiency

The best total HOFS system efficiency (E_s) for the HOFS capacitor charged to:

- 100 mJ was 2.1% for HOFS 3 and 3.4% for HOFS 14 in the first- and second-generation HOFS systems, respectively
- 220 mJ was 1.9% for HOFS 6 and 3.0% for HOFS 13 in the first- and second-generation HOFS systems, respectively.

E_s for HOFS 13 and 14 would increase if the cell-to-FO distance were to be increased from 4.78 to 5.72 mm as was done for HOFS 14′.

7.2 HOFS System Charge Time

The shortest charge times (T_s) for the HOFS capacitor charged to

- 100 mJ was 0.62 s for HOFS 4 and 0.35 s for HOFS 12 in the first- and second-generation HOFS systems, respectively.
- 220 mJ was 1.4 s for HOFS 6 and 0.74 s for HOFS 13 in the first- and second-generation HOFS systems, respectively.

T_s for HOFS 12 and 13 would decrease if the cell-to-FO distance were to be increased from 4.78 to 5.77 mm as was done for HOFS 14′.

Figure 145 summarizes the best efficiencies measured in a system. The figure also summarizes what should be possible to achieve in the near future. The predicted best HOFS system efficiency can be increased to 19.2% if

- the LD efficiency is increased to 50%
- the 200-μm FO transmission is increased to 96% by Ar-coating the ends
- the hybrid solar cell efficiency is increased to 50% by developing and tailoring it to LD-type illumination
- the dc-dc converter efficiency is increased to 80% by matching its input impedance to that of the hybrid cell.

These improvements are all realistic and achievable.

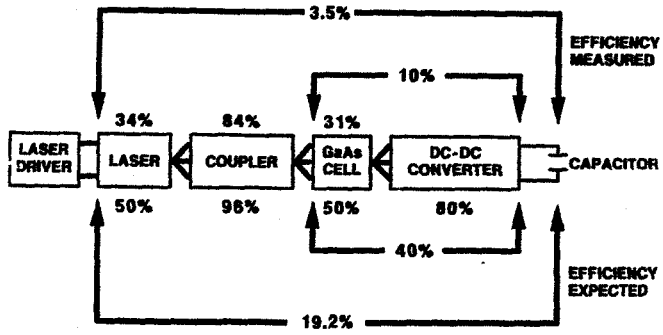

Figure 145. Block Diagram Summarizing HOFS System and Component Efficiencies for the Best HOFS System (14), Measured and Predicted HOFS System, and Component Efficiencies Achievable in the Near Future

References

[1]L. C. Yang and V. J. Menichelli, "Detonation of Insensitive High Explosives by a Q-Switched Ruby Laser," *Appl Phys Lett*, 19(11) December 1, 1971.

[2]M. J. Barbarisi and E. G. Kessler, "Initiation of Secondary Explosive by Means of Laser Radiation," Technical Report 3861, Picatinny Arsenal, Dover, NJ, 1969.

[3]C. L. Wright, C. L. Mavis, and M. J. Landry, *Feasibility of a Laser Firing System for Secondary Explosives (U)*, SAND77-8025 (Albuquerque, NM: Sandia National Laboratories, March 1978). Confidential.

[4]J. Baoren, C. Danming, W. Zuoni, L. Yulian, Z. Kering, L. Xufa, and L. Yide, "Experimental Studies on PETN, Detonators Initiated by Laser Radiation," *Proceedings of International Symposium on Pyrotechnics and Explosives, October 12-15, 1987, Beijing, China*, pp 49-56.

[5]W. M. Trott, "Optical Studies of Laser-Driven Flyers," presented at Spring Meeting of APS, 1986.

[6]D. Paisley, Los Alamos National Laboratory, Los Alamos, NM, private communication, October 1987.

[7]M. M. Robertson, "Power Transfer Via Fiber Optics," *Proceedings of the Thirtieth Electronic Components Conference*, 1980.

[8]M. M. Robertson and J. P. Wolfe, *Powering an MC2901 Electronic Assembly by Optical Means*, SAND80-1736 (Albuquerque, NM: Sandia National Laboratories, 1980).

[9]A. Santic and M. Neuman, "A Low-Voltage dc-dc Converter for Implanted Electronic Circuits," *J of Bioengineering*, 1:357-368 (1977).

[10]R. P. Roberts, "Optic Coupling in Fire Sets Applications," *Proceedings of the Tenth Annual Joint Firing System Conference*, Oct. 22-23, 1985, pp47-61.

[11]D. R. Scifres, R. D. Burnham, and W. Streifer, "High-Power-Coupled Multiple-Striped Quantum Well Injection Lasers," *Appl Phys Lett*, 41:118-120 (1982).

[12]D. R. Scifres, R. D. Burnham, and W. Streifer, "Lateral Grating Array High-Power CW Visible Semiconductor Laser," *Electronic Letters*, 18:549-550 (1982).

[13]D. R. Scifres, R. D. Burnham, and W. Streifer, "Continuous-Wave, High-Power, High-Temperature Semiconductor Laser Phase-Locked Arrays," *Appl Phys Lett*, 41:1030-32 (1982).

[14]B. A. Tuttle, B. H. Rose, R. G. Keefe, and D. J. Brunty, *Optical Energy Transfer Subassemblies*, SAND87-0163 (Albuquerque, NM: Sandia National Laboratories, April 1987).

[15]L. A. D'Asaro, "Advances in GaAs Junction Lasers With Stripe Geometry," *J Lumin* 7:310-337 (1973).

[16]D. R. Scifres, C. Lindstrom, R. D. Burnham, W. Streifer, and T. L. Paoli, "Phase-Locked (GaAl)As Laser Diode Emitting 2.6 W CW From a Single Mirror," *Electronic Letters*, 19:169-171 (1983).

[17]W. Streifer, R. D. Burnham, T. L. Paoli, and D. R. Scifres, "Phased Array Diode Lasers," *Laser Focus*, 20:100-109 (1984).

[18]R. D. Dupries and P. D. Dapkus, "Room-Temperature Operation of $Ga_{(1-x)}Al_xAs/GaAs$ Double-Heterostructure Laser Grown by Metalorganic Chemical Vapor Deposition," *Appl Phys Lett*, 3:466-468 (1977).

[19]G. Harnagel, D. Welch, P. Cross, and D. R. Scifres, "High-Power Laser Arrays: A Progress Report," *Lasers and Applications*, 5:135-138 (June 1986).

[20]D. R. Scifres, D. Welsh, G. Harnagel, P. Cross, H. Kung, N. Strifer, and J. Berger, "Power Limits, Efficiency, and Reliability of 1-D and 2-D Laser Diodes and Diode Arrays," *SPIE O-E/Lase, 1988, Conference 893, High-Power Laser Diodes and Application*, Paper 893-901 (1988).

[21]D. Welsh, B. Chang, and D. R. Scifres, "High-Power 8-W CW Single-Quantum Well Laser Diode Array," *Electronic Letters*, 24:113-115 (1988).

[22]P. Tihanyi, D. K. Wagner, A. J. Roza, H. J. Vollmer, and C. M. Harding, "High-Power AlGaAs/GaAs Single-Quantum Well Lasers With Chemically Assisted Ion-Beam-Etched Mirrors," *Appl Phys Lett*, 50:1640-41 (1987).

[23]E. J. Frieble, G. G. Askins, M. E. Gingerich, and K. J. Long, "Optical-Fiber Waveguides in Radiation Environments II," *Nuclear Instrumentation and Methods in Physics*, pp 355-369 (1984).

[24]H. Gozen, A. Tanaka, T. Utsumi, T. Maeda, and S. Okamoto, "Radiation-Resistant Pure-Silica-Core Single-Mode Fibers," *Proceedings of the Conference on Electrical Insulation and Dielectric Phenomena, October 21-25, 1984*, IEEE Catalog No. 84CH-1994-3, pp 65-70.

[25]K. Koizumi, K. Nishizawa, and K. Sono, *SELFOC Handbook* (Clark, NJ: Nippon Sheet Glass America, Inc., a subsidiary of Nippon Sheet Glass Co., Ltd., 1980).

[26]K. Sono, *SELFOC Technology: Its Application*, Nippon Sheet Glass Co. Ltd., Clark, NJ, 1987.

[27]*Data Sheet, SELFOC Micro Lens Specifications*, Nippon Sheet Glass America, Inc., August 1987.

[28]R. L. Rypma, "Laser Beam Profiling the Automated Way," *Photonic Spectra*, 21:67-74 (1987).

[29]*Semiconductor and Semimetals, Volume 22: Lightwave Communication Technology. Part C: Semiconductor Injection Lasers, II, Light-Emitting Diodes*, W. T. Tsang, ed. (New York: Academic Press, 1985) p 62.

[30]J. C. Dyment, L. A. D'Asaro, J. C. North, B. I. Miller, and J. E. Ripper, "Proton Bombardment Formation of Stripe-Geometry Heterostructure Lasers for 300°K CW Operation," *Proceedings of IEEE*, 60:726-728 (1972).

[31]H. Yonezu, I. Sakuma, K. Kobayashi, T. Kamejuma, M. Uano, and Y. Narinichi, "A GaAs-Al_x $Ga_{1-x}As$ Double Heterostructure Planar Stripe Laser," *J Appl Phys*, 12:1585-92 (1973).

[32]N. Chinone, R. Ito, and O. Nokada, "Limitations of Power Outputs From Continuous Operating GaAs-$Ga_{1-x}Al_x$ Double-Heterostructure Lasers," *J Appl Phys*, 47:785-786 (1976).

[33]D. Welsh and R. Klein, Spectra Diode Laboratory, San Jose, CA, private communication, October 1987.

[34]G. L. Harnagel, T. L. Paoli, R. L. Thornton, R. D. Burnham, and D. L. Smith, "Accelerated Aging of 100-mW CW Multiple-Stripe GaAlAs Lasers Grown by Metalorganic Chemical Vapor Deposition," *Appl Phys Lett*, 46:118-120 (1985).

[35]H. J. Hovel, *Semiconductor and Semimetals, Volume 11: Solar Cells* (New York: Academic Press, Inc., 1975), p 70.

[36]P. G. Borden, "A Monolithic Series-Connected $Al_{0.93}$ $Ga_{0.07}$ As/GaAs Solar Cell Array," *Appl Phys Lett*, 35:553-554 (1979).

DISTRIBUTION:

1	Space Power Institute Attn: Dr. E. Clothiaux 231 Leach Center Auburn University Auburn, AL 36849
1	Whittaker Laser Products Attn: J. Petrick 410 E. Western Ave. Avondale, AZ 85323
2	Los Alamos National Laboratory Attn: D. Paisley, M-7 R. McCormick, M-7 Los Alamos, NM 87545
2	Lawrence Livermore National Laboratory Attn: R. E. Lee, L368 C. T. Cuddihy, L-125 PO Box 808 Livermore, CA 94550
1	Monsanto Research Corp. Mound Facility Attn: J. Cheng PO Box 32 Miamisburg, OH 45342
1	Lockheed Missiles Space Co., Inc. Attn: Werner A. Gans, 0/80-09 B/154 1111 Lockheed Way Sunnyvale, CA 94089-3504
1	Bendix, Kansas City Division Attn: W. J. Kirk, D/341, MF39 2000 East 95th St. Kansas City, MO 64131

1	1120	J. B. Gerardo
1	1160	A. Owyoung
1	1270	J. K. Rice
1	2000	G. T. Cheney
1	2300	J. L. Wirth
1	2311	T. D. Donham
1	2360	P. A. Longmire
1	2361	T. J. Williams
5	2362	M. J. Landry
1	2362	M. B. Murphy
1	2364	J. F Jones, Jr.
1	2364	A. Mittas
3	2364	J. W. Rupert
1	2500	R. L. Schwoebel
1	2510	D. H. Anderson
1	2512	J. G. Harlan
1	2513	D. E. Mitchell
1	2514	L. L. Bonzon
1	2515	P. D. Wilcox
1	2520	N. J. Magnani
1	2530	G. M. Ferguson
1	2531	R. F. Carson
1	2531	M. M Robertson
1	2531	E. P. Royer
1	2531	W. D. Williams
1	2531	T. L. Woolston
1	2543	S. F. Kuehn
1	2543	K. G. McCaughey
1	2543	P. J. Wilson
1	2560	J. T. Cutchen
1	4000	M. R. Kestenbaum
1	5100	H. W. Schmitt
1	5160	G. R. Otey
1	5161	K. D. Nokes
1	5166	K. D. Meeks
1	5166	R. C. Hartwig
1	5166	R. E. Setchell
1	6224	D. G. Schueler, Actg.
1	6224	J. M. Gee
1	6224	B. R. Hansen
1	7100	C. D. Broyles
1	7132	A. B. Church
1	7232	R. D. Pedersen
1	7232	S. D. Spray
1	7240	R. T. Johnson
1	7500	D. M. Olson
1	8100	E. E. Ives
1	8300	P. L. Mattern
1	8400	R. C. Wayne
1	9000	R. L. Hagengruber
1	8525	J. A. Wackerly
5	3141	S. A. Landenberger
8	3141-1	C. L. Ward For DOE/OSTI
3	3151	W. I. Klein